PRECISION MEASUREMENT OF THE NEUTRON ASYMMETRY A_1^n AT LARGE BJORKEN X AT 12 GEV JEFFERSON LAB

Mingyu Chen

Newport News, Virginia

Bachelor of Science, University of California Santa Barbara, 2016

A Dissertation submitted to the Graduate Faculty

of the University of Virginia in Candidacy for the Degree of

Doctor of Philosophy

Department of Physics

University of Virginia

Fall 2023

Xiaochao Zheng, Chair

Nilanga Liyanage. Member

Donal Day. Member

Sara Maloni. GSAS Rep

Jianping Chen. Member

ii

Precision Measurement of the Neutron Asymmetry A_1^n at Large Bjorken x at 12 GeV Jefferson Lab

Mingyu Chen

(ABSTRACT)

The virtual photon asymmetry A_1 is one of the fundamental quantities that provide information on the spin structure of the nucleon. The value of A_1 at high x_{Bj} is of particular interest because valence quarks dominate in this region, which makes it a relatively clean region to study the nucleon structure. Several theoretical calculations, including naive SU(6) quark model, relativistic constituent quark model (RCQM), perturbative QCD (pQCD), predict the behavior for A_1 and the quark polarization in the high x_{Bj} valence quark region. The A_1^n experiment during the 6 GeV JLab era showed that A_1^n turns positive at $x \sim 0.5$, while up to the highest measured x value of 0.61 the down quark polarization $\Delta d/d$ remains negative, in contrast to the pQCD prediction. Subsequent theoretical studies following the 6 GeV results claimed that quark orbital angular momentum could delay the upward turn of $\Delta d/d$ to higher x_{Bj} or the non-perturbative nature of the strong interaction could keep it negative all the way to $x_{Bj} = 1$ as predicted in a Schwinger-Dyson approach with di-quark model assumptions. With the 12 GeV upgrade of JLab, a new experiment on A_1^n (E12-06-110)[1] was carried out using a 10.4 GeV beam, a polarized ^{3}He target, and the HMS and the Super-HMS (spectrometers) in Hall C. This measurement reached a deeper valence quark region, reaching up to $x \sim 0.75$. This thesis reports on the 3He asymmetries $A_\parallel$, $A_\perp$, A_1^{3He}, and A_2^{3He} without radiative corrections.

Dedication

This thesis is dedicated to my parents, who have supported me throughout my educational journey. Thank you for helping me see this adventure through to the end.

Acknowledgments

I express my sincere gratitude to my advisor, Dr. Xiaochao Zheng, for her unwavering support and guidance throughout my Ph.D. journey. I extend my appreciation to Dr. Brad Sawatzky and Dr. Todd Averett at the College of William and Mary, along with other collaborators. Their assistance and mentorship during the experimental data collection and analysis were instrumental. Special thanks go to my colleagues during this experiment, including William Henry, Arun Tadepalli, Junhao Chen, Murchhana Roy, and Melanie Cardona. The support from the engineering team, technical staff, and survey group at Jefferson Lab was indispensable for the success of the experiment. I am grateful to my committee members, Dr. Nilanga Liyanage, Dr. Donal Day, Dr. Jian-Ping Chen and Dr. Sara Maloni, for dedicating their time and expertise to serve on my advisory committee. Dr. Donal Day's insightful comments played a crucial role in the completion of my dissertation. A heartfelt acknowledgment goes to Nguyen Ton, whose introduction led me to the outstanding research opportunity at Jefferson Lab, allowing me to join the polarized ^{3}He target group and initiate my Ph.D. research. I also thank my colleagues at the University of Virginia for their insights and assistance in my research endeavors. Special gratitude to Jixie Zhang and Michael Nycz for sharing their expertise in experimental nuclear physics and helping me navigate the analysis software.

Contents

viii

x

List of Figures

List of Tables

Chapter 1

Introduction

This experiment (E12-06-110) conducted in Hall C at Jefferson Lab aimed to measure the neutron spin asymmetry, A_1^n, in the far valence domain. The goal was to improve our understanding of how the total spin of a nucleon emerges from the intrinsic spin and orbital momentum of its constituents—quarks and gluons.

Using the Jaffe-Manohar spin sum rule (Jaffe and A. Manohar 1990), the nucleon spin can be decomposed into four components, which are valence and sea quark intrinsic spin $\Delta \sum$, quark orbital angular momentum L_q, gluon intrinsic spin ΔG, and gluon orbital angular momentum L_g:

$$\frac{1}{2} = \frac{1}{2} \Delta \sum + \Delta G + L_q + L_g \tag{1.1}$$

Initially, it was believed that quark intrinsic spin would be the dominant contributor to nucleon spin. The static quark model which predicted it contributed $\sim 100\%$, and even relativistic quark models predicting a hefty $\sim 60\%$ from the intrinsic quark spin and $\sim 40\%$ from their orbital angular momentum (OAM) (Aidala et al. 2013).

However, early experiments in the 80s, particularly on the proton showed that the intrinsic quark spin contributed little to the overall proton spin (Ashman et al. 1988).

Current understanding suggests that quark intrinsic spin contributes roughly 30%

(S. E. Kuhn, J. P. Chen, and Leader 2009), while gluons contribute about 20%(Florian et al. 2014), with considerable uncertainties, especially in the small x region. This uncertainty leaves about half of the gluon spin source attributed to the angular momentum of quarks and gluons.

Inclusive Deep Inelastic Scattering (DIS) measurements in the high x region at Jefferson Lab are primarily influenced by contributions from valence quarks, with nearly no sensitivity to gluons and sea quarks (Deur, Brodsky, and De Téramond 2018). This experimental simplicity, devoid of complications from gluons and sea quarks, allows theories and models to offer predictions. Comparing experimental data with these theoretical predictions allows us to understand the nucleon's structure. This comparison helps determine whether the spin structure is primarily governed by perturbative QCD (pQCD predictions) or non-perturbative effects (Dyson-Schwinger Equations predictions). Additionally, in the context of pQCD, it can shed light on the significance of orbital angular momentum contributions (pQCD with OAM vs. without OAM).

Chapter 2

Physics Motivation for Measuring A_1^n at high x_{Bj}

2.1 Electron Scattering and Deep Inelastic scattering

The simplest depiction of electron scattering with a nucleus is the concept of one-photon exchange. This scenario, illustrated in Figure 2.1, involves the electron's initial and final 4-momentum denoted as $k^\mu = (E, \vec{k})$ and $k'^\mu = (E', \vec{k'})$.

$$k' = (E', \vec{k'})$$
$$s'$$

$$P' = (E'_t, \vec{P'})$$
$$S'$$

$$q = (\nu, \vec{q})$$

$$k = (E, \vec{k})$$
$$s$$

$$P = (M, \vec{0})$$
$$S$$
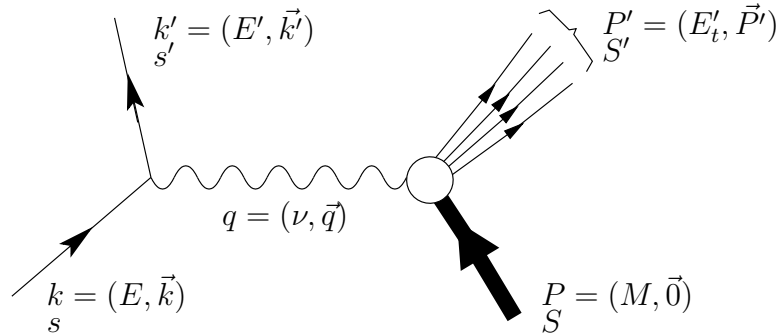
Figure 2.1: Electron scattering with a nucleus through one-photon exchange (Zheng 2002).

In the laboratory frame, with a fixed target mass $p^\mu = (M_t, \vec{0})$, the virtuality of the exchanged photon is denoted as $Q^2 \equiv -q^2$, with $q^\mu = k^\mu - k'^\mu = (\nu, \vec{q})$ representing

the four-momentum of the exchanged photon. The invariant mass, denoted as W, can be expressed as follows:

$$W \equiv \sqrt{(q+p)^2} \equiv \sqrt{M^2 + 2M\nu - Q^2}. \tag{2.1}$$

The energy transfer, denoted as ν, represents the amount of energy exchanged or transferred in a given process:

$$\nu = E - E'. \tag{2.2}$$

The four-momentum transfer-squared, denoted as Q^2, refers to the square of the 4-momentum transferred in this process:

$$Q^2 = -q^2 = -(k - k')^2 = 4EE' \sin^2\left(\frac{\theta}{2}\right), \tag{2.3}$$

as $m_e \ll E, E'$. Figure 2.2 illustrates the cross section for inclusive electron scattering from a nuclear target, where it is plotted as a function of the momentum transfer Q^2 and the energy transfer ν. Depending on the specific values of Q^2 and ν, electron scattering is categorized into various regions, including elastic scattering, quasi-elastic scattering, the resonance region, and the deep inelastic scattering region.

- Elastic Scattering:

   When the values of Q^2 and ν are low, which satisfy $\nu = \frac{Q^2}{2M}$ where M is the mass of the target. For elastic scattering, the spatial resolution is not sufficiently high to observe the interior composition of the target. Consequently, the target nucleus remains unchanged, and the electron scatters elastically. In this elastic scattering, the momentum transfer is evenly distributed among the nucleons.
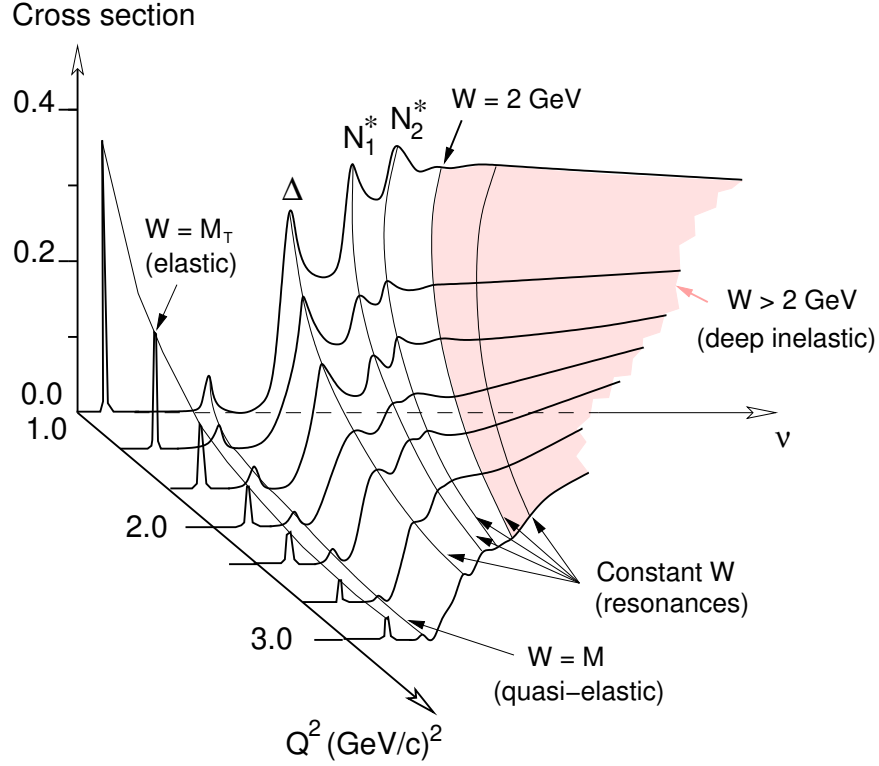
Figure 2.2: Cross section for inclusive electron scattering from a light nuclear target as a function of Q^2 and ν. The units for cross section is arbitrary (Zheng 2002).

The invariant mass for elastic scattering can be expressed as $W^2 \equiv M_T^2 + 2M_t\nu - Q^2 = M_T^2$, where M_T represents the mass of the target.

- Quasi-elastic Scattering:

  Quasi-elastic scattering occurs when the energy transfer ν is greater than the nuclear binding energy, and the invariant mass W^2 equals the square of the scattered nucleon mass M^2 ($W^2 = M^2$). In this process, the electron scatters elastically from one of the nucleons inside target nucleus. Thus nucleons within the nucleus are not stationary and they possess an initial momentum of approximately 55-250 MeV due to their motion within the target nucleus (Povh, Rith, and Scholz 2004). This motion leads to the broadening of the quasi-elastic

peak, which is centered at $\nu = \frac{Q^2}{2M}$, where ν represents the energy loss from the elastic scattering of a free nucleon.

- Resonance:

  As the values of Q^2 and ν continue to increase, the nucleon enters excited states, commonly known as the resonance region. The resonance region typically refers to the range of $1.2 < W < 2.0$ GeV/c^2. In this region, the quarks within the nucleon absorb the virtual photon and form nucleon resonances. The invariant mass for the resonance region is given by $W^2 \equiv M^2 + 2M\nu - Q^2 = M_{N^*}^2$, where M_{N^*} represents the mass of the resonance N^*. The $\Delta(1232)$, with a mass of $M_\Delta = 1.232$ GeV/c^2 and total spin $J = \frac{3}{2}$, is the first observed resonance. In inclusive experiments, the $\Delta(1232)$ is typically the only clearly visible resonance. Higher resonances may be observed beyond $W > 1.4$ GeV/c^2, with overlapping tails. In addition, the resonance peak extend beyond W > 2 GeV GeV/c^2 which exhibits a high twist in the scattering diagram. This broad resonance appears as a continuous curve.

- Deep Inelastic Scattering (DIS):

  As Q^2 and ν reach very large values, the resonance strengths decrease, leading to the entry into the deep inelastic scattering (DIS) region. In this dissertation, the DIS region refers to $W > 2$ GeV/c^2 region. In the DIS region, the partonic structure of the nucleon is probed as the electron scatters off a quark or antiquark that behaves as an asymptotically free particle within the nucleon. To quantify the fraction of the nucleon's momentum carried by the struck quark in the nucleon's infinite momentum frame, the dimensionless Bjorken scaling variable x is defined:

$$x = x_{Bj} \equiv \frac{Q^2}{2P \cdot q} = \frac{Q^2}{2M\nu}, \tag{2.4}$$

when the target nucleon remains fixed in position.

The main focus of the A_1^n experiment (E12-06-110) was to study the phenomenon of deep inelastic scattering (DIS) region.

2.2   Unpolarized and Polarized Structure functions

The expression for the differential cross section of the lepton scattering process involving one-photon exchange, as depicted in Figure 2.1, is given by:

$$\frac{d^2\sigma}{d\Omega dE'} = \frac{\alpha^2 E'}{Q^4 E} L_{\mu\nu} W^{\mu\nu}, \tag{2.5}$$

where α represents the electromagnetic fine structure constant. For an incoming lepton with a helicity of $\pm 1/2$, the leptonic tensor $L_{\mu\nu}$ can be written as follows:

$$L_{\mu\nu}(k, s; k', s') = \left[\bar{u}(k', s')\gamma_\mu u(k, s)\right]^* \left[\bar{u}(k', s')\gamma_\nu u(k, s)\right], \tag{2.6}$$

where k and k' represent the four-momentum of the lepton, while s and s' denote the lepton spin four-vectors. When the interchange $\mu \leftrightarrow \nu$ is performed, the symmetric part (S) of the leptonic tensor $L_{\mu\nu}$ corresponds to an unpolarized lepton. On the other hand, the anti-symmetric part (A) of $L_{\mu\nu}$ corresponds to a polarized lepton, with the lepton spin information taken into account.

$$L^{\mu\nu} = 2k^\mu k'^\nu + 2k'^\mu k^\nu + g^{\mu\nu} q^2 \mp 2i\epsilon^{\mu\nu\lambda\rho} k_\lambda k'_\rho \tag{2.7}$$

The hadronic tensor $W_{\mu\nu}$ is composed of both a symmetric part (S) and an anti-

symmetric part (A):

$$W_{\mu\nu}(q; P, S) = W_{\mu\nu}^{(S)}(q; P) + iW_{\mu\nu}^{(A)}(q; P, S). \tag{2.8}$$

The structure functions $W_{1,2}$ (unpolarized) and $G_{1,2}$ (polarized) can be obtained from the symmetric and anti-symmetric parts of the hadronic tensor $W_{\mu\nu}$, which are:

$$\frac{1}{2M}W_{\mu\nu}^{(S)}(q; P) = \left(-g_{\mu\nu} + \frac{q_\mu q_\nu}{q^2}\right)W_1(P \cdot q, q^2)$$
$$+ \left[\left(P_\mu - \frac{P \cdot q}{q^2}q_\mu\right)\left(P_\nu - \frac{P \cdot q}{q^2}q_\nu\right)\right]\frac{W_2(P \cdot q, q^2)}{M^2} \tag{2.9}$$

$$\frac{1}{2M}W_{\mu\nu}^{(A)}(q; P, S) = \epsilon_{\mu\nu\alpha\beta}q^\alpha \left\{ MS^\beta G_1(P \cdot q, q^2) \right.$$
$$\left. + \left[(P \cdot q)S^\beta - (S \cdot q)P^\beta\right]\frac{G_2(P \cdot q, q^2)}{M} \right\}. \tag{2.10}$$

To investigate the inelastic region, it is common to define dimensionless structure functions for the spin-independent part as $F_{1,2}$:

$$F_1(x, Q^2) = MW_1(\nu, Q^2) \tag{2.11}$$

$$F_2(x, Q^2) = \nu W_2(\nu, Q^2), \tag{2.12}$$

and spin-dependent part as $g_{1,2}$:

$$g_1(x, Q^2) = M\nu G_1(\nu, Q^2) \tag{2.13}$$

$$g_2(x, Q^2) = \nu^2 G_2(\nu, Q^2). \tag{2.14}$$

- Unpolarized Structure Function:
  The cross section for the scattering of unpolarized electrons off an unpolarized

target can be described as follows:

$$\frac{\mathrm{d}^2\sigma}{\mathrm{d}\Omega\mathrm{d}E'} = \left(\frac{\mathrm{d}^2\sigma}{\mathrm{d}\Omega}\right)_{Mott}\left[W_2(P\cdot q, Q^2) + 2W_1(P\cdot q, Q^2)\tan^2\frac{\theta}{2}\right], \quad (2.15)$$

where the Mott cross section is given by:

$$\left(\frac{\mathrm{d}^2\sigma}{\mathrm{d}\Omega}\right)_{Mott} = \frac{\alpha^2\cos^2\frac{\theta}{2}}{4E^2\sin^4\frac{\theta}{2}}. \quad (2.16)$$

The Mott cross section characterizes the scattering of relativistic electrons from a point-like particle. From equations 2.11 and 2.12, it can be deduced that the unpolarized structure functions F_1 and F_2 satisfy the following relation:

$$F_1(x, Q^2) = \frac{F_2(x, Q^2)(1+\gamma^2)}{2x\left(1 + R(x, Q^2)\right)}, \quad (2.17)$$

where the parameter γ^2 is defined as the ratio of Q^2 to ν^2, which can be expressed as $\gamma^2 = \frac{Q^2}{\nu^2} = \frac{(2Mx)^2}{Q^2}$. In equation 2.17, the variable R represents the ratio of longitudinal to transverse virtual photon cross sections:

$$R \equiv \frac{\sigma_L}{\sigma_T}. \quad (2.18)$$

Hence, the expression for the unpolarized cross section, as given in equation 2.15, can be written in terms of the structure functions F_1 and F_2:

$$\frac{\mathrm{d}^2\sigma}{\mathrm{d}\Omega\mathrm{d}E'} = \left(\frac{\mathrm{d}^2\sigma}{\mathrm{d}\Omega}\right)_{Mott}\left[\frac{1}{\nu}F_2(x, Q^2) + \frac{2}{M}F_1(x, Q^2)\tan^2\frac{\theta}{2}\right]. \quad (2.19)$$

An alternative definition for the unpolarized structure function per nucleon,

denoted as F_1' and F_2', can be given as follows:

$$F_1' = \frac{F_1}{A}, F_2' = \frac{F_2}{A}. \tag{2.20}$$

In this dissertation, only the unpolarized structure functions F_1 and F_2 are utilized to define the unpolarized structure functions, without incorporating the nuclear target mass number A.

- Polarized Structure Function:

  When a polarized lepton with spin s interacts with a polarized target, the discrepancy between the cross sections for the target with spin S and the target with spin $-S$ can be expressed as follows:

$$
\begin{aligned}
\frac{d^2\sigma_{s,S}}{d\Omega\,dE'} & - \frac{d^2\sigma_{s,-S}}{d\Omega\,dE'} \\
& = \frac{8m\alpha^2 E'}{q^4 E}\Big\{ \big[(q\cdot S)(q\cdot s) + Q^2(s\cdot S)\big]\,MG_1(P\cdot q, Q^2) \\
& \quad + Q^2\big[(s\cdot S)(P\cdot q) - (q\cdot S)(P\cdot s)\big]\frac{G_2(P\cdot q, Q^2)}{M}\Big\}. \tag{2.21}
\end{aligned}
$$

where G_1 and G_2 represent the polarized structure functions, as defined in equations 2.13 and 2.14. When the lepton spin is longitudinally polarized and the nucleon target is fixed with spin S and spin $-S$, equation 2.21 can be rewritten as:

$$
\begin{aligned}
\frac{d^2\sigma_{,S}}{d\Omega\,dE'} - \frac{d^2\sigma_{,-S}}{d\Omega\,dE'} = & -\frac{4\alpha^2}{Q^2}\frac{E'}{E} \tag{2.22} \\
& \times \Big\{ \big[E\cos\beta + E'\cos\Theta\big]MG_1 + 2EE'\big[\cos\Theta - \cos\beta\big]G_2\Big\},
\end{aligned}
$$

where Θ represents the angle between the scattered electron $\overrightarrow{k'}$ and the nucleon

spin $\overrightarrow{S}$, while β represents the angle between the incident electron momentum $\overrightarrow{k}$ and the target spin direction $\overrightarrow{S}$.

$$\cos \Theta = \sin \theta \sin \beta \cos \phi + \cos \theta \cos \beta \ , \qquad (2.23)$$

where θ refers to the angle of electron scattering, and ϕ represents the azimuthal angle. These angles are illustrated in Figure 2.3.

When the target nucleons are longitudinally polarized, setting $\beta = 0$ and $\Theta = 0$ in the equation provides the difference between the cross sections:

$$\frac{d^2\sigma}{d\Omega dE'} - \frac{d^2\sigma}{d\Omega dE'} = \frac{4\alpha^2 E'}{\nu E Q^2}\left[(E + E'\cos\theta)g_1(x,Q^2) - 2Mxg_2(x,Q^2)\right] . \ (2.24)$$

When the target nucleons are transversely polarized, setting $\beta = \pi/2$ and $\Theta = \theta$ in the equation yields the difference between the cross sections:

$$\frac{d^2\sigma}{d\Omega dE'} - \frac{d^2\sigma}{d\Omega dE'} = \frac{4\alpha^2 E'^2}{\nu E Q^2}\sin\theta\left[g_1(x,Q^2) + \frac{2ME}{\nu}g_2(x,Q^2)\right] . \qquad (2.25)$$

2.3 Virtual Photon-Nucleon Asymmetries

Virtual photon asymmetries are calculated based on the helicity decomposition of the scattering cross sections between virtual photons and nucleons. The process involves circularly polarized virtual photons with helicity values of +1 or -1 interacting with longitudinally polarized nucleons. In this scenario, two helicity cross sections, namely
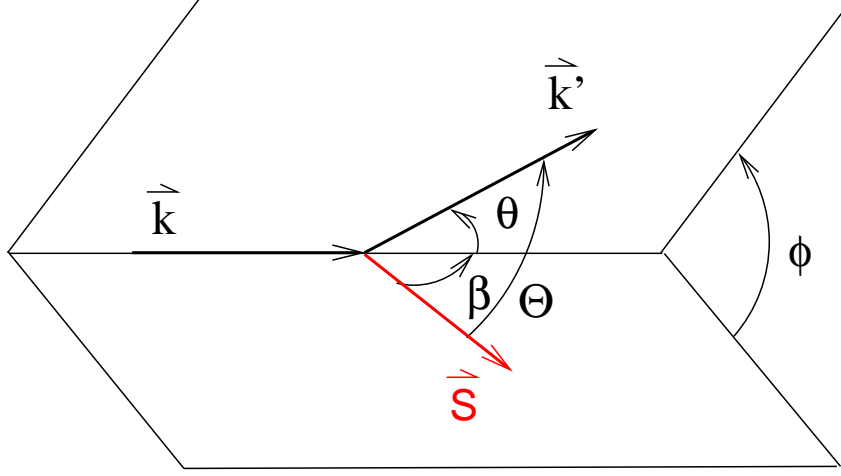
Figure 2.3: Angles for polarized electron scattering (Zheng 2002).

$\sigma_{1/2}$ and $\sigma_{3/2}$, play a crucial role (Aneesh V. Manohar 1992):

$$\sigma_{1/2} = \frac{4\pi\alpha}{MK}(F_1 + g_1 - \gamma^2 g_2) \tag{2.26}$$

$$\sigma_{3/2} = \frac{4\pi\alpha}{MK}(F_1 - g_1 + \gamma^2 g_2), \tag{2.27}$$

where the structure functions F_1, F_2, g_1, and g_2 are all dependent on the variables (x, Q^2), while $\gamma^2 = \frac{(2Mx)^2}{Q^2}$ with M be the nucleon mass and the virtual photon flux factor $K = \nu(1-x)$ in the Hand convention (Hand 1963). The subscript 1/2 (or 3/2) represents the projection of the total spin along the direction of the virtual photon momentum vector $\vec{q}$. It indicates whether the virtual photon spin is anti-parallel (1-1/2=1/2) or parallel (1+1/2=3/2) to the nucleon spin. Figure 2.4 visually demonstrates this scattering process.

Then the longitudinal asymmetry A_1 is given by:

$$A_1(x, Q^2) \equiv \frac{\sigma_{1/2} - \sigma_{3/2}}{\sigma_{1/2} + \sigma_{3/2}} = \frac{g_1(x, Q^2) - \gamma^2 g_2(x, Q^2)}{F_1(x, Q^2)} . \tag{2.28}$$

The cross-section σ_{LT} corresponds to the interference between the longitudinal and
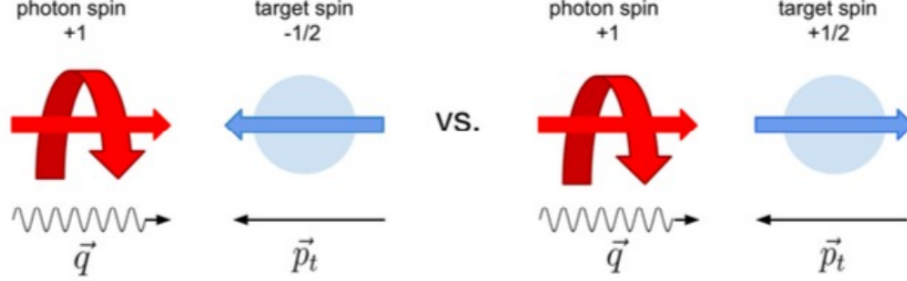
Figure 2.4: Virtual photon with helicity (± 1) scatters off a longitudinally polarized nucleon. Figure on left for anti-parallel spin projection while figure on right for parallel spin projection (Cardona 2023).

transverse virtual photon-nucleon amplitudes (Aneesh V. Manohar 1992):

$$\sigma_{LT} = \frac{4\pi\alpha}{MK}\gamma(g_1 + g_2). \tag{2.29}$$

Then A_2 is defined as virtual photon asymmetry that arises from the interference between transverse and longitudinal virtual photon-nucleon amplitudes:

$$A_2(x, Q^2) \equiv \frac{2\sigma_{LT}}{\sigma_{1/2} + \sigma_{3/2}} = \frac{\gamma[g_1(x, Q^2) + g_2(x, Q^2)]}{F_1(x, Q^2)} . \tag{2.30}$$

From Equations 2.28 and 2.30, the relation between asymmetry A_1, A_2 and ration $\frac{g_1(x,Q^2)}{F_1(x,Q^2)}$ is:

$$A_1(x, Q^2) + \gamma A_2(x, Q^2) = (1 + \gamma^2)\frac{g_1(x, Q^2)}{F_1(x, Q^2)} . \tag{2.31}$$

In addition, the asymmetry A_2 is constrained by the Soffer Bound (Soffer and Teryaev 2000):

$$A_2(x, Q^2) \leqslant \sqrt{\frac{R(x, Q^2)}{2}\left[1 + A_1(x, Q^2)\right]} , \tag{2.32}$$

which is a function of A_1 and the ratio $R \equiv \sigma_L/\sigma_T$.

In experiments, it is often challenging to align the spin direction of the virtual photon with the target spin direction while maintaining flexibility in other kinematic variables. As an alternative, the spin of the incident electron can be aligned parallel or anti-parallel, or perpendicular or anti-perpendicular to the target spin. The virtual photon asymmetries can be connected to the measured lepton asymmetries through polarization and kinematic factors.

- Longitudinal Electron Asymmetry:

  For a target polarized parallel to the beam direction, the longitudinal electron asymmetry measured in the experiment can be expressed in terms of the differences between the cross-sections $(\sigma_{\downarrow\Uparrow}, \sigma_{\uparrow\Uparrow})$ for longitudinally polarized particles:

$$A_\parallel \equiv \frac{\sigma_{\downarrow\Uparrow} - \sigma_{\uparrow\Uparrow}}{\sigma_{\downarrow\Uparrow} + \sigma_{\uparrow\Uparrow}} = \frac{1-\epsilon}{(1-\epsilon R)W_1}\Big[M(E + E'\cos\theta)G_1 - Q^2 G_2\Big] . \quad (2.33)$$

- Transverse Electron Asymmetry:

  When the electron has longitudinal polarization and the nucleon is transversely polarized, the transverse electron asymmetry is determined based on the differences between the cross-sections $(\sigma_{\downarrow\Rightarrow}, \sigma_{\uparrow\Rightarrow})$ for transversely polarized particles (R. G. Roberts 1994):

$$A_\perp \equiv \frac{\sigma_{\downarrow\Rightarrow} - \sigma_{\uparrow\Rightarrow}}{\sigma_{\downarrow\Rightarrow} + \sigma_{\uparrow\Rightarrow}} = \frac{(1-\epsilon)E'}{(1-\epsilon R)W_1}\Big[MG_1 + 2EG_2\Big]\cos\theta . \quad (2.34)$$

The electron asymmetries can be connected to the photon-nucleon asymmetries A_1 and A_2 through a set of kinematic factors:

$$A_\parallel = D(A_1 + \eta A_2) \qquad (2.35)$$

$$A_\perp = d(A_2 - \xi A_1). \qquad (2.36)$$

The virtual photon polarization factor D is denoted as:

$$D = \frac{1 - (1 - y)\epsilon}{1 + \epsilon R}, \qquad (2.37)$$

where $y \equiv \nu/E$ representing the fraction of energy loss of the scattered electron, and ϵ, indicating the magnitude of the virtual photon's transverse polarization:

$$\epsilon = 1/\left[1 + 2(1 + 1/\gamma^2)\tan^2(\theta/2)\right], \qquad (2.38)$$

where θ represents the scattering angle. The expression for the rest of kinematic factors in equation 2.35 and equation 2.36 are:

$$\eta = (\epsilon\sqrt{Q^2})/(E - E'\epsilon) \qquad (2.39)$$

$$\xi = \eta(1 + \epsilon)/(2\epsilon) \qquad (2.40)$$

$$d = D\sqrt{2\epsilon/(1 + \epsilon)}. \qquad (2.41)$$

By rearranging equations 2.35 and 2.36, we can derive equations expressing A_1 and A_2 in terms of $A_{\parallel}$ and $A_{\perp}$:

$$A_1 = \frac{1}{D(1+\eta\xi)}A_{\parallel} - \frac{\eta}{d(1+\eta\xi)}A_{\perp} \tag{2.42}$$

$$A_2 = \frac{\xi}{D(1+\eta\xi)}A_{\parallel} + \frac{1}{d(1+\eta\xi)}A_{\perp}. \tag{2.43}$$

The measurement of asymmetries in spin-structure functions is advantageous due to its relative nature, which helps to mitigate several systematic uncertainties through cancellation. Additionally, it is relatively straightforward to control the polarization directions of the electrons during the experiment. These factors contribute to the simplification of extracting spin-structure functions from asymmetry measurements. By utilizing the known unpolarized structure function $F_1(x, Q^2)$, we can extract the polarized structure functions from the measured electron asymmetries $A_{\parallel}$ and $A_{\perp}$:

$$g_1(x, Q^2) = \frac{F_1(x, Q^2)}{D'}\left[A_{\parallel} + \tan(\theta/2) \cdot A_{\perp}\right] \tag{2.44}$$

$$g_2(x, Q^2) = \frac{F_1(x, Q^2)}{D'}\frac{y}{2\sin\theta}\left[\frac{E + E'\cos\theta}{E'}A_{\perp} - \sin\theta \cdot A_{\parallel}\right]. \tag{2.45}$$

where the kinematic factor D' is expressed as follows:

$$D' = \frac{(1-\epsilon)(2-y)}{y\left[1 + \epsilon R(x, Q^2)\right]} . \tag{2.46}$$

2.4   Large Bjorken limit as $x_{Bj} \to 1$

The virtual photon asymmetry, denoted as A_1, plays a critical role in providing valuable information about the spin properties of the nucleon. Understanding and determining A_1 in the high x region (where $x > 0.5$) is of great significance, primarily due to the dominance of valence quarks, as illustrated in Figure 2.5. This region offers a relatively clean domain for exploring the spin structure of the nucleon. Additionally, various theoretical calculations exist, resulting in different predictions at high x. By obtaining precise data, we can evaluate and determine which models align with experimental observations and contribute to our understanding of nucleon spin structure. In the context of the E12-06-110 experiment, our primary focus was directed towards investigating the neutron A_1^n. However, exploring the high-x region poses significant challenges due to the limited occurrence of events, resulting in low event rates. Moreover, studying the neutron itself presents difficulties as a consequence of the unavailability of a free neutron target. By utilizing Jefferson Lab's 12 GeV-era polarized ^{3}He target as an effective neutron target, researchers have attained the required luminosity to thoroughly examine and differentiate among various predictions in the high-x region. Theoretical predictions gain significance as x approaches 1 within the deep inelastic regime ($W > 2$ GeV), allowing for the resolution of the partonic structure of nucleons.
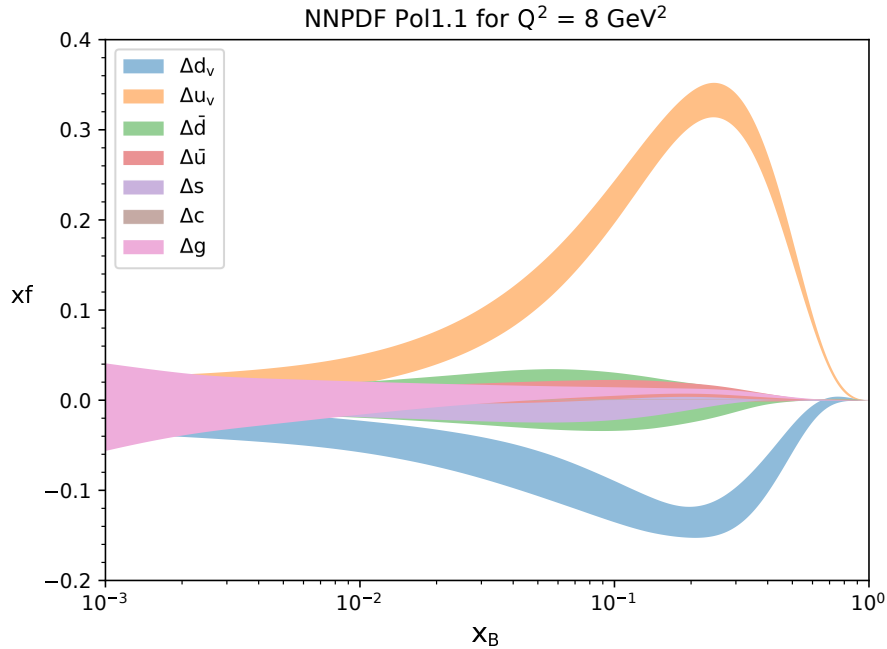
Figure 2.5: Polarized valence and sea quark parton distribution functions (PDFs) for the proton at $Q^2 = 8 GeV^2$ from the NNPDFpol1.1 parameterization. u_v and $\overline{u}$ are the up valence and sea quark polarized PDFs (Ball et al. 2022).

2.5 Theoretical Predictions for Neutron Spin Structure

In this section, we will delve into several theoretical predictions concerning the neutron asymmetry denoted as A_1^n.

- Basic SU(6) Model:

  A constituent quark can be perceived as an "unadorned" or inherent valence quark that undergoes dressing due to surrounding quraks and gluons. Similar to the fundamental quarks in Quantum Chromodynamics (QCD), constituent quarks are fermions possessing a spin of $1/2$ and exhibit conserved charges. However, they possess effective masses that exceed the current quark masses

utilized in perturbative QCD (pQCD). Although this model has proven suc-
cessful in explaining various aspects of hadronic physics, its failure arising from
the assumption of SU(6) symmetry has motivated the development of more
intricate models. The non-relativistic constituent quark model represents the
nucleon using a symmetric SU(6) wavefunction in the current quark frameworks.
This wavefunction, displayed in Figure 2.6, accounts for spin and isospin values
of $1/2$, while excluding the orbital angular momentum of the three constituent
quarks. For a neutron polarized along the $+Z$ direction with spin $S = 1/2$ and
$S_z = +1/2$, the corresponding wavefunction is expressed as (Close 1979):

$$
\begin{aligned}
|n \uparrow\rangle_{S=1/2, S_Z=+1/2} = \ & \frac{1}{\sqrt{2}} |d \uparrow (ud)_{S=0, S_Z=0}\rangle + \frac{1}{\sqrt{18}} |d \uparrow (ud)_{S=1, S_Z=0}\rangle \\
& - \frac{1}{3} |d \downarrow (ud)_{S=1, S_Z=1}\rangle - \frac{1}{3} |u \uparrow (dd)_{S=1, S_Z=0}\rangle \\
& - \frac{\sqrt{2}}{3} |u \downarrow (dd)_{S=1, S_Z=1}\rangle .
\end{aligned}
\tag{2.47}
$$
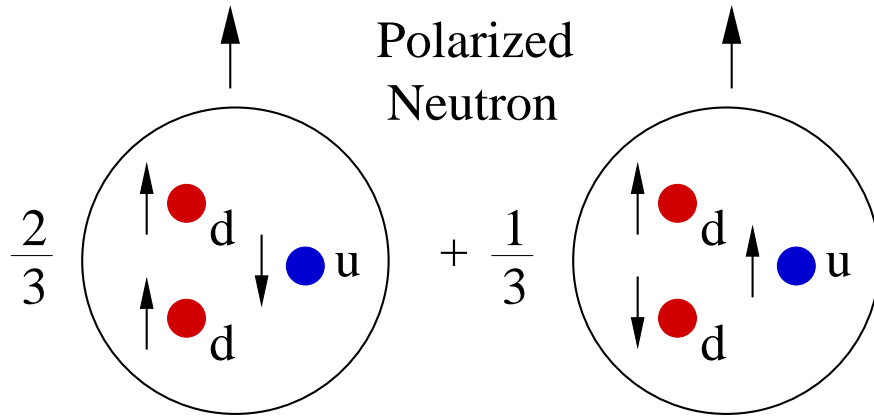
Figure 2.6: The neutron's SU(6) wave-function. (Zheng 2002)

The subscript S in the equation denotes the overall spin of the "diquark" state,
while S_z represents its projection along the $+Z$ direction. By interchanging the

u and d quarks in Equation 2.47, we obtain the wavefunction for the proton. In the case of SU(6) being a perfect symmetry, both diquark states with $S = 0$ and $S = 1$ contribute equally. By calculating the probability of finding each quark in a specific spin state and combining them, the following predictions can be obtained:

$$A_1^p = \frac{5}{9}, A_1^n = 0, \frac{\Delta u}{u} = \frac{2}{3}, \frac{\Delta d}{d} = \frac{1}{3}. \tag{2.48}$$

In order to assess SU(6) symmetry, the ratio F_2^n/F_2^p in the valence quark region is examined, employing the definitions of structure functions in terms of unpolarized Parton Distribution Functions (PDFs). The convention $u(x) \equiv u^p(x)$, $d(x) \equiv d^p(x)$, and $s(x) \equiv s^p(x)$ is adopted to represent the PDFs of the proton. In the case of the neutron, one finds $u^n(x) = d^p(x) = d(x)$ and $d^n(x) = u^p(x) = u(x)$ based on isospin symmetry. The assumption is made that the strange quark distribution for the neutron is identical to that of the proton, thus $s^n(x) = s^p(x) = s(x)$. It is important to note that all notations for PDFs refer to the proton unless specifically stated otherwise. The ratios of F_2 for the neutron compared to the proton are given by:

$$R^{np} \equiv \frac{F_2^n}{F_2^p} = \frac{u(x) + 4d(x)}{4u(x) + d(x)}. \tag{2.49}$$

In the context of Deep Inelastic Scattering (DIS), when considering exact SU(6) symmetry, it implies that the valence quark Probability Distribution Functions (PDFs) exhibit equivalent distributions, specifically $u(x) = 2d(x)$ for all values

of x:

$$R^{np} = \frac{2}{3}. \tag{2.50}$$

The measurements conducted by SLAC on this ratio (Bodek 1973) are presented in Figure 2.7 below, demonstrating that $R^{np} \neq \frac{2}{3}$ and thereby indicating the breakdown of SU(6) symmetry (Carlitz 1975). Consequently, the development of additional models for A_1 becomes necessary.
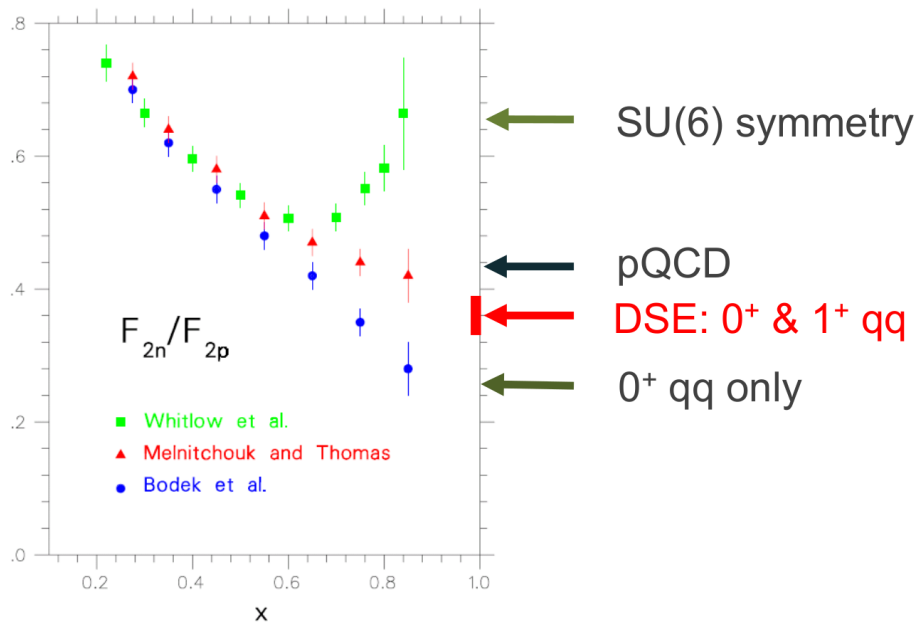
Figure 2.7: The global data set for F_2^n/F_2^P essentially unknown at large x due to uncertainties in deuterium nuclear corrections in F_2^n data, in stark contrast to the SU(6) prediction of 2/3 (Gomez et al. 1994).

- SU(6) Breaking and Hyperfine Perturbed Constituent Quark Model (CQM): In the relativistic constituent quark model (RCQM), calculations often incorporate the assumption that SU(6) symmetry breaking occurs due to a color hyperfine interaction between quarks. This interaction leads to a reduction in

energy for spectator-quark pairs in a spin singlet state compared to those in a spin triplet state. As a result, there is an increased likelihood, particularly at high x, that the struck quark carries the spin of the nucleon (A. V. Manohar 1994). These predictions can be summarized as follows for the case of x = 1:

$$A_1^p = 1, A_1^n = 1, \text{ and } \frac{\Delta u}{u} = 1, \frac{\Delta d}{d} = -\frac{1}{3}. \tag{2.51}$$

When examining Figure 2.7, it becomes evident that these predictions align with the data observed in the high-x region.

- Perturbative QCD:

  As $x \to 1$, the interaction of the virtual photon with high-energy quarks allows for perturbative treatment due to the weak coupling between the partons. The initial application of perturbative Quantum Chromodynamics (pQCD) was carried out by Farrar and Jackson (Farrar and Jackson 1975), assuming zero orbital angular momentum for the quarks. When a virtual photon probes the nucleon, the quarks within the diquark state can have their spins either anti-aligned ($S = 0$) or aligned ($S = 1$). Quarks in the $S = 0$ state undergo a spin-flip through the exchange of a transversely polarized gluon, while those in the S = 1 state exchange a longitudinally polarized gluon without spin-flip, thereby conserving angular momentum in both cases. The ratio of the smaller momentum of the quark-pair to the larger momentum of the longitudinally polarized gluon suppresses this mode. Since the $S = 0$ mode dominates as $x \to 1$, the struck quark must carry the helicity of the nucleon, a phenomenon known as "Hadron Helicity Conservation" (HHC). Brodsky, Burkardt, and Schmidt (BBS) performed a fit to proton g_1 data obtained from SLAC E142 and the

SMC experiment at CERN, incorporating HHC in the large-x region (Brodsky, Burkardt, and I. Schmidt 1995). Later, Leader, Siderov, and Stamenov (LSS) expanded upon the parameterizations of helicity-dependent quark distributions (Δq) by incorporating Q^2 evolution and directly fitting to global A_1 data, including the neutron. The resulting pQCD fit with HHC is known as the LSS(BSS) fit. In the limit of $x \to 1$, it provides the following predictions:

$$A_1^p = 1, A_1^n = 1, \ \frac{\Delta u}{u} = 1, \frac{\Delta d}{d} = 1, \ \text{and} \ R^{np} = \frac{3}{7}. \tag{2.52}$$

As there is no valid physical basis to assume that quarks have zero orbital angular momentum (Ralson, Jain, and Buniy 2005) the LSS group conducted fits to g_1^n/F_1^n at leading and next-to-leading order (NLO) in Q^2 without the constraints imposed by Hadron Helicity Conservation (HHC). In the same year, Avakian et al. developed a perturbative Quantum Chromodynamics (pQCD) calculation that explicitly incorporates Fock states with non-zero quark orbital angular momentum (Avakian et al. 2007). These Fock states exhibit logarithmic enhancements in helicity-flip amplitudes. Specifically, at large x, the positive helicity state (where the quark spin aligns with the nucleon spin) scales as $(1-x)^3$, while the negative helicity state scales as $(1-x)^5 log^2(1-x)$. This has a significant impact, particularly on $\Delta d/d$. The improved agreement of the LSS and Avakian et al. fits with the data (depicted in Figure 2.8 as "pQCD with angular momentum") compared to the parameterizations requiring HHC (depicted as "pQCD") suggests the significant contribution of quark orbital angular momentum to the spin of the nucleon.

- Statistical Model:

There is an alternative model that utilizes a statistical approach, wherein the nucleon is regarded as a gas consisting of massless partons (quarks, anti-quarks, gluons) in equilibrium within a finite volume at a specific temperature (Bourrely, Soffer, and Buccella 2002). In this model, the distribution of the partons, denoted as $p(x)$, at a given input energy scale Q_0^2, is expressed as:

$$p(x) \propto (exp\frac{x - X_{0p}}{\bar{x}} \pm 1)^{-1}. \tag{2.53}$$

In this equation, the addition operation is employed for the quarks and anti-quarks, following Fermi-Dirac distributions, while subtraction is used for the gluons, following Bose-Einstein distributions. X_{0p} represents a constant that can be considered analogous to a thermodynamic potential for the parton p, and $\bar{x}$ serves as a universal temperature for all partons. Through a global next-to-leading order (NLO) Quantum Chromodynamics (QCD) analysis, this statistical parameterization was applied to both unpolarized and polarized Deep Inelastic Scattering (DIS) data, resulting in the determination of eight optimal parameters. The chiral nature of Quantum Chromodynamics (QCD) leads to two important properties of the thermodynamic potential: the potential for a quark with helicity h is opposite in sign to that of an anti-quark with helicity $-h$, and the potential for gluons is zero. Furthermore, the observed dominance of u quarks over d quarks in DIS data (specifically in the proton) indicates that the total potential for u quarks is greater than that of d quarks. Consequently, the model yields the following predictions in the limit of $x \to 1$:

$$A_1^p = 0.80, A_1^n = 0.30, \text{ and } \frac{\Delta u}{u} = 0.77, \frac{\Delta d}{d} = -0.35. \tag{2.54}$$

The statistical approach, which takes into account the overall characteristics of partons, is expected to provide a good theoretical representation of the low-x region. In this region, the sea quarks and gluons play a dominant role, creating a diverse "parton zoo." Notably, the statistical model tends to fit the data quite well in the low-x region and continues to perform reasonably as $x > 0.60$, where the influence of valence quarks becomes more significant.

- Nambu–Jona-Lasinio (NJL) Model:

  A range of chiral soliton models exists, which operate in the low-energy, non-perturbative regime where quarks and gluons are strongly coupled and behave collectively when probed. These models are based on the concept of chiral symmetry breaking and are used to make predictions for structure functions and their moments. In the QCD Lagrangian with N_f massless flavors, there is a large global "chiral" symmetry under unitary flavor transformations of the left- and right-handed quark fields, or under $U(N_f){\times}U_R(N_f)$ rotations. If this symmetry were exact, one would expect a degeneracy in the parity of all states with otherwise identical quantum numbers. However, this is not observed in reality, as there are significant mass differences between states with the same quantum numbers but opposite parities. For instance, the mass difference between the vector meson and axial a1 meson is approximately 500 MeV (1260 MeV - 770 MeV), and the mass difference between the nucleon and its parity partner, the N(1535) resonance, is approximately 600 MeV. These mass differences cannot be explained solely by the small current quark masses ($mu \approx 4$MeV, $md \approx 7$ MeV, and $ms \approx 150$ MeV), which explicitly break chiral symmetry. It is therefore understood that chiral symmetry is strongly and spontaneously broken, with the associated order parameter known as the "chiral condensate" on the

order of ~ 100 MeV. Expanding upon the treatment of the nucleon within the framework of chirality, QCD has been generalized to an arbitrarily large number of colors, N_c (Dashen and Aneesh V. Manohar 1993). This allows for the use of a perturbative approach at low energies, where $1/N_c$ serves as the expansion parameter. Consequently, a description of the nucleon emerges within an effective theory where many mesons and glueballs interact weakly, bringing the valence quarks together. Interestingly, the successful description of mass splittings in the baryon octet and decuplet has been achieved by employing a large Nc, despite the fact that the true value in nature is only three. One notable description that treats the nucleon as a chiral soliton is the Nambu-Jona-Lasinio (NJL) model (Cloet, Bentz, and Thomas 2005).In this model, hadronic currents are described by quark degrees of freedom and are based on a local four-fermion interaction with $U(1){\times}SU(2)_L{\times}SU(2)_R$ chiral symmetry.

- Dyson-Schwinger Equations:

  The latest addition to the array of spin-structure models is one that examines the strong interaction using the Dyson-Schwinger Equations (DSEs) (C. D. Roberts, Holt, and S. M. Schmidt 2013) .These calculations focus on the region around $x \sim 1$, where the nucleon's elastic form factors G_E and G_M can be linked to predictions of Parton Distribution Functions (PDFs) at large-x via a Poincare covariant Faddeev amplitude. In constructing the Faddeev equation, a dressed-quark propagator that is both momentum-dependent and independent is utilized, resulting in both "realistic" and "contact" predictions. The predictions derived from the realistic description are as follows:

  $$A_1^p = 0.59, A_1^n = 0.17, \text{ and } \frac{\Delta u}{u} = 0.65, \frac{\Delta d}{d} = -0.26. \tag{2.55}$$

Similarly, the predictions derived within the contact picture are as follows:

$$A_1^p = 0.88, A_1^n = 0.34, \text{ and } \frac{\Delta u}{u} = 0.88, \frac{\Delta d}{d} = -0.33. \tag{2.56}$$

These findings highlight the significance of non-pointlike diquark correlations within the nucleon, which naturally emerge as a consequence of chiral symmetry breaking.

2.6 Predictions for A_1^n and PDF

The Table 2.1 listed the predictions for $x = 1$ value of various models, while Figure 2.9 visually displays the theoretical predictions of PDFs from these models, which will be further explored in Section 2.7.

Model	$\frac{F_2^n}{F_2^p}$	$\frac{d}{u}$	$\frac{\Delta d}{\Delta u}$	$\frac{\Delta u}{u}$	$\frac{\Delta d}{d}$	A_1^n	A_1^p
DSE-1	0.49	0.28	-0.11	0.65	-0.26	0.17	0.59
DSE-2	0.41	0.18	-0.07	0.88	-0.33	0.34	0.88
$0_{[ud]}^+$	$\frac{1}{4}$	0	0	1	0	1	1
NJL	0.43	0.2	-0.06	0.8	-0.25	0.35	0.77
SU(6)	$\frac{2}{3}$	$\frac{1}{2}$	$-\frac{1}{4}$	$\frac{2}{3}$	$-\frac{1}{3}$	0	$\frac{5}{9}$
CQM	$\frac{1}{4}$	0	0	1	$-\frac{1}{3}$	1	1
pQCD	$\frac{3}{7}$	$\frac{1}{5}$	$\frac{1}{5}$	1	1	1	1

Table 2.1: Predictions for $x = 1$ value of various models (C. D. Roberts, Holt, and S. M. Schmidt 2013).

2.7 Existing experimental results for A_1^n at large x_{Bj}

Existing experimental evaluations of A_1^n using a ^{3}He target have been carried out at SLAC, DESY (HERMES), and Jefferson Lab. The corresponding values are presented in Table 2.2 and graphically represented in Figure 2.8.

Experiment	x Coverage	Q^2 Coverage (GeV^2)
SLAC E142	$0.03 \sim x \sim 0.60$	2
SLAC E154	$0.014 \sim x \sim 0.700$	$1 \sim 17$
HERMES	$0.023 \sim x \sim 0.600$	$1 \sim 15$
JLAB E99-117	$0.327 \sim x \sim 0.601$	$2.7 \sim 4.8$
JLAB E06-014	$0.277 \sim x \sim 0.548$	3.08

Table 2.2: Existing measurements of A_1^n using ^{3}He targets (Cardona 2023).
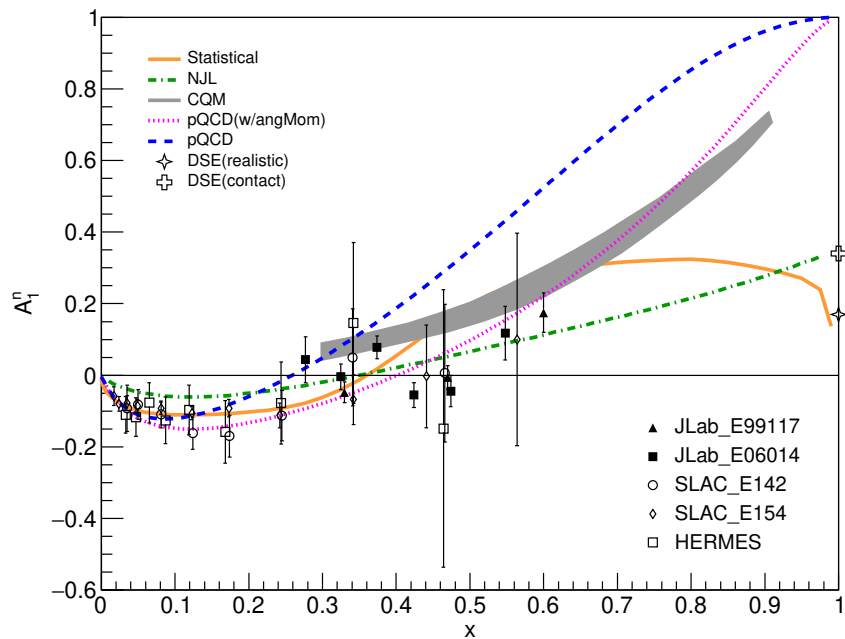
Figure 2.8: The existing global data for A_1^n, obtained using a polarized ^{3}He target, is combined with predictions derived from various theoretical models. These models include the relativistic constituent quark model (CQM), statistical models, Nambu-Jona-Lasinio (NJL) model, and two Dyson-Schwinger equation (DSE)-based approaches that intersect at $x = 1$. In the perturbative Quantum Chromodynamics (pQCD) model with the LSS (BSS) parameterization, quark Orbital Angular Momentum (OAM) is assumed to be absent, while the Avakian et al. parameterization explicitly allows for quark OAM (Flay et al. 2016).
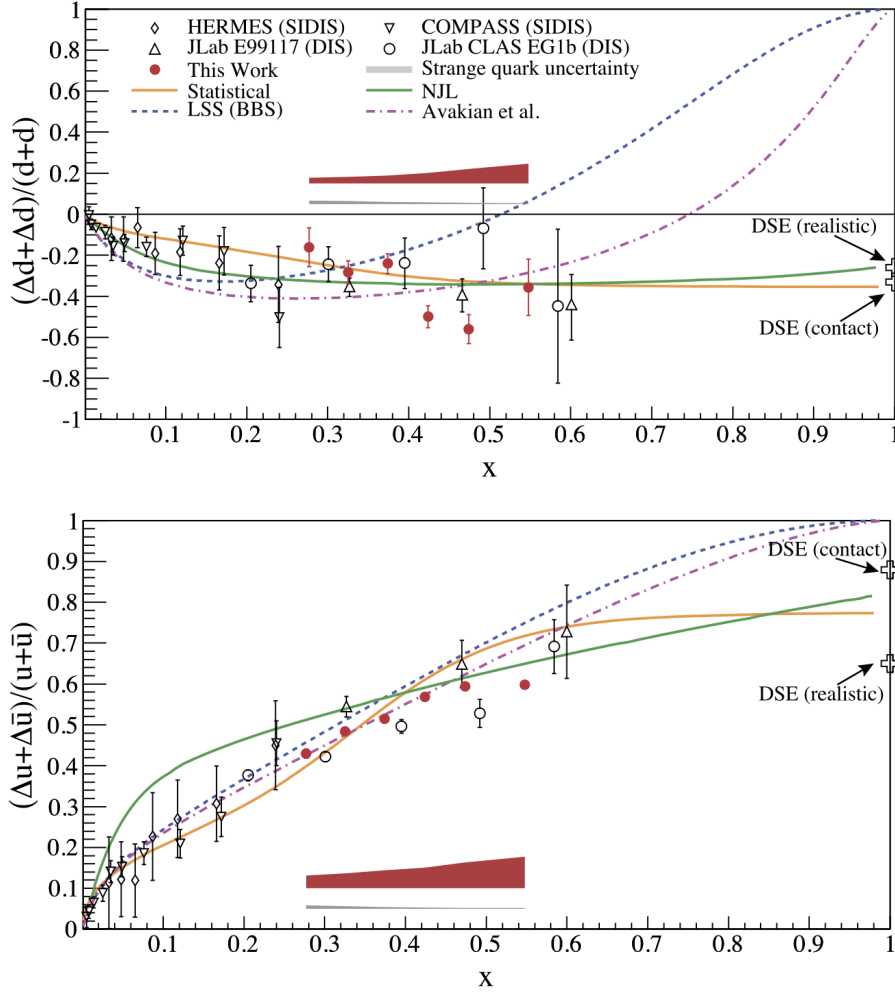
Figure 2.9: The results obtained from the Jefferson Lab E06-014 experiment are depicted by filled circles, showcasing the ratios $(\Delta d + \Delta \bar{d})/(d + \bar{d})$ (top) and $(\Delta u + \Delta \bar{u})/(u + \bar{u})$ (bottom). In addition, the graph includes inclusive Deep Inelastic Scattering (DIS) data from Jefferson Lab E99117 and Jefferson Lab CLAS EG1b, as well as semi-inclusive DIS data from HERMES and COMPASS, reconstructed according to the methodology outlined in the text. Various models and parameterizations mentioned in section 2.6 are also plotted for comparison (Flay et al. 2016).

Chapter 3

The A_1^n Experiment

Data collection for experiment E12-06-110 took place at Jefferson Lab's experimental Hall C, utilizing the upgraded polarized electron beam generated by the Continuous Electron Beam Accelerator Facility (CEBAF). The bird's-eye view of the Thomas Jefferson Accelerator Facility is shown in figure 3.1. The polarized ^{3}He target system was installed and commissioned between November 2019 and January 2020. The production-level data-taking phase spanned from January 12, 2020, to March 13, 2020. Another experiment E12-06-121 was carried out after E12-06-110, which utilized the same polarized ^{3}He target and measured d_2^n, a moment of the neutron spin structure functions. The measurement of the neutron spin asymmetry A_1^n were carried out using two spectrometers, namely the High Momentum Spectrometer (HMS) and the Super High Momentum Spectrometer (SHMS), positioned at 30 degrees on opposite sides of the 30 μA, 10.38 GeV beamline, as shown in Figure 3.2. Data was collected with the SHMS central momentum values set to 2.6 GeV and 3.4 GeV, and the HMS at 2.9 GeV and 3.5 GeV, see Table 3.1. This enabled the determination of the electron double-spin asymmetries $A_\parallel$ and $A_\perp$ for inclusive ^{3}He in the far valence domain (0.61 < x < 0.77) and resonance region.

Measuring A_1^n in the large x region poses challenges due to the absence of a dense free neutron target for scattering experiments, given the neutron's short lifetime of approximately 15 minutes. The requirement for high polarized luminosity is necessary

Figure 3.1: The bird's-eye view of the Thomas Jefferson National Accelerator Facility (*JLab Campus Site Map* 2019).

Kine	Spec	E_b (GeV)	E_0 (GeV)	θ (°)	Production Time (hours)	Cell
3	HMS	10.38	2.90	30.0	88.0	Bigbrother
4	HMS	10.38	3.50	30.0	511.0	Dutch & Bigbrother
B	SHMS	10.38	2.60	30.0	511.0	Dutch & Bigbrother
C	SHMS	10.38	3.40	30.0	88.0	Bigbrother

Table 3.1: Kinematics settings for DIS production runs.

to achieve high precision. Previous studies have used polarized deuteron and more recently polarized ^{3}He nuclear targets as effective substitutes for neutron targets. Consequently, nuclear corrections are needed to extract neutron-specific information. ^{3}He is a more favorable alternative as the majority of its spin arises from the neutron (approximately 86%), with the spins of the two protons anti-aligned and canceling each other, in contrast to the deuteron where about half of its spin originates from the proton. Neutron results obtained from the deuteron target entail larger uncertainties due to associated uncertainties in proton data worldwide.

The most recent high-precision measurement of A_1^n was conducted in Jefferson Lab's Hall A during experiment E06-014 in 2009, targeting the highest x-bin of 0.573 at $Q^2 = 4.848$ GeV^2 (Parno et al. 2015). Prior to that, the measurement was performed in Hall A's experiment E99-117 in 2001, reaching x = 0.601 at $Q^2 = 4.833$ GeV^2 (Zheng 2002). The objective of the E12-06-110 experiment was to improve upon these results by capitalizing on JLab's 12 GeV upgraded electron beam and a polarized target system that offered double the luminosity of its predecessors, reaching approximately 2×10^{36} cm^{-2}s^{-1}, the highest in the world. This experiment marked the first utilization of a polarized ^{3}He target in Hall C, following the energy upgrade at the lab.
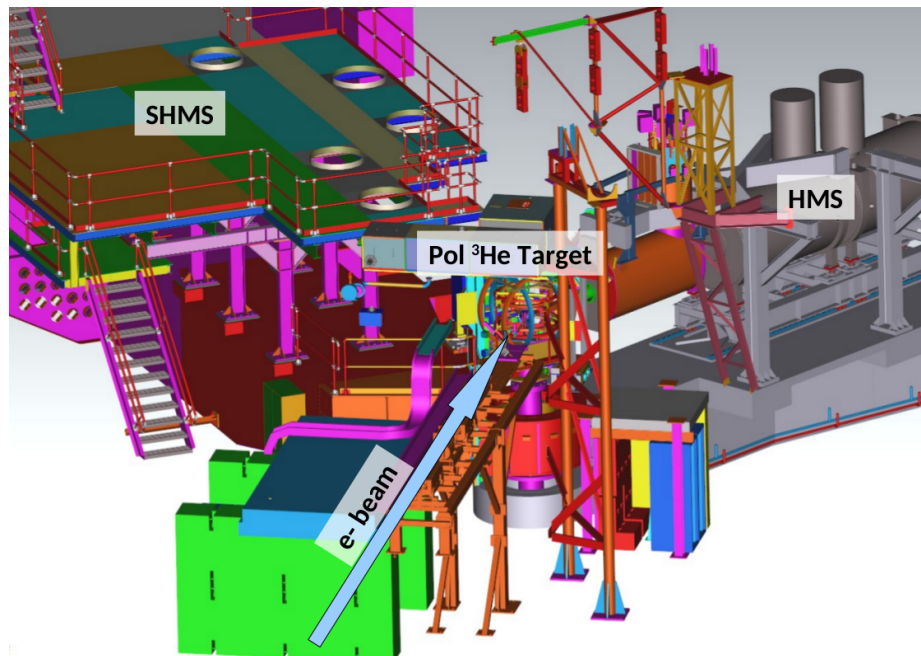
Figure 3.2: Experimental setup for the E12-06-110 experiment in Jefferson Lab Hall C.

3.1 The Electron accelerator

The Continuous Electron Beam Accelerator Facility (CEBAF) at Jefferson Lab provides a high-energy polarized electron beam, supplying up to 11 GeV of beam to experimental Halls A, B, and C, and up to 12 GeV to Hall D. The facility offers a continuous-wave electron beam with a polarization capability of approximately $\sim 85\%$ and currents up to 100 μA. Data collection with the 6 GeV beam ended in spring 2012, and commissioning with the upgraded beam energy began in winter 2017. The 6 GeV energy was achieved using a 67.5 MeV injector, two 1/4-mile long superconducting radio-frequency (SRF) linear accelerators (north and south linacs), and two magnetic recirculating arcs. Each linac consisted of twenty superconducting cryomodules, with eight niobium-made cavities in each module cooled to around 2.2 K using liquid ^{4}He supplied by the Central Helium Liquefier (CHL), as shown in Figure 3.3. The electrons reached their maximum energy of 6 GeV after five recirculations, making five passes through the RF separator at the end of the south linac.

To increase the maximum deliverable energy to 12 GeV, several modifications were implemented. The injector energy was raised to 123 MeV, and a fourth laser was added to the injector system to accommodate Hall D. Additionally, five new superconducting cryomodules were incorporated into each linac, bringing the total to 25 cryomodules per linac. A new CHL was installed, along with a new arc (Arc 10) to direct the beam towards Hall D. Furthermore, a 750 MHz 5th pass separator was introduced to separate the beam for Hall D. These modifications enabled all Halls to receive energy levels of 2.2 GeV at the first pass, 4.4 GeV at the second pass, 6.6 GeV at the third pass, 8.8 GeV at the fourth pass, and 11 GeV at the fifth pass. Hall D has the capacity to receive a 12 GeV beam during the 5.5th pass.

Polarized electrons are primarily generated through the photoelectric effect. In each
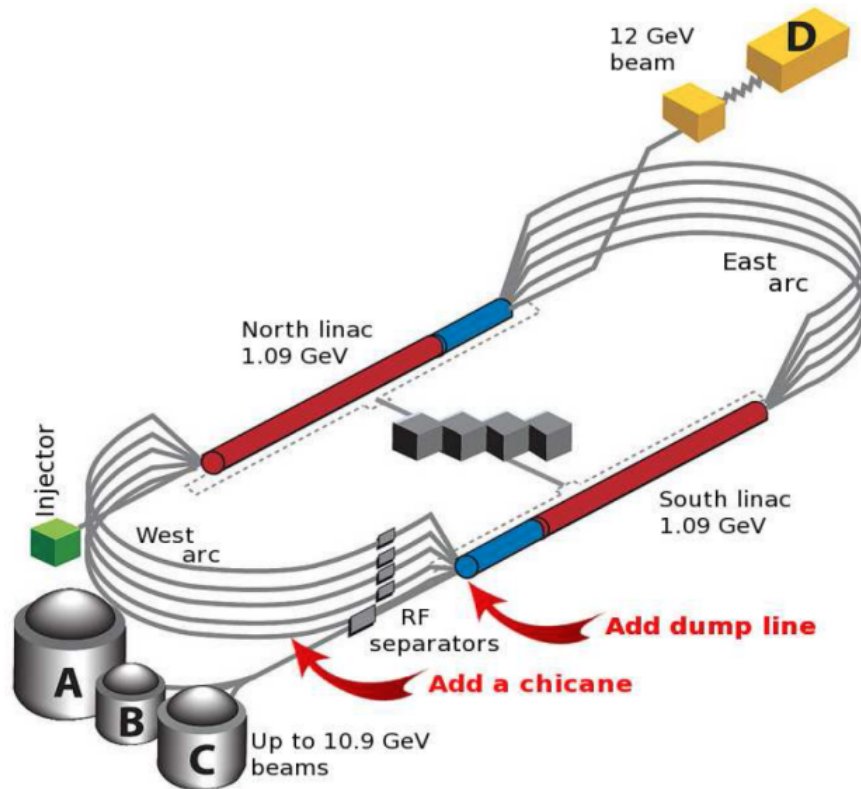
Figure 3.3: Continuous Electron Beam Accelerator Facility (CEBAF) after 12 GeV upgrade (Bogacz et al. 2016).

experimental Hall, a laser system is used as the initial source. This system consists of a 1560 nm seed laser, an ErYb-doped fiber amplifier, and a periodically poled lithium niobate (PPLN) crystal to enhance the photon frequency (Hansknecht and Poelker 2006). In two of the Halls, the lasers are gain-switched to achieve a repetition rate of 499 MHz, which is the third harmonic of the fundamental frequency (1497 MHz) of the accelerator. The other two Halls have lasers gain-switched to a repetition rate of 249.5 MHz. The lasers in each Hall are linearly polarized and directed towards a strained superlattice gallium arsenide (GaAs) photo-cathode using a set of optics. This arrangement allows for the extraction of polarized photo-electrons (Leemann, Douglas, and Krafft 2001).

3.2 Hall C beam Line

The beamline instrumentation, designed to measure the characteristics of the electron beam, was positioned upstream of the target, see figure 3.4. Among the crucial devices were the beam current monitors (BCMs), wire scanners (harps), beam position monitors (BPMs) and the Moller polarimetry setup. Detailed discussions about Moller polarimetry will follow in the section 3.3.
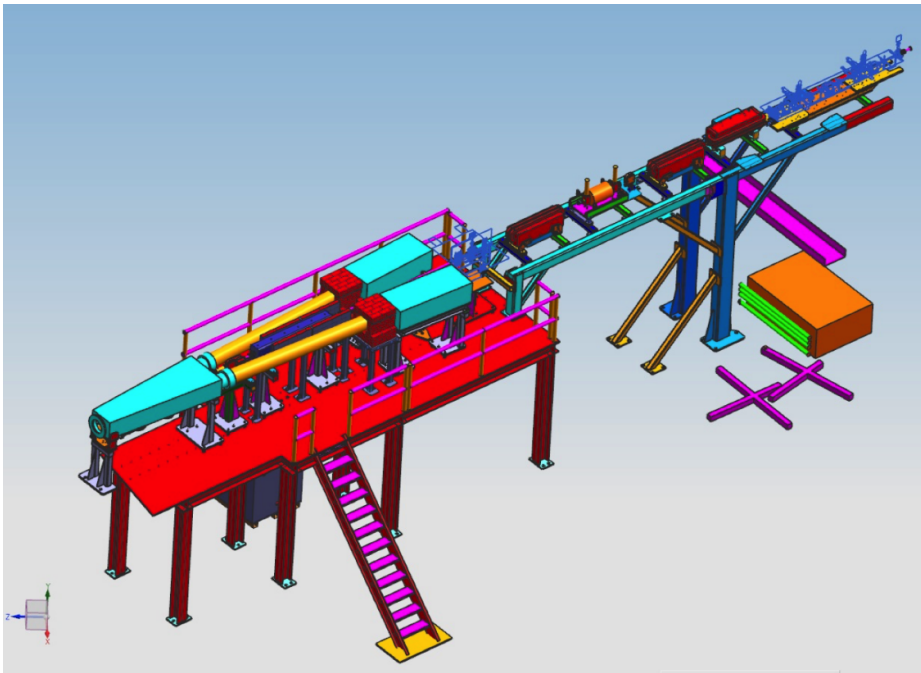
Figure 3.4: The perspective of the Hall C beam line is seen when looking from the hall's entrance towards the target region (S. Wood 2019).

- Beam Current Monitors:

  Several beam current monitors were positioned upstream of the designated target region, referred to as BCM1, BCM2, BCM4A, BCM4B, BCM4C, and the Unser monitor (shown in figure 3.5). All these monitors were connected to the EPICS system for data readout. In experiment E12-06-110, BCM1, BCM2, and

the Unser monitor were utilized as the primary system. The Unser monitor, functioning as a parametric current transformer, provided an absolute reference for beam current measurement. However, it experienced an offset drift over a few minutes during calibration runs, which was taken into account.The other BCMs were stable RF cavity monitors, tuned to the fundamental beam frequency of 1.497 GHz. During the calibration process of these RF cavities, the Unser monitor's drift was compensated for, and its readings were used for each run. Dave Mack performed the BCM calibration (Mack and S. A. Wood 2003). The BCM calibration was later verified by Melanie Cardona during the offline analysis of experimental data (Cardona 2023). For the DIS data collected at 5-pass (10.38 GeV), the average beam current was approximately 30 µA, while for elastic and delta resonance data taken at 1-pass (2.2 GeV), the beam current was around 5 µA. The total accumulated charge for each run was determined based on the readings from the BCMs.
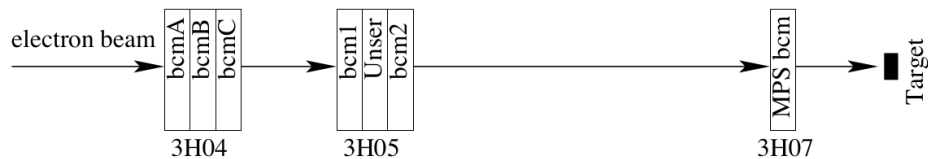
Figure 3.5: The diagram illustrating the beam current monitor system situated in Hall C (S. Wood 2019).

- Harps:

  The beamline comprises two wire scanners (harps), namely IHA3H07A and IHA3H07B, positioned 3.46 and 1.55 meters upstream of the target, respectively. Each scanner is equipped with a fork holding three wires oriented orthogonally to each other (two slanted and one vertical). The entire system is movable through the beam thanks to a stepper motor. When the wires come

into contact with the beam, they pick up small signals, which are then amplified and converted into digital form through ADCs. The beam's position is determined using a beam position encoder that generates pulses corresponding to the number of steps completed by the stepper motor. This calculation is done within the EPICS coordinate system. To establish the beam's position profile accurately, a Gaussian curve is fitted to the charge collected by the ADCs concerning the wire position. These scans are considered intrusive to the beam and are therefore not conducted during continuous data-taking for ongoing monitoring. Instead, they are carried out only at low currents (around 5µA) before regular experiment operations. These scans are essential for calibrating the Beam Position Monitors (BPMs), which are subsequently employed for real-time monitoring during the main experiment.

- Beam Position Monitors:

  To ascertain both the location and orientation of the beam on the experimental target, three Beam Position Monitors (BPMs) are strategically positioned at distances of 3.71 m (IPM3H07A), 2.25 m (IPM3H07B), and 1.23 m (IPM3H07C) upstream of the target point. These BPMs are comprised of cylindrical resonant cavities, housing a 4-wire antenna array tuned to the fundamental RF frequency of 1497 MHz of the beam. To determine the beam's relative position with high accuracy, the standard difference-over-sum technique is employed, providing results within 100 µm precision for currents exceeding 1 µA (S. Wood 2019). At regular intervals, the average beam positions from the BPMs, which are averaged over 0.3 seconds, are recorded and updated in the EPICS database with corresponding timestamps for reference.

- Electron Beam Energy Measurement:

For experiment E12-06-110 performed in Hall C, the Jefferson Lab Machine Control Center (MCC) took charge of measuring the beam energy. The basis for this measurement was the assumption that the electron beam followed a central trajectory through the dipole arc. This arc section in Hall C comprised eight dipole magnets, which deflected the electron beam at a bend angle of 37.5 degrees upon entering the hall. By considering both the beam positions and the bend angle at the entrance and exit of the arc, the beam energy was determined using the following formula (Arrington 1998):

$$E = \frac{k}{\theta_{arc}} \int_0^L B_\perp dL_\parallel, \tag{3.1}$$

where L is the arc length, and the bend angle θ_{arc} is obtained by comparing the relative orientation of the beam at both the entrance and exit of the arc through a survey. Additionally, a conversion constant (k) is utilized, equal to 0.29979 $\frac{GeV \cdot rad}{T \cdot m}$. The integrated field is determined by mapping the magnetic fields of the arc dipoles along with their respective dipole current (Yero 2019). As a result, the average beam energy during the 5-pass was found to be 10.384 GeV, with a statistical uncertainty of $\pm$ 0.003 GeV.

3.3 Beam Polarization Measurement

Beam polarization was determined using Moller polarimetry, which involved exploiting Moller scattering ($e^- e^- \rightarrow e^- e^-$), a Quantum Electrodynamics (QED) process with a precisely calculable cross-section. For an electron beam polarized in the longitudinal direction ($P_b^z \parallel \hat{z}$) colliding with a longitudinally-polarized target ($P_b^z \parallel \hat{z}$),

the cross-section in the center of mass frame is as follows:

$$\frac{d\sigma}{d\Omega} = \frac{d\sigma_0}{d\Omega}[1 + P_b^z P_t^z A_{zz}(\theta_{cm})], \tag{3.2}$$

where A_{zz} represents the analyzing power, which relies on the scattering angle in the center-of-mass frame, denoted as θ_{cm}.

$$A_{zz}(\theta_{cm}) = \frac{-\sin^2\theta_{cm}(7 + \cos^2\theta_{cm})}{3 + \cos^2\theta_{cm}} \tag{3.3}$$

At $\theta_{cm} = 90°$, it reaches its maximum value of 7/9. The electron beam's polarization was determined by measuring the cross-section asymmetry ϵ when the beam and target spins were parallel ($\uparrow\uparrow$) and anti-parallel ($\uparrow\downarrow$) to each other.

$$\epsilon = \frac{\frac{d\sigma\uparrow\uparrow}{d\Omega} - \frac{d\sigma\uparrow\downarrow}{d\Omega}}{\frac{d\sigma\uparrow\uparrow}{d\Omega} + \frac{d\sigma\uparrow\downarrow}{d\Omega}} = P_b^z P_t^z A_{zz}(\theta_{cm}) \tag{3.4}$$

By measuring the asymmetry ϵ along with the known target polarization P_t^z and analyzing power A_{zz}, the electron beam polarization can be determined:

$$P_b^z = \frac{\epsilon}{P_t^z A_{zz}}. \tag{3.5}$$

Please refer to Figure 3.6 for the components of the Moller Polarimeter. Electrons from the electron beam were scattered by a 4 µm thick iron foil, which was polarized at 8.016%±0.021% (Henry 2021) (Gaskell 2023b) using a superconducting solenoid to generate a 3-4 T magnetic field. After scattering, the electrons were directed through three quadrupole magnets (Q1, Q2, and Q3) towards two lead-glass calorimeters, which simultaneously measured them. To reduce the singles rates and accidental coincidences, a set of 7 collimators was placed between Q1 and Q2. Each of the

two calorimeters comprises a 16-channel plastic hodoscope connected to an array of photo-multiplier tubes (PMTs), a lead collimator for defining the out-of-plane angular acceptance, a SF2 lead-glass block ($20 \times 14 \times 23$ cm^3), and a 5" PMT at the end for signal read-out (Hauger et al. 2001). The longitudinal asymmetry ϵ is then calculated, and subsequently, the beam polarization is determined using Equation 3.5.
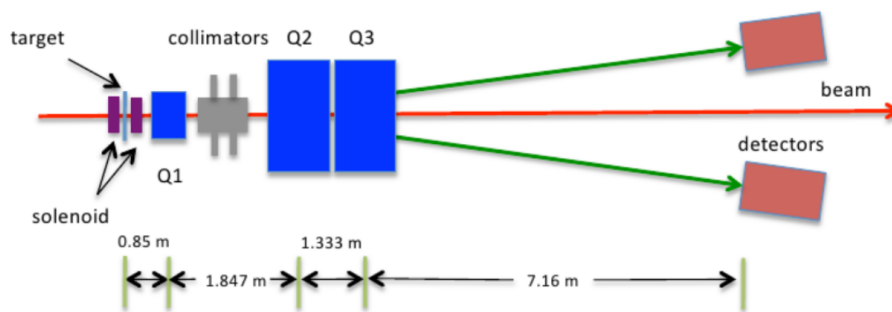
Figure 3.6: The arrangement of the target, quadrupoles, collimators, and detectors is depicted (Roy 2022).

Moller measurements were conducted on a weekly basis during the 12 GeV era, using a beam energy of 10.38 GeV and a current of 1 μA. The results obtained from these measurements are presented in Table 3.2, where each data point represents the average value from multiple runs conducted on the respective day. The runs were performed with the insertible half-wave plate (IHWP) in two different states: IN and OUT. The polarization sign was appropriately adjusted to ensure accurate measurements. The average beam polarization was determined to be $85.4\% \pm 0.3\%$. The systematic uncertainties associated with the beam polarization consisted of a $\sim 1.79\%$ uncertainty originating from device systematics and a $\sim 0.74\%$ uncertainty arising from the beam polarization variation. Thus the total systematic uncertainty of beam polarization with respect to each production is estimated to be $\delta P_{b_{sys}}/P_b \leq 2\%$. A better precision of 0.91% can be achieved at the run-by-run basis (Gaskell 2023a).

Date	Beam Polarization $P_b(\%)$	$\delta P_b(\%)$
01/18/20	85.75	0.43
01/27/20	86.47	0.55
02/03/20	85.46	0.56
02/12/20	87.00	0.65
02/18/20	84.55	0.45
02/26/20	85.00	0.29
03/06/20	85.18	0.40
03/12/20	85.20	0.37

Table 3.2: Moller polarimetry results during production period of E12-06-110 experiment (Cardona 2023).

3.4 Spectrometers

3.4.1 HMS

The HMS (High-Momentum Spectrometer) is situated on the right side of the electron beamline. It comprises three superconducting quadrupole magnets (Q1, Q2, Q3) and a dipole magnet. After scattering, the particle passes through Q1, Q2, and Q3 before reaching the dipole. The main purpose of the quadrupoles is to focus the scattered particles towards the spectrometer's focal plane, while the dipole is responsible for vertically bending the central momentum particle trajectories by 25 degrees in an upward direction. Following the dipole, there is a detector hut that houses a specific set of detectors, see figure 3.7.

- Drift Chambers:

  Upon exiting the dipole magnet, the particles encounter a pair of drift chambers (DC) within the detector hut, each containing six wire planes. These drift chambers serve the purpose of accurately measuring the particle's position and angle. The combination of this information with proper optics reconstruction
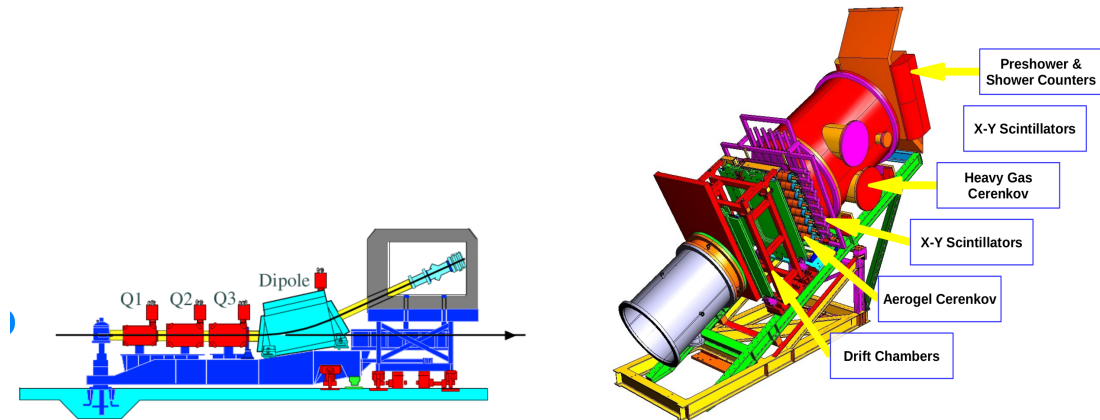
Figure 3.7: Left: The side view of the HMS shows both the magnets and the detector hut. Right: The detectors within the HMS hut (Yero 2019).

allows for the determination of the particle trajectory near the ^{3}He target. The HMS drift chambers cover an active region of 100 cm vertically and 50 cm horizontally. They are filled with a gas mixture of argon and ethane in equal proportions by weight. The wire planes in the first chamber are arranged in the order U, U', X, X', V', and V, while the wire planes in the second chamber are arranged in the order V, V', X', X, U', and U (S. Wood 2019).

- Hodoscopes:

  The HMS hodoscope consists of four hodoscope planes, with each plane equipped with scintillator bars that cover the particle's acceptance range. The hodoscope is designed with two pairs of planes. The first pair consists of one plane with horizontal bars (S1X) and another with vertical bars (S1Y), positioned immediately after the drift chambers. The second pair (S2X, S2Y) is located 2 meters away from the first pair. Photomultiplier tubes (PMTs) are attached to the end of each scintillator bar to detect scintillating light produced by the particles (S. Wood 2019). The hodoscopes serve multiple purposes: they provide a trigger for data acquisition, serve as a reference time for the drift chamber, and mea-

sure the time of flight between the two pairs of planes, which aids in particle identification (PID).

- Gas Cherenkov Detector:

  The HMS Cherenkov detector is employed for particle identification purposes. When a charged particle surpasses the speed of light within a particular medium, it induces polarization among the particles in that medium, leading to an electromagnetic disturbance. As the excited molecules in the medium return to their ground state, they emit photons, generating what is known as Cherenkov radiation:

$$\theta = \arccos(\frac{c}{nv}), \tag{3.6}$$

where the emission angle θ of the Cherenkov radiation depends on two factors: the refractive index n of the medium and the speed v of the charged particle within that medium. The critical velocity v_T at which a charged particle produces Cherenkov radiation depends on the medium's refractive index, which, in turn, is proportional to the gas pressure P with $(n - 1 \propto P)$ used in the detector. When two charged particles with different masses travel with the same momenta, their velocities will differ within the medium. By adjusting the gas pressure in the detector, the threshold velocity for Cherenkov radiation can be tuned to distinguish between these two particles with different masses. This technique is utilized to differentiate electrons from the background of pions. The HMS gas Cherenkov detector is composed of a cylindrical tank filled with C_4F_8O gas at 0.225 atm with pion threshold of 5.5 GeV/c (Sawatzky 2023). Inside the detector, there are two mirrors that focus the Cherenkov light onto two attached photo-multiplier tubes.

- Calorimeter:

  The HMS calorimeter is equipped with four sets of TF1 lead glass, with each set containing thirteen blocks. The first two stacks have two PMTs attached at both ends, while the last two stacks each have a single PMT. When high-energy particles pass through the lead glass, they produce a signal proportional to the total path length traveled by all particles above the Cherenkov threshold. The generation of photons due to the bremsstrahlung process and the subsequent production of electron-positron pairs create an electromagnetic shower. In this shower, electrons or positrons deposit a significant portion of their energy in the shower counter, which is then analyzed to distinguish between electrons and the background of pions (S. Wood 2019).

3.4.2 SHMS

The SHMS (Super High-Momentum Spectrometer) is positioned on the left side of the electron beamline, resembling the HMS setup. It comprises three superconducting quadrupole magnets (Q1, Q2, Q3) and a dipole magnet, just like the HMS. Additionally, it features an extra dipole magnet called the horizontal bender (HB), placed in front of Q1 (S. Wood 2019). As a result, the scattered particles first pass through the HB before continuing through the other magnets. Similar to the HMS, the quadrupoles in the SHMS are responsible for focusing the scattered particles towards the spectrometer's focal plane, and the dipole bends the central momentum particle trajectories vertically by 18.2 degrees in an upward direction. The unique purpose of the HB is to bend the central momentum particle trajectories to the left by 3 degrees, allowing the SHMS to reach the smallest scattering angle possible (5.5 degrees) (S. Wood 2019). After passing through the dipole, the detector hut comes
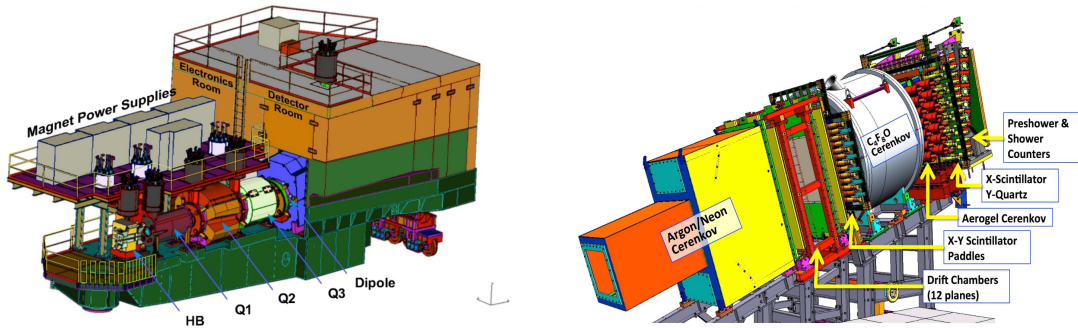
Figure 3.8: Left: The CAD Rendering of the SHMS shows both the magnets and the detector hut. Right: The detectors within the SHMS hut (S. Wood 2019).

into play, housing a set of detectors similar to the ones found in the HMS, see figure 3.8.

- Drift Chambers:

  The SHMS is also equipped with a pair of drift chambers (DC), and each chamber contains six wire planes. Positioned between each wire plane and before the first and after the last wire plane is a copper-coated mylar cathode plane. These drift chambers play a crucial role in accurately measuring the particle's position and angle within the detector hut. Covering an active region of 80 cm in the vertical and horizontal directions, the SHMS drift chambers contain an equal mixture (by weight) of argon and ethane gas. The wire planes in the first chamber are arranged in the order U, U', X, X', V', and V, while the wire planes in the second chamber are arranged in the order V, V', X', X, U', and U (S. Wood 2019).

- Hodoscopes:

  The SHMS hodoscope is comprised of four hodoscope planes (S1X, S1Y, S2X, S2Y), and each plane contains a set of scintillator bars that cover the particles' acceptance range. The S1X and S1Y planes each have 13 scintillator paddles,

while the S2X plane contains 14 scintillator paddles. In contrast, the S2Y plane is constructed with 21 bars made of Corning HPFS 7980 Fused Silica (quartz) (S. Wood 2019).All the paddles and bars are equipped with attached PMTs (Photomultiplier Tubes) to detect and read out the scintillating light from the paddles and Cherenkov radiation from the quartz bars, respectively.

- Gas Cherenkov Detector:

  The noble gas Cherenkov (NGC) detector of the SHMS comprises a cylindrical tank filled with N_2 gas at an operating pressure of 1 atm. The tank is equipped with four mirrors that focus the Cherenkov light onto four attached PMTs (Photomultiplier Tubes). The operating principle of this detector is identical to the one described in the preceding HMS section. For this detector, the threshold energy required to generate Cherenkov radiation for electrons is 21.6 MeV, while for pions, the threshold is 5.7 GeV (Sawatzky 2023).

  The heavy gas Cherenkov (HGC) detector of the SHMS was filled with C_4F_8 at 0.35 atm with pion threshold at 4.4 GeV/c. However, while the SHMS HGC data were available in the data stream, but this detector was not considered important for our run group (Sawatzky 2023).

- Calorimeter:

  The final detector within the SHMS detector hut is the lead glass shower counter, positioned behind the S2Y hodoscope plane. It consists of two parts: the pre-shower and the shower. The pre-shower is situated before the main shower section, serving to enhance particle identification (PID) by detecting electromagnetic showers at an early stage (S. Wood 2019).

Chapter 4

The Polarized ^{3}He Target

Polarized targets have been widely used for experiments to study the nucleon inner structure. Since free neutron has short life time of 880.2 seconds (Nakamura et al. 2010), there is no free neutron target for electron scattering experiments. Since most of the ^{3}He spin is carried by the unpaired neutron, polarized ^{3}He targets have been widely used as an effective polarized neutron target in electron scattering experiments to study the spin structure of neutron (Bissey et al. 2002). Over the past a couple of decades, polarized ^{3}He targets had been successfully utilized in thirteen electron scattering experiments during JLab 6 GeV era. At JLab, a technique called Spin-Exchange Optical Pumping (SEOP) is used to polarized the ^{3}He target (Chupp et al. 1987). For the past decade, several developments including Rb-K hybrid alkali system and high power narrow line-width diode lasers were implemented to the polarized ^{3}He target in order to reach higher ^{3}He polarization with world record luminosity. As JLab completed 12 GeV upgrade in 2017, there are seven upcoming approved polarized ^{3}He target experiments. Upgrade of the target with convection cell and Pulse Nuclear Magnetic Resonance (PNMR) polarimetry were completed for the first 12 GeV era experiment A_1^n (E12-06-110) with collaboration of d_2^n (E12-06-121) in JLab Hall C. For typical $10^{22}/cm^2$ high-density target used in these collaboration experiments, the maximum polarization reached over 50% under $30\mu A$ electron beam, thus here luminosity of $2 \times 10^{36}/cm^2/s$ was achieved.

4.1 Spin Exchange Optical Pumping

- Optical Pumping:

  To initiate the polarization of ^{3}He nucleus, a polarized electron source is created, capable of transferring its spin to ^{3}He. This polarized electron source is generated from the outermost shell of Rb and K atoms, which are vaporized and combined with the ^{3}He gas. Through the process of optical pumping, circularly polarized photons are employed to polarize the outermost-shell electrons in Rb. Subsequently, this polarization is transferred to the K atom and eventually to the ^{3}He nuclei. In order to explain the concept of optical pumping, we initially disregard the spin of the Rb nucleus. The Rb atom contains a single outermost shell electron in its ground state, known as the $5S_{1/2}$ state. By utilizing 795 nm infrared lasers, the Rb atom's ground state can be excited to the $5P_{1/2}$ state. When subjected to an external magnetic field, both states experience Zeeman splitting, resulting in two sub-levels with $m_J = \pm 1/2$. As shown in Figure 4.1, when a polarized laser light is present, with its spin direction aligned with the magnetic field, only the excitation from $5S_{1/2}$ with $m_J = -1/2$ to $5P_{1/2}$ with $m_J = +1/2$ occurs, and vice versa. Subsequently, the excited atoms undergo decay to both $m_J = \pm 1/2$ sub-levels. Through the use of circularly polarized laser for pumping, the alkali vapor rapidly attains a high level of polarization. Due to the relatively weak external magnetic field (typically at $25G$) applied to the target, the hyperfine interaction prevails over the Zeeman splitting, resulting in a significantly stronger influence (Appelt et al. 1998). The hyperfine structure Hamiltonian, denoted as $\hat{H}$, describes the Rb ground state in the

presence of a static magnetic field $\vec{B}$ (Kopfermann [1959]):

$$\hat{H} = Ag\vec{I}\vec{S} + g_e\mu_B S_z B_z - \frac{\mu_I}{I}I_z B_z. \tag{4.1}$$
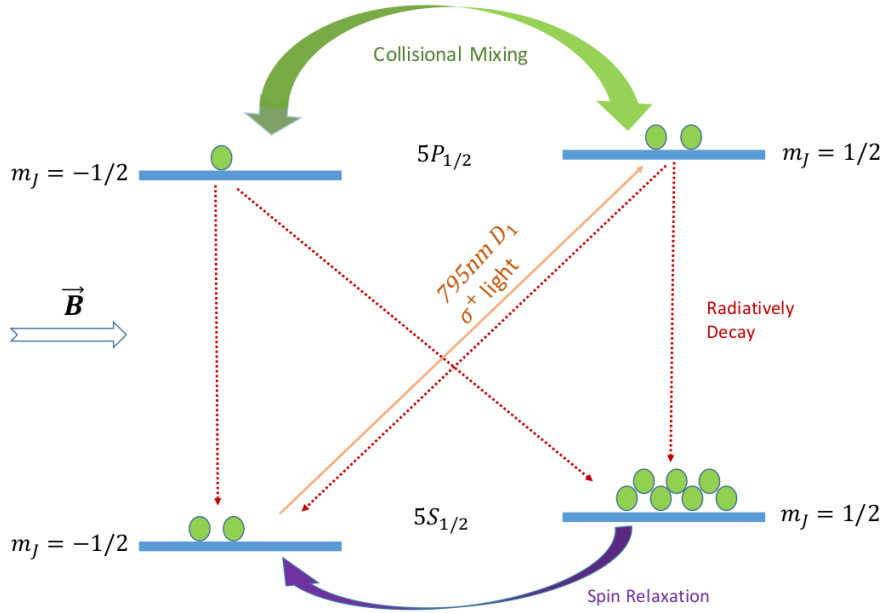
Figure 4.1: Using circularly polarized lasers to optical pumping Rb (Liu [2017]).

The initial component of the Hamiltonian signifies the vector coupling that occurs between the electron spin and the nuclear spin. The second element characterizes the interaction between the electron spin and the magnetic field $\vec{B}$, which possesses a strength denoted as $\mu_e = g_e\mu_B$. Here, $g_e = 2.00232$ corresponds to the electron g value, and $\mu_B = 0.0579$ MeV/T is the Bohr magneton. The third term accounts for the coupling between the nuclear spin and the magnetic field, involving the nuclear magneton $\mu_I = 4.26426$ MeV/T. The eigenstates of the combined angular momentum of the ^{85}Rb atom are identified by the quantum number $F = I \pm S$, which represents the sum of the nuclear spin vector $\vec{I}$ and the electron spin vector $\vec{S}$. When an external magnetic

field is present, it leads to the division of the F state into sub-levels, specifically $2F + 1$ sub-levels, see Figure 4.2. Under the influence of a right circularly polarized laser light, the Rb atom pumping towards the $m_F = F = I + 1/2$ state, while a left circularly polarized laser light promotes pumping towards the $m_F = -F = I - 1/2$ state.Upon the spontaneous decay of the excited atoms to the $m_J = -1/2$ state, photons are emitted, possessing an identical wavelength as the pumping laser. These emitted photons have the potential to depolarize Rb atoms and consequently diminish the efficiency of the pumping process. To counteract this, a minute quantity (0.1 amg) of nitrogen gas is introduced into the sample (Xiong et al. 2001). Nitrogen, being a diatomic molecule, possesses vibrational and rotational degrees of freedom that facilitate the absorption of energy. This enables the radiation-less decay of Rb atoms, which becomes the predominant process, accounting for about 95% of the overall decay.

- Spin Exchange:

  The concept of spin exchange is demonstrated in Figure 4.3. Once Rb atoms are polarized through optical pumping, they transfer their polarization to K atoms and eventually to the ^{3}He nucleus. The exchange of spin between the two alkali metals occurs at a significant rate, with the spin-exchange cross section being considerably large. In fact, the spin-exchange rate is more than 200 times faster than the typical spin-relaxation rates of alkali metals (HAPPER 1972), (Babcock et al. 2003). As a result, the K vapor exhibits an electron polarization that is approximately equivalent to that of the Rb vapor. In the presence of a mixture of polarized Rb and K alkali gases along with ^{3}He, the electron polarization of the alkali atoms can be transferred to the nuclei of ^{3}He. The transfer of angular momentum primarily occurs through collisions between
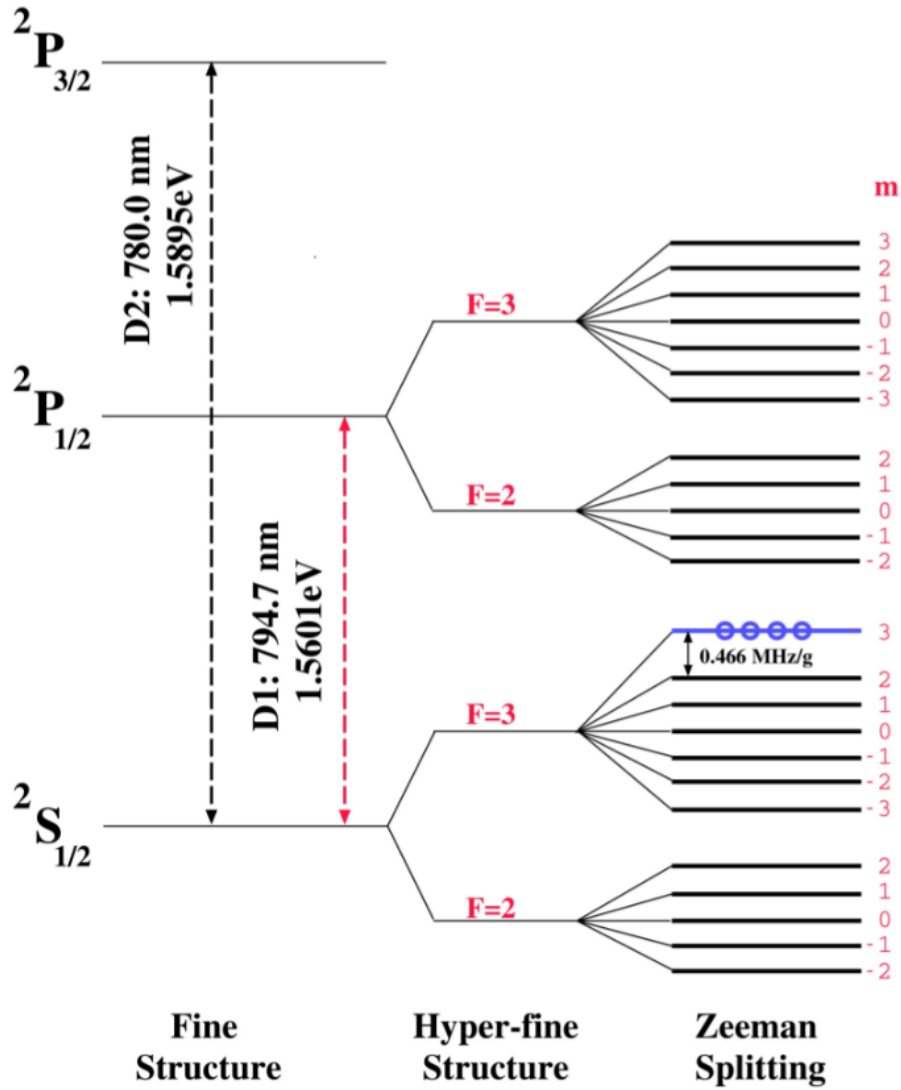
Figure 4.2: With an external magnetic field, the splitting of the energy levels of ^{85}Rb (Slifer 2004).

the atoms. The interaction between alkali atoms and ^{3}He nuclei involves both isotropic hyperfine interaction and spin-rotation interaction. During these collisions, the exchange of spin is facilitated by the hyperfine interaction between the electron of the alkali atom and the nucleus of ^{3}He (Qian et al. 2011):

$$H_{SE} = \alpha \vec{I} \cdot \vec{S}, \tag{4.2}$$

where $\vec{I}$ represents the nuclear spin of ^{3}He, $\vec{S}$ represents the spin of the alkali electron, and α denotes the coupling constant. While determining the precise value of α is challenging, experimental measurements have been conducted to determine the spin-exchange rates γ_{SE} for ^{3}He as a function of alkali density:

$$\gamma_{SE} = k_{SE}^A [A], \tag{4.3}$$

where $[A]$ represents the density of alkali metal, and k_{SE}^A represents the rate constant for spin exchange associated with the specific alkali metal. The following equation describes the rate at which the polarization of ^{3}He changes during the hybrid spin exchange optical pumping process (Babcock et al. 2003):

$$\frac{dP_{^3He}}{dt} = \gamma_{SE}(P_A - P_{^3He}) - \Gamma_{^3He}P_{^3He}, \tag{4.4}$$

where P_A represents the spin polarization of the alkali atoms, and $P_{^3He}$ represents the spin polarization of the ^{3}He nuclei. The term $\Gamma_{^3He}$ denotes the depolarization rate of the ^{3}He nuclei, which arises from various factors such as target polarization, magnetic field gradients, and collisions with the walls. In equation 4.4, $\gamma_{SE} = \kappa_{Rb} + \kappa_K$ where the spin exchange coefficients $\kappa_{Rb} = (6.8 \pm 0.2) \times 10^{-20} \text{cm}^3/\text{s}$ and $\kappa_K = (6.1 \pm 0.4) \times 10^{-20} \text{cm}^3/\text{s}$ (Babcock et al. 2003).

Then the spin-exchange efficiencies, denoted as η_{SE} per ^{3}He nucleus, are determined by the ratio of the spin exchange constant for alkali-^{3}He collisions to the total alkali spin relaxation rate. The measured spin-exchange efficiency was approximately 25% for ^{39}K-^{3}He interactions, while η_{SE} was around 2% for
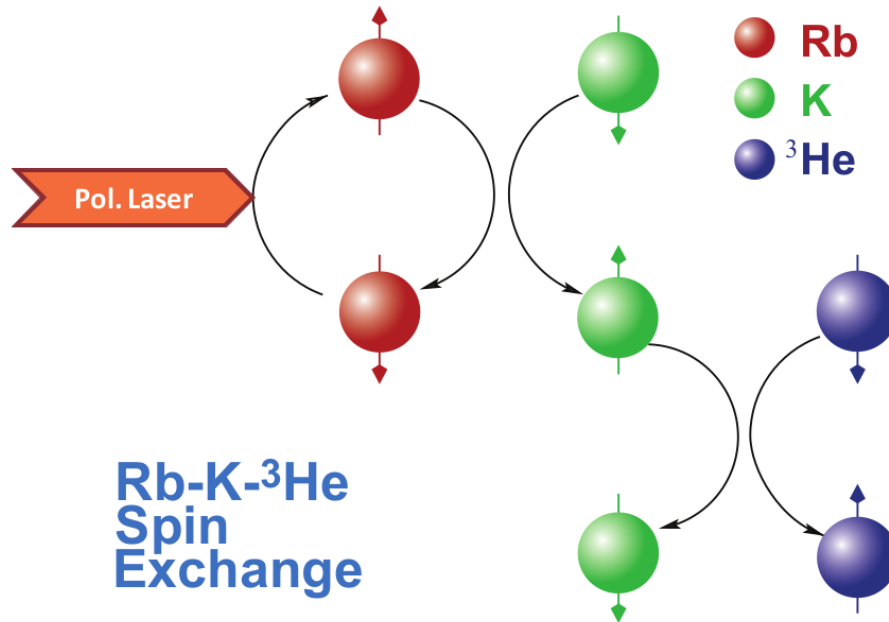
Figure 4.3: The exchange of spin in a hybrid cell containing both Rb and K (Kolarkar 2008).

^{85}Rb-^{3}He interactions, see Figure 4.4. This difference can be mainly attributed to the slower relaxation time of K compared to Rb (Ben-Amar Baranga et al. 1998).

The spin-exchange efficiency was examined in relation to the number density ratios of $[^{39}$K$]/[^{85}$Rb$]$, and a ratio of approximately 5 is typically chosen for optimal performance (W. C. Chen et al. 2007).Notably, this ratio was also the value used for the production target cells in the E12-06-110 experiment.

- Laser System and Target Optics:
  The laser system used in the E12-06-110 experiment consisted of eight 30 W diode lasers operating at a wavelength of 795 nm. These lasers, provided by a company called Raytum Photonics, had a line-width of approximately 0.2 nm
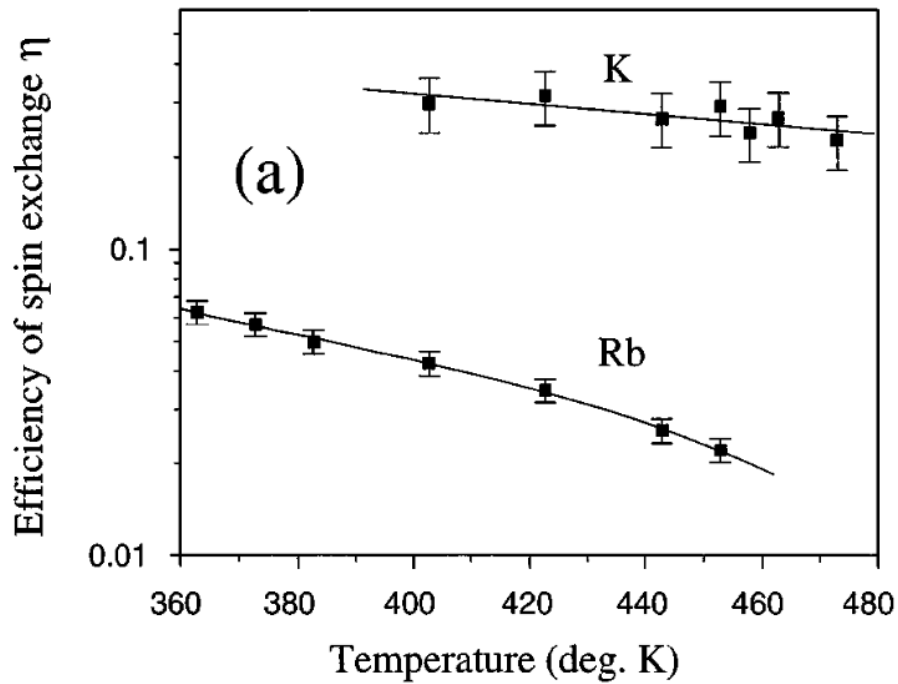
Figure 4.4: Comparison of spin exchange efficiencies, depicted on a logarithmic scale, between ^{3}He-Rb (with 7.0 amagat of ^{3}He) and ^{3}He-K (with 6.9 amagat of ^{3}He) as a function of temperature (Amarian et al. 2002).

and were operated at a current of 35-40 A and a temperature ranging from 15°C to 26.5°C. Each laser was remotely controlled and monitored through EPICS.The laser beam was transmitted from laser room to the hall through eight optical fibers, each approximately 110 meters in length. The optical fibers had a radius of aperture of 0.6 mm and an output divergence angle of 0.22 radians. During the transmission, there was a power loss of approximately 10%. As depicted in Figure 4.5, two sets of four laser beams were combined using a 4-to-1 combiner (one set for longitudinal configuration while the other set for transverse configuration). Each set delivered approximately 80 W of power at the polarized cell's pumping chamber.
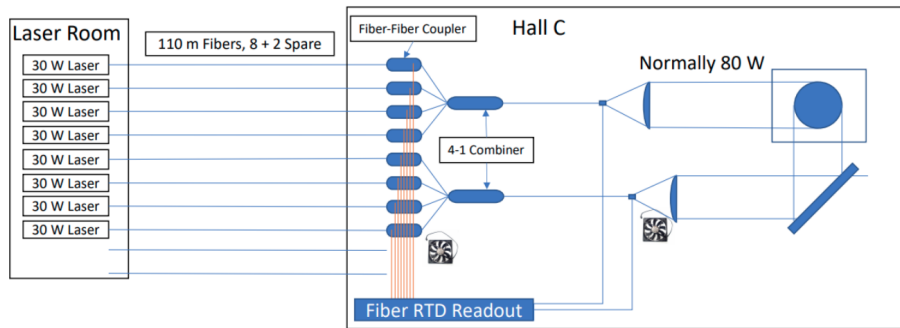
Figure 4.5: Using long optical fibers (110 meter) to transmit lasers from the laser room to Hall C (Roy 2022).
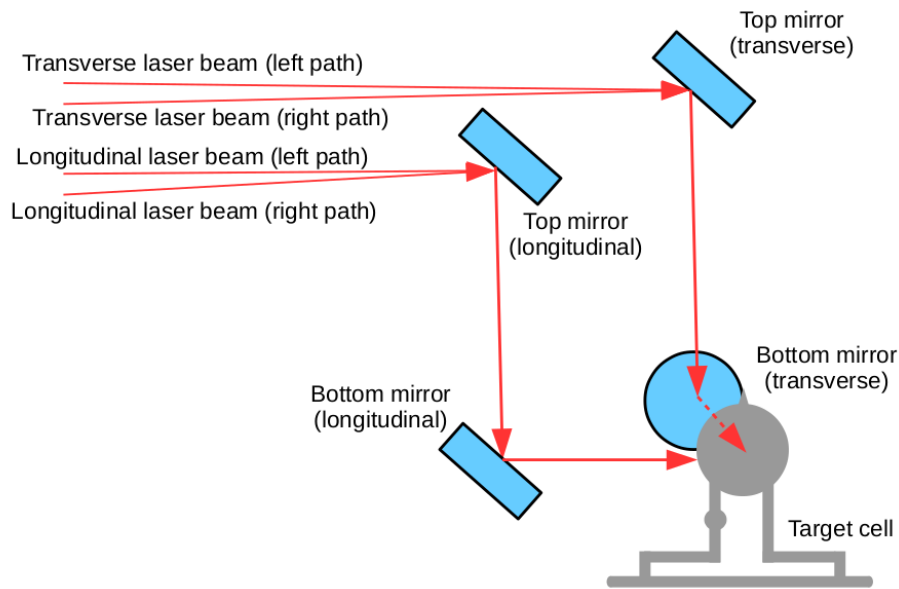
Figure 4.6: The orientations of the top and bottom mirrors redirect the laser beam towards the pumping chamber in longitudinal direction and transverse direction (Roy 2022).

To convert the combined laser beam from unpolarized to circularly polarized, it passed through a series of optical components, including lenses, beam splitters, waveplates, and mirrors. These components were arranged on an optics table, with a separate setup for longitudinal or transverse configuration, within a dedicated black box next to the target enclosure. As the left demonstration in
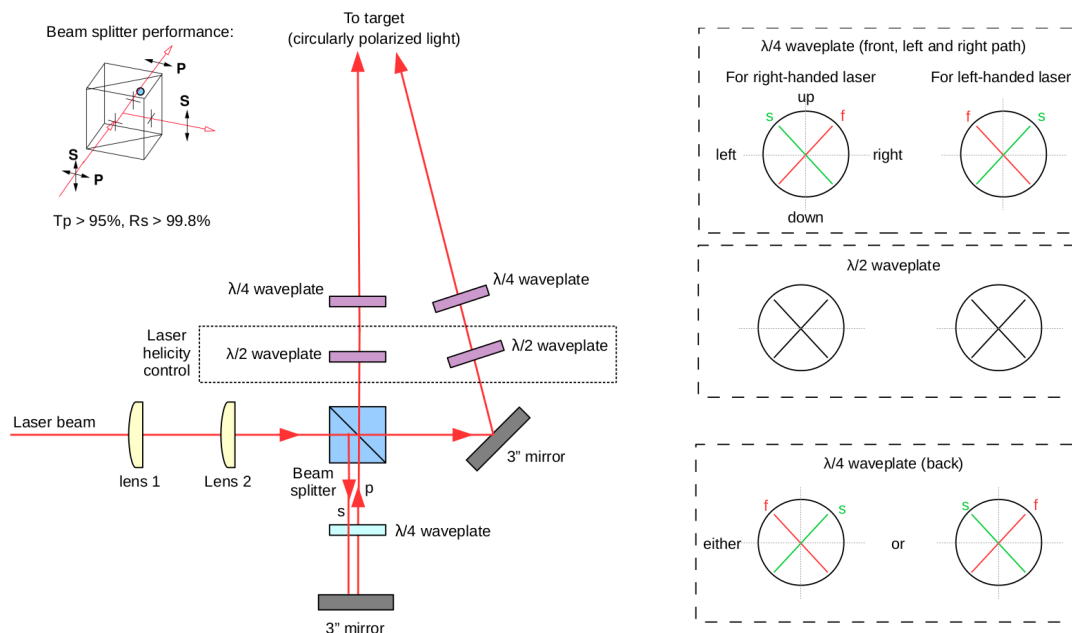
Figure 4.7: Left: an overhead perspective of the optical setup within the optics enclosure. Right: the orientations of the fast and slow axis of the waveplates in the direction facing the target (Roy 2022).

figure 4.5, the optical procedure involved focusing the output of the combiner with convex lenses and directing it to a beam splitter cube. This resulted in two components: a linearly polarized p-wave component and a linearly polarized s-wave component. The p-wave component underwent a series of reflections and passed through waveplates to convert it to circularly polarized light, while the s-wave component underwent a different set of reflections and waveplate conversions. Both components were then combined into a single ray, reflected off mirrors, and directed towards the target pumping chamber, with the aim of achieving a spot size of 3.5 inches, matching the diameter of the polarized cell, see figure 4.6.

Adjustments and optimization of the half waveplate allowed for switching between right and left circular polarization, see the right illustration in Figure 4.7.

4.2 Polarized ^3He Target Cell

Over the past a couple of decades, polarized ^{3}He targets had been successfully utilized at SALC and utilized in thirteen electron scattering experiments during JLab 6 GeV era (Liu 2017). The performance of ^{3}He target cell was improved through out experiments. One of the improvements was the usage of hybrid alkali with addition of K (Riordan et al. 2010). This technique increased the efficiency of spin exchange. Another major improvement was the usage of high power and narrow bend diode lasers (COMET) instead of broad-width diode lasers (Coherent) (Huang et al. 2012). The usage of narrow bend laser modules further increased optical pumping efficiency and reduce depolarization effect from unabsorbed lights. With above improvements, the typical $10^{22}/cm^2$ high-density target reached 60% polarization under $15uA$ electron beam and achieved world record luminosity of $2 \times 10^{36}/cm^2/s$ (Liu 2017).

For approved JLab 12 GeV Era experiments, Gordon's group at UVa finished the design and test of convection cell, see Figure 4.8 (Dolph et al. 2011).

For E12-06-110 (A_1^n) and E12-06-121 (d_2^n) experiments experiments, the desired luminosity is $2 \times 10^{36}/cm^2/s$ where the$10^{22}/cm^2$ high-density target cell reach over 50% polarization under 30 μA beam. Figure 4.10 shows the how the convection cell was installed in Hall C. The convection is needed to reduce the ^{3}He polarization gradient between pumping chamber and target chamber. For diffusion cell, the polarization gradient is about $5\% - 10\%$; while convection cell can reduce polarization gradient to 1% (Liu 2017). As shown in Figure 4.11, convection condition is established by adding a convection Kapton heater (polyimide film) on one of the transfer tube. By sending radio-frequency (RF) signal with Larmor frequency at PNMR Coil, we create depolarization at 1-inch sphere region. Then we could measure the depolarization
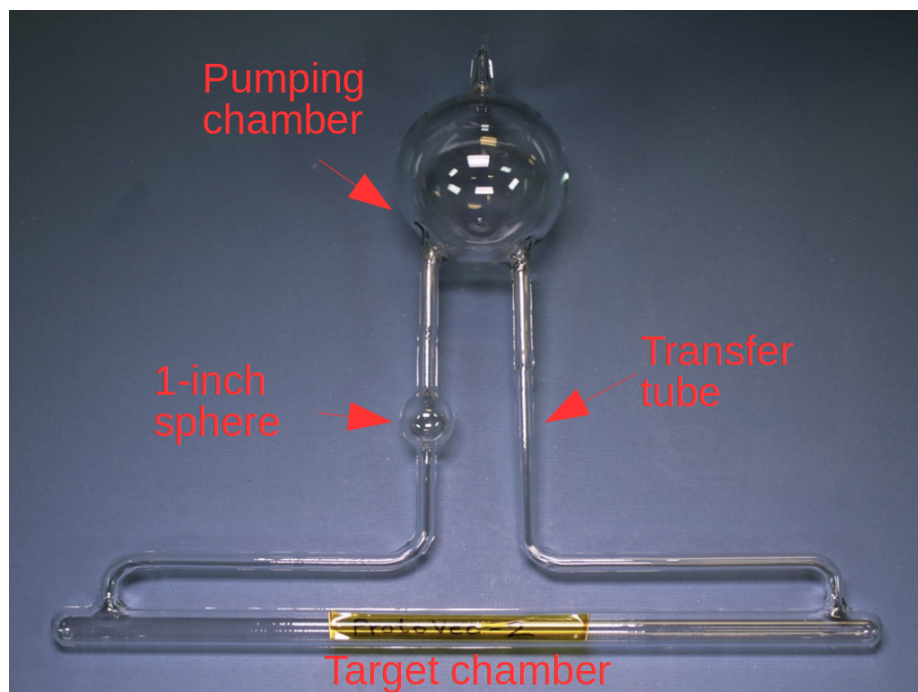
Figure 4.8: The convection design of polarized ^{3}He target cell

dip of NMR-AFP signal amplitude through out the target chamber with upstream and down stream NMR pick-up coils. As shown in Figure 4.14, with known distance between upstream and down stream NMR pick-up coils, we could estimate the convection speed from the dip time difference for upstream pick-up coils and downstream pick-up coils. Under normal convection condition, the typical convection speed along the target chamber is around $6.0cm/min \pm 0.1cm/min$.

4.3 NMR Polarimetry

NMR polarimetry involves determining the polarization of ^{3}He by analyzing the magnetic field generated by the nuclear spins when they undergo modulation. The principle of NMR polarimetry can be described as follows: When a freely moving particle with a magnetic moment $\vec{M} = \gamma \vec{I}$ is placed within an external magnetic field B_0, it
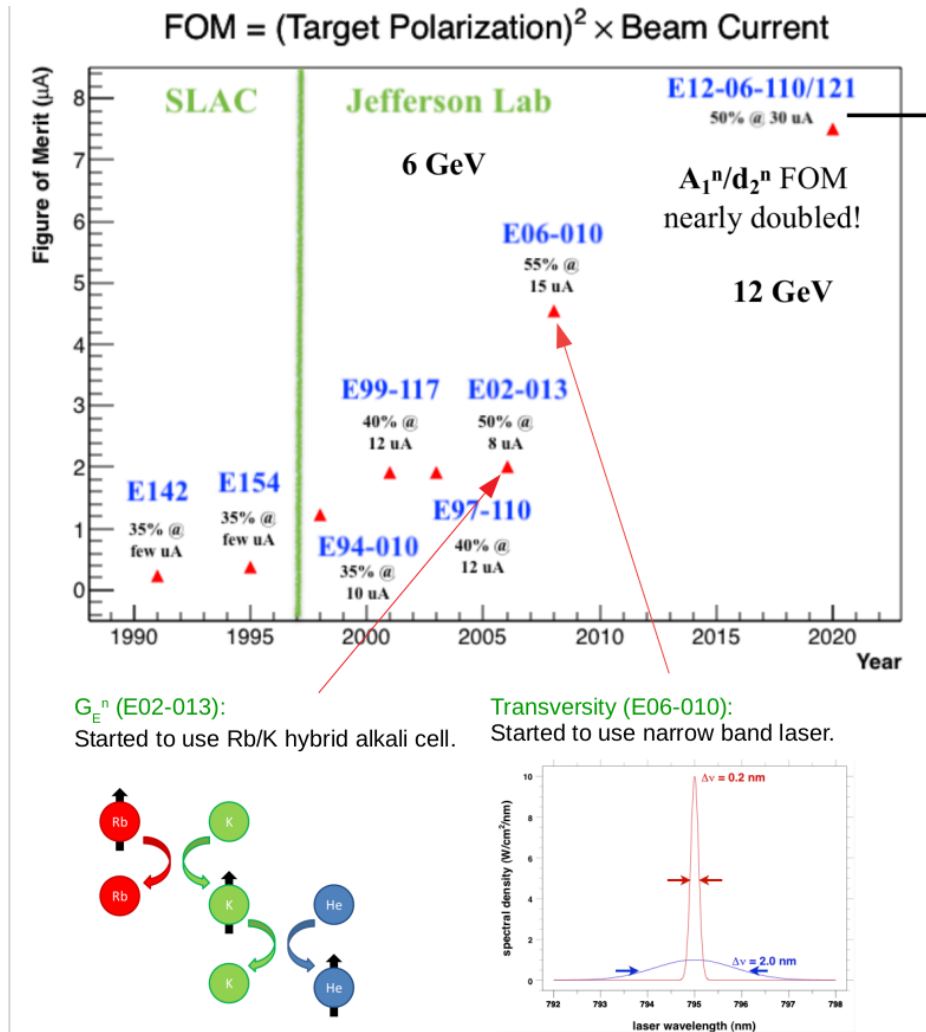
Figure 4.9: The performance evolution of the ^{3}He target systems used in experiments at SLAC and Jefferson Lab is depicted in a graph showing the figure of merits as a function of year.

undergoes a torque, denoted as τ, in the laboratory frame:

$$\tau = \vec{M} \times \vec{B_0} \qquad (4.5)$$

$$(\frac{d\vec{I}}{dt})_{lab} = \vec{M} \times \vec{B_0} \qquad (4.6)$$

$$(\frac{d\vec{M}}{dt})_{lab} = \gamma\vec{M} \times \vec{B}_0. \qquad (4.7)$$
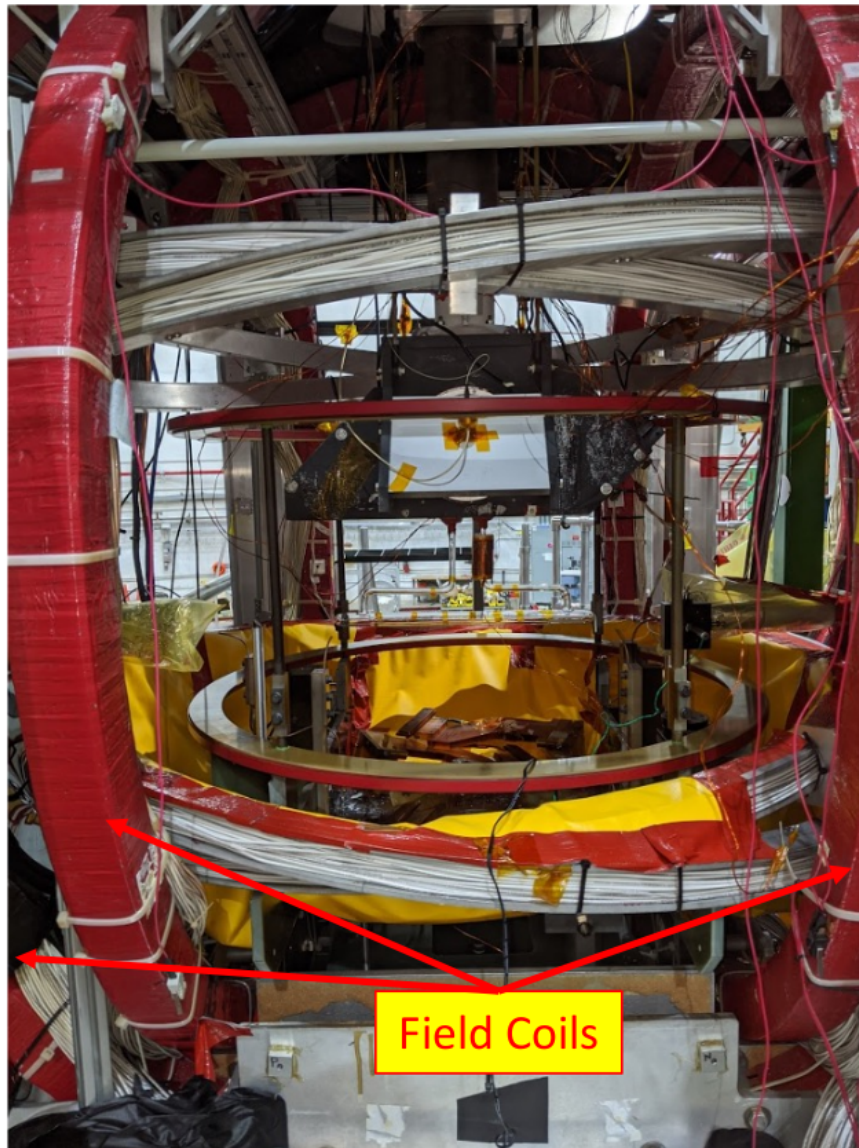
Figure 4.10: The mechanical design of polarized ^{3}He target cell installed in JLab Hall C.

The particle's magnetic moment initiates a rotational motion around the applied magnetic field, known as the holding magnetic field, with a frequency $\omega_L = \gamma B_0$ which is recognized as the Larmor frequency. In our specific scenario, the holding magnetic field B_0 is oriented along the $+\hat{z}$ direction. Now, an alternating RF field,
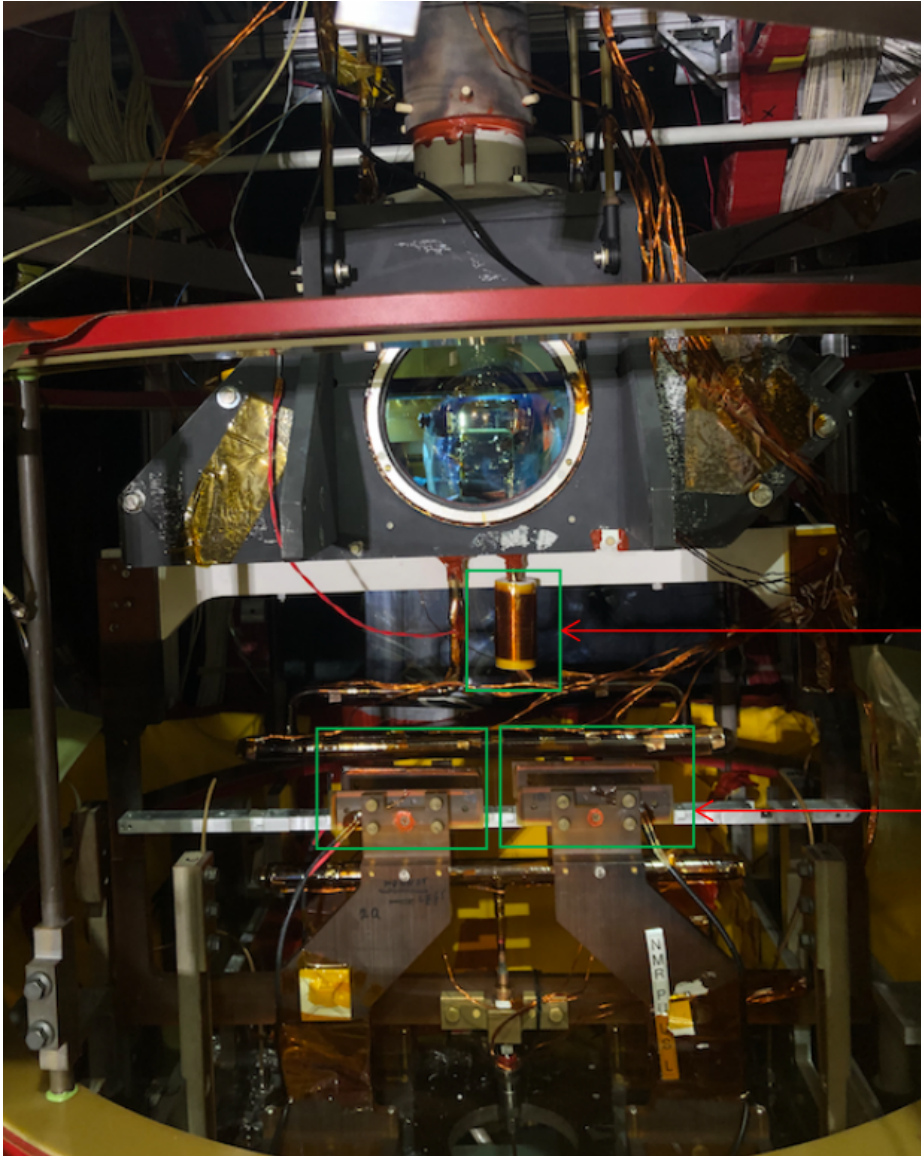
Figure 4.11: Convection cell setup for convection speed test. Convection flow direction is from down stream to upstream with transfer tube temperature gradient $+30°C$ between right transfer tube and left transfer tube.

denoted as B_{RF}, oscillates vertically with a frequency of $\pm\omega$ relative to the holding
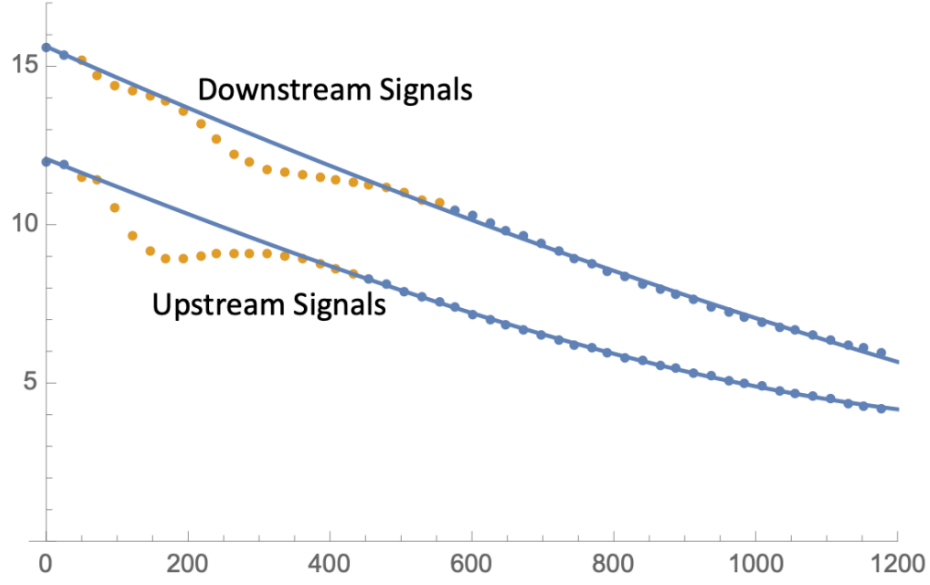
Figure 4.12: Convection speed test results. The yellow curve on top is target chamber downstream NMR (pick-up coils on right side) signal amplitude, while the yellow curve on bottom is target chamber upstream NMR (pick-up coils on left side) signal amplitude. The measured convection speed is $6.0cm/min \pm 0.1cm/min$.

field. This RF field possesses two components, as delineated below:

$$\vec{B}_{RF} = 2B_{RF}\cos\omega t\hat{x} \tag{4.8}$$

$$\vec{B}_{RF} = B_{RF}(\cos\omega t\hat{x} + \sin\omega t\hat{y}) + B_{RF}(\cos\omega t\hat{x} - \sin\omega t\hat{y}). \tag{4.9}$$

By employing the positive frequency approximation, the negatuve frequency component of the RF field will be disregarded. Then Equation 4.7 is altered into a frame of reference that rotates at the identical frequency $(+\omega)$ as the external RF field. Within this rotating frame, the alteration in the magnetic moment's rate is formulated as:

$$(\frac{d\vec{M}}{dt})_{rot} = (\frac{d\vec{M}}{dt})_{lab} + \vec{\omega} \times \vec{M} \tag{4.10}$$

$$= \gamma\vec{M} \times \vec{B}_0 + \vec{\omega} \times \vec{M} \tag{4.11}$$

$$= \gamma\vec{M} \times (\vec{B}_0 - \frac{\vec{\omega}}{\gamma}). \tag{4.12}$$
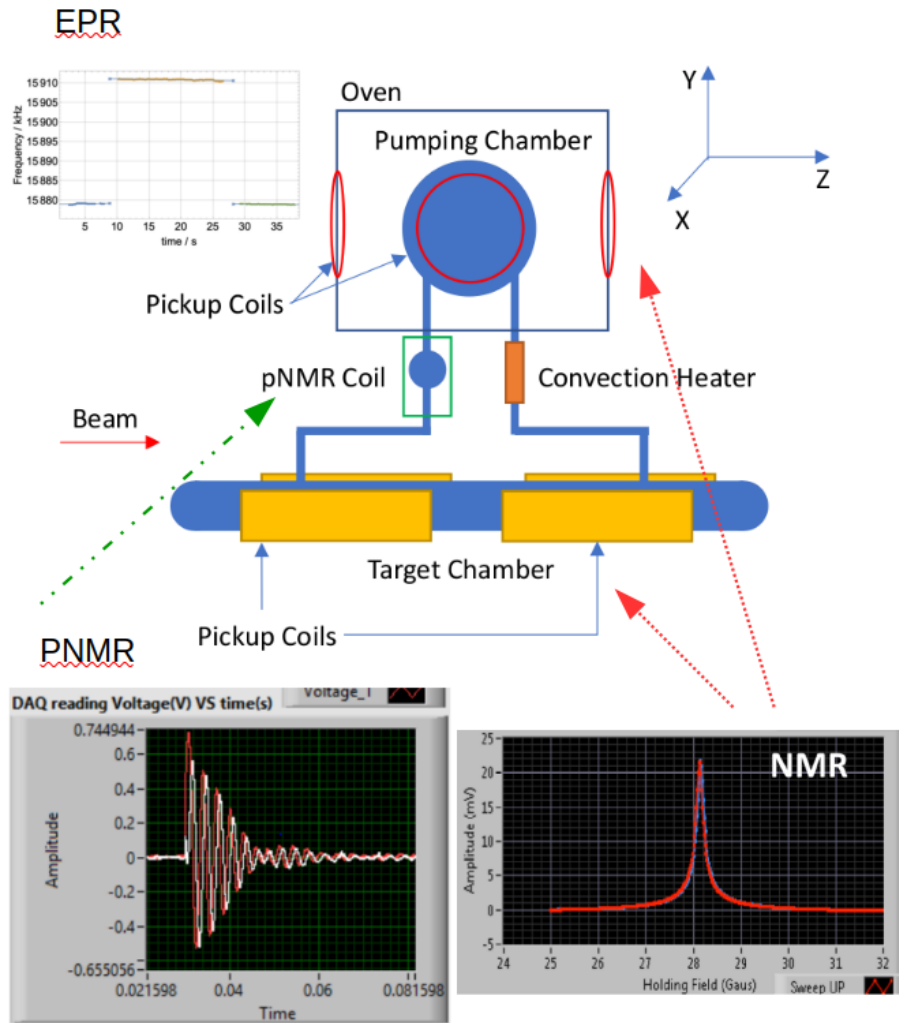
Figure 4.13: Experiment E12-06-110 employed three different polarimetry methods, each located in specific areas within the target cell. The EPR (Electron Paramagnetic Resonance) method, located at the top, measured the absolute polarization within the pumping chamber. This measurement was found to be nearly equal to the polarization within the target chamber due to convection flow. The PNMR (polarized Nuclear Magnetic Resonance) method was conducted at the transfer tube, while NMR measurements were performed at both the target and pumping chambers. Both PNMR and NMR methods were relative measurements.

With external RF field $\vec{B}_{RF}$, Equation 4.12 becomes:

$$(\frac{d\vec{M}}{dt})_{rot} = \gamma\vec{M} \times (\vec{B}_0 - \frac{\vec{\omega}}{\gamma} + \vec{B}_{RF}) \tag{4.13}$$

$$= \gamma\vec{M} \times \vec{B}_{eff}. \tag{4.14}$$

where the effective magnetic field $\overrightarrow{B}_{eff} = \overrightarrow{B}_0 - \frac{\vec{\omega}}{\gamma} + \overrightarrow{B}_{RF}$. For the experiment E12-06-110, the NMR measurements were performed using the field sweep method, which the strength of the holding field is swept around the resonance field $B_0 = \frac{\omega}{\gamma}$. During a NMR field sweep, the Adiabatic Fast Passage (AFP) conditions are maintained for a successful ^{3}He spin flip:

$$\frac{1}{T_2} \ll \frac{1}{B_{RF}} |\frac{dB_{RF}}{dt}| \ll \omega. \tag{4.15}$$

Here, T_2 denotes the relaxation time of the ^{3}He nuclear spin within the transverse plane. To meet the conditions for adiabatic fast passage (AFP), the field sweep must be rapid enough to prevent the nuclear spins from relaxing extensively, yet slow enough for the nuclear spins to effectively track the sweep.During the experiment E12-06-121, the NMR field sweep was conducted approximately every 5 hours. As depicted in Figure 4.12, during the NMR flip, the movement of the nuclear spin induces a magnetic field variation that correlates with the 3He polarization value. This fluctuating magnetic field generates an oscillating voltage across the NMR pickup coils encompassing the target cell. This voltage is then detected by a lock-in amplifier, configured with a reference frequency set at $f_L = \omega_L/2\pi$. The measured voltage achieves its maximum amplitude when $\omega = \omega_L$, leading to the detection of a resonance peak in the magnetic field. The magnitude of the signal peak corresponds to the 3He polarization and is mathematically represented as:

$$S \propto \frac{P_{^3He}\mu_{^3He}B_{RF}}{\sqrt{(B_0 - \frac{\omega}{\gamma})^2 + B_{RF}^2}}, \tag{4.16}$$

where $P_{^3He}$ is the ^{3}He polarization, while $\mu_{^3He} = 6.706984 \times 10^{-14} \frac{MeV}{T}$ represents the magnetic moment of ^{3}He.
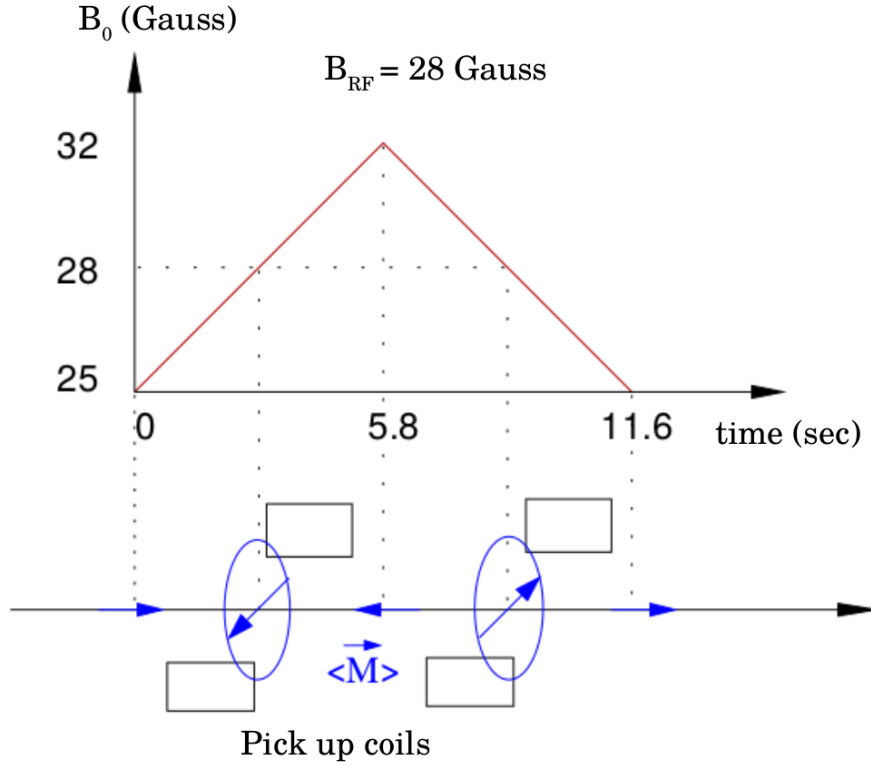
Figure 4.14: ^{3}He spin flip using AFP with holding field sweep method.

In our experimental setup, the RF frequency was set at 91 KHz, aligning with a resonance point at $B_0 = 28$ Gauss. The field sweep was conducted within the range of 25 Gauss to 32 Gauss. The signals from the pick-up coils were recorded using both the X and Y channels of the lock-in amplifier. These signals were measured in millivolts and were correlated with the holding field strength B in Gauss. The signal amplitudes, denoted as $S(B)$, were subjected to fitting procedures outlined by:

$$S(B) = \frac{A_{max}B_1}{\sqrt{B_1^2 + (B - B_0)^2}} + a + bB + cB^2. \qquad (4.17)$$

In this equation, B_0 stands for the resonant field, while B_1 represents the holding field. The parameter A_{max} is determined through a free fitting process and signifies the maximum amplitude. Additionally, the parameters a, b, and c are other free

fitting parameters. Both the X and Y channels are fitted using Equation 4.17, and their outcomes are merged to derive the ultimate signal amplitude along with its associated uncertainty:

$$A_{final} = \sqrt{(A_{max,X})^2 + (A_{max,Y})^2} \tag{4.18}$$

$$\Delta A_{final} = \sqrt{\frac{(A_{max,X} \cdot \Delta A_{max,X})^2 + (A_{max,Y} \cdot \Delta A_{max,Y})^2}{A_{final}^2}}. \tag{4.19}$$

An example NMR signal plot with holding fied at longitudinal direction ($180°$) is demonstrated in Figure 4.15. The NMR measurements provide a relative measurement of ^{3}He polarization, while Section 4.4 shown how the NMR measurements are combined with EPR measurements to yield an absolute measurement of the ^{3}He polarization. This combination leads to the determination of a calibration constant, expressed in units of $\%/mV$. Further calibrations conducted for each cell encompass NMR-AFP loss tests, see Table 4.1. These tests assess the polarization loss induced by measurements for each NMR field sweep. For typical NMR field sweep, both up-sweep and down-sweep are carried out, enabling the ^{3}He spins to revert to their original direction.

Cell	Field Direction (°)	Field Gradient (mG/cm)	AFP Loss in PC (%)	AFP Loss in TC (%)
Dutch	90	<30	0.9	0.9
	180	<30	2	0.9
Big Brother	90	<30	0.9	0.9
	180	<30	1.7	0.4

Table 4.1: NMR AFP Loss
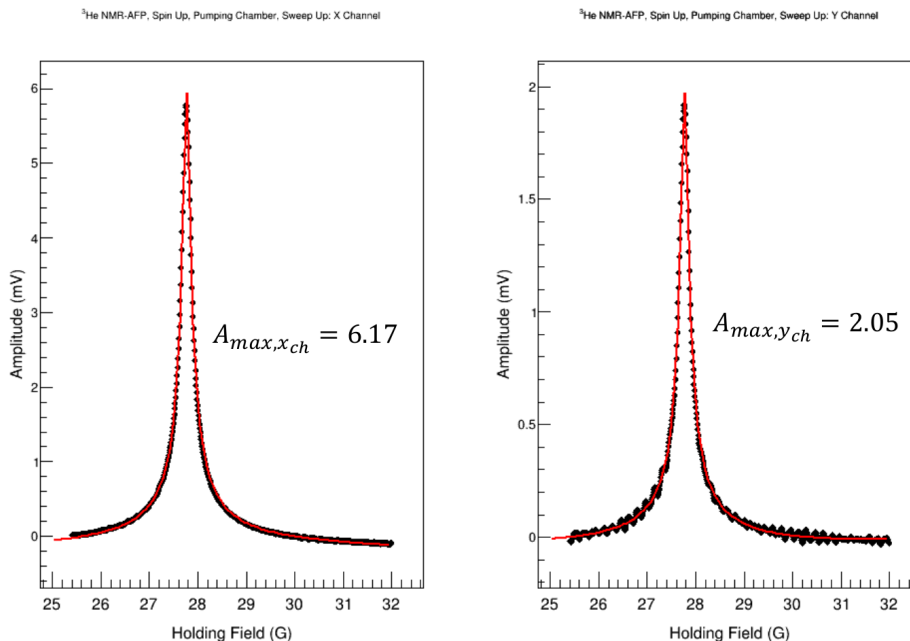
Figure 4.15: The raw AFP-NMR field sweep signals captured by the pick-up coils in the pumping chamber were recorded and subsequently re-plotted. These raw signals were then fitted with a red curve.

4.4 EPR Polarimetry

Within EPR polarimetry, the determination of ^{3}He polarization involves observing the Zeeman splitting of atomic energy levels containing unpaired electrons when subjected to an external magnetic field. Specifically, EPR analysis is conducted on the alkali atoms within the target cell. This process allows for the measurement of the absolute ^{3}He polarization, which subsequently serves as a calibration for NMR measurements. Figure 4.2 illustrates the Zeeman splitting of ^{85}Rb energy levels. Upon exposure to a 795 nm right (or left) circularly polarized laser in the pumping chamber, all Rb atoms become polarized into the $m_F = 3$ or $m_F = -3$ substate of the $S_{1/2}$ level. The separation between the $m_F = 3$ and $m_F = 2$ (or $m_F = -3$ and $m_F = -2$) levels, referred to as the EPR transition frequency, hinges on factors such as the external magnetic field B_0, the spin exchange collisions between the alkali atom and ^{3}He, and

the minor magnetic field generated from the polarization of ^{3}He:

$$\Delta\nu_{EPR} = \Delta\nu_{B_0} + \Delta\nu_{SE} + \Delta\nu_{^3He}. \tag{4.20}$$

The alteration in the EPR frequency due to changes in the induced magnetic field caused by ^{3}He spins serves as a means to quantify ^{3}He polarization in EPR polarimetry. In the course of EPR measurement, the orientation of ^{3}He spins is reversed through AFP. This alteration in spin direction is in relation to the external magnetic field. When the spins align with $\vec{B}_0$, the resultant magnetic field turns into $\vec{B}_0 - \vec{B}_{^3He}$, where $\vec{B}_{^3He}$ represents the magnetic field produced by the ^{3}He spins. Conversely, upon the spins being flipped back to their initial orientation, the effective magnetic field becomes $\vec{B}_0 + \vec{B}_{^3He}$. Ensuring the stability of the holding magnetic field helps eliminate the impact of the holding magnetic field on frequency shift. The frequency shift arising from ^{3}He polarization can be formulated as follows:

$$\Delta\nu_{EPR} = (\frac{d\nu_{EPR}}{dB_0})(\Delta B_{^3He} + \Delta B_{SE}). \tag{4.21}$$

The alteration in EPR frequency resulting from variations in the holding magnetic field, which is denoted as $\frac{\Delta\nu_{EPR}}{dB_0}$, is determined using the Breit-Rabi formula (M. V. Romalis and Cates 1998). The magnetic field ΔB_{SE} that arises due to spin exchange collisions, termed , can be expressed as follows:

$$\Delta\nu_{EPR} = (\frac{d\nu_{EPR}}{dB_0})(\Delta B_{^3He} + \Delta B_{SE}), \tag{4.22}$$

where g_e represents the gyromagnetic ratio, $_B$ stands for the Bohr magneton, Γ_{SE} represents the rate of spin exchange (between Rb and ^{3}He) per Rb atom, K_z signifies the z-component of ^{3}He spin, and $K_{^3He}$ is referred to as the frequency shift parame-

ter. The magnetic field resulting from the polarized ^{3}He, denoted as $\Delta B_{^3He}$, can be expressed as:

$$\Delta B_{^3He} = c\eta_{^3He}\mu_{^3He}P_{^3He}, \tag{4.23}$$

where the coefficient c is derived from the geometry of the pumping chamber, $\eta_{^3He}$ represents the number density of ^3He, and $P_{^3He}$ denotes the polarization of ^{3}He. By breaking down the terms ΔB_{SE} and ΔB_0 in Equation 4.21 using the expressions in Equation 4.22 and Equation 4.23, the resulting frequency shift $\Delta\nu_{EPR}$ is related to the ^{3}He polarization as:

$$\Delta\nu_{EPR} = c(\frac{d\nu_{EPR}}{dB_0})\kappa_0\eta_{^3He}\mu_{^3He}P_{^3He}, \tag{4.24}$$

where $\kappa_0 = \kappa_{00}T_{ref} + \kappa_{0T}(T - T_{ref})$ is contingent on factors like the geometry of the cell and temperature, which is the predominant source of error. The κ_0 values for the target cells employed in the experiment were furnished by the University of Virginia team (Katugampola et al. 2021).In the case of the spherical pumping chamber, the constant $c = 8\pi/3$. The absolute polarization of ^{3}He is then derived using the subsequent formula:

$$P_{^3He} = \frac{\Delta\nu_{EPR}}{\frac{8\pi}{3}\left(\frac{d\nu_{EPR}}{dB_0}\right)\kappa_0\eta_{^3He}\mu_{^3He}}. \tag{4.25}$$

In order to measure the frequency shift, an RF coil positioned adjacent to the pumping chamber, perpendicular to the holding field coils, was energized by a function generator set to match the Rb/K EPR transition frequency. For instance, let's consider the RF function generator adjusted to the EPR transition frequency corresponding to the $m_F = 3$ and $m_F = 2$ energy separation. Through optical pumping, all Rb elec-

trons were oriented into the $m_F = 3$ state before the EPR RF field was introduced (Cardona 2023). The RF field prompted the Rb electrons to transition to the $m_F = 2$ state and were subsequently re-excited to level P1 by absorbing 795 nm laser light. As a result of this repolarization process, when the Rb electrons returned to the $S_{1/2}$ level, it led to elevated photon emission linked to the D_1 transition $P_{1/2} \rightarrow S_{1/2}$ at a wavelength of 795 nm. Given the thermal interplay between the P1 and P3 levels, there was also photon emission related to the D_2 transition $P_{3/2} \rightarrow S_{1/2}$ at 780 nm wavelength (Cardona 2023). Despite the same quantity of D_1 and D_2 light emission, the D_1 photons couldn't be discerned from the substantial D_1 background originating from the incident pumping laser. Consequently, only the D_2 photons were detected by a photodiode equipped with a narrow band-pass filter (Cardona 2023). When the frequency of the RF function generator was modulated, the photodiode's voltage took on the shape of a Lorentzian function as it was swept through the EPR transition frequency. A lock-in amplifier was synchronized with the transition frequency, and this frequency reading was recorded by the computer (Cardona 2023). Following the EPR AFP flip, there was a change in the readout value of the EPR transition frequency. By quantifying this difference as $\Delta\nu_{EPR}$, the ^{3}He polarization value was derived using Equation 4.25.

Figure 4.16 depicted below displays the frequency spectra over time for a standard NMR-AFP frequency sweep, performed during E12-06-110, that flips the ^{3}He spins. Initially, the ^{3}He nuclei are polarized in the "low-energy" configuration, aligning their spins in an anti-parallel manner to the holding field. After the spin flip, their spins become aligned parallel to the holding field, and another NMR-AFP frequency sweep is executed to restore their original orientation. The central value indicates the resonant EPR frequency for the ^{39}K $m_F = -2 \rightarrow m_F = -1$ transition, approximately 19

MHz (Cardona 2023). The difference between the initial frequency and the ending frequency following the first NMR-AFP frequency sweep amounts to $2\Delta\nu_{EPR} \sim 61$ kHz, which is proportional to the ^{3}He polarization $P_{^3He}$. For this particular EPR measurement, the corresponding $\frac{d\nu_{EPR}}{dB_0} \sim 880\text{kHz/G}$. As illustrated in Figure 4.16,
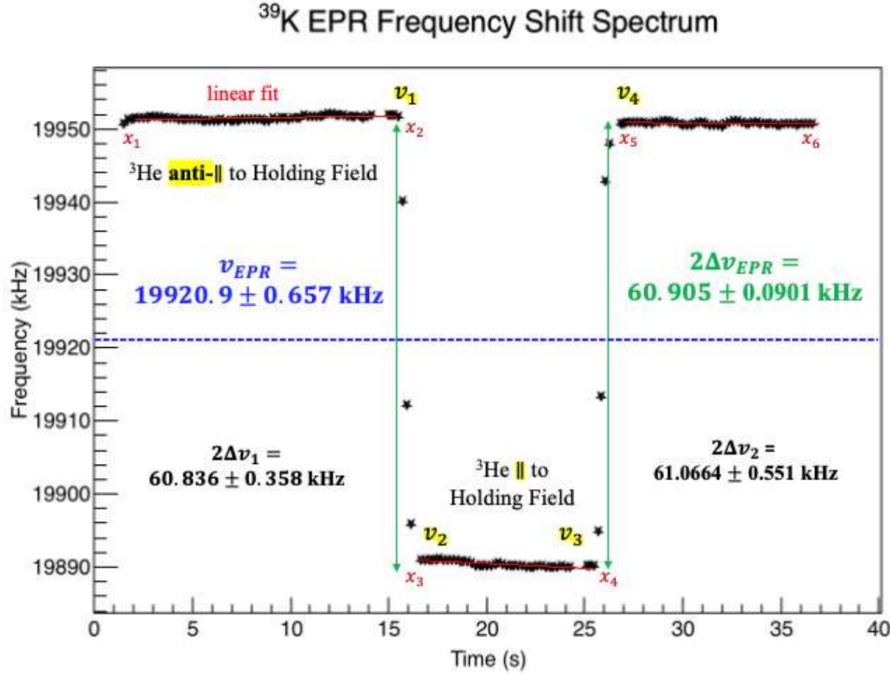
Figure 4.16: A typical AFP-NMR frequency flip technique is employed to extract the EPR frequency difference $2\Delta\nu_{EPR}$ which is represented by the green line. The EPR frequency difference is utilized to determine the polarization of ^{3}He. The EPR frequency of 39K, denoted as ν_{EPR}, is displayed in blue.

the three sets of pairs $(x_1,\ x_2)$, $(x_3,\ x_4)$, and $(x_5,\ x_6)$ are subjected to individual linear fits, with their corresponding fit parameters and coordinates employed to derive the highlighted edge frequencies ν_1, ν_2, ν_3, and ν_4 shown in yellow below. For instance, by utilizing the endpoint x_2 and the linear fit parameters p_0 and p_1 between x_1 and x_2, we obtain $\nu_1 = p_0 + p_1 x_2$ (Cardona 2023). The corresponding uncertainty $\delta\nu_1 = \sqrt{(\Delta p_1 x_2)^2 + (\Delta p_1)^2}$ is calculated, taking into account the errors Δp_0 and Δp_1 from the linear fit. The edge frequencies are then utilized to compute $2\Delta\nu_1$ and $2\Delta\nu_2$,

along with their associated errors, as indicated by the following equation:

$$2\Delta\nu_1 = \nu_1 - \nu_2, \delta(2\Delta\nu_1) = \sqrt{(\delta\nu_1)^2 + (\delta\nu_2)^2} \tag{4.26}$$

$$2\Delta\nu_2 = \nu_4 - \nu_3, \delta(2\Delta\nu_2) = \sqrt{(\delta\nu_3)^2 + (\delta\nu_4)^2}. \tag{4.27}$$

Then ν_{EPR} is the average of the two sets of edge frequencies with corresponding uncertainty $\delta\nu_{EPR}$:

$$\nu_{EPR} = \frac{1}{2}(\frac{\nu_1 + \nu_4}{2}) + \frac{\nu_2 + \nu_3}{2}) \tag{4.28}$$

$$\delta\nu_{EPR} = \frac{1}{2}\sqrt{(\delta\nu_1)^2 + (\delta\nu_2)^2 + (\delta\nu_3)^2 + (\delta\nu_4)^2}. \tag{4.29}$$

Thus $2\Delta\nu_{EPR}$ and its corresponding uncertainty $\delta(2\Delta\nu_{EPR})$ are computed by:

$$2\Delta\nu_{EPR} = \frac{\frac{2\Delta\nu_1}{(\delta(2\Delta\nu_1))^2} + \frac{2\Delta\nu_2}{(\delta(2\Delta\nu_2))^2}}{\frac{1}{(\delta(2\Delta\nu_1))^2} + \frac{1}{(\delta(2\Delta\nu_2))^2}} \tag{4.30}$$

$$\delta(2\Delta\nu_{EPR}) = \frac{1}{\frac{1}{(\delta(2\Delta\nu_1))^2} + \frac{1}{(\delta(2\Delta\nu_2))^2}}. \tag{4.31}$$

The EPR frequency alteration caused by the polarization of ^{3}He is minor, usually around $\nu_{EPR}/(2\Delta\nu_{EPR}) \approx 0.3\%$. With such a shift observed under the experiment's typical cell conditions, a polarization of $\sim 35\%$ is attained (Cardona 2023).

As previously discussed, EPR measurements provide an absolute value of ^{3}He polarization, and the NMR measurements were calibrated based on EPR data. To perform the calibration, NMR measurements were conducted both before and after an EPR measurement. This NMR/EPR calibration process was carried out whenever there was any alteration in configuration (such as changes in polarization direction or the

replacement of the production cell). The calibration constant $C_{EPR-NMR}$ is:

$$P_{^3He}^{EPR} = C_{EPR-NMR} \cdot C_{conv} \cdot s, \tag{4.32}$$

where s represents the height of the NMR signal peak, and C_{conv} stands for the convection constant. The determination of the convection constant involved considering the NMR AFP loss results (Table 4.1) under convection condition. The EPR analysis was carried out by M. Cardona (Cardona 2023), and the results for production cells used in experiment E12-06-110 is listed in Table 4.2.

Cell	Field Direction (°)	NMR/EPR CC (%/mV)
Dutch	90	5.12±0.13
	180	9.52±0.37
Big Brother	90	5.01±0.44
	180	8.27±0.21

Table 4.2: NMR/EPR Calibration Constant

4.5 PNMR Polarimetry

For JLab 6 GeV era experiments, Adiabatic Fast Passage Nuclear Magnetic Resonance (AFP-NMR) and Electron Paramagnetic Resonance (EPR) were developed to measured the ^{3}He polarization inside the target chamber. The absolute EPR measurement at pumping chamber was used to provide the calibration constant for the relative AFP-NMR measurement at target chamber to obtain the ^{3}He polarization. For JLab 12 GeV Upgrade, while keeping using AFP-NMR and EPR for target cell polarimetry, we developed the Pulse NMR (PNMR) system which will be a new polarimetry for polarized ^{3}He target cell. A PNMR measurement is preformed by

sending a RF pulse at Larmor frequency of ^{3}He to the PNMR coil. This RF pulse will create a RF magnetic field at PNMR coil with amplitude H_1 orthogonal to the holding field axis. Thus the RF pulse will tip the ^{3}He spin near the PNMR coil away from holding field axis (Liu 2017):

$$\theta_{tip} = \frac{1}{2}\gamma H_1 t_{pulse}, \tag{4.33}$$

where γ is the gyro-magnetic ratio, and t_{pulse} is the duration of RF pulse. When RF pulse ends, the spin precesses back to its initial state and experience free induction decay (FID). This FID signal is picked up by the PNMR coil. The amplitude of FID signal envelope will measure the transverse component of magnetic moment proportional to ^{3}He polarization (Liu 2017):

$$S(t) \propto M_z \sin\theta_{tip}\cos(\omega t + \phi)\exp(-\frac{t}{T_2}), \tag{4.34}$$

The newly developed PNMR has several advantages. First, a PNMR measurement will take shorter time to complete and will cause less depolarization compare to AFP-NMR. In addition, for future metallic end cells, since the metallic ends will attenuate RF signal at target chamber, PNMR will provide local polarimetry at transfer tube (Liu 2017). For the PNMR system R&D work, the former graduate students have developed a prototype PNMR with radio-frequency (RF) mixer and oscilloscope (Liu 2017).By replacing the RF mixer and oscilloscope with a lock-in amplifier and a fast DAQ card, I was able to finalized the PNMR system with smaller resolution uncertainty and better tracking of smaller PNMR signals, see Figure 4.17.

During the d_2^n experiment, on target cell "Briana" and "Tommy" I calibrated PNMR signal amplitude with NMR peak height. Thus, I have reached PNMR vs. NMR
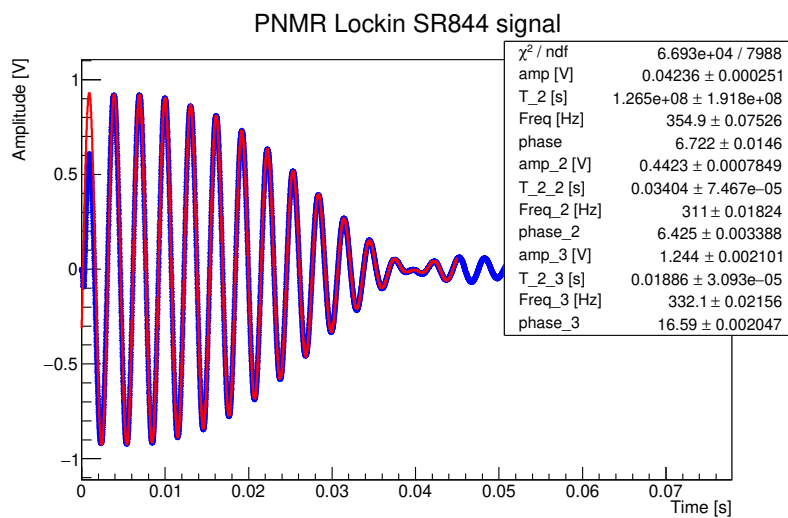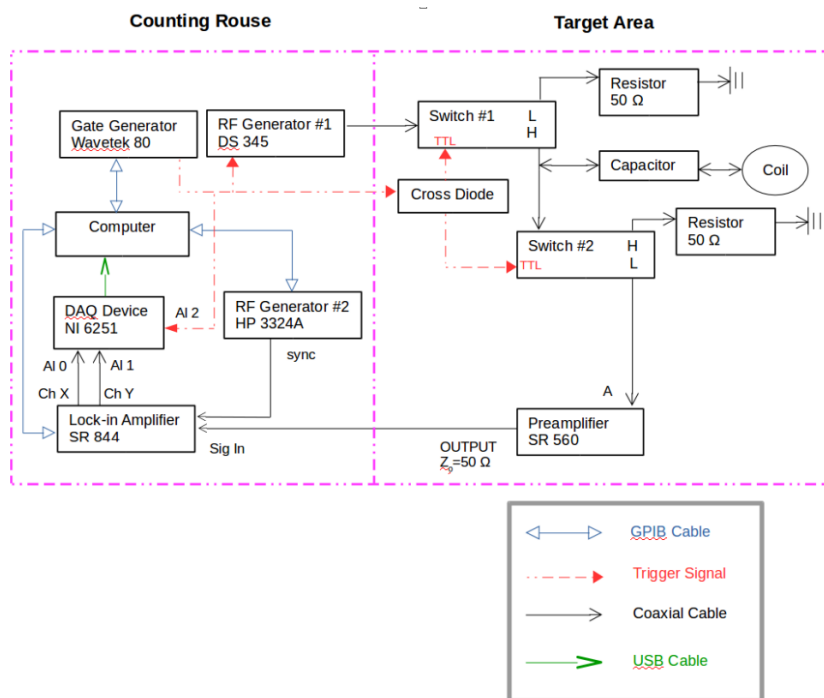
Figure 4.17: (Top) PNMR system with Lock-in amplifier and fast DAQ card set up. (Bottom) Typical PNMR FID signal.

measurement precision to about $\pm 2\%$ as in Figure 4.18.
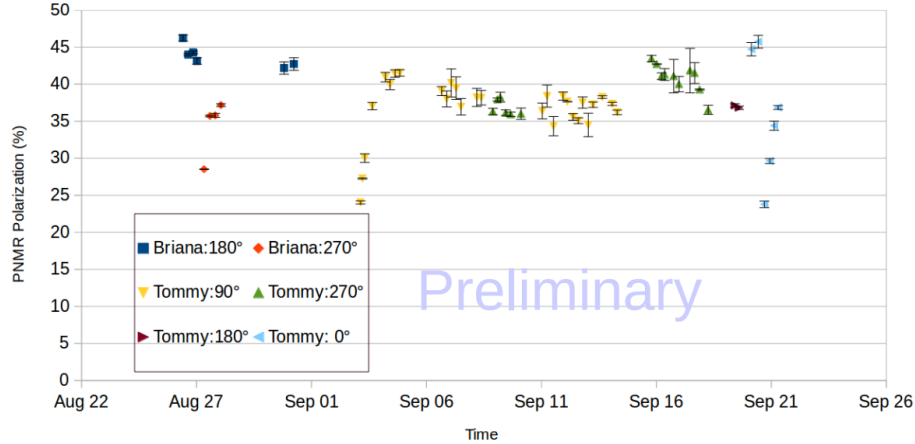
Figure 4.18: PNMR measurements calibrated with AFP-NMR.

4.6 Target Polarization Performance

Cell Dutch and Cell Bigbrother were the two polarized ^{3}He production cells used in the A_1^n experiment. The production cells were characterized at the University of Virginia and Jefferson Lab. The maximum ^{3}He polarization measured at University of Virginia without the electron beam on cell Dutch was 52% with a cold spin down lifetime of 29.4 hours, and 60% with a cold spin down lifetime of 26 hours for Big Brother. The target chamber cell wall thickness measurements were done at Jefferson Lab by using an ultra- sonic thickness gauge (Olympus 45 MG). For cell Dutch, the average wall thicknesses on "TC front" side (-y of the target) and "TC rear" side (+y of the target) were $1.29mm\pm0.01mm$ and $1.34mm\pm0.01mm$. For cell Big Brother, average wall thickness on "TC front" side (-y of the target) and "TC rear" side (+y of the target) were $1.52mm\pm0.01mm$ and $1.41\pm0.01mm$. The ^{3}He fill density and target cell end window thickness measurements were performed at the University

of Virginia. Measurement results for polarized ^{3}He target cell Dutch and cell Big Brother are listed in Table 4.3.

Cell	$^3He\ \rho_{fill}$ (amg)	$N_2\ \rho_{fill}$ (amg)	V_{PC} (cc)	V_{TC} (cc)	V_{TT} (cc)	Entrance Window Thickness (μm)	Exit Window Thickness (μm)
Dutch	7.76	0.115	180.68	68.02	19.78	134.142	143.475
	±0.13	±0.001				±0.063	±0.072
Big Brother	7.09	0.11	184.65	63.32	20.49	138.196	100.874
	±0.12	±0.001				±0.059	±0.070

Table 4.3: Measurement results for polarized ^{3}He target cell Dutch and cell Big Brother. Where the filling ^{3}He density and N_2 density is measured in amagats; the pumping chamber, target chamber and transfer tube volumes are measured in cubic centimeters; the entrance (upstream +z of the target) window and exit (downstream -z of the target) window thickness is measured in micrometers.
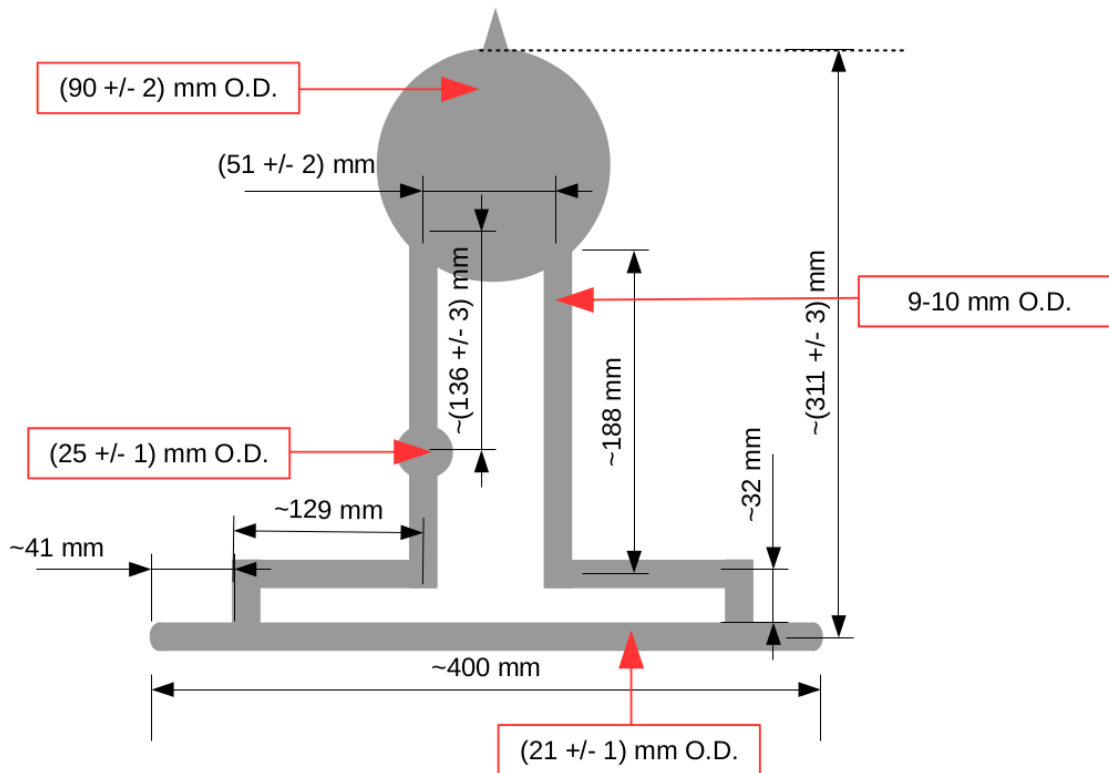
Figure 4.19: Typical dimension of production cells used in E12-06-110 experiment.

While the filling ^{3}He density were measured when the target cell in room temperature ($\sim 20°C$), the ^{3}He number density n_{PC} (n_{TC}) during the A_1^n experimental production condition was corrected by temperature of ^{3}He in pumping chamber and target chamber:

$$n_{PC} = \frac{\rho_{^3He}V_{tot}}{\frac{V_{TC}T_{PC}}{T_{TC}} + \frac{V_{TT}T_{PC}}{T_{TT}} + V_{PC}} \tag{4.35}$$

$$n_{TC} = \frac{\rho_{^3He}V_{tot}}{\frac{V_{PC}T_{TC}}{T_{PC}} + \frac{V_{TT}T_{TC}}{T_{TT}} + V_{TC}}, \tag{4.36}$$

where $V_{tot} = V_{PC}+V_{TC}+V_{TT}$ is the total volume of the cell. T_{PC} (T_{TC}) is the estimated internal ^{3}He temperature in pumping chamber (target chamber). While T_{TC} could be estimated from the mean value of 5 target chamber RTD readings. Since the high power lasers used in SEOP process produce significant heat inside pumping chamber. T_{PC} is greater than the temperature values measured by two RTDs attached on the surface of pumping chamber glass. Therefore a temperature test was conducted by taken several NMR measurements with the pumping lasers on (signal amplitude S^{on} in mV) and off (S^{off} in mV) and the average of the two RTD readings on the pumping chamber under each condition was $T_{PC}^{on(off)}$. Thus the pumping chamber temperature $T_{PC} = T_{test}$ obtained from the target cell temperature test:

$$T_{test} = \frac{V_{PC}T_{TC}^{on}}{\frac{S^{off}}{S^{on}}\frac{T_{TC}^{on}}{T_{TC}^{off}}\frac{T_C^{on}}{T_C^{off}}[V_{tot} + V_{PC}(\frac{T_{TC}^{on}}{T_{PC}^{off}})] - V_{tot} + V_{PC}}, \tag{4.37}$$

where T_{TC} is the average surface temperature of the target chamber and T_C is the average surface temperature at the center location of target chamber (located between the two sets of NMR pick-up coils). The temperature tests and studies were conducted by Junhao Chen, and the relative uncertainty for temperature-corrected

^{3}He number density is about 2%. Table 4.4 shows the list of temperature of ^{3}He inside pumping chamber (target chamber) and temperature-corrected ^{3}He number densities in pumping chamber (target chamber).

Cell	$T_{PC}(^\circ C)$	$T_{TT}(^\circ C)$	$T_{TC}(^\circ C)$	n_{PC}(**amg**)	n_{TC}(**amg**)
Dutch	245±5	38±1	37±1	6.56±0.13	10.94±0.22
Big Brother	245±5	38±1	31±1	6.01±0.12	10.24±0.21

Table 4.4: For A_1^n experimental production condition, the internal temperature for pumping chamber is obtained from temperature study while the internal temperature for target chamber is obtained from the mean value of 5 target chamber RTD readings. Then based on the ^{3}He filling density, the temperature corrected ^{3}He number densities in pumping chamber and target chamber are determined by the temperature study.

During A_1^n experiment, for every 4 or 5 one-hour production runs, NMR measurements are done at the start and at the end of each set of production runs in order to obtain a relative measurement of the ^{3}He target polarization within the pumping chamber and target chamber. Then all the NMR measurements are calibrated with the absolute polarization measurement with EPR within the pumping chamber. With NMR/EPR calibration constants for pumping chamber C_{PC}^{EPR} in Table 4.2, the following formulas are used to obtain polarization within the target chamber at the start P_{TC}^{init} and end P_{TC}^{end} of a certain run:

$$P_{TC}^{init} = \frac{S_{PC}^{upsweep}\beta^2 + S_{PC}^{downsweep}\beta}{2}C_{PC}^{EPR}C_{TCPC} \tag{4.38}$$

$$P_{TC}^{end} = \frac{S_{PC}^{upsweep} + (S_{PC}^{downsweep}/\beta)}{2}C_{PC}^{EPR}C_{TCPC}, \tag{4.39}$$

where C_{TCPC} is the polarization ratio between the target chamber and pumping chamber. $C_{TCPC} = 0.996$ and $\triangle C_{TCPC} = 0.002$ by solving the two-chamber convection

model equations. β is whole cell polarization loss:

$$\beta = 1 - \frac{\alpha_{PC} n_{PC} V_{PC} + \alpha_{TC} n_{TC} V_{TC}}{n_{PC} V_{PC} + n_{TC} V_{TC}}, \tag{4.40}$$

where α_{PC} (α_{TC}) is the pumping chamber (target chamber) AFP loss, n_{PC} (n_{TC}) is the (temperature-corrected) ^{3}He number densities in the pumping chamber (target chamber), and V_{PC} (V_{TC}) are the corresponding volumes.

The next step is to linearly interpolating polarization with run time:

$$P_{TC}^{run_n} = P_{TC}^{init} + (P_{TC}^{end} - P_{TC}^{init})\frac{T_{run_n}^{midpoint} - T_{nmr}^{init}}{T_{nmr}^{end} - T_{nmr}^{init}}, \tag{4.41}$$

where $P_{TC}^{run_n}$ is the target polarization for certain production run with run number n. $T_{run_n}^{midpoint}$ is the midpoint time for given run n and $T_{nmr}^{end} - T_{nmr}^{init}$ is the total time duration of the most recent NMR measurement. Figure 4.20 shows the The maximum ^{3}He reached was $\sim 60\%+$, and over 55% in $30\mu A$ beam. According to analysis done by Melanie Cardona (Cardona 2023) for relative and absolute part of systemic uncertainty, the total system uncertainty for target polarization interpolation is $\triangle P_t/P_t \leq 4\%$ see table. 4.5.

^3He **Target Quantity**	**Rel. Error** (%)
^{39}K-^{3}He κ_0	0.8
^{3}He PC and TC Densities	2
N_2 Dilution	0.3
PC Temperature (K)	1
TC Temperature (K)	0.3
NMR/EPR Calibration Constants (Statistical)	2.0/7.0

Table 4.5: Relative systemic uncertainty for polarized ^{3}He target polarization. In summary, systemic uncertainty for target polarization interpolation is $\Delta P_t/P_t \leq 4\%$ (Cardona 2023).
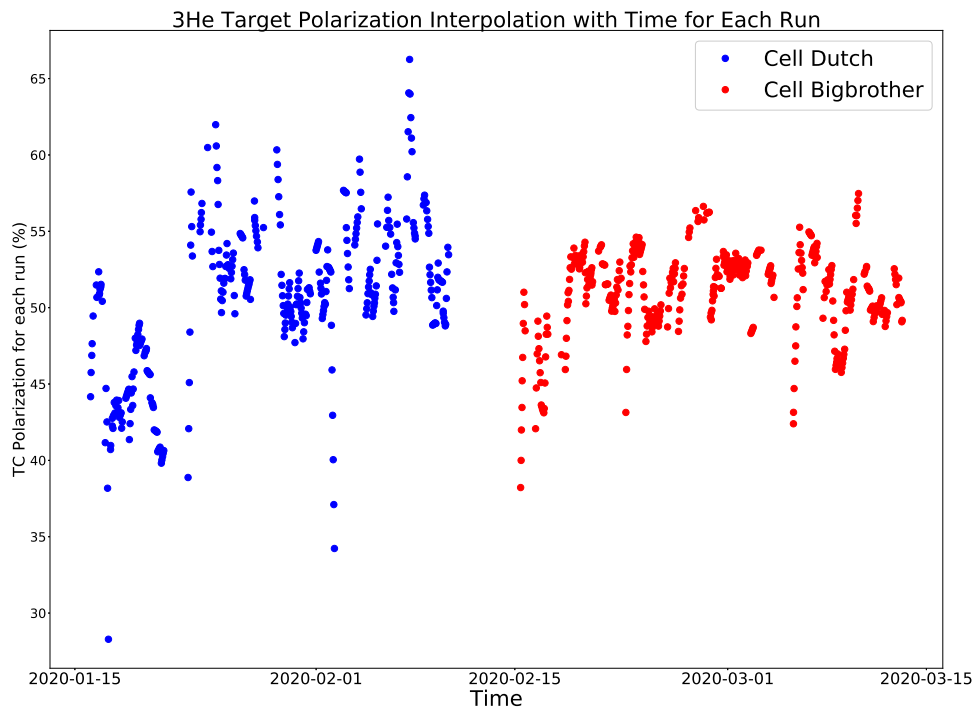
Figure 4.20: ^{3}He target polarization interpolation vs. Time for each good production run during A_1^n experiment.

Chapter 5

Data Analysis

5.1 Overview of asymmetry analysis

The primary objective of the data analysis in experiment E12-06-110 is to deduce the electron asymmetry, both $A_\perp$ and $A_\parallel$, for deep inelastic scattering involving electrons and ^{3}He nuclei. From these extracted values, the ^{3}He asymmetry $A_1^{^3He}$ and $A_2^{^3He}$ can be computed. Furthermore, considering nuclear corrections, additional calculations are performed to determine the virtual photon asymmetries A_1^n and A_2^n, along with the ratios of structure functions g_1^n/F_1^n and g_2^n/F_2^n. The analysis procedure, as depicted in Figure 5.1, outlines the series of steps followed after the initial collection of raw data. This chapter provides an in-depth exploration of each step in the analysis procedure up to the extraction of ^{3}He asymmetries.

5.2 Runs and Events Selection

Prior to conducting more advanced analysis on the acquired raw data, a series of initial steps including reference time cuts, detector time window cuts, and detector calibrations must be undertaken. These preliminary measures are essential to select good production run and ensure the reliability of the replayed data. These detector analysis studies were performed by Melanie Cardona. More information can be found
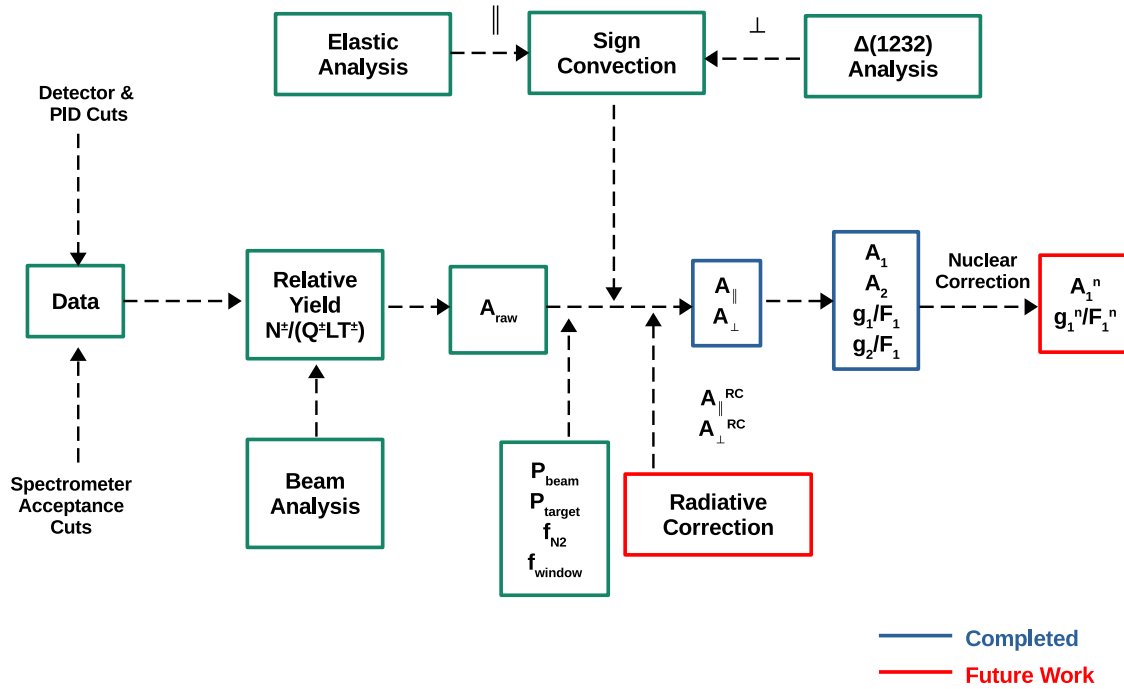
Figure 5.1: The experimental data analysis flowchart aims to extract the virtual photon asymmetries A_1^n.

in this reference (Cardona 2023).

5.3   Elastic Analysis

The initial momentum of the incoming electron beam remained constant along the $0°$ axis, directed towards the beam dump, with its spin direction being inverted at a frequency of 120 Hz (Cardona 2022). However, the spin direction of the ^{3}He nuclei remained fixed along the $0°$ axis for the longitudinal configuration, as depicted in Figure 5.2. Elastic scattering data were exclusively gathered using the SHMS. The

raw asymmetries during the 1-pass period from the elastic runs or delta resonance runs is:

$$A_{\parallel,\perp}^{raw} = \frac{\frac{N^+}{\eta_{LT}^+ Q^+} - \frac{N^-}{\eta_{LT}^- Q^-}}{\frac{N^+}{\eta_{LT}^+ Q^+} + \frac{N^-}{\eta_{LT}^- Q^-}}, \tag{5.1}$$

for the Hall C analyzer "hcana," N^+ represents the incident electrons that underwent scattering with a beam helicity of +1, occurring at 0° (Cardona 2022). Longitudinal asymmetries are essentially created by contrasting cross-sectional differences based on the relative alignment of beam and target spins:

$$A_{\parallel}^{phys} = \frac{A_{\parallel}^{raw}}{D P_b P_t} = \frac{\sigma^{\downarrow\Uparrow} - \sigma^{\uparrow\Uparrow}}{\sigma^{\downarrow\Uparrow} + \sigma^{\uparrow\Uparrow}}, \tag{5.2}$$

where D is the dilution factor (includes nitrogen dilution and glass windows dilution), P_b is electron beam polarization and P_t is the ^{3}He target polarization. When we compare equations 5.1 and 5.2, it becomes evident that N^+ is meant to represent the count of incident electrons whose spins align anti-parallel to both the beam momentum and the spins of the ^{3}He target (Cardona 2022). According to the first row of the table illustrated in Figure 5.6, data were collected during this time frame under an IHWP state of "OUT" (for the given Wein-flip state), where positive counts were obtained from incident electrons with spins parallel to the target spins. For these runs, a correction factor of -1 should be applied due to the reversed alignment as per the definition (Cardona 2022). Hence, this correction was applied when establishing the asymmetries for the elastic runs, as depicted in Figure 5.3. The sign of the total asymmetry resulting from all runs was subsequently compared with the sign calculated from theory, which predicts a negative elastic asymmetry for incident electrons with spins anti-parallel to the target spins. Hence, it was determined that adopting

this sign convention for the specific combination of beam-pass and Wein-flip state was accurate.
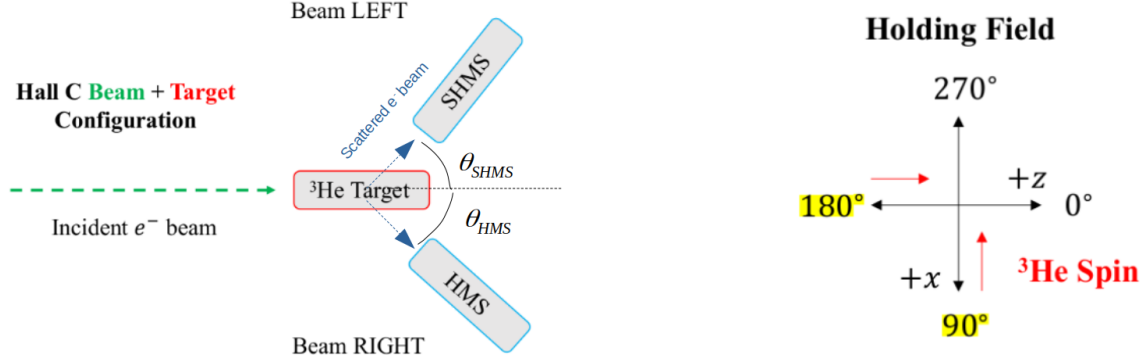
Figure 5.2: Definition of the two ^{3}He spin directions (red) used during E12-06-110, relative to the incident electron beam (green) and holding field orientations (black). The ^{3}He target was consistently pumped in the low-energy state (in order to reduce the risk of Masing (Michael V Romalis 1998)), with the spin of ^{3}He opposite to the holding field, throughout the data collection period (Cardona 2023).

In the transverse configuration, the ^{3}He spin direction was maintained steady along the 270° axis, directed to the left side of the beam, as illustrated in Figure 5.2. Similar to the case of elastic scattering, it was crucial to precisely understand the meaning of N^+ (and consequently N^-) to ensure confidence in the asymmetry signs. By definition, the transverse asymmetries originate from disparities in cross-sections based on the alignment of beam and target spins relative to each other:

$$A_\perp^{phys} = \frac{A_\perp^{raw}}{DP_bP_t} = \frac{\sigma^{\downarrow\Rightarrow} - \sigma^{\uparrow\Rightarrow}}{\sigma^{\downarrow\Rightarrow} + \sigma^{\uparrow\Rightarrow}}. \tag{5.3}$$

When we compare equations 5.1 and 5.3, it's evident that N^+ should represent the count of scattered electrons whose spins are oriented in an anti-parallel manner to the direction of the beam (Cardona 2022). Moreover, these incident electrons should be detected on the same side of the beam where the ^{3}He target spins are pointing.
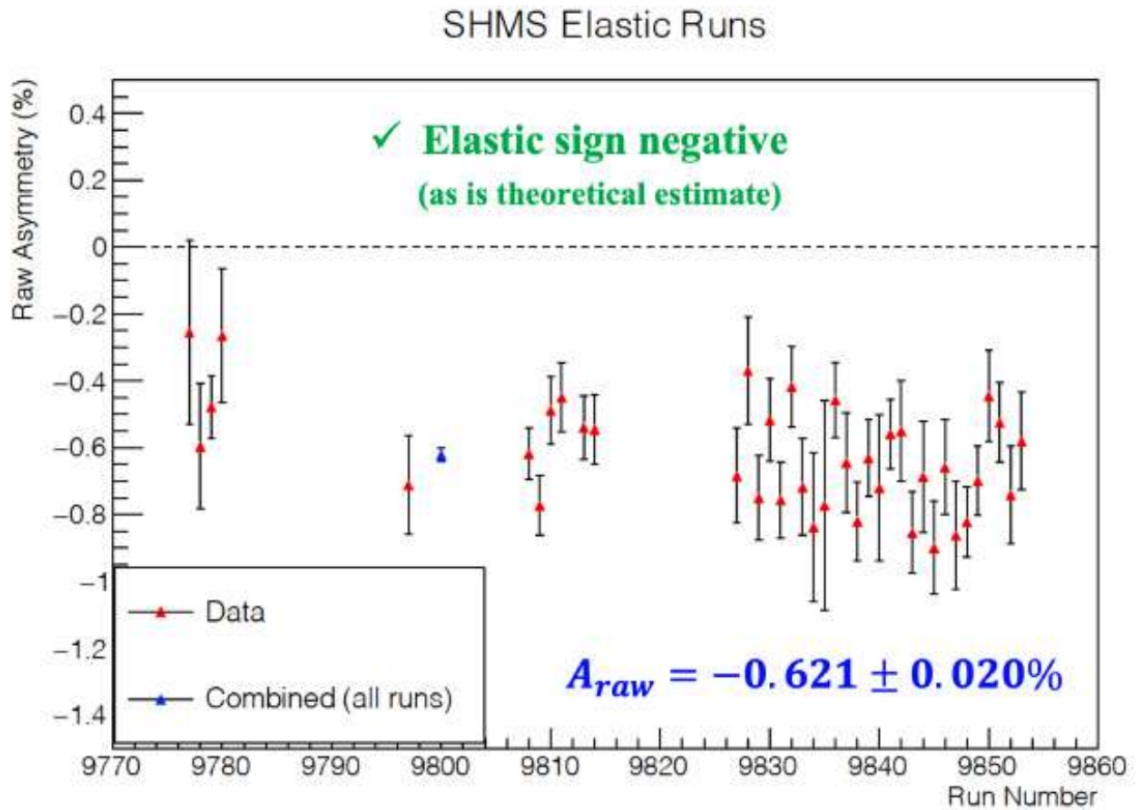
Figure 5.3: The raw asymmetries resulting from elastic scattering of electrons on ^{3}He measured by the SHMS. The central momentum configuration of the spectrometer was set to 2.1286 GeV, situated at an angle of 8.5 degrees (Cardona 2022). The combined A_{raw} (blue point) for all elastic runs is negative which consists to the theoretical expected sign of A_{raw}. Thus N^+ should describe the number of incident electrons whose spin is anti-parallel to the ^{3}He target spin.

Given that the SHMS is positioned on the left side of the beam, while the HMS is on the right, the same approach used for the elastic asymmetries, which involves correction factors for IHWP states, should be adopted for analyzing the SHMS delta runs. Conversely, the opposite approach should be followed for the HMS delta runs. Following this procedure should yield delta asymmetries with opposing signs – positive for the combined SHMS value and negative for the combined HMS value (Cardona 2022). This assertion was confirmed and is illustrated in Figure 5.4 and Figure 5.5.
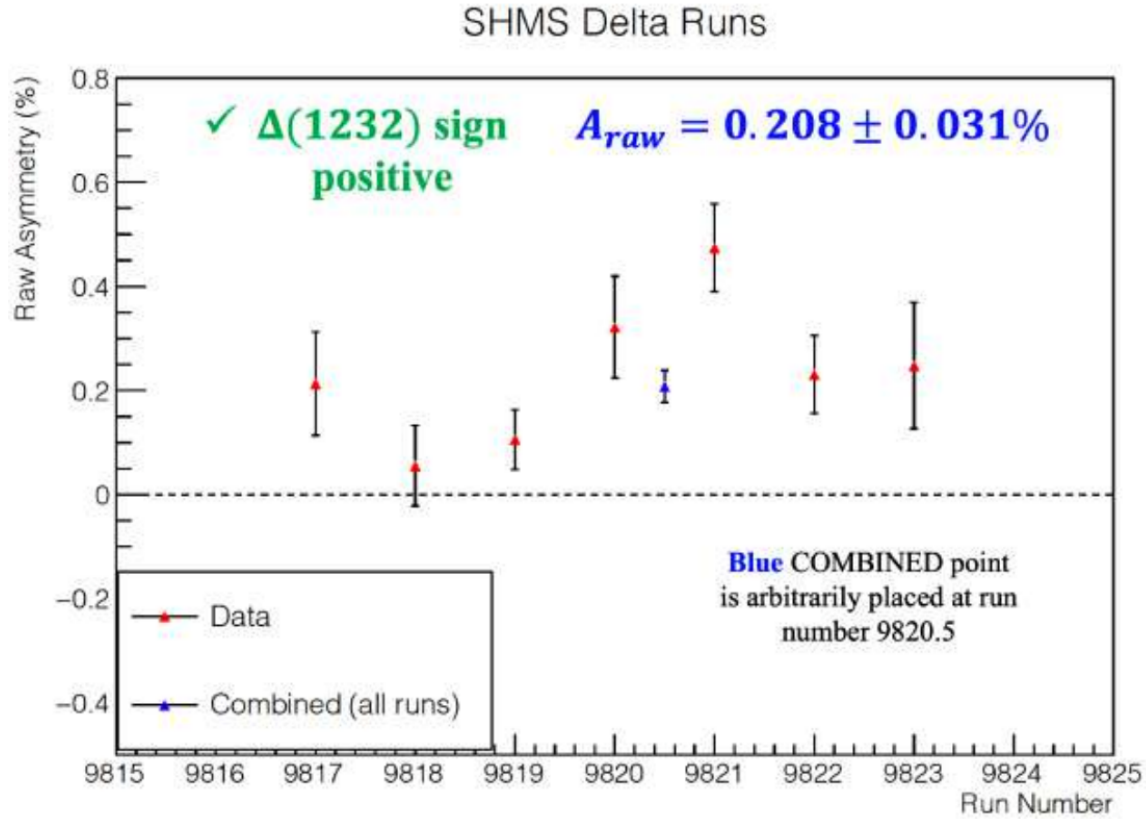
Figure 5.4: The SHMS spectrometer was configured with a central momentum of 1.7583 GeV, situated at an angle of 8.5 degrees on the beam left (Cardona 2022). The combined A_{raw} (blue point) for all delta resonance SHMS runs is positive which consists to the theoretical expected sign of A_{raw}. Thus N^+ should describe the number of incident electrons whose spin is anti-parallel to the beam direction and the scatted electrons being detected on the same side of the beam as that to which the ^{3}He spins are pointing.

5.4 Detector PID cuts and Efficiencies

Particle identification investigations were conducted utilizing the Cherenkov detector and calorimeter, as outlined in Section 3.4. The primary source of background was attributed to pions. The effectiveness of particle identification was determined by two variables: electron efficiency and pion rejection factor.

- Electron efficiency:

HMS Delta Runs
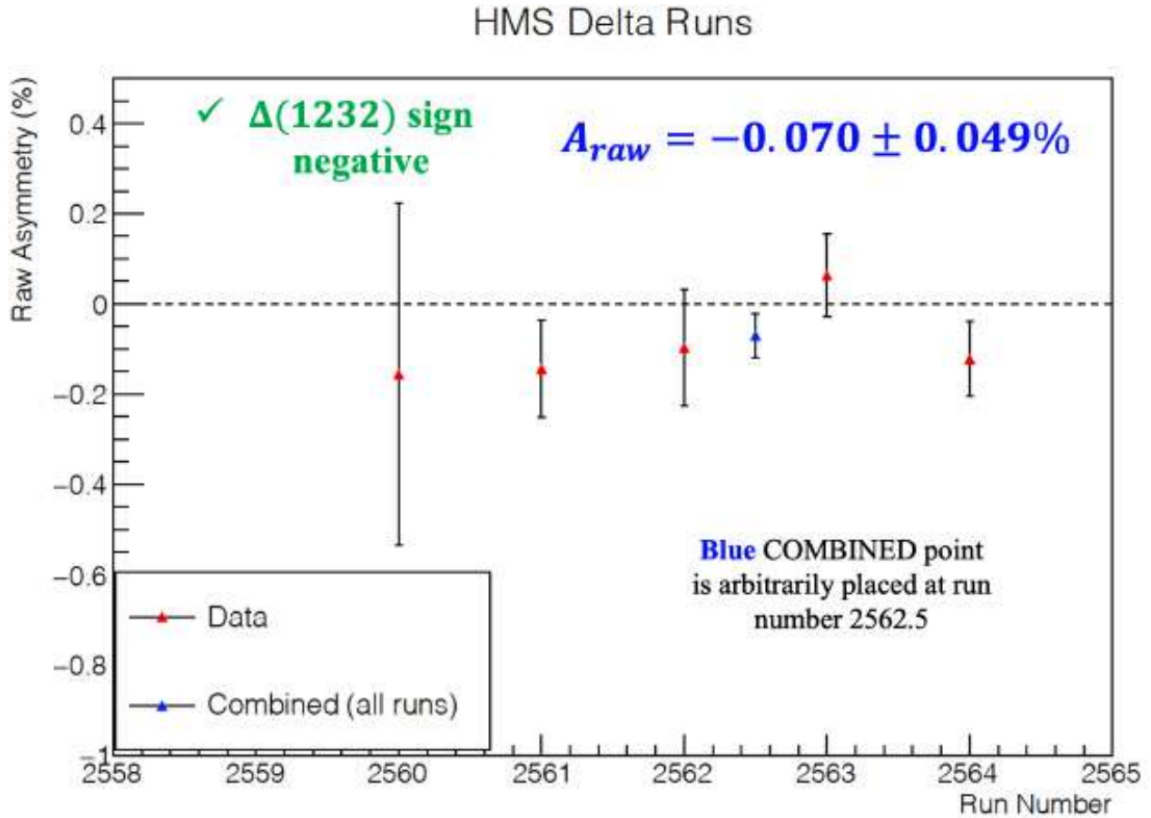
Figure 5.5: The HMS spectrometer was configured with a central momentum of 1.7583 GeV, situated at an angle of 11.5 degrees on the beam right (Cardona 2022). The combined A_{raw} (blue point) for all delta resonance HMS runs is negative which consists to the theoretical expected sign of A_{raw}. Thus N^+ should describe the number of incident electrons whose spin is anti-parallel to the beam direction and the scatted electrons being detected on the same side of the beam as that to which the ^{3}He spins are pointing.

The electron detection efficiency measures the capability of a detector to separate electrons from backgrounds (mostly pions). It is calculated as the ratio of the detected electron count N_d by the particle identification (PID) detector to the count of electrons in a well-defined electron sample N_s determined through the use of a sampling detector:

$$\epsilon = \frac{N_d}{N_s}. \tag{5.4}$$

Period	e⁻ spin direction: IHWP = IN	e⁻ spin direction: IHWP = OUT	³He spin direction
1-pass: SHMS 9777 - 9853	UPSTREAM $(\vec{e}^- \text{ anti-} \parallel \overrightarrow{^3He})$ $(\vec{e}^- \text{ anti-} \parallel \text{ beam direction})$	DOWNSTREAM $(\vec{e}^- \parallel \overrightarrow{^3He})$ $(\vec{e}^- \parallel \text{ beam direction})$	180°: DOWNSTREAM 90°: BEAM LEFT
5-pass: SHMS 9871 - 10354 HMS 2696 - 3162	**pass change** DOWNSTREAM $(\vec{e}^- \parallel \overrightarrow{^3He})$ $(\vec{e}^- \parallel \text{ beam direction})$	UPSTREAM $(\vec{e}^- \text{ anti-} \parallel \overrightarrow{^3He})$ $(\vec{e}^- \text{ anti-} \parallel \text{ beam direction})$	180°:DOWNSTREAM 90°: BEAM LEFT
5-pass: SHMS 10355 - 10759 HMS 3163 - 3580	UPSTREAM $(\vec{e}^- \text{ anti-} \parallel \overrightarrow{^3He})$ $(\vec{e}^- \text{ anti-} \parallel \text{ beam direction})$	**Wein-flip** DOWNSTREAM $(\vec{e}^- \parallel \overrightarrow{^3He})$ $(\vec{e}^- \parallel \text{ beam direction})$	180°: DOWNSTREAM 90°: BEAM LEFT

Figure 5.6: The summary of beam spin orientation (upstream, downstream) relative to the IHWP state, organized by time period, along with the target spin direction in relation to the holding field orientation (Cardona 2022).

With the assumption that the detected electron count follow Binomial distribution, the corresponding statistical error is:

$$\delta\sigma_\epsilon = \frac{1}{N_s}\sqrt{N_d(1 - \frac{N_d}{N_s})}. \tag{5.5}$$

- Pion rejection factor:

  Apart from assessing a detector's ability to detect electrons accurately, it's equally important to understand its capability to distinguish and reject pions. This aspect is defined by the ratio of the count of pions within an initial pion sample N_s determined through the sampling detector to the count of those erroneously identified as electrons by the particle identification (PID) detector within the same pion sample:

$$PRF = \frac{N_s}{N_d}. \tag{5.6}$$

Then according to Binomial Statistics the corresponding statistical error is:

$$\delta_{PRF} = PRF \cdot \sqrt{\frac{1 - (\frac{1}{PRF})}{N_d}}. \tag{5.7}$$

For the particle identification (PID) studies, the same YP and XP target acceptance cuts as the DIS production runs used cuts were applied, see Table 5.3 and Table 5.4. However, the z_{tg} target cut was adjusted. In order to maximize the available number of electrons for analysis and improve statistical precision, the entrance and exit windows of the glass ^{3}He cell were included in the samples. As a result, the vertex z target cuts are set to $z_{tg} = (-22, 22)$ cm (Cardona 2021). These investigations were conducted for both the low-momentum and high-momentum settings in the deep inelastic scattering (DIS) region (2.6 GeV and 3.4 GeV for the SHMS, and 2.9 GeV and 3.5 GeV for the HMS). The findings were consistent across both settings, leading to the same PID criteria being adopted to formulate the asymmetries (Cardona 2021). Consequently, the subsequent discussion will focus on representative plots solely from the low-momentum settings. Specifically, SHMS runs 10334-10347 and HMS runs 3181-3205 were linked together to execute the low-momentum PID analysis for each spectrometer (Cardona 2021).

5.4.1   HMS PID Cuts

- Calorimeter Efficiencies and PRFs:

To assess its ability to detect electrons, the Gas Cherenkov was initially utilized as the sampling detector to select the electron sample N_s by imposing a strict
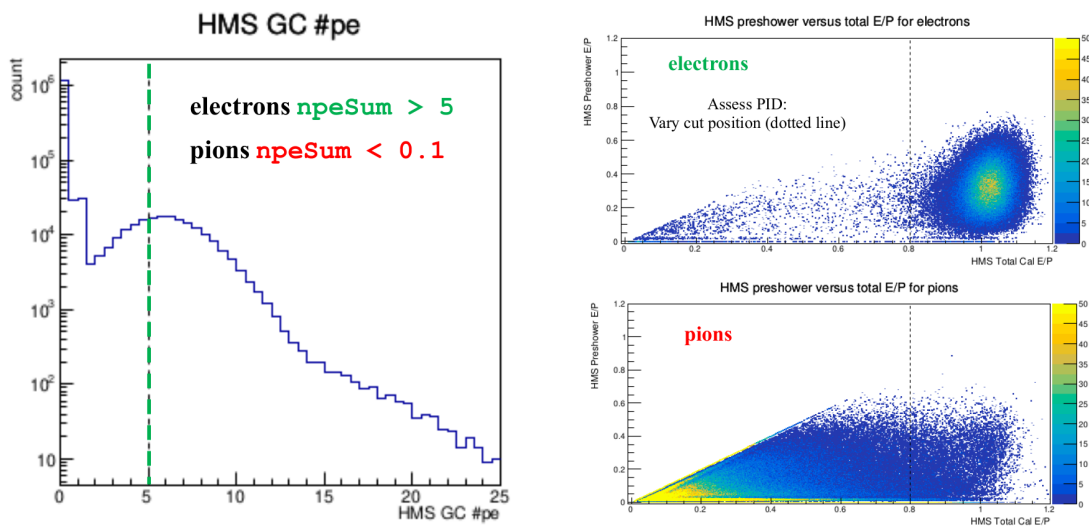
Figure 5.7: Left: HMS Gas Cherenkov number of photo-electron (npe) distribution. The npe distribution is summed over both PMTs and the dotted green line represents the cut npeSum> 5 in order to select electrons. Top-Right: Pre-shower E/P vs total E/P distribution of selected electrons with a cut of npeSum> 5. Bottom-Right: E/P vs total E/P distribution selected pions with a cut of npeSum < 0.1. The solid black line at a total E/P value of 0.80 represents the chosen calorimeter E/P cut that was ultimately applied in the analysis to identify clean electrons (Cardona 2021).
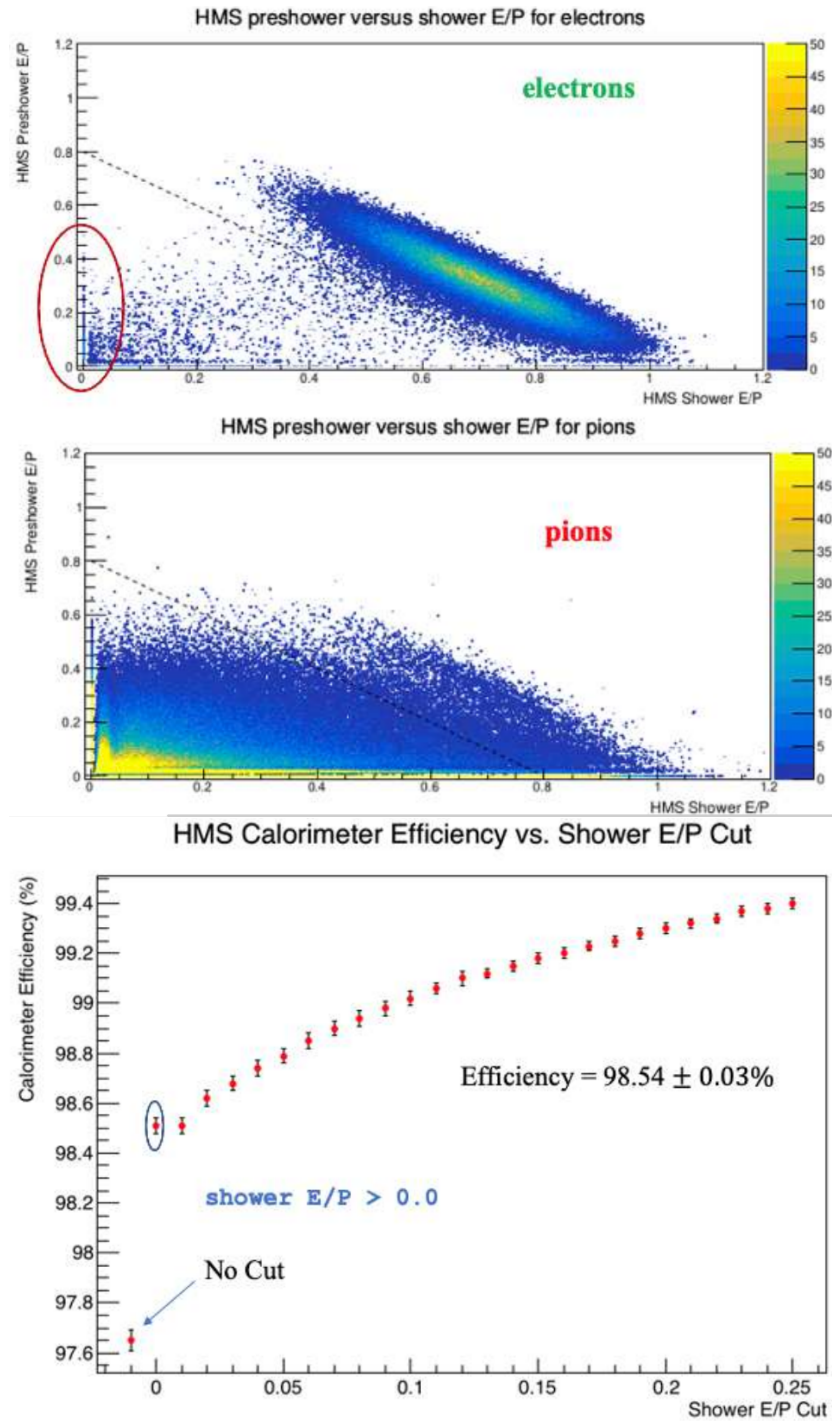
Figure 5.8: Top: 2D plots depicting the normalized energy deposition in the pre-shower and shower for electrons (upper part) and pions (lower part). Within the plot, there is a marked area highlighted in red, which corresponds to a grouping of low-energy events as electrons from HGC cut npeSum> 5. Bottom: The electron detection efficiencies as a function of shower E/P cuts varying between 0 and 0.25, with the point at a shower E/P < 0 for no shower cut (Cardona 2021).

cut on its number of photo-electrons (npe) distribution, illustrated on the left side of Figure 5.7. This cut was set at HMS Gas Cherenkov npesum > 5 (Cardona 2021). The Gas Cherenkov contained N_4F_8O gas at 0.225 atm, which resulted in a pion threshold energy of around 5.5 GeV (Sawatzky 2023). Since the highest central momentum setting used for the HMS during data collection was smaller than this threshold (3.5 GeV), theoretically, no pions should have generated any photo-electrons within the Cherenkov detector. Therefore, the pion sample was identified as the particles passing a cut of HMS Gas Cherenkov npesum < 0.1 (Cardona 2021).

The normalized energy deposition within the pre-shower of the calorimeter, relative to its momentum (H.cal.eprtracknorm), was plotted against the total normalized energy (sum of pre-shower and shower) of the best track detected within the calorimeter (H.cal.etracknorm). These plots are displayed for both the selected electron sample N_s (top right of Figure 5.7) and the pion sample (bottom right). Electrons within N_s that also met the HMS calorimeter best track normalized energy > 0.80 cut, which served as the Particle Identification (PID) cut in this case, were considered as detected by the calorimeter, denoted as N_d (Cardona 2021) . Electrons tend to deposit most of their energy within the calorimeter. However, similar to the SHMS calorimeter, there is a cluster of events within the electron sample N_s that have a total calorimeter E/P value close to 0. This cluster is indicated by the red circled region in the top right plot of Figure 5.7. These events are likely secondary, low-energy electrons generated from pions scattering off the windows of the Gas Cherenkov and then being absorbed in the pre-shower (Cardona 2021). As a result, these particles are excluded from the electron sample N_s but included in the pion sample used to

calculate the PRFs.

The normalized energy deposition (E/P) for both the electron and pion samples within the pre-shower and shower components is presented in Figure 5.10. The electron efficiency was determined by varying the shower E/P cuts and calculating it as a function of these cuts. The efficiency exhibits a slight increase in the range of approximately 98.5% to 99.5% for all shower E/P > 0 cuts, contrary to the plateau observed for the same cut in the SHMS, which reaches around 99.4% (Cardona 2021). Consequently, a shower E/P > 0 cut was added in conjunction with the npe sum > 5 cut to define the electron sample N_s. Electrons that pass this additional PID cut, HMS calorimeter best track normalized energy > 0.80, form the subset detected by the calorimeter, N_d (Cardona 2021) . The electron detection efficiency is then computed using Equation 5.4.

For the pion sample N_s, identified based on HGC data (particles passing HMS Gas Cherenkov npesum < 0.1), the pion rejection factor is calculated using Equation 5.6, considering the pions within N_s that survive the HMS calorimeter cut (HMS calorimeter best track normalized energy > 0.80) (Cardona 2021). Both the electron efficiency and pion rejection factor are plotted as functions of varying HMS calorimeter best track normalized energy cut positions, as shown in Figure 5.9. A balance between the electron efficiency ϵ and the PRF must be maintained since tightening the PID cut on HMS calorimeter best track normalized energy results in a drop in electron efficiency but an increase in pion suppression. A cut of HMS calorimeter best track normalized energy > 0.80 provides a reasonably high efficiency of $\epsilon \sim 98.5\%$ and a moderate PRF of approximately 80 (Cardona 2021).

For PID study done on HMS calorimeter, an additional PID cut utilizing the

pre-shower was applied to both the electron and pion samples to enhance the PRF without significantly compromising the electron efficiency. The study was conducted to assess the electron efficiency and pion rejection factors as functions of varying pre-shower cuts, ranging from HMS calorimeter normalized energy deposition > 0 to HMS calorimeter normalized energy deposition > 0.10 (Cardona 2021). These results are presented in Figure 5.10. Once again, this pre-shower cut was incorporated in addition to the standard PID cut of HMS calorimeter best track normalized energy > 0.80, which was applied to both the electron and pion samples N_s to compute N_d (Cardona 2021).
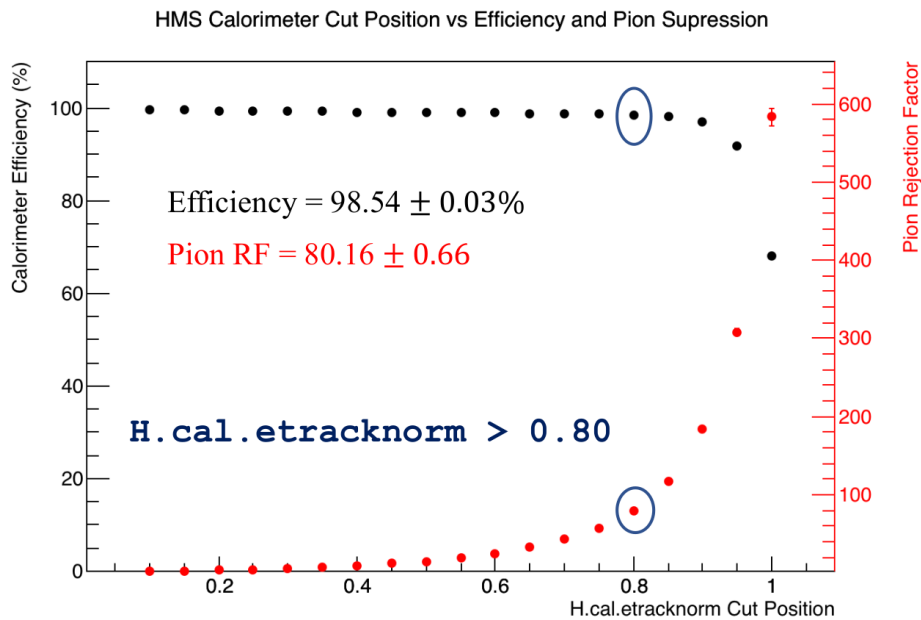
Figure 5.9: Plotted electron efficiency as the black points and Pion Rejection Factor as the red points for the HMS calorimeter. These metrics are plotted against different total calorimeter energy E/P cuts. Notably, when using a cut of HMS calorimeter best track normalized energy (H.cal.etracknorm > 0.80), it results in an efficiency of $\epsilon = 98.54\%$ and a moderately high Pion Rejection Factor of PRF $= 80.16$, both points highlighted in blue circle (Cardona 2021).

- HGC Efficiencies and PRFs:

  To assess the Heavy Gas Cherenkov detector's performance as a PID device, a
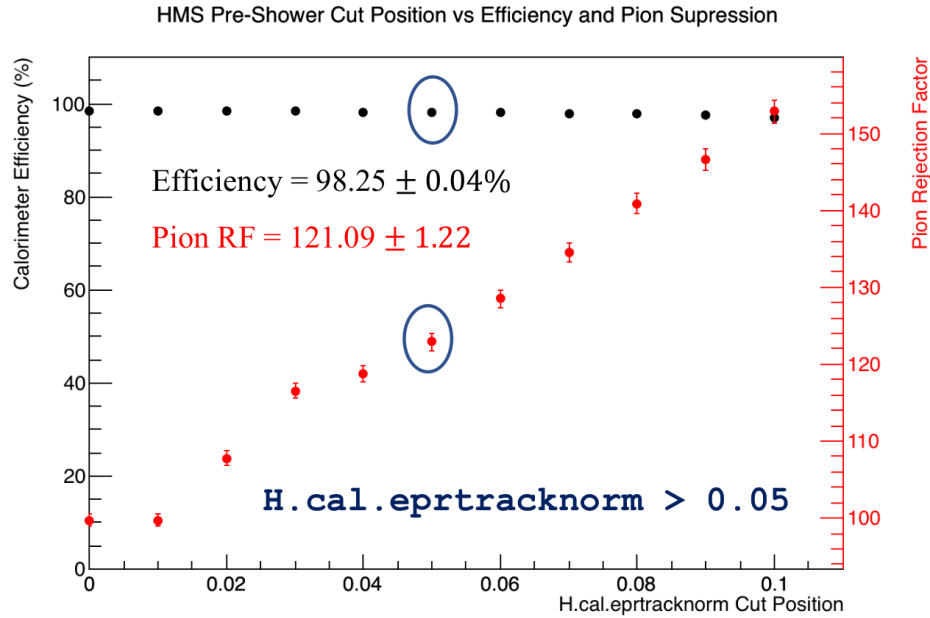
Figure 5.10: Plotted electron efficiency as the black points and Pion Rejection Factor as the red points for the HMS calorimeter. These metrics are plotted against different pre-shower energy E/P cuts. With a pre-shower normalized energy deposit threshold of HMS calorimeter normalized energy deposition (H.cal.eprtracknorm> 0.05), the electron detection efficiency ϵ experiences only a minor decrease, going from 98.54% to 98.25%. However, there is a significant increase in the PRF value from approximately 80 to about 121 (Cardona 2021).

different approach was taken. This time, the calorimeter was employed to select both the electron and pion samples N_s, and then the Heavy Gas Cherenkov (HGC) was used to apply a PID cut to estimate the number of surviving electrons and pions N_d. A two-dimensional cut was applied to the HMS calorimeter, considering both the pre-shower and total (pre-shower + shower) energy deposition, as illustrated in the right-hand side of Figure 5.11. For the electron sample (used as N_s in Eq. 5.4), the selection criteria were set as follows: 0.90 < HMS calorimeter best track normalized energy < 1.15 && 0.10 < HMS calorimeter normalized energy deposition < 0.50. For the pion sample (serving as N_s in Equation 5.6), the criteria were: 0.02 < HMS calorimeter best track normal-
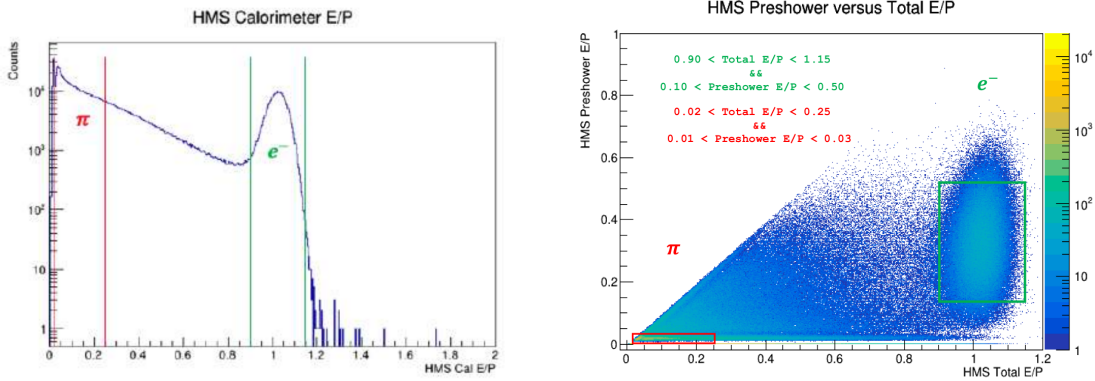
Figure 5.11: Left: A 1D plot showing the normalized total energy deposition within the HMS calorimeter. The red lines represent the energy limits for selecting pions, while the green lines represent those for selecting electrons. Right: A two-dimensional plot displaying the energy deposited within the pre-shower versus the energy within the entire calorimeter which is shower plus pre-shower. The red lines indicate the pre-shower and total energy boundaries for selecting pions, while the green lines indicate those for selecting electrons (Cardona 2021).

ized energy < 0.25 && $0.01 <$ HMS calorimeter normalized energy deposition < 0.03 (Cardona 2021). Figure 5.12 presents the npe distribution within the HGC after applying these calorimeter cuts. The middle plot displays the distribution after applying the electron sample cuts, while the right plot shows the distribution after applying the pion sample cuts. Corresponding efficiencies and pion rejection factors are depicted as a function of various HMS Gas Cherenkov npesum PID cuts in Figure 5.13. In this context, the number of electrons and pions that pass this PID cut serve as N_d in equations 5.4 and 5.6, respectively.

- HMS PID Summary:

  In the analysis, clean scattered electrons detected by the HMS were identified using a calorimeter cut criterion of HMS calorimeter best track normalized energy > 0.80 in combination with an HGC npe sum cut of HMS Gas Cherenkov npesum > 1 (Cardona 2021). The final PRF, achieved by combining the per-
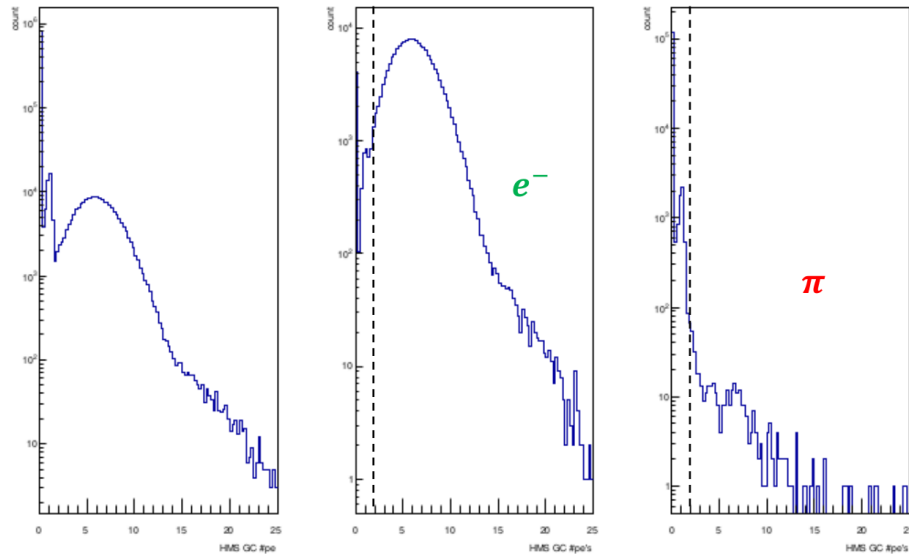
Figure 5.12: Left: The distribution showing the total number of photo-electrons summed across both PMTs of the HGC, without applying any calorimeter sample cuts. Middle: The npe distribution after implementing the 2D calorimeter criteria to choose electrons. Right: The npe distribution after employing the 2D calorimeter criteria to choose pions. The solid black lines represent a cut position of HMS Gas Cherenkov npesum (H.cer.npeSum > 1)(Cardona 2021).

formance of both the Cherenkov detectors and calorimeters in a multiplicative manner, exceeded the experimental target of 10^3 (Cardona 2021). As illustrated in Figure 5.10, the implementation of a pre-shower cut significantly enhanced the PRF while causing only minimal loss in electron efficiency. For instance, applying a pre-shower cut like HMS calorimeter normalized energy deposition > 0.05, in addition to the previously mentioned criteria, resulted in asymmetry measurements consistent with those obtained without it, accompanied by similar error bars (Cardona 2021). A summary of the PID studies conducted on the HMS for the 2.9 GeV and 3.5 GeV DIS settings is presented in Table 5.1.
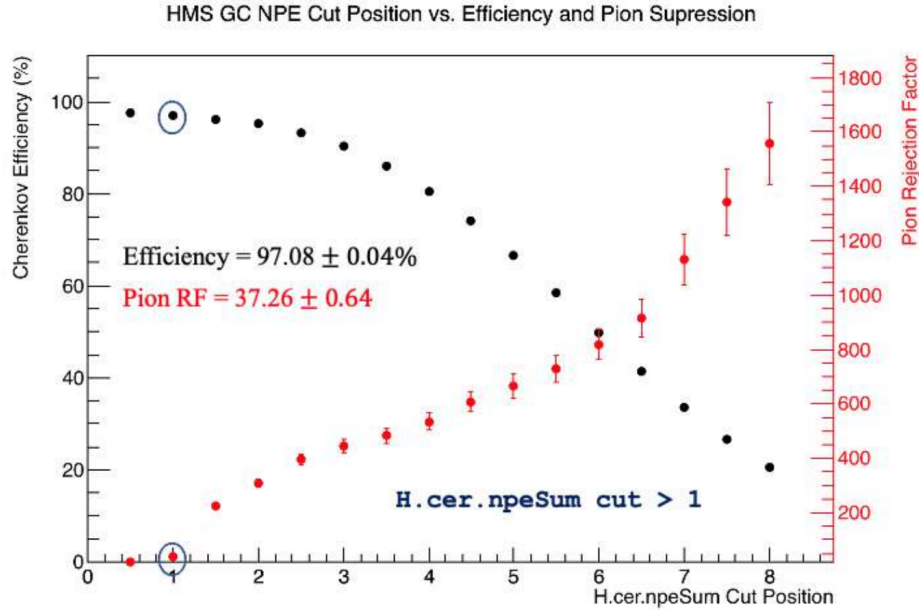
Figure 5.13: Electron efficiency plotted as black points and Pion Rejection Factor ploted as plotted as red points of the HMS HGC plotted against different PID cuts applied to the npe sum distribution. The blue circle highlights the efficiency and PRF values associated with a cut of HMS Gas Cherenkov npesum (H.cer.npeSum> 1), which is the cut ultimately employed in this analysis to identify valid electrons (Cardona 2021).

5.4.2 SHMS PID Cuts

- Calorimeter Efficiencies and PRFs:

  To evaluate the SHMS calorimeter's electron detection capabilities, the Noble Gas Cherenkov (NGC) was initially employed as the sampling detector to select the electron sample N_s through a strict cut on the number of photo-electrons (npe) distribution, depicted in the left part of Figure 5.15. The specific cut chosen for this purpose was SHMS Nobel Gas Cherenkov npesum > 8 (Cardona 2021). The NGC, which used N_2 gas at 1 atm, had a pion threshold energy of 5.7 GeV (Sawatzky 2023). Given that the highest SHMS central momentum setting employed during data collection was below 3.4 GeV, it was theoretically expected that no pions would generate photo-electrons in the Cherenkov de-

P_c	Cher.Cut	Cher.Eff.	PRF	Cal.Cut	Cal.Eff.	PRF	Comb.PRF
2.9 GeV	#npe>1	97.08%	37.26	E/P>0.8	98.54%	80.16	2987
		±0.04%	±0.64		±0.03%	±0.66	±57
3.5 GeV	#npe>1	97.84%	33.75	E/P>0.8	98.87%	76.35	2577
		±0.04%	±0.99		±0.05%	±1.34	±88

Table 5.1: HMS PID summary for all central momentum settings P_c during the DIS production run. By multiplying the pion rejection factor (PRF) derived from the HGC study and the PRF from the calorimeter study, the combined pion rejection factors are obtained. The resulting values of combined pion rejection factors exceed the targeted value of 10^3 (Cardona 2021).

tector. As such, the pion sample was defined as the particles passing a cut of SHMS Nobel Gas Cherenkov npesum < 0.1 (Cardona 2021). The energy of the best track deposited within the pre-shower of the calorimeter, normalized by its momentum SHMS calorimeter normalized energy deposition, has been graphed against the total energy (pre-shower plus shower) of the best track deposited within the calorimeter, also normalized by its momentum SHMS calorimeter best track normalized energy. This is shown for the selected electron sample N_s in the upper right part of Figure 5.15 and for the pion sample in the lower right. Among the electrons in N_s, those that meet the criterion of SHMS calorimeter best track normalized energy > 0.80 (the PID cut in this instance) are considered detected by the calorimeter N_d (Cardona 2021). Electrons primarily deposit most of their energy within the calorimeter. Interestingly, there is a cluster of events that pass the electron sample cut with a total calorimeter E/P value close to 0, as highlighted in the red-circled region in the upper right plot of Figure 5.15. As these particles can't be genuine electrons, it's likely that they are secondary, low-energy electrons generated by pions scattering off the NGC windows and subsequently getting absorbed in the pre-shower. Hence, these particles are excluded from the electron sample N_s but included in the
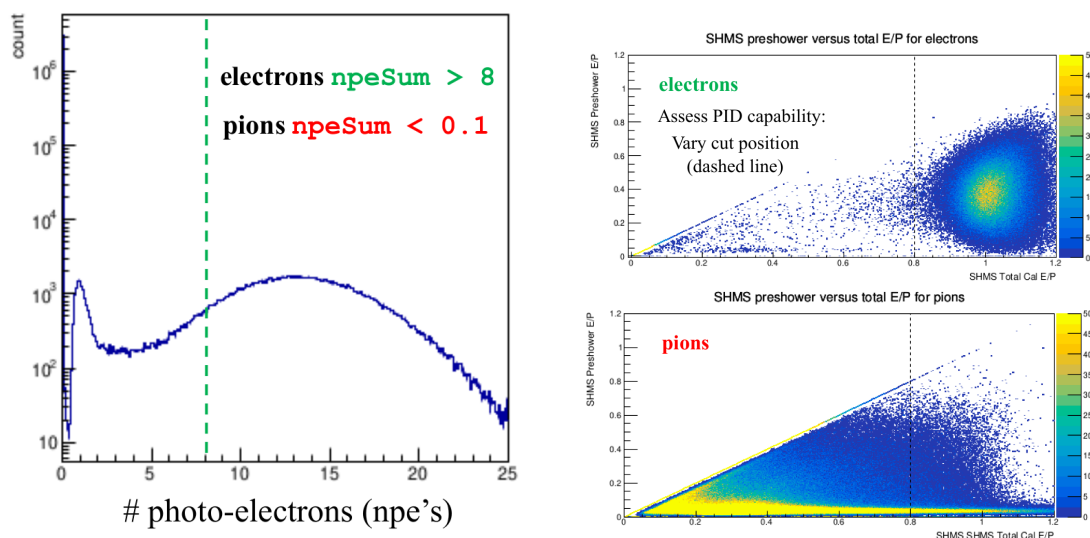
Figure 5.14: Left: Distribution of the number of photo-electrons (npe) in the SHMS Noble Gas Cherenkov detector, obtained by summing the signals from all four PMTs. A cut at 8 npe's (indicated by the dotted green line) was chosen to select electrons. Top Right: Scatter plot of pre-shower energy normalized by momentum (Pre-shower E/P) versus total energy normalized by momentum (total E/P) for electrons selected with a cut based on a sum of npe > 8. Bottom Right: Scatter plot of energy normalized by momentum (E/P) versus total energy normalized by momentum (total E/P) for pions selected with a cut based on a sum of npe < 0.1. The solid black line at total E/P == 0.80 represents the calorimeter E/P cut position used in the analysis to identify clean electrons (Cardona 2021).

pion sample used to compute the Pion Rejection Factors PRFs (Cardona 2021). Another possibility is that these events did not find a cluster in the shower that matches a track (Cardona 2021). In general, a track must be within a certain proximity to the mean location of the cluster to be considered a match (typically around 7.5 cm). The normalized energy deposition E/P within the pre-shower and shower for both the electron and pion samples is presented in Figure 5.15.

The electron efficiency was determined by varying shower E/P cuts, defined as SHMS calorimeter best track normalized energy - SHMS calorimeter normalized energy deposition. Figure 5.16 demonstrates that the efficiency remains relatively constant between 99.4% and 99.6% for all shower $E/P > 0$ cuts.

Therefore, a shower $E/P > 0$ cut was chosen in addition to the $npeSum > 8$ cut for the electron sample N_s condition. Electrons that pass the PID cut using SHMS calorimeter best track normalized energy > 0.80 constitute the electrons detected by the calorimeter N_d (Cardona 2021). The electron detection efficiency is then calculated based on Equation 5.4.

On the other hand, the pion sample N_s was determined by the NGC, comprising those particles that pass a cut of SHMS Nobel Gas Cherenkov npesum < 0.1 (Cardona 2021). The pions N_d that survive the SHMS calorimeter cut using SHMS calorimeter best track normalized energy > 0.80 contribute to calculating the Pion Rejection Factor (PRF), as per Equation 5.6 (Cardona 2021).

These two measures are plotted as a function of the varying SHMS calorimeter best track normalized energy cut position, as depicted in Figure 5.17. Striking a balance between efficiency ϵ and PRF is essential, given that tightening the PID cut on SHMS calorimeter best track normalized energy results in a decrease in electron efficiency while increasing pion suppression. A cut of SHMS calorimeter best track normalized energy > 0.80 leads to a high efficiency of $\epsilon > 99\%$ and a low PRF of approximately 25 (Cardona 2021).

To enhance the PRF with minimal impact on electron e^- efficiency, an additional PID cut was applied using the pre-shower data for both the electron and pion samples, as identified by the NGC. The SHMS pre-shower consists of a single 10 cm-thick layer of TF-1 lead-glass with a density of 3.86 g/cm^3, and pions, on average, deposit approximately 57.9 MeV of energy within the pre-shower.

An investigation of electron efficiency and PRFs was conducted by varying the pre-shower cut, which ranged from SHMS calorimeter normalized energy depo-
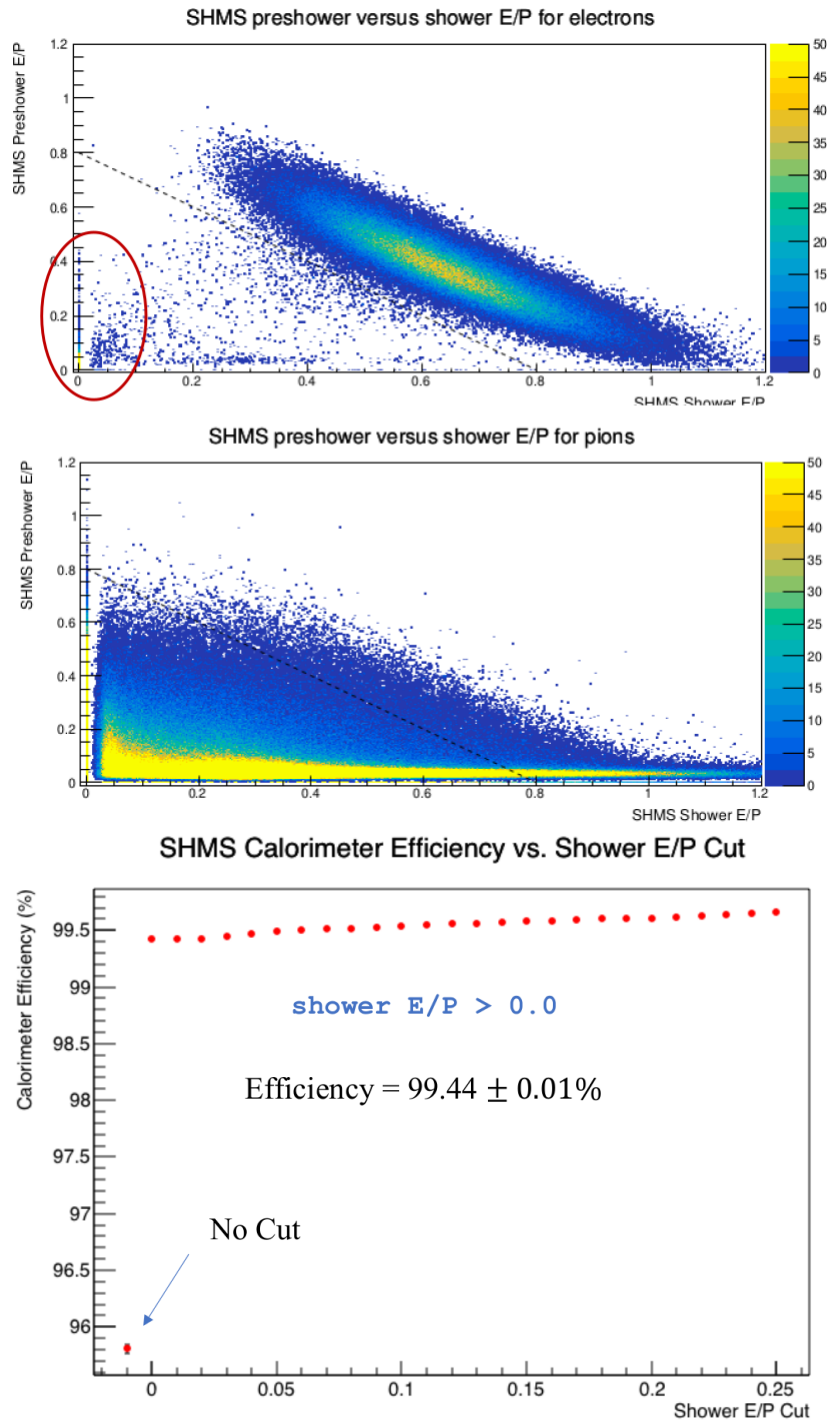
Figure 5.15: Top: 2D plots depicting the normalized energy deposition in the pre-shower and shower for electrons (upper part) and pions (lower part). Within the plot, there is a marked area highlighted in red, which corresponds to a grouping of low-energy events as electrons from NGC cut npeSum> 8. Bottom: The electron detection efficiencies as a function of shower E/P cuts varying between 0 and 0.25, with the point at a shower E/P < 0 for no shower cut (Cardona 2021).

sition > 0 to SHMS calorimeter normalized energy deposition > 0.10 (Cardona 2021). The results of this study are presented in Figure 5.18. This pre-shower cut was implemented in addition to the standard PID cut of SHMS calorimeter best track normalized energy > 0.80 that was applied to both the electron e^- and pion π^- samples N_s to subsequently calculate the number of detected particles N_d (Cardona 2021).

Electron **Efficiency** and **PRF** as a function of E/P cut position
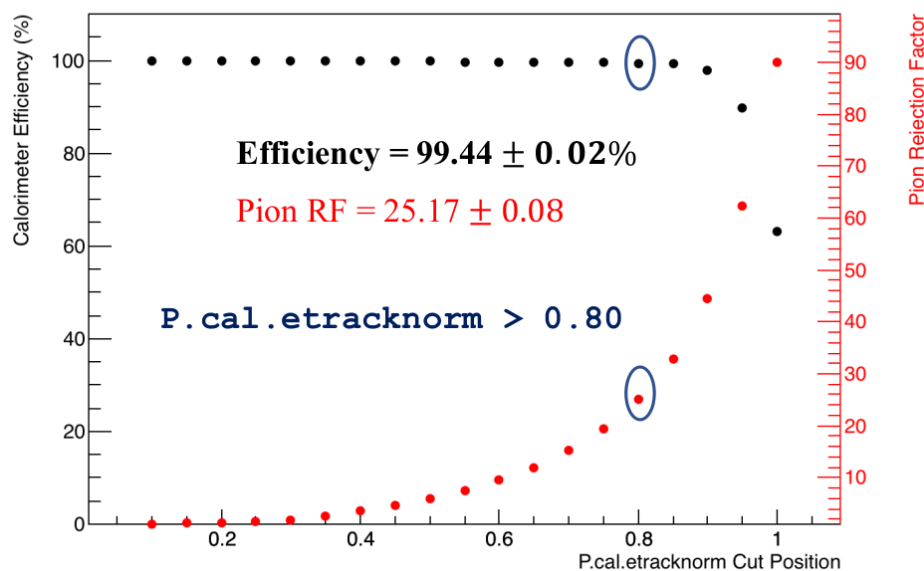
Figure 5.16: Plotted electron efficiency as the black points and Pion Rejection Factor as the red points for the HMS calorimeter. These metrics are plotted against different total calorimeter energy E/P cuts. Notably, when using a cut of SHMS calorimeter best track normalized energy (P.cal.etracknorm > 0.80), it results in an efficiency of $\epsilon = 99.44\%$ and a moderately high Pion Rejection Factor of PRF $= 25.17$, both points highlighted in blue circles (Cardona 2021).

- NGC Efficiencies and PRFs:

  To assess the effectiveness of the Noble Gas Cherenkov NGC as a Particle Identification (PID) detector, a different approach was employed. In this method, the calorimeter was utilized to select the electron and pion samples N_s, while
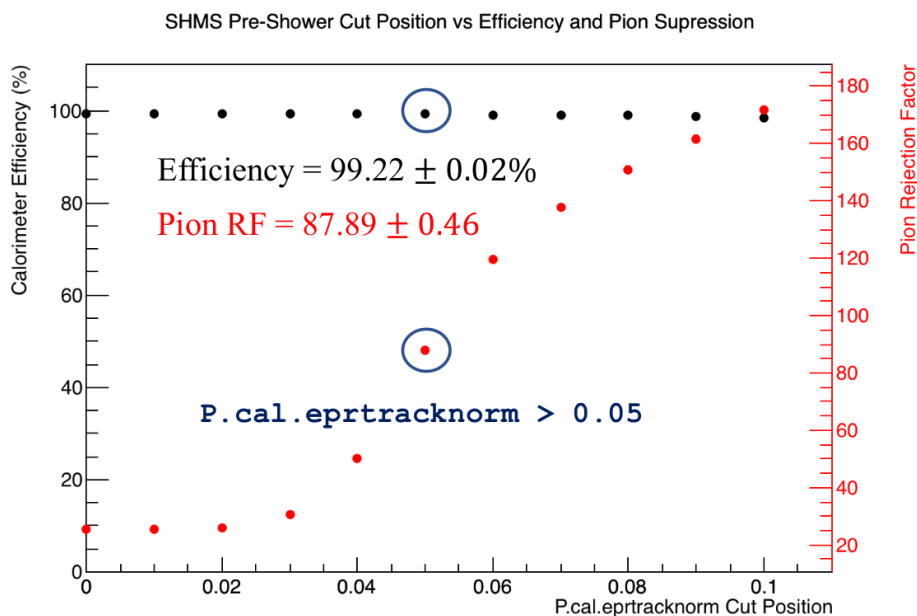
Figure 5.17: Plotted electron efficiency as the black points and Pion Rejection Factor as the red points for the HMS calorimeter. These metrics are plotted against different pre-shower energy E/P cuts. With a pre-shower normalized energy deposit threshold of SHMS calorimeter normalized energy deposition (P.cal.eprtracknorm > 0.05), the electron detection efficiency ϵ experiences only a minor decrease, going from 99.44% to 99.22%. However, there is a significant increase in the PRF value from approximately 25 to about 88 (Cardona 2021).

the NGC was used to apply a PID cut to estimate the number of electrons and pions that successfully pass this cut N_d (Cardona 2021).

Electrons and pions display distinctive patterns of energy deposition within the calorimeter, as evident in Figure 5.18. On the left side of the figure, it's clear that electrons predominantly deposit the majority of their energy, whereas pions deposit only a fraction of their energy. Further differentiation between these particles can be achieved by examining their energy deposition within the pre-shower, as shown on the right side of the figure. Consequently, a 2D cut was implemented on the SHMS calorimeter, combining the pre-shower and total energy deposition which is pre-shower plus shower, to select electrons and
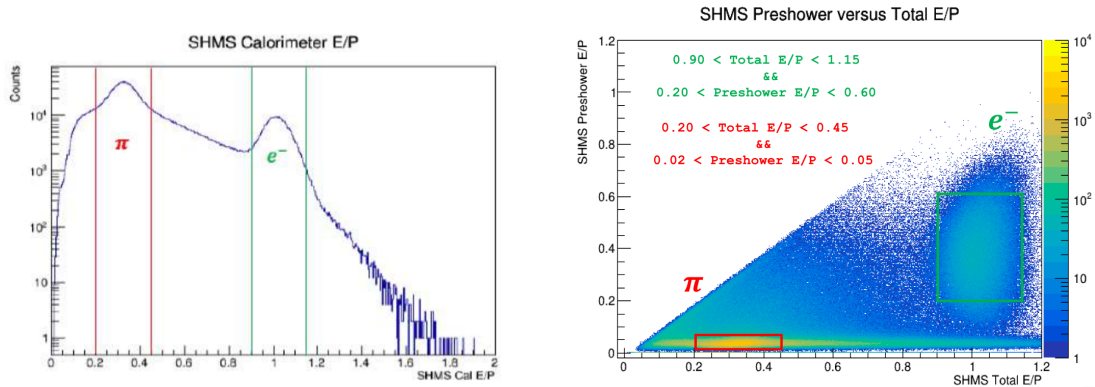
Figure 5.18: Left: A 1D plot showing the normalized total energy deposition within the SHMS calorimeter. The red lines represent the energy limits for selecting pions, while the green lines represent those for selecting electrons. Right: A two-dimensional plot displaying the energy deposited within the pre-shower versus the energy within the entire calorimeter which is shower plus pre-shower. The red lines indicate the pre-shower and total energy boundaries for selecting pions, while the green lines indicate those for selecting electrons (Cardona 2021).

pions.

For the electron sample N_s in Equation 5.4, particles were chosen based on the following criteria: $0.90 <$ SHMS calorimeter best track normalized energy < 1.15 and $0.20 <$ SHMS calorimeter normalized energy deposition < 0.60 (Cardona 2021). The pion sample also serving as N_s in Equation 5.6 included particles that satisfied the following conditions: $0.20 <$ SHMS calorimeter best track normalized energy < 0.45 and $0.02 <$ SHMS calorimeter normalized energy deposition < 0.05 (Cardona 2021). It was essential for the calorimeter-based cuts identifying electrons to be stringent. Widening the total energy to momentum (E/P) bounds from 0.90 and 1.15 to 0.80 and 1.20 resulted in a roughly 3% reduction in efficiency when applying a PID cut based on the NGC's number of photo-electrons npeSum > 2 (Cardona 2021).

The npe distribution within the NGC, following the application of these calorimeter cuts, is displayed in Figure 5.19. The middle plot illustrates the distribution
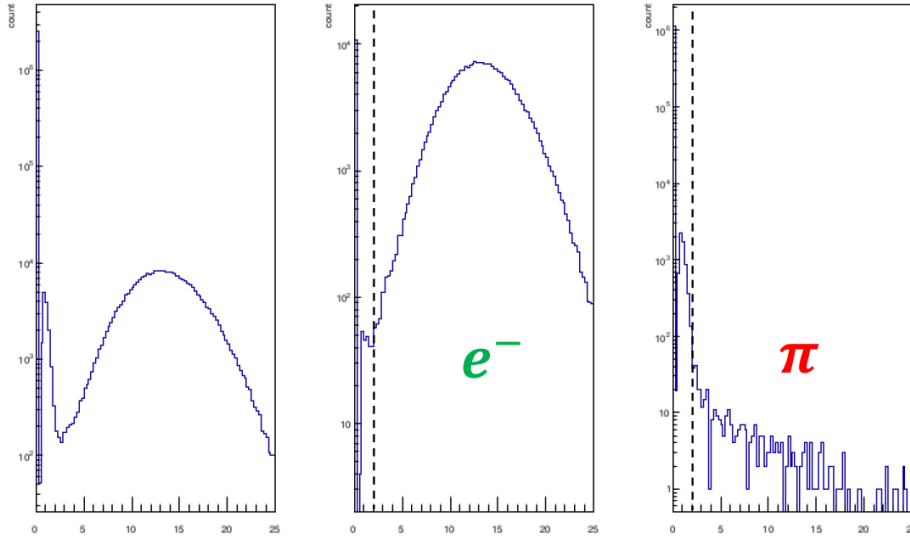
NGC # of photo-electrons

Figure 5.19: Left: The distribution showing the total number of photo-electrons summed across both PMTs of the NGC, without applying any calorimeter sample cuts. Middle: The npe distribution after implementing the 2D calorimeter criteria to choose electrons. Right: The npe distribution after employing the 2D calorimeter criteria to choose pions. The solid black lines represent a cut position of SHMS Nobel Gas Cherenkov npesum > 2 (Cardona 2021).

after implementing the electron sample cuts, while the right plot shows the distribution after the pion sample cuts. The corresponding efficiencies and pion rejection factors for different PID cuts based on the number of photo-electrons in the NGC SHMS Nobel Gas Cherenkov npesum are depicted in Figure 5.20. In this scenario, the number of electrons and pions that satisfy this PID cut serves as N_d in Equation 5.4 and Equation 5.6 (Cardona 2021).

- SHMS PID Summary:

  When determining the final PID cuts to be applied in the analysis, the selection of cuts for both the calorimeter and Cherenkov detector is made with the objective of achieving a high efficiency to maximize the available statistics,
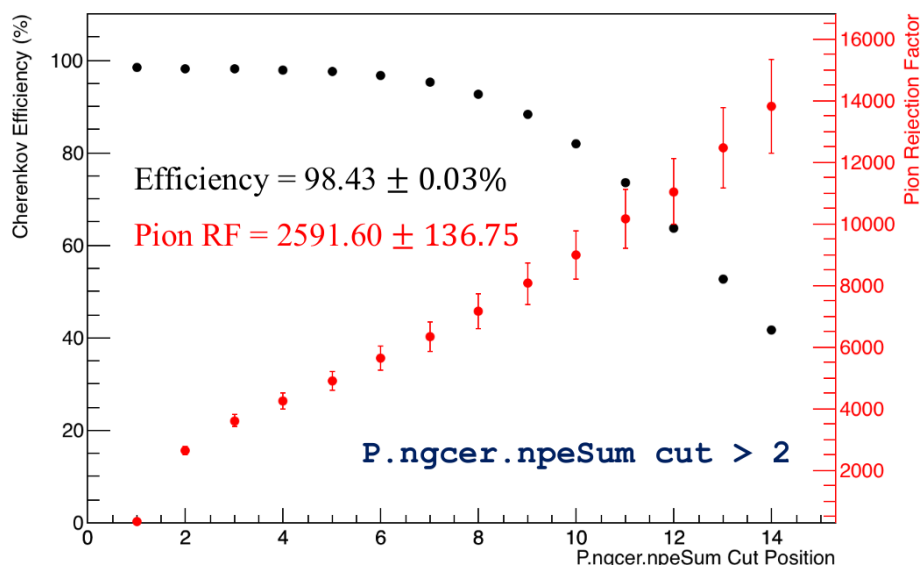
Figure 5.20: Electron Detection Efficiency plotted as black points and Pion Rejection Factor ploted as plotted as red points of the SHMS NGC plotted against different PID cuts applied to the npe sum distribution. The blue circle highlights the efficiency and PRF values associated with a cut of SHMS Nobel Gas Cherenkov npesum (P.ngcer.npeSum > 2), which is the cut ultimately employed in this analysis to identify valid electrons (Cardona 2021).

along with a high pion rejection factor to minimize any potential contamination by pions. In the case of identifying clean scattered electrons measured by the SHMS, the chosen criteria included a calorimeter cut based on SHMS calorimeter best track normalized energy > 0.80 and an NGC cut using the number of photo-electrons SHMS Nobel Gas Cherenkov npesum > 2 (Cardona 2021). These criteria were the ultimate choices to distinguish the electrons effectively.

As illustrated in Figure 5.17, the incorporation of a pre-shower cut has the effect of increasing the PRF with only a minimal reduction in electron efficiency. For example, introducing a cut of SHMS calorimeter normalized energy deposition > 0.05, in addition to the previously mentioned criteria, produced asymmetries consistent with those obtained without this cut, and the associated error bars

were of similar magnitude (Cardona 2021). A summary of the PID studies conducted for the SHMS under the 2.6 GeV and 3.4 GeV DIS settings is presented in Table 5.2.

P_c	Cher.Cut	Cher.Eff.	PRF	Cal.Cut	Cal.Eff.	PRF	Comb.PRF
2.6 GeV	#npe>2	98.43%	2591	E/P>0.8	99.44%	25.17	65231
		±0.03%	±137		±0.02%	±0.08	±3448
3.4 GeV	#npe>2	99.43%	2907	E/P>0.8	99.32%	38.35	112947
		±0.03%	±620		±0.03%	±0.35	±24098

Table 5.2: SHMS PID summary for all central momentum settings P_c during the DIS production run. By multiplying the pion rejection factor (PRF) derived from the NGC study and the PRF from the calorimeter study, the combined pion rejection factors are obtained. The resulting values of combined pion rejection factors exceed the targeted value of 10^3 (Cardona 2021).

- Beam Scraping Studies and PID Cuts:

  During the production run, an unfortunate incident occurred where the electron beam position deviated from the central axis along the center of the target cell on February 21, 2020, and the beam position wasn't corrected until March 5th, 2020. Throughout this period, the incident electron beam scattered off other materials (primarily the target chamber glass walls) besides the polarized ^{3}He gas. This led to an increase in counts, referred to as "beam scraping." The beam scraping study (conducted by Melanie Cardona) concluded that the PID cuts used for HMS and SHMS (shown in Table 5.8 and Table 5.9) already remove the additional counts from beam scraping. Therefore, no special treatment was applied to these production runs affected by beam scraping when extracting asymmetries. For more details, refer to this reference (Cardona 2023).

5.5   DIS analysis

5.5.1 z cut and window dilution

The window dilution study serves as a guide for establishing z_{tg}^{recon} cuts in the target chamber of the production cell to filter out events originating from the glass windows while retaining the majority of events from within the ^3He target chamber. This study also involves estimating the window dilution factor for specific production run conditions (target cell, kinematics, and spectrometer) based on a combination of simulated results and experimental data.

The goal of this study is to ensure that, for certain production run conditions (target cell, kinematic setting, and spectrometer), the window dilution factor remains within a minimal variation of less than 3%. To achieve this, an appropriate set of z_{tg}^{recon} target cuts is determined while still minimize the statistical uncertainty $\delta A_{phys_{stat}}$. Subsequently, the replayed z_{tg}^{recon} yield histogram is divided into 13 x_{Bj} bins to calculate both the statistical and systematic uncertainties associated with each x_{Bj} bin cut.

- Window Dilution:

  The replayed empty reference cell yield histograms for both the upstream and downstream window regions are denoted as h_{up}^{em} and h_{down}^{em}, respectively. These these histograms are scaled by a factor determined by the corresponding window thickness ratio, which is $\frac{\sigma_{up}^{^3He}}{\sigma_{up}^{em}}$ for the upstream window and $\frac{\sigma_{down}^{^3He}}{\sigma_{down}^{em}}$ for the downstream window. Then the above values are multiplied by the radiative correction ratios, given as $\frac{L_{up}^{^3He}}{L_{up}^{em}}$ for the upstream window and $\frac{L_{down}^{^3He}}{L_{down}^{em}}$ for the

downstream window:

$$h_{upwincomp} = h_{up}^{em} \frac{\sigma_{up}^{^3He} L_{up}^{^3He}}{\sigma_{up}^{em} L_{up}^{em}} \tag{5.8}$$

$$h_{downwincomp} = h_{down}^{em} \frac{\sigma_{down}^{^3He} L_{down}^{^3He}}{\sigma_{down}^{em} L_{down}^{em}}. \tag{5.9}$$

The window dilution factor is determined for a specific z_{tg}^{recon} cut. The z_{tg}^{recon} cut is defined by the region extending from $-z_{lower}$ cm to $+z_{upper}$ cm relative to the z_{tg}^{recon} position at the center of the target chamber. To do this, the integrated area $N_0^{tot} = N_0^{^3He} + N_0^{bkgd}$ within the z_{tg}^{recon} cut from the replayed pol ^3He target cell z_{tg}^{recon} yield histogram $h_{^3He}$ was calculated. Simultaneously, the integrated area $N_0^{up(down)wincomp}$ within the same ztg^{recon} cut was obtained from the scaled empty reference target cell z_{tg}^{recon} yield histogram $h_{up(down)wincomp}$.

Then the window dilution factor f_{win} is determined:

$$f_{win} = \frac{N_0^{upwincomp} + N_0^{downwincomp}}{N_0^{^3He} + N_0^{bkgd}} = \frac{N_0^{upwincomp} + N_0^{downwincomp}}{N_0^{tot}}. \tag{5.10}$$

Since the physics asymmetry A_{phys} is extracted from the measured raw asymmetry A_{raw} as is:

$$A_{phys} = \frac{A_{raw}}{P_b P_t D_{N_2} D_{win}} = \frac{A_{raw}}{P_b P_t D_{N_2}(1 - f_{win})}, \tag{5.11}$$

the optimal window cut should minimize δA_{phys}:

$$\delta A_{phys} \propto \frac{1}{\sqrt{N_0^{^3He}}(1 - f_{win})}. \tag{5.12}$$

For production cell "Dutch" and empty reference cell "Will," the downstream window's z cut remained fixed at $z = +18.0$ cm away from the target chamber's

center position. We adjusted the z cut for the upstream window to minimize δA_{phys} The final window cut extends from -17 cm to +18 cm concerning the z_{tg}^{recon} position of the target center, and it produced the least δA_{phys}, see Figure 5.21 and Figure 5.22.
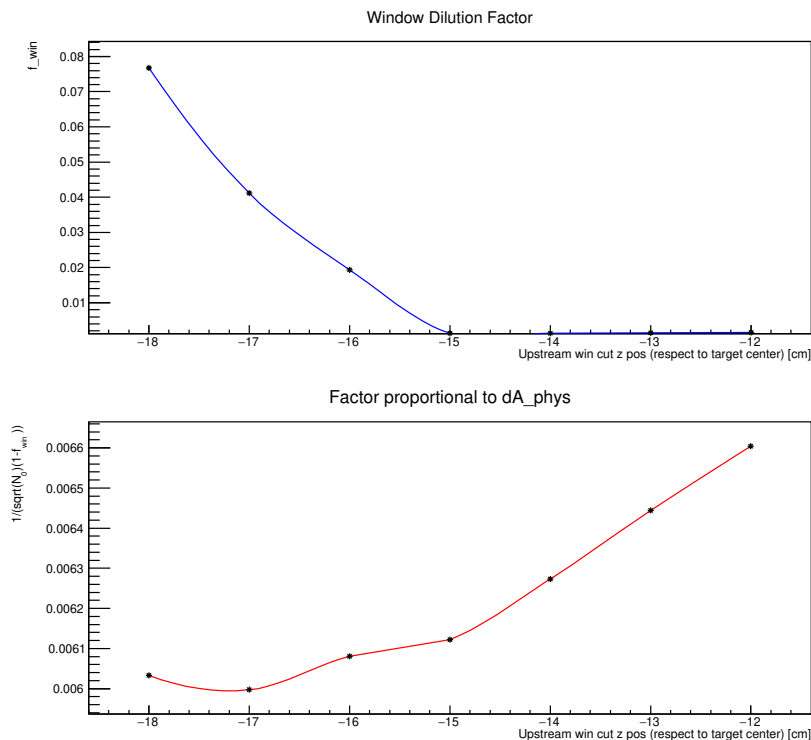
Figure 5.21: Window dilution factor and δA_{phys} for production cell Dutch and empty reference cell Will at HMS kine 4. Fixed downstream window z cut at $z = +18.0$ cm respect to target center and adjust upstream window z cut position. (At kin-4 ($E_p = -3.5$GeV, 30°), HMS 2771 was used for pol ^3He DIS run with holding field Longitudinal 180° and HMS 3077 was used for empty DIS run with holding field Transverse 90°.

- Replayed Data and Radiated Cross Section:

  Replayed Root Files:

  In order to isolate the contributions of the windows and ^3He in specific DIS
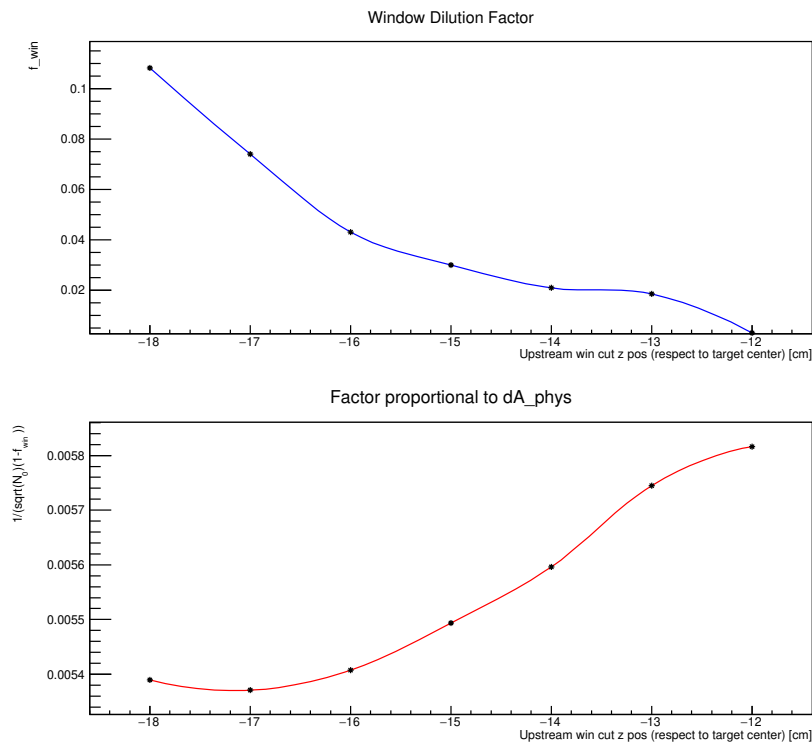
Figure 5.22: Window dilution factor and δA_{phys} for production cell Dutch and empty reference cell Will at SHMS kine B. Fixed downstream window z cut at $z = +18.0$ cm respect to target center and adjust upstream window z cut position. (At kin-B $(E_p = -3.4\text{GeV}, 30°)$, SHMS 9956 was used for pol ^3He DIS run with holding field Longitudinal 180° and SHMS 10267 was used for empty DIS run with holding field Transverse 90°.

kinematics, we combine all replayed production cell runs[1] and their corresponding empty reference cell runs. By using these runs, we calculate the average values of E' and θ_{scatt} for a particular x_{Bj} bin. This is achieved by applying the respective x_{Bj} cuts, as depicted in Figure 5.23.
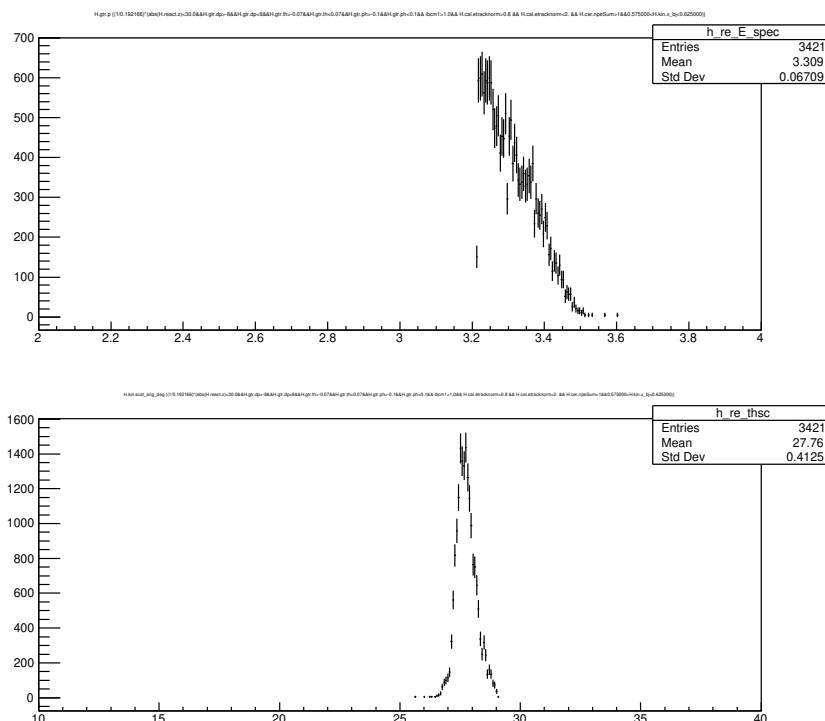
Figure 5.23: The mean E' was obtained from the replayed histogram H.gtr.p and the mean θ_{scatt} was obtained from replayed histogram H.kin.scat_ang_deg for production cell Dutch at HMS kine 4. The x_{Bj} bin shown is centered at $x = 0.60$ with a full range of $x = (0.55, 0.65)$.

Simulated Radiated Cross Section

To calculate the radiative corrections for rescaling the replayed empty reference cell yield histogram, we require the ratio of the radiative cross-section, which

---

[1]The replayed root files used for calculating window dilution are from the pass1v4 version. These files can be located in ifarm under:

/cache/hallc/c-polhe3/analysis/REPLAYS/pass1v4/

In this replay, we have enhanced the vertex reconstruction compared to the previous replays. Additionally, we've integrated THcReactionPoint into the analyzer scripts.

is $\frac{\sigma_{up(down)}^{^3He}}{\sigma_{up(down)}^{em}}$. The measured cross-section includes contributions from interactions with materials (ionization, bremsstrahlung) and vertex effects (bremsstrahlung). The radiated cross-section is given by:

$$\sigma_{rad} = \sigma_{Born} + \sigma_{RC}. \tag{5.13}$$

The "rc-externals" along with the function F1F2IN09 was used to generate a square grid using p0 and theta0 as inputs, resulting in σ_{rad} as the output. Subsequently, the radiated cross-section was extracted by applying bilinear interpolation based on the mean values of E' and θ_{scatt} within a specified x_{Bj} bin. Specifically, for the production cell at HMS kine 4, the input variable ranges for the square grid are E' from 3.0 to 4.0 GeV with step of 0.01 GeV and θ_{scatt} from 25.6° to 34.4° with step of 0.02°. Figure 5.24 shows the radiated cross-section as a function of x_{Bj} for the Dutch upstream window.

Hence, by using the radiated cross-section, σ_{rad} values obtained from the "rc-externals" grid for both the production ^3He cell and the empty reference cell, the scaling factor is calculated as the product of the corresponding window thickness ratio and the rad_{corr} ratio, for upstream(downstream) windows: $\frac{\sigma_{up(down)}^{^3He} L_{up(down)}^{^3He}}{\sigma_{up(down)}^{em} L_{up(down)}^{em}}$. Using the replayed runs from both the production ^3He cell and the empty reference cell, Figures 5.24 to Figure 5.28 illustrate a comparison between the z_{tg}^{recon} yield histogram with and without the application of the scale factor to the empty reference cell yield histogram.

- Statistical Uncertainty:

  The statistical uncertainty is associated with the total number of replayed events obtained from all the combined replayed runs. To calculate this uncertainty,
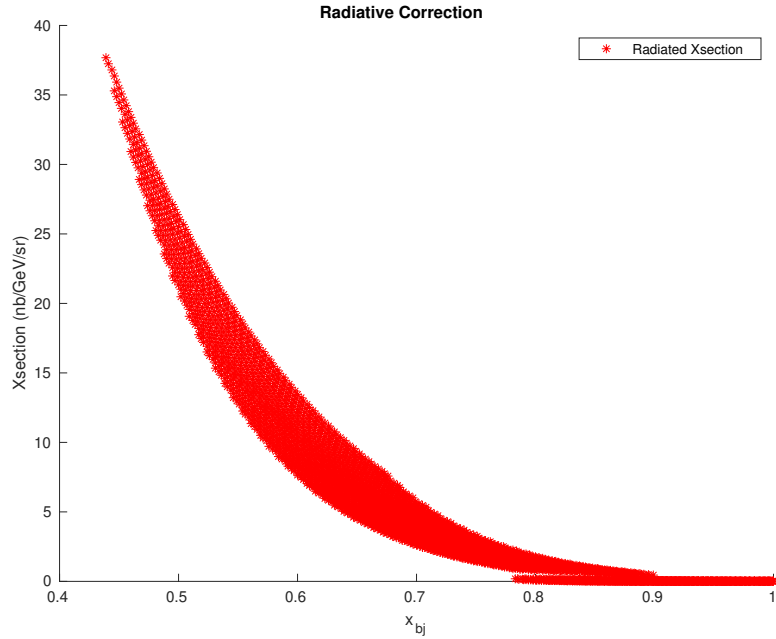
Figure 5.24: Radiated xsection for production cell Dutch upstream window at HMS kine 4

we start by obtaining the total number of replayed events within the window z cut from the z_{tg}^{recon} histogram of the polarized ^3He target cell, denoted as $n_0^{^3He}$. Similarly, from the z_{tg}^{recon} histogram of the empty reference cell, we obtain the total number of replayed events within the window z cut for both the upstream and downstream window regions, denoted as $n_0^{up(down)wincomp}$. The uncertainty is then calculated using the formula:

$$\delta n_0^{up(down)wincomp} = \sqrt{n_0^{up(down)wincomp}}. \tag{5.14}$$

Then the statistical uncertainty for f_{win_stat} is:

$$\frac{\delta f_{win\_stat}}{f_{win}} = \sqrt{\frac{1}{n_0^{upwincomp} + n_0^{downwincomp}} + \frac{1}{n_0^{tot}}}. \tag{5.15}$$
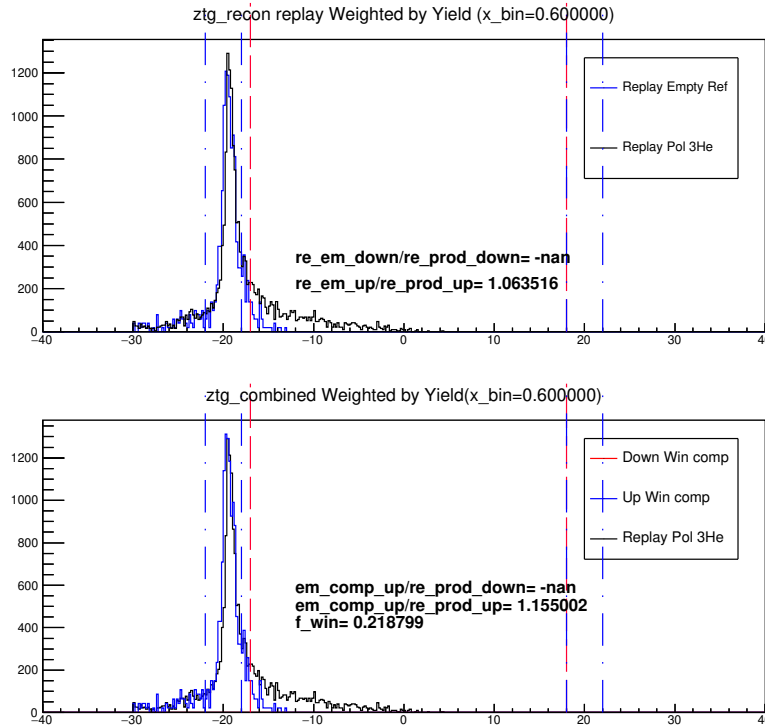
Figure 5.25: For x_{Bj} bin centered at 0.60, top plot shows z_{tg}^{recon} yield histogram make comparison between replayed production cell Dutch run and replayed empty reference cell run. While the bottom plot scaled z_{tg}^{recon} yield histogram for replayed empty reference cell run by corresponding window thickness ratio times rad corr ratio for upstream(downstream) window. For example, the upstream window histogram obtained from the empty cell run needs to be scaled by 1.155 to produce the expected window histogram for the polarized ^{3}He cell. And there is no count from the downstream window, hence no valid ratio could be extracted (nan). At kin-4 ($E_p = -3.5$GeV, $30°$), HMS 2771 was used for pol ^3He DIS run with holding field Longitudinal $180°$ and HMS 3077 was used for empty DIS run with holding field Transverse $90°$)
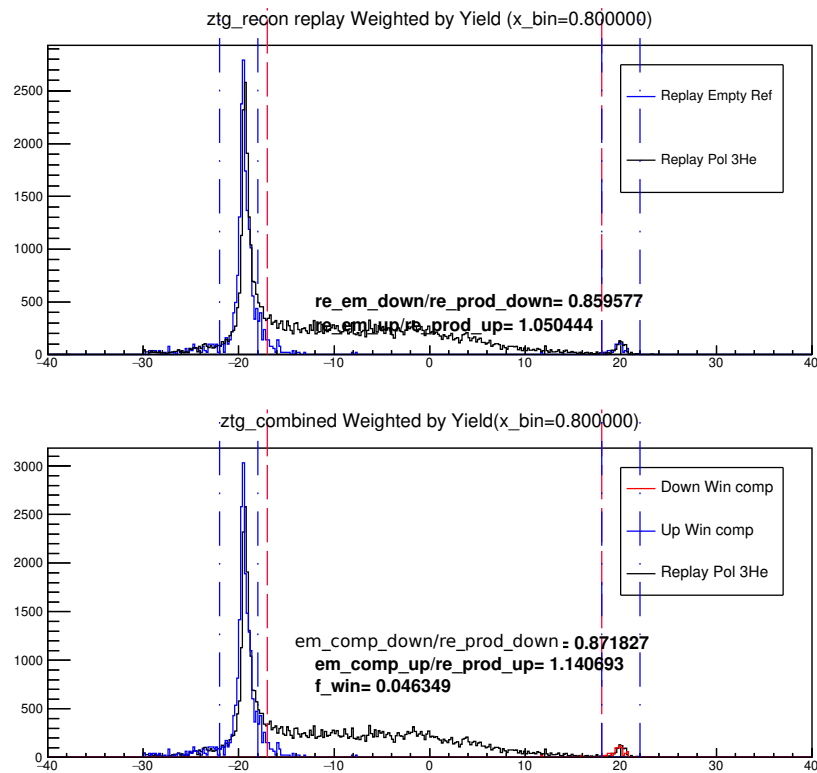
Figure 5.26: For x_{Bj} bin centered at 0.80, top plot shows z_{tg}^{recon} yield histogram make comparison between replayed production cell Dutch run and replayed empty reference cell run. While the bottom plot scaled z_{tg}^{recon} yield histogram for replayed empty reference cell run by corresponding window thickness ratio times rad corr ratio for upstream(downstream) window. For example, the upstream window histogram obtained from the empty cell run needs to be scaled by 1.141 while the downstream window histogram obtained from the empty cell run needs to be scaled by 0.872 to produce the expected window histogram for the polarized ^{3}He cell. At kin-4 ($E_p = -3.5$GeV, 30°), HMS 2771 was used for pol ^3He DIS run with holding field Longitudinal 180° and HMS 3077 was used for empty DIS run with holding field Transverse 90°)
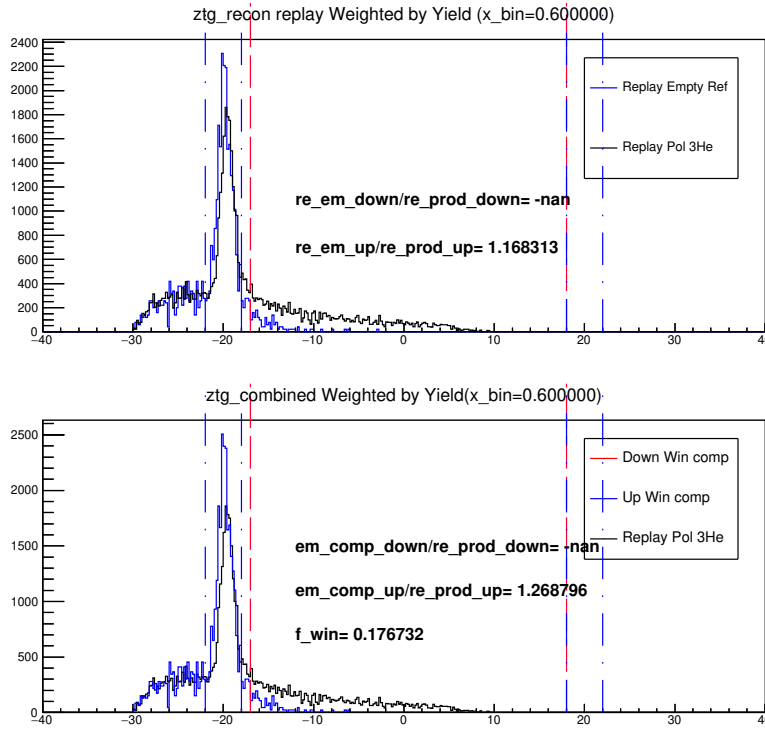
Figure 5.27: For x_{Bj} bin centered at 0.60, top z_{tg}^{recon} yield histogram make comparison between replayed production cell Dutch run and replayed empty reference cell run. While the bottom plot scaled z_{tg}^{recon} yield histogram for replayed empty reference cell run by corresponding window thickness ratio times rad corr ratio for upstream(downstream) window. For example, the upstream window histogram obtained from the empty cell run needs to be scaled by 1.269 to produce the expected window histogram for the polarized ^{3}He cell. And there is no count from the downstream window, hence no valid ratio could be extracted (nan). (At kin-B ($E_p = -3.4$GeV, 30°), SHMS 9956 was used for pol ^3He DIS run with holding field Longitudinal 180° and SHMS 10267 was used for empty DIS run with holding field Transverse 90°)
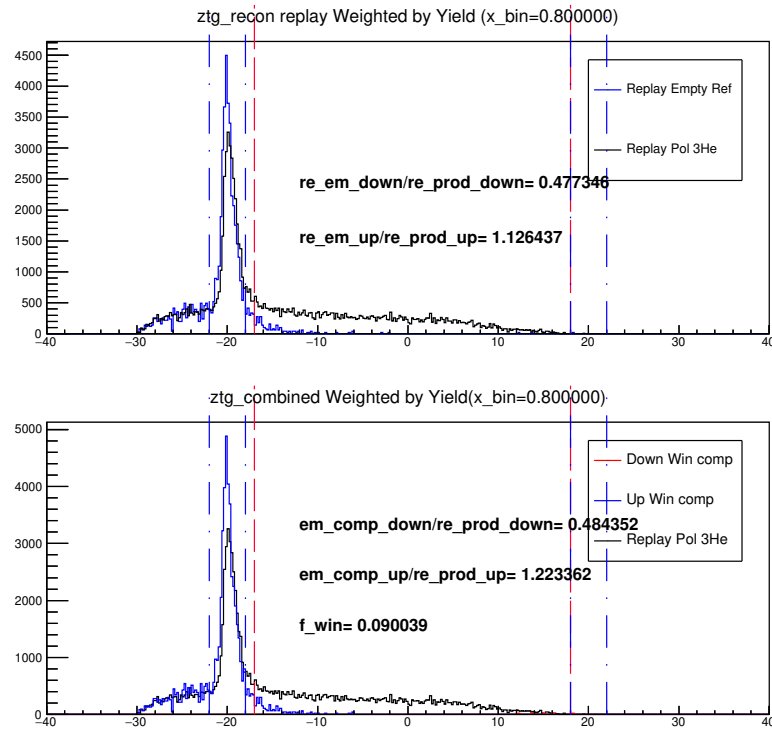
Figure 5.28: For x_{Bj} bin centered at 0.80, top z_{tg}^{recon} yield histogram make comparison between replayed production cell Dutch run and replayed empty reference cell run .While the bottom plot scaled z_{tg}^{recon} yield histogram for replayed empty reference cell run by corresponding window thickness ratio times rad corr ratio for upstream(downstream) window. For example, the upstream window histogram obtained from the empty cell run needs to be scaled by 1.223 while the downstream window histogram obtained from the empty cell run needs to be scaled by 0.484 to produce the expected window histogram for the polarized ^{3}He cell. (At kin-B ($E_p = -3.4$GeV, $30°$), SHMS 9956 was used for pol ${}^3He$ DIS run with holding field Longitudinal $180°$ and SHMS 10267 was used for empty DIS run with holding field Transverse $90°$)

- Systematic Uncertainty:

The systematic uncertainty is associated with two components: the systemic uncertainty in window position and the systematic uncertainty in window thickness. For the systematic uncertainty in window thickness, we obtain $\delta L_{up(down)}$, which represents the systematic uncertainty in window thickness for both the upstream and downstream windows. Regarding the systematic uncertainty in window position, we utilize the uncertainty in the mean value obtained from the Gaussian peak fit for the z_{tg}^{recon} histogram peak for both the upstream and downstream window regions. After introducing this window position uncertainty, we perform the rc-externals again and generate another grid for radiated cross-sections. As a result, $\delta\sigma_{up(down)}$ is calculated as the difference between the radiated cross-sections extracted from the two rc-external grids, one with the window position uncertainty added and the other without. This approach enables us to determine $\delta\sigma_{up(down)}$ for both the upstream and downstream windows from the systematic uncertainty in window position.

Then obtain uncertainty:

$$\delta N_0^{upwincomp} = N_0^{upwincomp}\sqrt{(\frac{\delta\sigma_{up}^{^3He}}{\sigma_{up}^{^3He}})^2 + (\frac{\delta\sigma_{up}^{em}}{\sigma_{up}^{em}})^2 + (\frac{\delta L_{up}^{^3He}}{L_{up}^{^3He}})^2 + (\frac{\delta L_{up}^{em}}{L_{up}^{em}})^2}.$$
$$(5.16)$$

$$\delta N_0^{downwincomp} = N_0^{downwincomp}\sqrt{(\frac{\delta\sigma_{down}^{^3He}}{\sigma_{down}^{^3He}})^2 + (\frac{\delta\sigma_{down}^{em}}{\sigma_{down}^{em}})^2 + (\frac{\delta L_{down}^{^3He}}{L_{down}^{^3He}})^2 + (\frac{\delta L_{down}^{em}}{L_{down}^{em}})^2}$$
$$(5.17)$$

Then the systematic uncertainty for f_{win_sys} is:

$$\frac{\delta f_{win\_sys}}{f_{win}} = \frac{\sqrt{(\delta N_0^{upwincomp})^2 + (\delta N_0^{downwincomp})^2}}{N_0^{^3He}}.$$
$$(5.18)$$

Using the equations described earlier, Figures 5.28 and 5.29 illustrate the statistical and systematic uncertainties associated with the window dilution factor for the production cell Dutch in HMS kinematics 4 and SHMS kinematics B.

For production cell Bigbrother, see Figure A.5 and A.6 in Appendix A for the window dilution factors at high momentum settings HMS kinematics 4 and SHMS kinematics B. While Figures A.11 and A.12 display the window dilution factors at low momentum settings HMS kinematics 3 SHMS kinematics C.
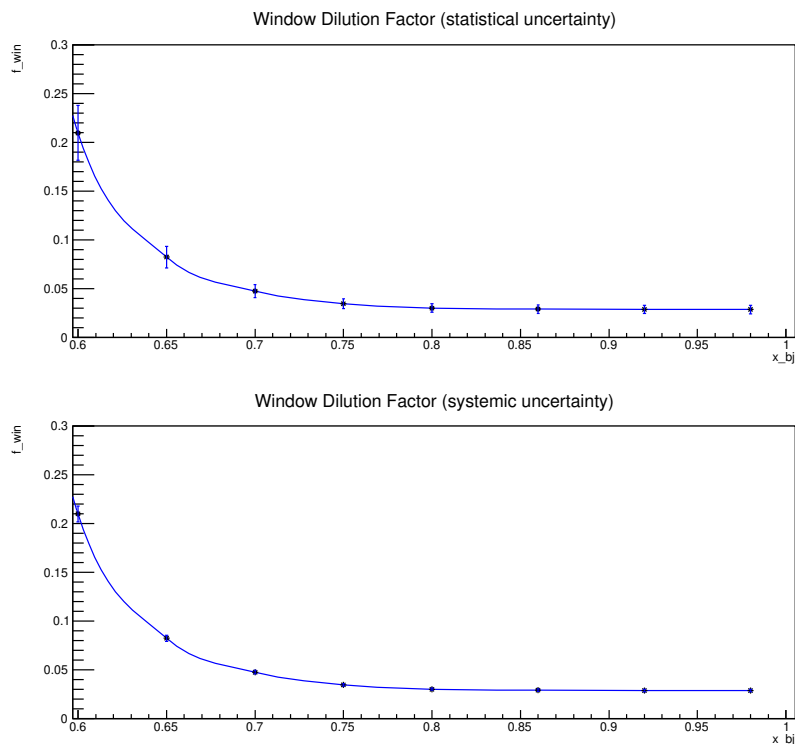
Figure 5.29: Window dilution for cell Dutch at kine-4 ($E_p = -3.5$GeV, $30°$), with statistical uncertainty δf_{win_stat} shown in the top plot and the systematic uncertainty δf_{win_sys} shown in the bottom plot. For δf_{win_sys}, uncertainty for production cell Dutch upstream (downstream) window thickness is $\pm 2 * 10^{-5}$ cm and for empty reference cell Will upstream (downstream) window thickness is $\pm 5.1 * 10^{-4}$ cm. While the uncertainty for production cell Dutch and empty reference cell Will upstream (downstream) window position is ± 0.2 cm. (HMS 2771 was used for pol ^3He DIS run with holding field Longitudinal $180°$ and HMS 3077 was used for empty DIS run with holding field Transverse $90°$)
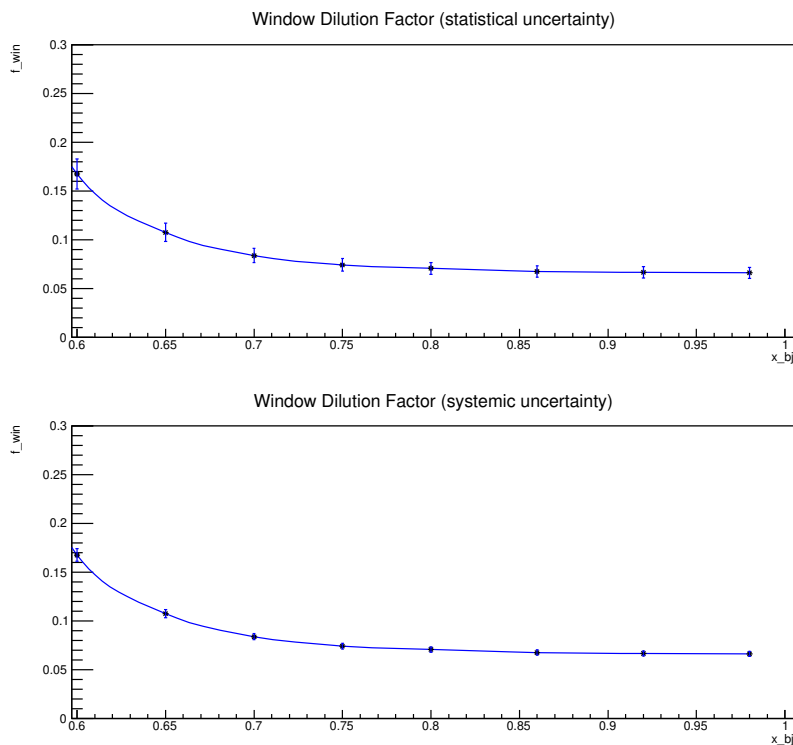
Figure 5.30: Window dilution for cell Dutch at kine-B ($E_p = -3.4$GeV, $30°$), with statistical uncertainty δf_{win_stat} shown in the top plot and the systematic uncertainty δf_{win_sys} shown in the bottom plot. For δf_{win_sys}, uncertainty for production cell Dutch upstream (downstream) window thickness is $\pm 2 * 10^{-5}$ cm and for empty reference cell Will upstream (downstream) window thickness is $\pm 5.1 * 10^{-4}$ cm. While the uncertainty for production cell Dutch and empty reference cell Will upstream (downstream) window position is ± 0.2 cm. (SHMS 9956 was used for pol ^3He DIS run with holding field Longitudinal $180°$ and SHMS 10267 was used for empty DIS run with holding field Transverse $90°$)

In conclusion, a cut of $z_{tg} = (-15, 15)$ cm was used in the data analysis. Then from Figure 5.21 and Figure 5.22, $f_{win} = 0.03$ for SHMS and is negligible for HMS. The average systemic uncertainty for window dilution factor is $\delta D_{win} = \delta(1 - f_{win}) \leq 0.3\%$.

5.5.2 Spectrometer Acceptance Cuts

To ensure the reliability of the events used for extracting the asymmetries, spectrometer acceptance cuts are applied. These cuts serve two main purposes:

1)The first purpose is to ensure that the events fall within regions where the optical properties of the spectrometer are well-understood. This is achieved through cuts on the momentum acceptance, often denoted as $\delta p/p$ or simply "delta."

2) The second purpose is to confirm that the events result from collisions involving the polarized ^{3}He gas and not interactions with the glass windows of the target cell. To achieve this, cuts are applied to a variable related to the reaction vertex position, typically denoted as "z." This is particularly important when the electron beamline runs parallel to the polarized ^{3}He target cell.

Furthermore, incident electrons can scatter relative to the beamline along the vertex z-axis, which can be interpreted as angular distributions. These angular distributions are determined using tangents, with $\tan(\phi)$ representing the horizontal component (dy/dz) and $\tan(\theta)$ representing the vertical component (dx/dz). These parameters are often referred to as YPtar and XPtar.

The specific values for these cuts on the HMS and SHMS are provided in Table 5.3 and Table 5.4. The optimal θ, ϕ cuts for HMS and SHMS are obtained from spectrometer acceptance study which the details are presented in Appendix B.

Variable	Cut on HCANA Leaf
Delta [%]	-8 < H.gtr.dp < 8
Z [cm]	-15 < H.react.z < 15
dx/dz (Xptar) $\theta[rad]$	-0.06 < H.gtr.th < 0.06
dy/dz (Yptar) $\phi[rad]$	-0.1 < H.gtr.ph < 0.1

Table 5.3: Spectrometer HMS acceptance cuts.

Variable	Cut on HCANA Leaf
Delta [%]	-10 < P.gtr.dp < 22
Z [cm]	-15 < P.react.z < 15
dx/dz (Xptar) $\theta[rad]$	-0.035 < P.gtr.th < 0.035
dy/dz (Yptar) $\phi[rad]$	-0.029 < P.gtr.ph < 0.034

Table 5.4: Spectrometer SHMS acceptance cuts.

5.5.3 N_2 Dilution

The nitrogen dilution factor D_{N_2} is calculated by comparing the count rates observed in data acquired using a reference cell filled with nitrogen gas with those obtained from data collected using the ^{3}He target cell. D_{N_2} is quantified as follows:

$$D_{N_2} = 1 - \frac{\sum_{N_2}(N_2)}{\sum_{tot}(^3He)} \frac{Q(^3He)}{Q(N_2)} \frac{t_{LT}(^3He)}{t_{LT}(N_2)} \frac{n_{N_2}(^3He)}{n_{N_2}(N_2)} \tag{5.19}$$

$$= 1 - \frac{Yield_{N_2}(N_2)}{Yield_{tot}(^3He)} \cdot \frac{n_{N_2}(^3He)}{n_{N_2}(N_2)}, \tag{5.20}$$

where $\sum_{N_2}(N_2)$ and $\sum_{tot}(^3He)$ represent the total counts that satisfy the current, acceptance, and PID cuts for both N_2 reference cell runs and production runs, respectively. The pre-scale factors for the N_2 and ^3He target runs are denoted by $t_{ps}(N_2)$ and $t_{ps}(^3He)$ respectively. Since both pre-scale factors are equal to 1 during the corresponding runs, we ignore effect of pre-scale factor for the following calculation. It is essential to normalize these counts based on the total charge deposited on both targets, denoted as $Q(^3He)$ and $Q(N_2)$. Furthermore, $t_{LT}(N_2)$ and $t_{LT}(^3He)$ refer to

the live times in the corresponding runs. The terms $n_{N_2}(N_2)$ and $n_{N_2}(^3He)$ correspond to the number densities of nitrogen present in the N_2 reference cell and ^3He production cell, respectively. In order to obtain the uncertainty for nitrogen dilution factor $\sigma(D_{N_2})$, the variable $Yield$ is introduced into Equation 5.20. Then $Yield$ and its uncertainty $\sigma(Yield)$ is:

$$Yield = \frac{\sum}{Q \cdot t_{LT}} \tag{5.21}$$

$$\sigma(Yield) = Yield \cdot \sqrt{\frac{1}{\sum}}, \tag{5.22}$$

where $\sum$ represents the good event from T(spectrometer) tree with current cut, no PID cuts or spectrometer cuts, s is the scaler from TSP(helicity scaler) tree with current cut. Therefore, the live times and its corresponding uncertainty are computed by:

$$t_{LT} = \frac{\sum}{s} \tag{5.23}$$

$$\sigma(t_{LT}) = t_{LT} * \sqrt{\frac{1}{\sum} + \frac{1}{s}}. \tag{5.24}$$

Cell Name	$\rho_{fill_{N_2}}$ (amg)	f_{TC}	$n_{N_2}^{TC}$ (amg)
Dutch	0.115 ±0.001	1.270 ±0.002	0.163±0.0016
Big Brother	0.110 ±0.001	1.327±0.002	0.146±0.0015

Table 5.5: N_2 filling density and N_2 number density inside target chamber for ^{3}He production cells.

The number density of nitrogen gas $n_{N_2}^{TC}$ in the target chamber of ^3He cells used during data collection was determined by taking the filling densities $\rho_{fill_{N_2}}$ for the

"Dutch" and "Big Brother" cells (see Table 5.5) and adjusted by a scaling factor f_{TC}:

$$n_{N_2}^{TC}(^3He) = \rho_{fill_{N_2}} \cdot f_{TC}. \tag{5.25}$$

The scaling factor f_{TC} that depends on the volume and temperature of three different locations within the target cells: the pumping chamber (PC), the transfer tube (TT), and the target chamber (TC), see Table 4.4:

$$f_{TC} = V_{tot} \cdot (V_{TC} + V_{PC}\frac{T_{TC}}{T_{PC}} + V_{TT}\frac{T_{TC}}{T_{TT}})^{-1}. \tag{5.26}$$

Then the average values of $n_{N_2}^{TC}$ for Cell Dutch and Cell BigBrother are listed in Table 5.5. For nitrogen reference cell runs, the reference cell Will's average temperature was at approximately $37 \pm 1°C$. The measured number density of nitrogen gas within the reference cell was found to be approximately 8.690 ± 0.006 amg.

The combined Yields and nitrogen dilution factors D_{N_2} for each spectrometer and each kinematics are listed in Table 5.6 and Table 5.7.

Cell Name	Target Type	Kine	Yield	N_2 Dilution
Will	Ref-N2	Kine-4	140200±1300	NA
Bigbrother	Pol-3He	Kine-4	24120±32	1-(0.0977±0.0026)
Dutch	Pol-3He	Kine-4	25795±34	1-(0.1019±0.0019)
Will	Ref-N2	Kine-3	436600±3600	NA
Bigbrother	Pol-3He	Kine-3	78210±110	1-(0.0938±0.0012)

Table 5.6: N_2 dilution factor D_{N_2} for HMS.

5.5.4 Summary of Analysis Cuts

Table 5.8 and Table 5.9 outline the summary for total cuts applied to the dataset for the purpose of selecting a clean sample of scattered electrons, which was crucial for

Cell Name	Target Type	Kine	Yield	N_2 **Dilution**
Will	Ref-N2	Kine-B	179100±1500	NA
Bigbrother	Pol-3He	Kine-B	32125±39	1-(0.0937±0.0012)
Dutch	Pol-3He	Kine-B	34474±40	1-(0.0975±0.0013)
Will	Ref-N2	Kine-C	759800±4700	NA
Bigbrother	Pol-3He	Kine-C	138060±150	1-(0.0925±0.0011)

Table 5.7: N_2 dilution factor D_{N_2} for SHMS.

generating the asymmetries for DIS production runs. Notably, since the production of pions is notably less prevalent in elastic and delta scattering events conducted with 1-pass electron beam as opposed to DIS scattering events with 5-pass electron beam, a less stringent Cherenkov detector criterion (SHMS Nobel Gas Cherenkov npesum > 1) was employed to identify electrons in the case of SHMS at 1-pass. These specific cuts were implemented to establish the count datasets. In order to correct the counts for any potential biases, the beam trip cut (ibcm1 > 3 μA) was only applied to the helicity-sorted charge and live-time datasets.

Variable	Cut on HCANA Leaf
Delta [%]	-8 < H.gtr.dp < 8
dx/dz (Xptar) $\theta[rad]$	-0.06 < H.gtr.th < 0.06
dy/dz (Yptar) $\phi[rad]$	-0.1 < H.gtr.ph < 0.1
Z [cm]	-15 < H.react.z < 15
NPE	H.cer.npeSum>1.0
Cal E/P	0.8 < H.cal.etracknorm< 2.0

Table 5.8: HMS: Total Analysis Cuts. All in addition to a "ibcm1>3 μA" electron beam current cut.

5.6 Physics Asymmetry

In order to obtain physics asymmetry for DIS production runs, additional correction to the raw asymmetry presented in Equation 5.1 are necessary, including the polar-

Variable	Cut on HCANA Leaf
Delta [%]	-10 < P.gtr.dp < 22
dx/dz (Xptar) $\theta[rad]$	-0.035 < P.gtr.th < 0.035
dy/dz (Yptar) $\phi[rad]$	-0.029 < P.gtr.ph < 0.034
Z [cm]	-15 < P.react.z < 15
NPE	P.ngcer.npeSum>2.0 (5-pass)
Cal E/P	0.8 < P.cal.etracknorm< 2.0

Table 5.9: SHMS: Total Analysis Cuts. All in addition to a "ibcm1>3 μA" electron beam current cut.

ization of the ^{3}He target P_t, the polarization of the beam P_b and dilution factor D (includes nitrogen dilution and glass windows dilution). Since the sign of asymmetry depend on the "IHWP/target-spin" setting with the consideration of Wein flip during the production periods (see section 5.3), we compute $A_{phys,uncorr}$ first and subsequently apply the sign correction. Then for each "IHWP/target-spin" setting i_{set}, the physics asymmetry could be expressed as the following for each production run i:

$$A_{phys,uncorr} = \left(\frac{\frac{\sum N_i^+/P_{t_i} P_{b_i} \eta_{LT_i}^+}{\sum Q_i^+} - \frac{\sum N_i^-/P_{t_i} P_{b_i} \eta_{LT_i}^-}{\sum Q_i^-}}{\frac{\sum N_i^+/P_{t_i} P_{b_i} \eta_{LT_i}^+}{\sum Q_i^+} + \frac{\sum N_i^-/P_{t_i} P_{b_i} \eta_{LT_i}^-}{\sum Q_i^-}}\right)/D, \tag{5.27}$$

with defined yield variable $\bar{N}^\pm$ and the corresponding uncertainty $\delta\bar{N}^\pm$:

$$\bar{N}^\pm = \sum \frac{N_i^\pm}{P_{t_i} P_{b_i} \eta_{LT_i}^\pm} \tag{5.28}$$

$$\delta\bar{N}^\pm = \sqrt{\sum \frac{N_i^\pm}{(P_{t_i} P_{b_i} \eta_{LT_i}^\pm)^2}}. \tag{5.29}$$

The statistical uncertainty of physics asymmetry is:

$$\delta A_{phys_{stat}} = \frac{2}{D} \sum Q^+ \sum Q^- \sqrt{\frac{(\bar{N}^+ \delta\bar{N}^-)^2 + (\bar{N}^- \delta\bar{N}^+)^2}{(\sum Q^- \bar{N}^+ + \sum Q^+ \bar{N}^-)^4}}. \tag{5.30}$$

Then with the "IHWP/target-spin" setting sign correction listed in Figure 5.6, the sign corrected asymmetry is:

$$A_{phys} = sign * (A_{phys,uncorr}) \tag{5.31}$$

$$\delta A_{phys} = \delta A_{phys,uncorr}. \tag{5.32}$$

While the combined physics asymmetry and combined statistical uncertainty for each i_{set} is calculated by following equations:

$$(A_{phys})_{comb} = \frac{\sum \frac{(A_{phys})_{i_{set}}}{(\delta A_{phys_{stat}})^2_{i_{set}}}}{\sum \frac{1}{(\delta A_{phys_{stat}})^2_{i_{set}}}} \tag{5.33}$$

$$(\delta A_{phys_{stat}})_{comb} = \sqrt{\frac{1}{\sum \frac{1}{(\delta A_{phys_{stat}})^2_{i_{set}}}}}. \tag{5.34}$$

The systematic uncertainty is estimated by:

$$\delta A_{phys_{sys}} = A_{phys}\sqrt{(\frac{\delta D}{D})^2 + (\frac{\delta P_{t_{sys}}}{P_t})^2 + (\frac{\delta P_{b_{sys}}}{P_b})^2 + (\frac{\delta A_{raw_{sys}}}{A_{raw}})^2}. \tag{5.35}$$

A systematic uncertainty of $\delta P_{b_{sys}}/P_b \leq 2\%$ and $\delta P_{t_{sys}}/P_t \leq 4\%$ was applied in Equation 5.35. The $\delta D/D$ are listed in Table 5.6 and Table 5.7, while $\delta A_{raw_{sys}}/A_{raw}$ comes from Spectrometer Acceptance and PID studies. Then the systematic uncertainties is combined by the following equation:

$$(\delta A_{phys_{sys}})_{comb} = \frac{\sum \frac{(\delta A_{phys_{sys}})_{i_{set}}}{(\delta A_{phys_{stat}})^2_{i_{set}}}}{\sum \frac{1}{(\delta A_{phys_{stat}})^2_{i_{set}}}}. \tag{5.36}$$

Thus the total error is the combination of statistical uncertainty and systematic uncertainty:

$$\delta A_{phys_{tot}} = \sqrt{\delta A^2_{phys_{stat}} + \delta A^2_{phys_{sys}}}. \tag{5.37}$$

The physics asymmetries are listed in Tables 6.1 and 6.4. The events are initially grouped in E' bin width set to 20 MeV and later combined into 100 MeV, see chapter 6. Then the corresponding x-bin values for the combined 100 MeV E' bins are obtained from the mean x_{Bj} value of events included in certain E' bin (see second column in Table 6.1 and 6.4).

Chapter 6

Results and Conclusions

6.1 ^{3}He Asymmetry with DIS Cuts

Table 6.1 below displays the physics asymmetries measured by the HMS and SHMS with DIS cuts ($W > 2$ GeV). The table includes statistical uncertainties as well as systematic uncertainties arising from factors such as beam polarization ($\delta P_{b_{sys}}/P_b \leq 2\%$), target polarization ($\delta P_{t_{sys}}/P_t \leq 4\%$), window dilution ($\delta D_{win}/D_{win}$), N_2 dilution ($\delta D_{N_2}/D_{N_2}$) spectrometer acceptance and PID studies ($\delta A_{raw_{sys}}/A_{raw}$) for each E' bin.

Results for the ^{3}He asymmetries (A_1^{3He}, A_2^{3He} from Equation 2.42, 2.43) and structure function ratios (($\frac{g_1}{F_1}$)^{3He}, ($\frac{g_2}{F_1}$)^{3He} from Equation 2.44, 2.45) are in Tables 6.2 and Table 6.3 with DIS cuts ($W > 2$ GeV). These results include both statistical uncertainties and systematic uncertainties. Plot of A_1^{3He} is presented below in Figure. 6.1.

6.2 ^{3}He Asymmetry with no DIS Cuts

Table 6.4 displays the physics asymmetries measured by the HMS and SHMS with no DIS cuts. The table includes statistical uncertainties as well as systematic uncertainties arising from factors such as beam polarization ($\delta P_{b_{sys}}/P_b \leq 2\%$), target po-

E' (GeV)	x	Q^2 (GeV^2)	$A_\parallel$	$\delta A_{\parallel_{stat}}$	$\delta A_{\parallel_{sys}}$	$A_\perp$	$\delta A_{\perp_{stat}}$	$\delta A_{\perp_{sys}}$
2.3	0.42	6.41	-0.00615	0.00711	0.00078	-0.02459	0.01754	0.00128
2.4	0.44	6.58	-0.00233	0.00300	0.00125	0.00831	0.00729	0.00066
2.5	0.46	6.87	-0.00462	0.00326	0.00138	0.00093	0.00787	0.00085
2.6	0.49	7.18	0.00448	0.00356	0.00150	-0.01353	0.00864	0.00154
2.7	0.52	7.45	0.00402	0.00242	0.00106	0.00866	0.00626	0.00279
2.8	0.54	7.73	0.00348	0.00262	0.00097	0.01762	0.00666	0.00281
2.9	0.57	8.01	0.00753	0.00285	0.00095	0.01071	0.00746	0.00332
3	0.6	8.29	0.00827	0.00327	0.00111	0.01657	0.00834	0.00511
3.1	0.63	8.58	0.00217	0.00189	0.00080	0.00809	0.00480	0.00299
3.2	0.65	8.71	0.00177	0.00185	0.00066	0.00584	0.00433	0.00160
3.3	0.67	8.95	0.00477	0.00168	0.00076	0.00863	0.00372	0.00134
3.4	0.7	9.12	0.00352	0.00195	0.00066	0.01010	0.00435	0.00175
3.5	0.71	9.22	0.00550	0.00235	0.00039	0.00738	0.00524	0.00201
3.6	0.73	9.3	0.00730	0.00303	0.00055	0.00482	0.00679	0.00279
3.7	0.74	9.33	0.00848	0.00457	0.00061	0.00434	0.01039	0.00474

Table 6.1: Physics asymmetries with DIS $W > 2$ GeV cut.

E' (GeV)	x	Q^2 (GeV^2)	$A_1^{^3He}$	$\delta A_1^{^3He}{}_{stat}$	$\delta A_1^{^3He}{}_{sys}$	$A_2^{^3He}$	$\delta A_2^{^3He}{}_{stat}$	$\delta A_2^{^3He}{}_{sys}$
2.3	0.42	6.41	-0.00305	0.00840	0.00089	-0.03796	0.02622	0.00192
2.4	0.44	6.58	-0.00396	0.00356	0.00141	0.01186	0.01085	0.00102
2.5	0.46	6.87	-0.00537	0.00392	0.00157	0.00035	0.01164	0.00130
2.6	0.49	7.18	0.00754	0.00434	0.00173	-0.01886	0.01273	0.00229
2.7	0.52	7.45	0.00535	0.00303	0.00139	0.01266	0.00919	0.00411
2.8	0.54	7.73	0.00339	0.00331	0.00134	0.02542	0.00974	0.00413
2.9	0.57	8.01	0.00999	0.00367	0.00137	0.01631	0.01089	0.00484
3	0.6	8.29	0.01017	0.00426	0.00175	0.02478	0.01215	0.00743
3.1	0.63	8.58	0.00163	0.00249	0.00120	0.01190	0.00697	0.00433
3.2	0.65	8.71	0.00169	0.00242	0.00088	0.00855	0.00629	0.00232
3.3	0.67	8.95	0.00532	0.00221	0.00097	0.01300	0.00539	0.00195
3.4	0.7	9.12	0.00380	0.00260	0.00092	0.01474	0.00630	0.00253
3.5	0.71	9.22	0.00761	0.00318	0.00073	0.01116	0.00758	0.00290
3.6	0.73	9.3	0.01172	0.00417	0.00105	0.00771	0.00983	0.00402
3.7	0.74	9.33	0.01532	0.00639	0.00162	0.00695	0.01507	0.00683

Table 6.2: $A_1^{^3He}$ and $A_2^{^3He}$ with DIS $W > 2$ GeV cut.
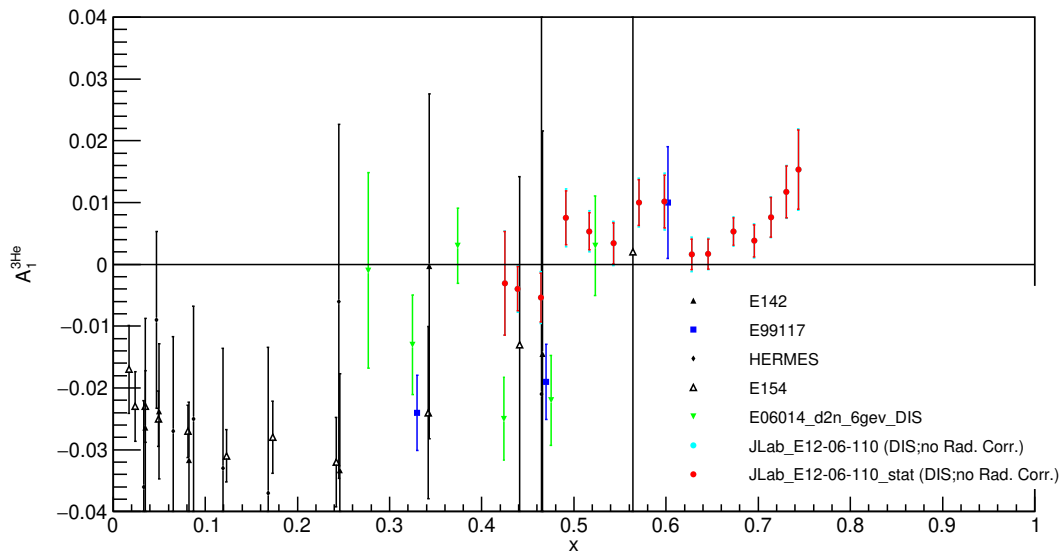
Figure 6.1: Results of A_1^{3He} as a function of x with DIS $W > 2$ GeV cut. The results for our experiment (JLab E12-06-110) are plotted with red circles, include only statistical uncertainty, while the cyan error bars (behind the red error bars and are barely visible) represent the total uncertainty ($\delta A_{1_{tot}}^{3He} = \sqrt{\delta(A_{1_{stat}}^{3He})^2 + \delta(A_{1_{sys}}^{3He})^2}$). Therefore, the systemic uncertainty is relatively small compared to the statistical uncertainty.

E' (GeV)	x	Q^2 (GeV^2)	$\left(\frac{g_1}{F_1}\right)^{3He}$	$\delta\left(\frac{g_1}{F_1}\right)^{3He}_{st}$	$\delta\left(\frac{g_1}{F_1}\right)^{3He}_{sys}$	$\left(\frac{g_2}{F_1}\right)^{3He}$	$\delta\left(\frac{g_2}{F_1}\right)^{3He}_{st}$	$\delta\left(\frac{g_2}{F_1}\right)^{3He}_{sys}$
2.3	0.42	6.41	-0.01365	0.00915	0.00091	-0.07108	0.05263	0.00385
2.4	0.44	6.58	-0.00016	0.00385	0.00136	0.02489	0.02110	0.00199
2.5	0.46	6.87	-0.00469	0.00420	0.00152	0.00452	0.02143	0.00238
2.6	0.49	7.18	0.00091	0.00462	0.00170	-0.03675	0.02219	0.00400
2.7	0.52	7.45	0.00478	0.00322	0.00152	0.02116	0.01525	0.00680
2.8	0.54	7.73	0.00642	0.00348	0.00147	0.04124	0.01539	0.00651
2.9	0.57	8.01	0.00891	0.00384	0.00151	0.02205	0.01635	0.00728
3	0.6	8.29	0.01101	0.00439	0.00197	0.03349	0.01734	0.01061
3.1	0.63	8.58	0.00406	0.00254	0.00129	0.01551	0.00945	0.00588
3.2	0.65	8.71	0.00303	0.00244	0.00090	0.01105	0.00833	0.00306
3.3	0.67	8.95	0.00658	0.00220	0.00095	0.01533	0.00682	0.00245
3.4	0.7	9.12	0.00555	0.00256	0.00091	0.01765	0.00761	0.00305
3.5	0.71	9.22	0.00639	0.00310	0.00075	0.01210	0.00877	0.00336
3.6	0.73	9.3	0.00693	0.00401	0.00104	0.00763	0.01092	0.00447
3.7	0.74	9.33	0.00712	0.00610	0.00159	0.00674	0.01614	0.00734

Table 6.3: $\left(\frac{g_1}{F_1}\right)^{3He}$ and $\left(\frac{g_2}{F_1}\right)^{3He}$ with DIS $W > 2$ GeV cut.

larization ($\delta P_{t_{sys}}/P_t \leq 4\%$), window dilution ($\delta D_{win}/D_{win}$), N_2 dilution ($\delta D_{N_2}/D_{N_2}$) spectrometer acceptance and PID studies ($\delta A_{raw_{sys}}/A_{raw}$) for each E' bin.

Results for the ^{3}He asymmetries (A_1^{3He}, A_2^{3He} from Equation 2.42, 2.43) and structure function ratios ($\left(\frac{g_1}{F_1}\right)^{3He}$, $\left(\frac{g_2}{F_1}\right)^{3He}$ from Equation 2.43, 2.45) are in Tables 6.5 and Table 6.6 with no DIS cuts. These results include both statistical uncertainties and systematic uncertainties. Plot of A_1^{3He} is presented below in Figure. 6.2.

6.3   Future Analysis

In the scattering process, electrons undergo energy loss due to various phenomena such as scattering from glass cell windows, bremsstrahlung, vertex processes, multi-photon emission, and vacuum polarization. These interactions lead to a shift in the actual

E' (GeV)	x	Q^2 (GeV^2)	$A_{\parallel}$	$\delta A_{\parallel_{stat}}$	$\delta A_{\parallel_{sys}}$	$A_{\perp}$	$\delta A_{\perp_{stat}}$	$\delta A_{\perp_{sys}}$
2.3	0.42	6.41	-0.00615	0.00711	0.00078	-0.02459	0.01754	0.00128
2.4	0.44	6.58	-0.00233	0.00300	0.00125	0.00831	0.00729	0.00066
2.5	0.46	6.87	-0.00462	0.00326	0.00138	0.00093	0.00787	0.00085
2.6	0.49	7.18	0.00448	0.00356	0.00150	-0.01353	0.00864	0.00154
2.7	0.52	7.45	0.00402	0.00242	0.00106	0.00866	0.00626	0.00279
2.8	0.54	7.73	0.00348	0.00262	0.00097	0.01762	0.00666	0.00281
2.9	0.57	8.01	0.00753	0.00285	0.00095	0.01071	0.00746	0.00332
3	0.6	8.29	0.00873	0.00323	0.00114	0.01520	0.00823	0.00517
3.1	0.63	8.58	0.00217	0.00189	0.00080	0.00809	0.00480	0.00299
3.2	0.65	8.71	0.00302	0.00200	0.00078	0.00500	0.00463	0.00149
3.3	0.67	8.97	0.00387	0.00180	0.00072	0.00936	0.00390	0.00134
3.4	0.71	9.26	0.00429	0.00206	0.00031	0.00627	0.00448	0.00174
3.5	0.74	9.5	0.00777	0.00239	0.00050	0.00723	0.00518	0.00254
3.6	0.77	9.75	0.00800	0.00282	0.00037	0.01034	0.00607	0.00309
3.7	0.8	10.01	0.00812	0.00346	0.00055	0.01797	0.00759	0.00378
3.8	0.83	10.29	0.00501	0.00584	0.00072	-0.00430	0.01359	0.00615
3.9	0.87	10.53	0.00717	0.00907	0.00111	-0.00852	0.02221	0.00948
4	0.9	10.77	0.01247	0.01179	0.00141	0.00376	0.02985	0.01257

Table 6.4: Physics asymmetries with no DIS cuts.
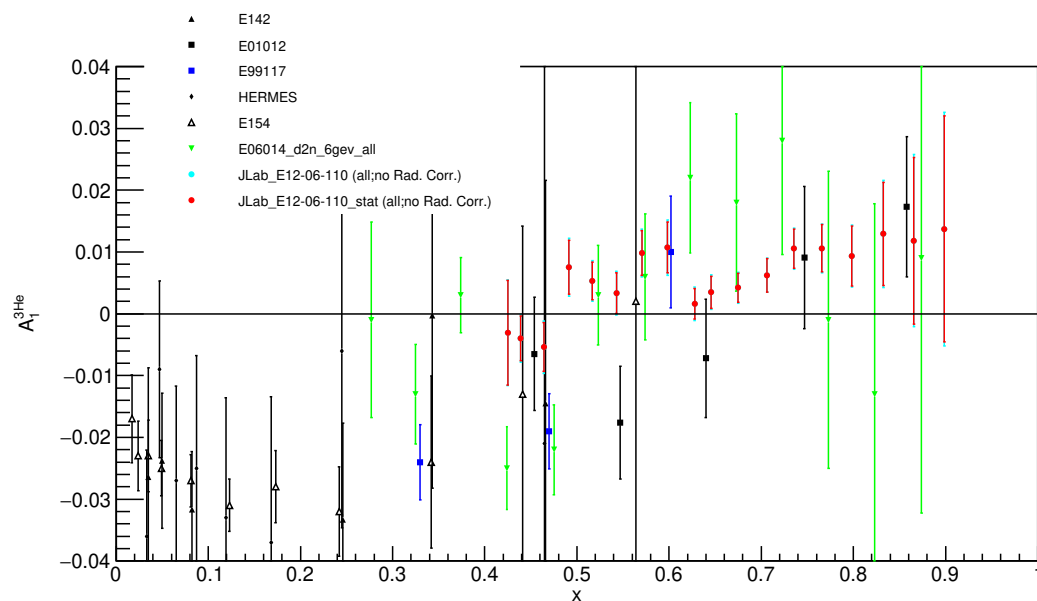
Figure 6.2: Results of A_1^{3He} as a function of x with no DIS cuts. The results for our experiment (JLab E12-06-110) are plotted with red circles, include only statistical uncertainty, while the cyan error bars (behind the red error bars and are barely visible) represent the total uncertainty ($\delta A_{1tot}^{3He} = \sqrt{\delta(A_{1stat}^{3He})^2 + \delta(A_{1sys}^{3He})^2}$). Therefore, the systemic uncertainty is relatively small compared to the statistical uncertainty.

E' (GeV)	x	Q^2 (GeV^2)	$A_1^{^3He}$	$\delta A_1^{^3He}{}_{stat}$	$\delta A_1^{^3He}{}_{sys}$	$A_2^{^3He}$	$\delta A_2^{^3He}{}_{stat}$	$\delta A_2^{^3He}{}_{sys}$
2.3	0.42	6.41	-0.00308	0.00848	0.00090	-0.03832	0.02646	0.00193
2.4	0.44	6.58	-0.00399	0.00359	0.00142	0.01195	0.01093	0.00103
2.5	0.46	6.87	-0.00540	0.00394	0.00157	0.00035	0.01169	0.00130
2.6	0.49	7.18	0.00754	0.00434	0.00173	-0.01886	0.01272	0.00229
2.7	0.52	7.45	0.00532	0.00301	0.00139	0.01259	0.00915	0.00409
2.8	0.54	7.73	0.00336	0.00328	0.00133	0.02520	0.00966	0.00409
2.9	0.57	8.01	0.00986	0.00362	0.00135	0.01607	0.01075	0.00478
3	0.6	8.29	0.01072	0.00413	0.00175	0.02258	0.01179	0.00740
3.1	0.63	8.58	0.00160	0.00245	0.00118	0.01168	0.00684	0.00425
3.2	0.65	8.71	0.00350	0.00259	0.00098	0.00746	0.00658	0.00212
3.3	0.67	8.97	0.00423	0.00233	0.00091	0.01349	0.00554	0.00191
3.4	0.71	9.26	0.00624	0.00271	0.00059	0.00908	0.00636	0.00246
3.5	0.74	9.5	0.01055	0.00318	0.00098	0.01116	0.00736	0.00359
3.6	0.77	9.75	0.01060	0.00382	0.00105	0.01546	0.00863	0.00437
3.7	0.8	10.01	0.00933	0.00482	0.00147	0.02598	0.01081	0.00535
3.8	0.83	10.29	0.01293	0.00836	0.00223	-0.00569	0.01942	0.00873
3.9	0.87	10.53	0.01182	0.01348	0.00351	-0.00943	0.03202	0.01359
4	0.9	10.77	0.01371	0.01828	0.00489	0.01073	0.04359	0.01824

Table 6.5: $A_1^{^3He}$ and $A_2^{^3He}$ with no DIS cuts.

E' (GeV)	x	Q^2 (GeV^2)	$\left(\frac{g_1}{F_1}\right)^{3He}$	$\delta\left(\frac{g_1}{F_1}\right)^{3He}_{st}$	$\delta\left(\frac{g_1}{F_1}\right)^{3He}_{sys}$	$\left(\frac{g_2}{F_1}\right)^{3He}$	$\delta\left(\frac{g_2}{F_1}\right)^{3He}_{st}$	$\delta\left(\frac{g_2}{F_1}\right)^{3He}_{sys}$
2.3	0.42	6.41	-0.01378	0.00923	0.00092	-0.07175	0.05312	0.00388
2.4	0.44	6.58	-0.00016	0.00388	0.00138	0.02508	0.02126	0.00200
2.5	0.46	6.87	-0.00471	0.00422	0.00153	0.00455	0.02152	0.00239
2.6	0.49	7.18	0.00091	0.00461	0.00170	-0.03675	0.02217	0.00399
2.7	0.52	7.45	0.00475	0.00321	0.00152	0.02105	0.01518	0.00677
2.8	0.54	7.73	0.00636	0.00345	0.00146	0.04087	0.01526	0.00645
2.9	0.57	8.01	0.00879	0.00379	0.00149	0.02172	0.01614	0.00718
3	0.6	8.29	0.01099	0.00426	0.00197	0.02978	0.01681	0.01056
3.1	0.63	8.58	0.00398	0.00249	0.00127	0.01522	0.00928	0.00577
3.2	0.65	8.71	0.00392	0.00259	0.00097	0.00875	0.00846	0.00272
3.3	0.67	8.97	0.00562	0.00229	0.00089	0.01612	0.00683	0.00236
3.4	0.71	9.26	0.00469	0.00264	0.00062	0.01012	0.00746	0.00289
3.5	0.74	9.5	0.00831	0.00307	0.00098	0.01042	0.00822	0.00402
3.6	0.77	9.75	0.00928	0.00363	0.00104	0.01479	0.00917	0.00466
3.7	0.8	10.01	0.01140	0.00454	0.00140	0.02537	0.01094	0.00543
3.8	0.83	10.29	0.00155	0.00778	0.00208	-0.00670	0.01872	0.00845
3.9	0.87	10.53	0.00545	0.01235	0.00314	-0.01347	0.02906	0.01234
4	0.9	10.77	0.01639	0.01648	0.00424	0.00049	0.03763	0.01577

Table 6.6: $\left(\frac{g_1}{F_1}\right)^{3He}$ and $\left(\frac{g_2}{F_1}\right)^{3He}$ with no DIS cuts.

incident energy of the electrons as well as the energy of the scattered electrons, resulting in a measured cross-section that differs from the true scattering cross-section. Correcting for these higher-order effects is referred to as radiative corrections. While internal corrections are necessary to consider internal Bremsstrahlung, vertex corrections, multi-photon emission, and vacuum polarization; external radiative corrections arise from the interactions of electrons with various materials before and after scattering the target. The internal and external corrections will be simultaneously performed using the Fortran program RADCOR (Mo and Tsai 1969).

There is a significant gap in the available kinematic coverage required by the A_1^n or d_2^n (the experiment that ran immediately after A_1^n) at 11 GeV radiative correction, see Figure 6.3. As a consequence, it becomes necessary to employ a model or utilize existing fits of ^{3}He cross sections as inputs for the radiative correction.

After radiative corrections are applied to ^{3}He asymmetries, the next step is to obtain neutron asymmetries and structure function ratios. This is referred to as "nuclear correction" which removes nuclear effects that arise from nuclear binding, shadowing, anti-shadowing, potential spin depolarization, Fermi motion, off-shell, and non-nucleonic degrees of freedom. In previous experiments, A_1^n was extracted from $A_1^{^3He}$:

$$A_1^n = \frac{1}{\tilde{P}_n} \frac{F_2^{^3He}}{F_2^n} (A_1^{^3He} - \tilde{P}_p \frac{F_2^p}{F_2^{^3He}} A_1^p), \tag{6.1}$$

where $\tilde{P}_p = P_p - 0.014$ and $\tilde{P}_n = P_n + 0.056$ while $P_p = -0.028^{+0.009}_{-0.004}$ and $P_n = 0.086^{+0.036}_{-0.02}$ are the effective nucleon polarization of the neutron and proton inside ^{3}He. Similarly, g_1^n/F_1^n is extracted from $g_1^{^3He}/F_1^{^3He}$:

$$\frac{g_1^n}{F_1^n} = \frac{1}{\tilde{P}_n} \frac{F_2^{^3He}}{F_2^n} (\frac{g_1^{^3He}}{F_1^{^3He}} - \tilde{P}_p \frac{F_2^p}{F_2^{^3He}} \frac{g_1^p}{F_1^p}). \tag{6.2}$$
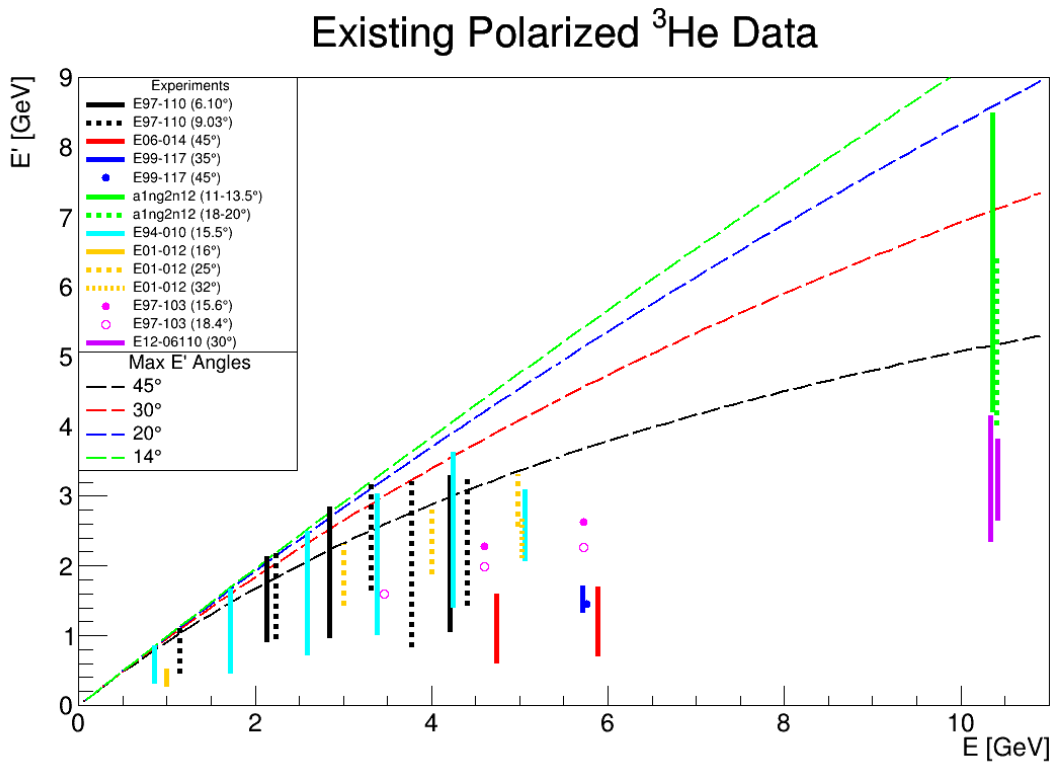
Figure 6.3: Kinematic coverage of all existing polarized ^{3}He experiments carried out at JLab. The 11 GeV A_1^n (green vertical line) and d_2^n (purple vertical line) experiments are shown on the far right. To perform radiative corrections, we need input data or model to cover the full region enclosed by elastic scattering curve, the experimental setting itself (vertical line on the far right), and a horizontal line (not drawn) that forms a (nearly) triangular shape. Figure created by Carter Hedinger (University of Virginia).

Once the neutron spin structure functions are extracted, they can be combined with data on the proton to further study the quark polarization. This allows for the separation of the ratios of polarized to unpolarized parton distribution functions (PDFs) for up and down quarks:

$$\frac{\Delta u + \Delta \bar{u}}{u + \bar{u}} = \frac{4}{15}\frac{g_1^p}{F_1^p}(4 + R^{du}) - \frac{1}{15}\frac{g_1^n}{F_1^n}(1 + 4R^{du}) \tag{6.3}$$

$$\frac{\Delta d + \Delta \bar{d}}{d + \bar{d}} = -\frac{1}{15}\frac{g_1^p}{F_1^p}(1 + \frac{4}{R^{du}}) + \frac{4}{15}\frac{g_1^n}{F_1^n}(4 + \frac{1}{R^{du}}), \tag{6.4}$$

where the ratio $R^{du} = \frac{d+\bar{d}}{u+\bar{u}}$ is obtained from parameterization. For A_1^p and g_1^p/F_1^p, we can either use second-order polynomial fits to the world data (Flay et al. 2016):

$$A_1^p = (0.044 \pm 0.007) + (1.423 \pm 0.078) \cdot x + (0.552 \pm 0.158) \cdot x^2 \tag{6.5}$$

$$g_1^p/F_1^p = (0.035 \pm 0.008) + (1.478 \pm 0.077) \cdot x + (1.010 \pm 0.128) \cdot x^2, \tag{6.6}$$

or use data from the 12 GeV JLab RGC experiments.

6.4 Conclusion

Physics asymmetries of $A_1^{^3He}$ with high precision have been successfully extracted in this experiment (E12-06-110). As illustrated in Figure 6.1, compared to previous experimental results from the JLab 6 GeV era E99117 (Zheng et al. 2004) and E06014 (Flay et al. 2016), the data collected in this experiment is consistent with the previous experimental results up to two sigmas for the middle x range ($0.4 < x < 0.6$). As x approaches 1 ($0.6 < x < 0.75$), the data collected in this experiment reveals an upward trend and this trend is characterized by a less steep slope compared with the

previous results.

When examining the existing global data for A_1^n (especially from E99117 and E06014), the observed trend from the present experiment suggests a closer alignment with the predictions of the NJL Model and DSE, as illustrated in Figure 2.8. However, definitive conclusions regarding which prediction aligns more closely with the results of this experiment can only be drawn after future work involving the extraction of A_1^n, which occurs after the completion of radiative corrections and nuclear corrections.

Concerning the flavor decomposition, after combining with proton data (existing world data plus the recently acquired CLAS12 data (S. Kuhn et al. 2006), the high precision neutron data will allow us to extract polarized to unpolarized parton distribution function (PDF) ratios $\Delta u/u$ and $(\Delta d/d)$ for large x region. These ratios will help us to understand the characteristics of spin structure in the unexplored deep valance quark region.

Bibliography

Kopfermann, H. (1959). *Nuclear Moments*. New York, USA: Academic Press.

Hand, L. N. (1963). "Experimental investigation of pion electroproduction". In: *Phys. Rev.* 129, pp. 1834–1846. DOI: 10.1103/PhysRev.129.1834.

Mo, Luke W. and Yung-Su Tsai (1969). "Radiative Corrections to Elastic and Inelastic e p and mu p Scattering". In: *Rev. Mod. Phys.* 41, pp. 205–235. DOI: 10.1103/RevModPhys.41.205.

HAPPER, WILLIAM (1972). "Optical Pumping". In: *Rev. Mod. Phys.* 44, pp. 169–249. DOI: 10.1103/RevModPhys.44.169.

Bodek, A. (1973). "Comment on the extraction of nucleon cross-sections from deuterium data". In: *Phys. Rev. D* 8, pp. 2331–2334. DOI: 10.1103/PhysRevD.8.2331.

Carlitz, Robert D. (1975). "SU(6) Symmetry Breaking Effects in Deep Inelastic Scattering". In: *Phys. Lett. B* 58, pp. 345–347. DOI: 10.1016/0370-2693(75)90670-X.

Farrar, Glennys R. and Darrell R. Jackson (Nov. 1975). "Pion and Nucleon Structure Functions near $x = 1$". In: *Phys. Rev. Lett.* 35 (21), pp. 1416–1419. DOI: 10.1103/PhysRevLett.35.1416. URL: https://link.aps.org/doi/10.1103/PhysRevLett.35.1416.

Close, F. E. (1979). *An Introduction to Quarks and Partons*. ISBN: 978-0-12-175152-4.

Chupp, T. E. et al. (1987). "Polarized, high-density, gaseous He-3 targets". In: *Phys. Rev. C* 36, pp. 2244–2251. DOI: 10.1103/PhysRevC.36.2244.

Ashman, J. et al. (1988). "A Measurement of the Spin Asymmetry and Determination of the Structure Function g(1) in Deep Inelastic Muon-Proton Scattering". In:

Phys. Lett. B 206. Ed. by V. W. Hughes and C. Cavata, p. 364. DOI: `10.1016/0370-2693(88)91523-7`.

Jaffe, R. L. and Aneesh Manohar (1990). "The G(1) Problem: Fact and Fantasy on the Spin of the Proton". In: *Nucl. Phys. B* 337, pp. 509–546. DOI: `10.1016/0550-3213(90)90506-9`.

Manohar, Aneesh V. (Mar. 1992). "An Introduction to spin dependent deep inelastic scattering". In: *Lake Louise Winter Institute: Symmetry and Spin in the Standard Model.* arXiv: `hep-ph/9204208`.

Dashen, Roger F. and Aneesh V. Manohar (1993). "Baryon - pion couplings from large N(c) QCD". In: *Phys. Lett. B* 315, pp. 425–430. DOI: `10.1016/0370-2693(93)91635-Z`. arXiv: `hep-ph/9307241`.

Gomez, J. et al. (1994). "Measurement of the A-dependence of deep inelastic electron scattering". In: *Phys. Rev. D* 49, pp. 4348–4372. DOI: `10.1103/PhysRevD.49.4348`.

Manohar, A. V. (1994). "Symmetry and Spin in the Standard Model". In: Chateau Lake Louise. URL: `https://arxiv.org/pdf/hep-ph/9209272.pdf`.

Roberts, R. G. (Feb. 1994). *The Structure of the proton: Deep inelastic scattering.* Cambridge Monographs on Mathematical Physics. Cambridge University Press. ISBN: 978-0-521-44944-1, 978-1-139-24244-8. DOI: `10.1017/CBO9780511564062`.

Brodsky, Stanley J., Matthias Burkardt, and Ivan Schmidt (1995). "Perturbative QCD constraints on the shape of polarized quark and gluon distributions". In: *Nucl. Phys. B* 441, pp. 197–214. DOI: `10.1016/0550-3213(95)00009-H`. arXiv: `hep-ph/9401328`.

Appelt, S. et al. (1998). "Theory of spin-exchange optical pumping of ^{3}He and ^{129}Xe". In: *Phys. Rev. A* 58, p. 1412. DOI: `10.1103/PhysRevA.58.1412`.

Arrington, J. R. (1998). "Inclusive Electron Scattering from Nuclei at $x > 1$ and High Q^2". PhD thesis. California Institute of Technology. DOI: `10.7907/wkge-my02`.

Ben-Amar Baranga, A. et al. (1998). "Polarization of 3He by spin exchange with optically pumped Rb and K vapors". In: *Physical review letters* 80.13, pp. 2801–2804. ISSN: 0031-9007. DOI: 10.1103/PhysRevLett.80.2801.

Romalis, M. V. and G. D. Cates (Oct. 1998). "Accurate ^{3}He polarimetry using the Rb Zeeman frequency shift due to the Rb$-^3$He spin-exchange collisions". In: *Phys. Rev. A* 58 (4), pp. 3004–3011. DOI: 10.1103/PhysRevA.58.3004. URL: https://link.aps.org/doi/10.1103/PhysRevA.58.3004.

Romalis, Michael V (1998). PhD thesis. Princeton U.

Soffer, Jacques and O. V. Teryaev (2000). "Positivity constraints and flavor dependence of higher twists". In: *Phys. Lett. B* 490, pp. 106–110. DOI: 10.1016/S0370-2693(00)00972-2. arXiv: hep-ph/0005132.

Hauger, M. et al. (2001). "A High precision polarimeter". In: *Nucl. Instrum. Meth. A* 462, pp. 382–392. DOI: 10.1016/S0168-9002(01)00197-8. arXiv: nucl-ex/9910013.

Leemann, C. W., D. R. Douglas, and G. A. Krafft (2001). "The Continuous Electron Beam Accelerator Facility: CEBAF at the Jefferson Laboratory". In: *Ann. Rev. Nucl. Part. Sci.* 51, pp. 413–450. DOI: 10.1146/annurev.nucl.51.101701.132327.

Xiong, F. et al. (2001). "Precision measurement of the spin dependent asymmetry in the threshold region of polarized He-3(polarized-e, e-prime)". In: *Phys. Rev. Lett.* 87, p. 242501. DOI: 10.1103/PhysRevLett.87.242501. arXiv: nucl-ex/0110008.

Amarian, M. et al. (2002). "The Q**2 evolution of the generalized Gerasimov-Drell-Hearn integral for the neutron using a He-3 target". In: *Phys. Rev. Lett.* 89, p. 242301. DOI: 10.1103/PhysRevLett.89.242301. arXiv: nucl-ex/0205020.

Bissey, Francois Rene Pierre et al. (2002). "Complete analysis of spin structure function g(1) of He-3". In: *Phys. Rev. C* 65, p. 064317. DOI: 10.1103/PhysRevC.65.064317. arXiv: hep-ph/0109069.

Bourrely, Claude, Jacques Soffer, and Franco Buccella (2002). "A Statistical approach for polarized parton distributions". In: *Eur. Phys. J. C* 23, pp. 487–501. DOI: 10.1007/s100520100855. arXiv: hep-ph/0109160.

Zheng, X. (2002). "Precision Measurement of Neutron Spin Asymmetry A_1^n at Large xbj Using CEBAF at 5.7 GeV". PhD thesis. Massachusetts Inst. of Technology (MIT), Cambridge, MA (United States). DOI: 10.2172/824895.

Babcock, E. et al. (2003). "Hybrid spin-exchange optical pumping of 3-He". In: *Phys. Rev. Lett.* 91, p. 123003. DOI: 10.1103/PhysRevLett.91.123003.

Mack, Dave and Stephen A. Wood (2003). *Hall C Expert Howto, BCM Calibration.* URL: https://hallcweb.jlab.org/document/howtos/bcm_calibration.pdf.

Povh, B., K. Rith, and C. Scholz (2004). *Particles and Nuclei.* Springer.

Slifer, K (2004). PhD thesis. Temple U.

Zheng, X. et al. (2004). "Precision measurement of the neutron spin asymmetry A1**N and spin flavor decomposition in the valence quark region". In: *Phys. Rev. Lett.* 92, p. 012004. DOI: 10.1103/PhysRevLett.92.012004. arXiv: nucl-ex/0308011.

Cloet, I. C., Wolfgang Bentz, and Anthony William Thomas (2005). "Nucleon quark distributions in a covariant quark-diquark model". In: *Phys. Lett. B* 621, pp. 246–252. DOI: 10.1016/j.physletb.2005.06.065. arXiv: hep-ph/0504229.

Ralson, J. P., P. Jain, and R. V. Buniy (2005). "Asymptotic behavior of nucleon electromagnetic form factors in time-like region". In: AIP Conf. DOI: 10.1140/epja/i2005-10164-5.

Hansknecht, J. and M. Poelker (2006). "Synchronous photoinjection using a frequency-doubled gain-switched fiber-coupled seed laser and ErYb-doped fiber amplifier". In: *Phys. Rev. ST Accel. Beams* 9, p. 063501. DOI: 10.1103/PhysRevSTAB.9.063501.

Kuhn, S. et al. (2006). "The longitudinal spin structure of the nuelcon". In: URL: https://www.jlab.org/exp_prog/proposals/proposal_updates/PR12-06-109_pac36.pdf.

Avakian, Harut et al. (2007). "Effect of Orbital Angular Momentum on Valence-Quark Helicity Distributions". In: *Phys. Rev. Lett.* 99, p. 082001. DOI: 10.1103/PhysRevLett.99.082001. arXiv: 0705.1553 [hep-ph].

Chen, W. C. et al. (Jan. 2007). "Spin-exchange optical pumping of ^{3}He with Rb-K mixtures and pure K". In: *Phys. Rev. A* 75 (1), p. 013416. DOI: 10.1103/PhysRevA.75.013416. URL: https://link.aps.org/doi/10.1103/PhysRevA.75.013416.

Kolarkar, Ameya (2008). "Precision Measurements of the Neutron Electric Form Factor at High Momentum Transfers". PhD thesis. Kentucky U. URL: https://uknowledge.uky.edu/gradschool_diss/612.

Kuhn, S. E., J. P. Chen, and E. Leader (2009). "Spin Structure of the Nucleon - Status and Recent Results". In: *Prog. Part. Nucl. Phys.* 63, pp. 1–50. DOI: 10.1016/j.ppnp.2009.02.001. arXiv: 0812.3535 [hep-ph].

Nakamura, K. et al. (2010). "Review of particle physics". In: *J. Phys. G* 37, p. 075021. DOI: 10.1088/0954-3899/37/7A/075021.

Riordan, S. et al. (2010). "Measurements of the Electric Form Factor of the Neutron up to $Q^2 = 3.4 GeV^2$ using the Reaction $^3He^{->}(e^{->}, e'n)pp$". In: *Phys. Rev. Lett.* 105, p. 262302. DOI: 10.1103/PhysRevLett.105.262302. arXiv: 1008.1738 [nucl-ex].

Dolph, P. A. M. et al. (2011). "Gas dynamics in high-luminosity polarized He-3 targets using diffusion and convection". In: *Phys. Rev. C* 84, p. 065201. DOI: 10.1103/PhysRevC.84.065201. arXiv: 1107.1902 [physics.ins-det].

Qian, X. et al. (2011). "Single Spin Asymmetries in Charged Pion Production from Semi-Inclusive Deep Inelastic Scattering on a Transversely Polarized ^{3}He Target". In: *Phys. Rev. Lett.* 107, p. 072003. DOI: 10.1103/PhysRevLett.107.072003. arXiv: 1106.0363 [nucl-ex].

Huang, J. et al. (2012). "Beam-Target Double Spin Asymmetry A_{LT} in Charged Pion Production from Deep Inelastic Scattering on a Transversely Polarized ^{3}He Target at $1.4 < Q^2 < 2.7$ GeV^2". In: *Phys. Rev. Lett.* 108, p. 052001. DOI: 10.1103/PhysRevLett.108.052001. arXiv: 1108.0489 [nucl-ex].

Aidala, Christine A. et al. (2013). "The Spin Structure of the Nucleon". In: *Rev. Mod. Phys.* 85, pp. 655–691. DOI: 10.1103/RevModPhys.85.655. arXiv: 1209.2803 [hep-ph].

Roberts, Craig D., Roy J. Holt, and Sebastian M. Schmidt (2013). "Nucleon spin structure at very high-x". In: *Phys. Lett. B* 727, pp. 249–254. DOI: 10.1016/j.physletb.2013.09.038. arXiv: 1308.1236 [nucl-th].

Florian, Daniel de et al. (2014). "Evidence for polarization of gluons in the proton". In: *Phys. Rev. Lett.* 113.1, p. 012001. DOI: 10.1103/PhysRevLett.113.012001. arXiv: 1404.4293 [hep-ph].

Parno, D. S. et al. (2015). "Precision Measurements of A_1^n in the Deep Inelastic Regime". In: *Phys. Lett. B* 744, pp. 309–314. DOI: 10.1016/j.physletb.2015.03.067. arXiv: 1406.1207 [nucl-ex].

Bogacz, S.A. et al. (2016). *A test of 5-pass energy recovery at CEBAF.*

Flay, D. et al. (2016). "Measurements of d_2^n and A_1^n: Probing the neutron spin structure". In: *Phys. Rev. D* 94.5, p. 052003. DOI: 10.1103/PhysRevD.94.052003. arXiv: 1603.03612 [nucl-ex].

Liu, Jie (2017). "The Proton Spin Structure Function g_2 at Low Q^2 and Applications of Polarized ^{3}He". PhD thesis. Virginia U. DOI: 10.18130/V3CM0X.

Deur, Alexandre, Stanley J. Brodsky, and Guy F. De Téramond (July 2018). "The Spin Structure of the Nucleon". In: DOI: 10.1088/1361-6633/ab0b8f. arXiv: 1807.05250 [hep-ph].

JLab Campus Site Map (2019). URL: https://www.jlab.org/about/visitors/site_map.

Wood, S.A., ed. (2019). *Hall C Standard-Equipment-Manual*. URL: https://hallcweb.jlab.org/safety-docs/current/Standard-Equipment-Manual.pdf.

Yero, Carlos (2019). *General Hall C Analysis Procedure in 12 GeV Era*. Tech. rep. Jefferson Lab. URL: https://hallcweb.jlab.org/DocDB/0010/001032/001/analysis_notes.pdf.

Cardona, Melanie (2021). *Updated SHMS/HMS PID Results for both DIS Settings*. Tech. rep. Temple U. URL: https://hallcweb.jlab.org/elogs/A1n+(E12-06-110)+Analysis/10.

Henry, Bill (2021). "Moller Polarimetry Measurements". In: Jefferson Lab. URL: https://indico.jlab.org/event/422/contributions/7625/attachments/6414/8507/hallcmoller2021.pdf.

Katugampola, Sumudu et al. (Sept. 2021). "Frequency shifts in the EPR spectrum of ^{39}K due to spin-exchange collisions with polarized ^{3}He and precise ^{3}He polarimetry". In: arXiv: 2109.04375 [physics.atom-ph].

Ball, Richard D. et al. (2022). "The path to proton structure at 1% accuracy". In: *Eur. Phys. J. C* 82.5, p. 428. DOI: 10.1140/epjc/s10052-022-10328-7. arXiv: 2109.02653 [hep-ph].

Cardona, Melanie (2022). *Sign Determination*. Tech. rep. Temple U. URL: https://hallcweb.jlab.org/elogs/A1n+(E12-06-110)+Analysis/31.

Roy, Murchhana (May 2022). "Extraction of Deep Inelastic Cross Sections Using a 10.4 GeV Electron Beam and a Polarized Helium-3 Target". In: URL: https://www.osti.gov/biblio/1969487.

Cardona, Melanie (2023). "Measuring the Neutron Spin Asymmetry A_1^n in the Valence Quark Region in Hall C at Jefferson Lab". PhD thesis. Temple U. DOI: 10.34944/dspace/8548.

Gaskell, Dave (2023a). *Beam polarization uncertainty for A_1^n*. Tech. rep. Jefferson Lab. URL: https://hallcweb.jlab.org/elogs/A1n-d2n+Combined+Analysis/139.

— (2023b). *Moller target polarization*. Tech. rep. Jefferson Lab. URL: https://hallcweb.jlab.org/elogs/A1n-d2n+Combined+Analysis/143.

Sawatzky, Brad (2023). *SHMS/HMS Cerenkov Detector settings for A_1^n/d_2^n run group*. Tech. rep. Jefferson Lab. URL: https://hallcweb.jlab.org/elogs/A1n-d2n+Combined+Analysis/141.

Appendices

Appendix A

Window Dilution

A.1 Production Cell Bigbrother and Reference Cell Will

During A_1^n experiment, production cell "Bigbrother" was employed for DIS runs corresponding to HMS kinematics 4 and 3, which correspond to SHMS kinematics B and C. Analyzing the z_{tg}^{recon} yield histogram revealed that the center of the production cell "Bigbrother" target chamber is located approximately -0.8 cm from a reference point. Simultaneously, the empty reference cell "Will" (with the target chamber center around -0.2 cm) underwent the same kinematics. To align both datasets, the empty reference cell's z_{tg}^{recon} yield histogram was shifted by -0.6 cm, ensuring that the centers of the production and empty reference cells coincided.

This alignment enabled the determination of the window dilution factor for cell "Bigbrother" with statistical and systemic uncertainties with the desired window z_{tg}^{recon} cut extending from -17 cm to +18 cm respect to the production cell's target center, see Figures B.1 through B.12.
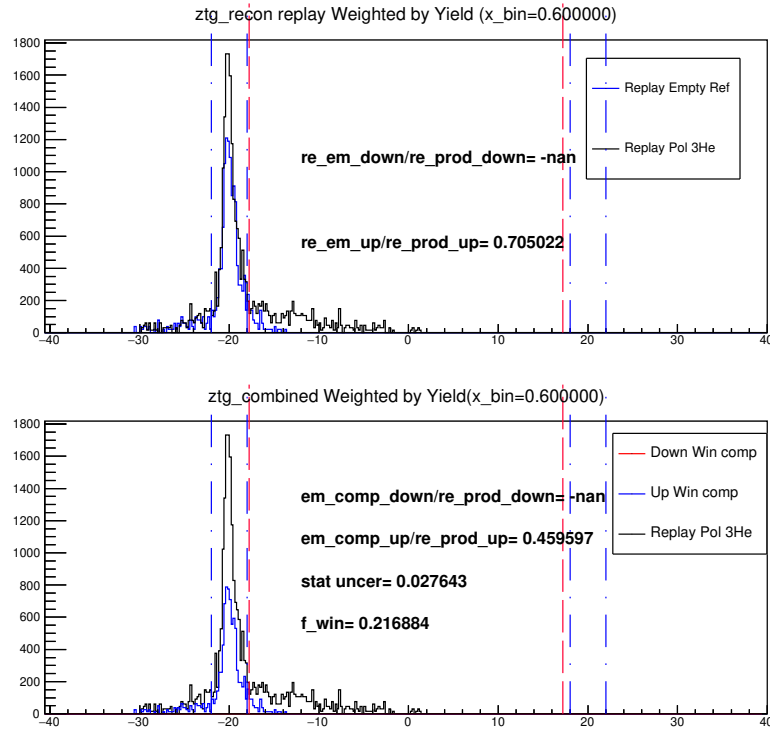
Figure A.1: For x_{bj} bin centered at 0.60, top plot shows z_{tg}^{recon} yield histogram make comparison between replayed production cell Bigbrother run and replayed empty reference cell run. While the bottom plot scaled z_{tg}^{recon} yield histogram for replayed empty reference cell run by corresponding window thickness ratio times rad corr ratio for upstream(downstream) window. (At kin-4 ($E_p = -3.5$GeV, $30°$), HMS 3408 was used for pol ^3He DIS run with holding field Transverse $90°$ and HMS 3077 was used with target center z_{tg}^{recon} shifted by -0.6cm for empty DIS run with holding field Transverse $90°$)
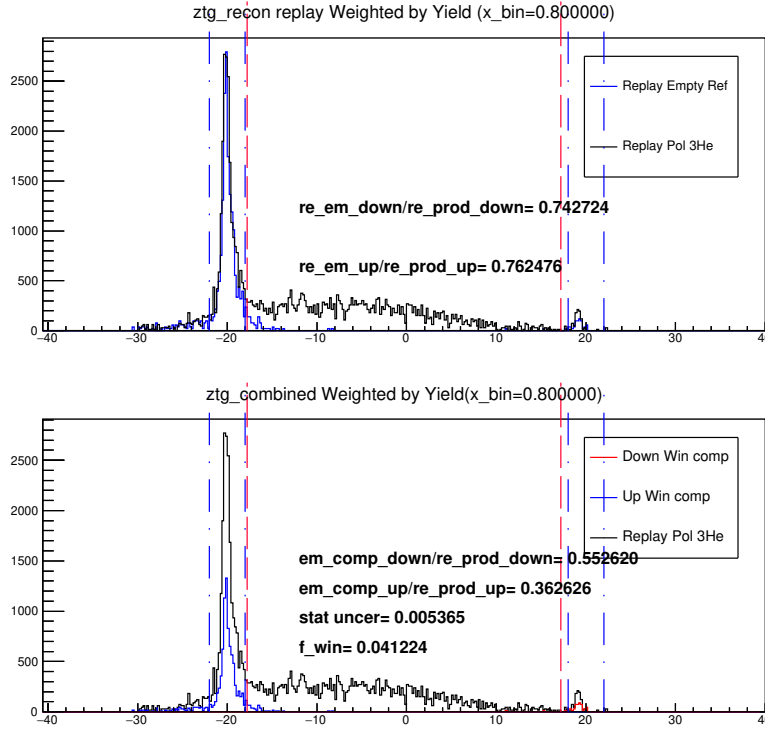
Figure A.2: For x_{bj} bin centered at 0.80, top plot shows z_{tg}^{recon} yield histogram make comparison between replayed production cell Bigbrother run and replayed empty reference cell run. While the bottom plot scaled z_{tg}^{recon} yield histogram for replayed empty reference cell run by corresponding window thickness ratio times rad corr ratio for upstream(downstream) window. (At kin-4 ($E_p = -3.5$GeV, 30°), HMS 3408 was used for pol ^3He DIS run with holding field Transverse 90° and HMS 3077 was used with target center z_{tg}^{recon} shifted by -0.6cm for empty DIS run with holding field Transverse 90°)
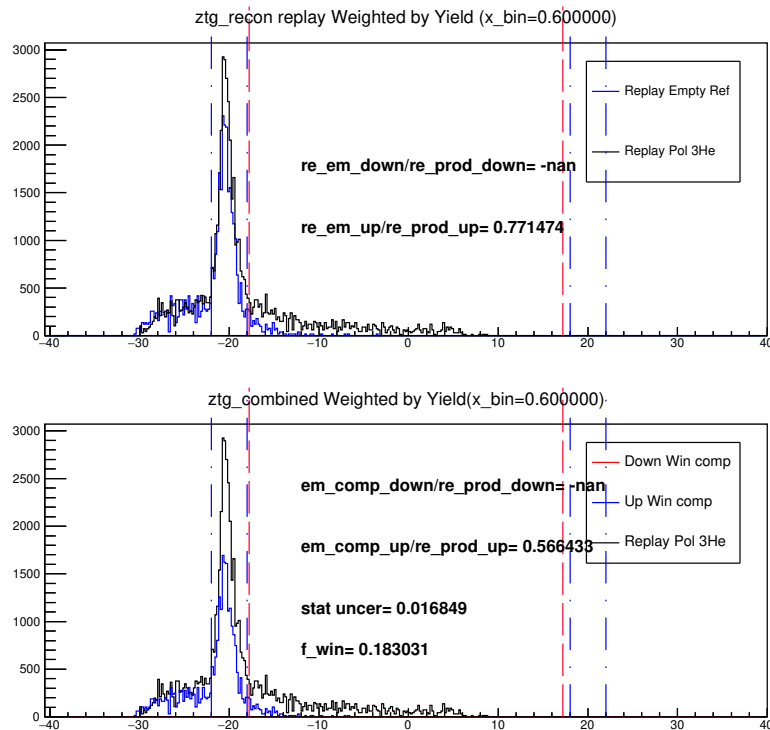
Figure A.3: For x_{bj} bin centered at 0.60, top z_{tg}^{recon} yield histogram make comparison between replayed production cell Bigbrother run and replayed empty reference cell run .While the bottom plot scaled z_{tg}^{recon} yield histogram for replayed empty reference cell run by corresponding window thickness ratio times rad corr ratio for upstream(downstream) window. (At kin-B ($E_p = -3.4$GeV, $30°$), SHMS 9956 was used for pol ^3He DIS run with holding field Longitudinal $180°$ and SHMS 10267 was used with target center z_{tg}^{recon} shifted by -0.6cm for empty DIS run with holding field Transverse $90°$)
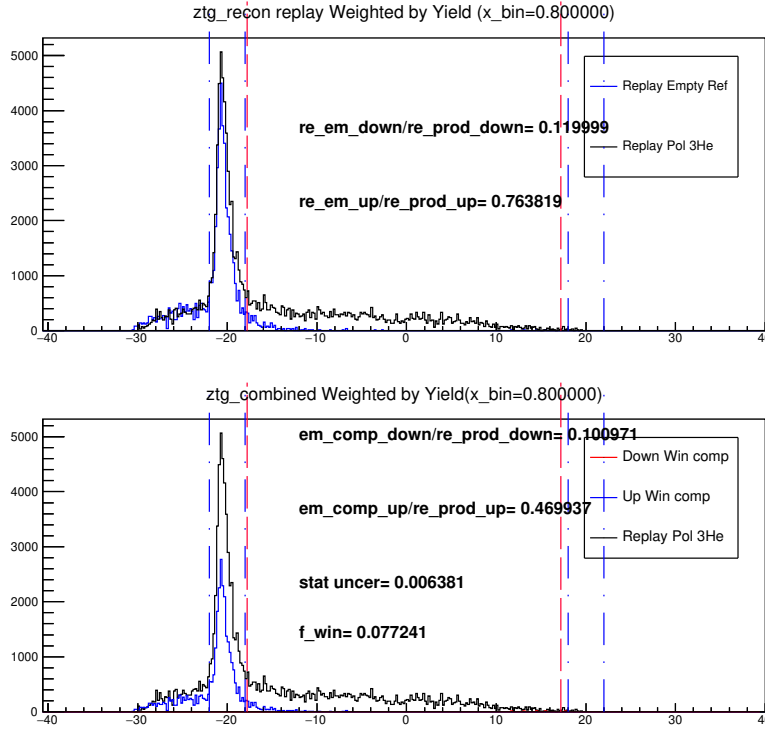
Figure A.4: For x_{bj} bin centered at 0.80, top z_{tg}^{recon} yield histogram make comparison between replayed production cell Bigbrother run and replayed empty reference cell run .While the bottom plot scaled z_{tg}^{recon} yield histogram for replayed empty reference cell run by corresponding window thickness ratio times rad corr ratio for upstream(downstream) window. (At kin-B ($E_p = -3.4$GeV, $30°$), SHMS 9956 was used for pol ^3He DIS run with holding field Longitudinal $180°$ and SHMS 10267 was used with target center z_{tg}^{recon} shifted by -0.6cm for empty DIS run with holding field Transverse $90°$)
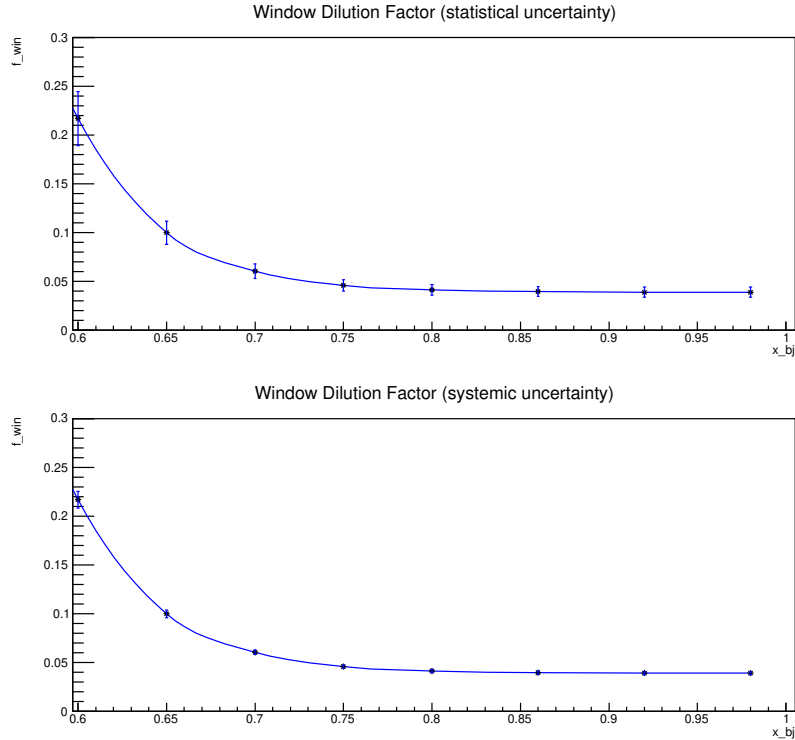
Figure A.5: Window dilution for cell Bigbrother at kine-4 ($E_p = -3.5$GeV, $30°$), with statistical uncertainty δf_{win_stat} shown in the top plot and the systematic uncertainty δf_{win_sys} shown in the bottom plot. For Δf_{win_sys}, uncertainty for production cell Bigbrother upstream (downstream) window thickness is $\pm 2*10^{-5}$ cm and for empty reference cell Will upstream (downstream) window thickness is $\pm 5.1*10^{-4}$ cm. While the uncertainty for production cell Bigbrother and empty reference cell Will upstream (downstream) window position is ± 0.2 cm. (HMS 3408 was used for pol ^3He DIS run with holding field Longitudinal $180°$ and HMS 3077 was used with target center z_{tg}^{recon} shifted by -0.6cm for empty DIS run with holding field Transverse $90°$)
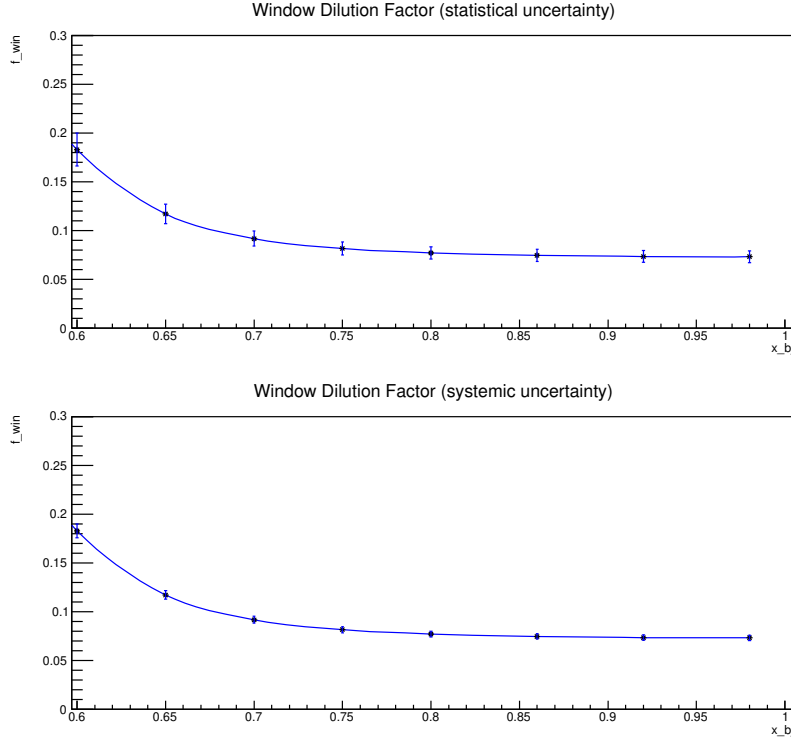
Figure A.6: Window dilution for cell Bigbrother at kine-B ($E_p = -3.4$GeV, $30°$), with statistical uncertainty δf_{win_stat} shown in the top plot and the systematic uncertainty δf_{win_sys} shown in the bottom plot. For Δf_{win_sys}, uncertainty for production cell Bigbrother upstream (downstream) window thickness is $\pm 2*10^{-5}$ cm and for empty reference cell Will upstream (downstream) window thickness is $\pm 5.1*10^{-4}$ cm. While the uncertainty for production cell Bigbrother and empty reference cell Will upstream (downstream) window position is ± 0.2 cm. (SHMS 9956 was used for pol ^3He DIS run with holding field Longitudinal $180°$ and SHMS 10267 was used with target center z_{tg}^{recon} shifted by -0.6cm for empty DIS run with holding field Transverse $90°$)

Figure A.7: For x_{bj} bin centered at 0.60, top plot shows z_{tg}^{recon} yield histogram make comparison between replayed production cell Bigbrother run and replayed empty reference cell run. While the bottom plot scaled z_{tg}^{recon} yield histogram for replayed empty reference cell run by corresponding window thickness ratio times rad corr ratio for upstream(downstream) window. (At kin-3 ($E_p = -2.9$GeV, 30°), use HMS 3149 for pol ^3He DIS run with holding field Transverse 90° and HMS 3072 with target center z_{tg}^{recon} shifted by -0.6cm for empty DIS run with holding field Transverse 90°)

162
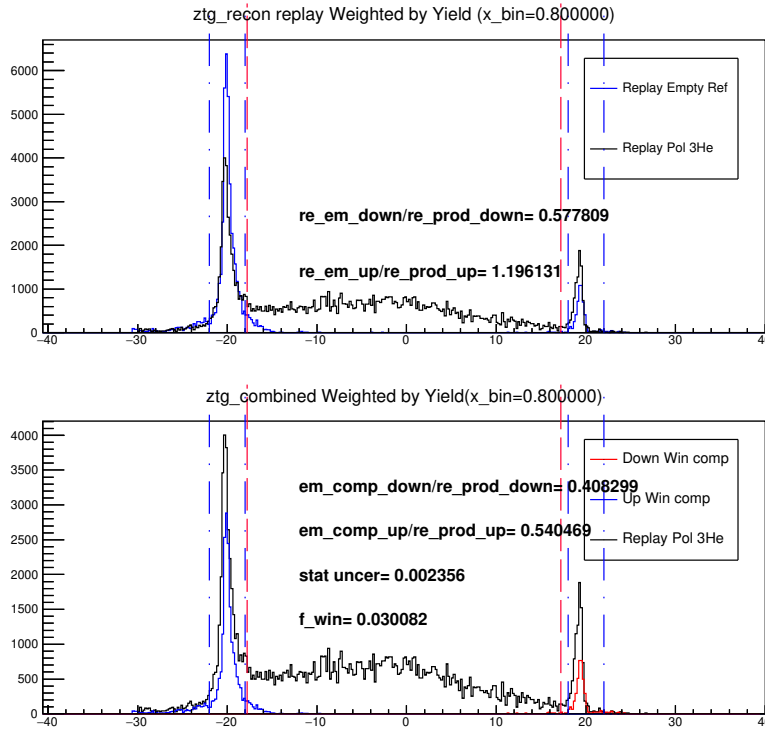
Figure A.8: For x_{bj} bin centered at 0.80, top plot shows z_{tg}^{recon} yield histogram make comparison between replayed production cell Bigbrother run and replayed empty reference cell run. While the bottom plot scaled z_{tg}^{recon} yield histogram for replayed empty reference cell run by corresponding window thickness ratio times rad corr ratio for upstream(downstream) window. (At kin-3 ($E_p = -2.9\text{GeV}$, 30°), HMS 3149 was used for pol ^3He DIS run with holding field Transverse 90° and HMS 3072 was used with target center z_{tg}^{recon} shifted by -0.6cm for empty DIS run with holding field Transverse 90°)
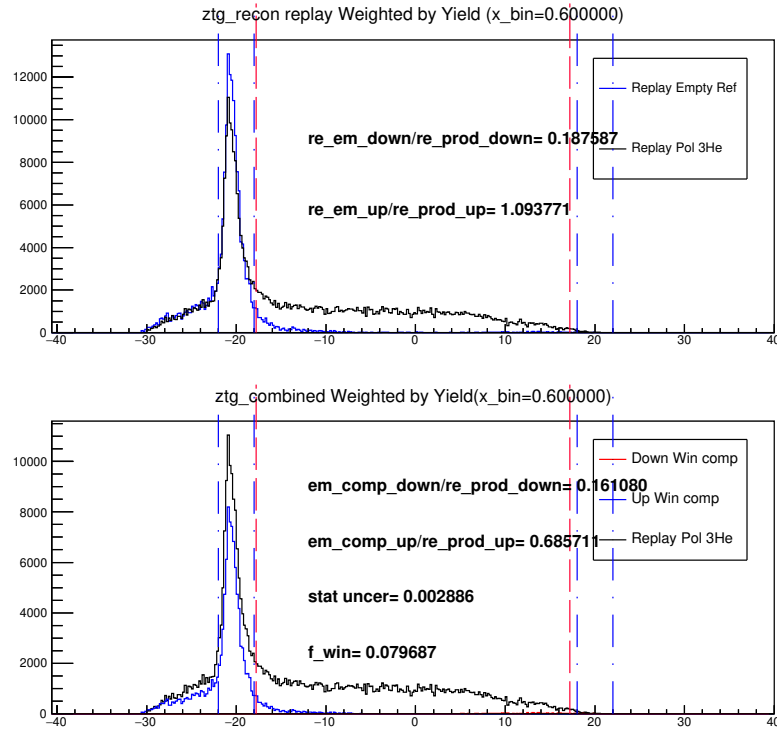
Figure A.9: For x_{bj} bin centered at 0.60, top z_{tg}^{recon} yield histogram make comparison between replayed production cell Bigbrother run and replayed empty reference cell run .While the bottom plot scaled z_{tg}^{recon} yield histogram for replayed empty reference cell run by corresponding window thickness ratio times rad corr ratio for upstream(downstream) window. (At kin-C ($E_p = -2.6$GeV, $30°$), SHMS 10345 was used for pol ^3He DIS run with holding field Longitudinal $180°$ and SHMS 10262 was used with target center z_{tg}^{recon} shifted by -0.6cm for empty DIS run with holding field Longitudinal $180°$)
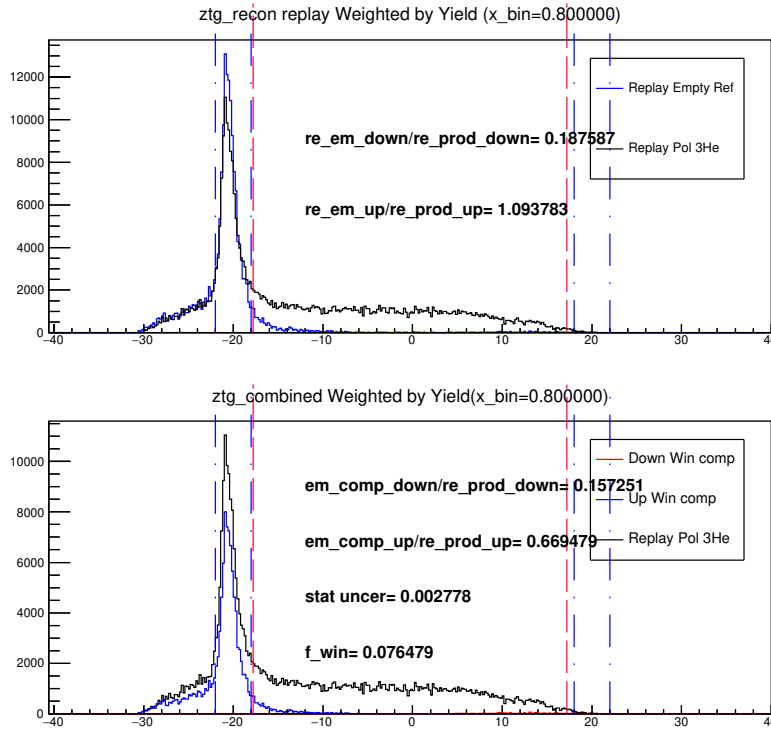
Figure A.10: For x_{bj} bin centered at 0.80, top z_{tg}^{recon} yield histogram make comparison between replayed production cell Bigbrother run and replayed empty reference cell run .While the bottom plot scaled z_{tg}^{recon} yield histogram for replayed empty reference cell run by corresponding window thickness ratio times rad corr ratio for upstream(downstream) window. (At kin-C ($E_p = -2.6$GeV, $30°$), SHMS was used 10345 for pol ^3He DIS run with holding field Longitudinal $180°$ and SHMS was used 10262 with target center z_{tg}^{recon} shifted by -0.6cm for empty DIS run with holding field Longitudinal $180°$)
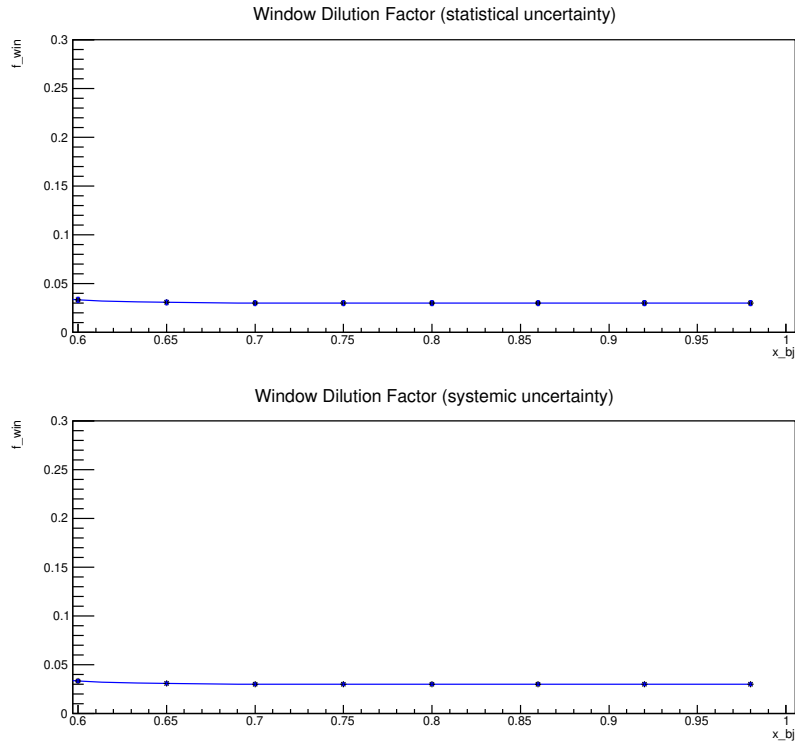
Figure A.11: Window dilution for cell Bigbrother at kine-3 ($E_p = -2.9$GeV, $30°$), with statistical uncertainty δf_{win_stat} shown in the top plot and the systematic uncertainty δf_{win_sys} shown in the bottom plot. For Δf_{win_sys}, uncertainty for production cell Bigbrother upstream (downstream) window thickness is $\pm 2 * 10^{-5}$ cm and for empty reference cell Will upstream (downstream) window thickness is $\pm 5.1 * 10^{-4}$ cm. While the uncertainty for production cell Bigbrother and empty reference cell Will upstream (downstream) window position is ± 0.2 cm. (HMS 3149 was used for pol ^3He DIS run with holding field Transverse $90°$ and HMS was used 3072 with target center z_{tg}^{recon} shifted by -0.6cm for empty DIS run with holding field Transverse $90°$)
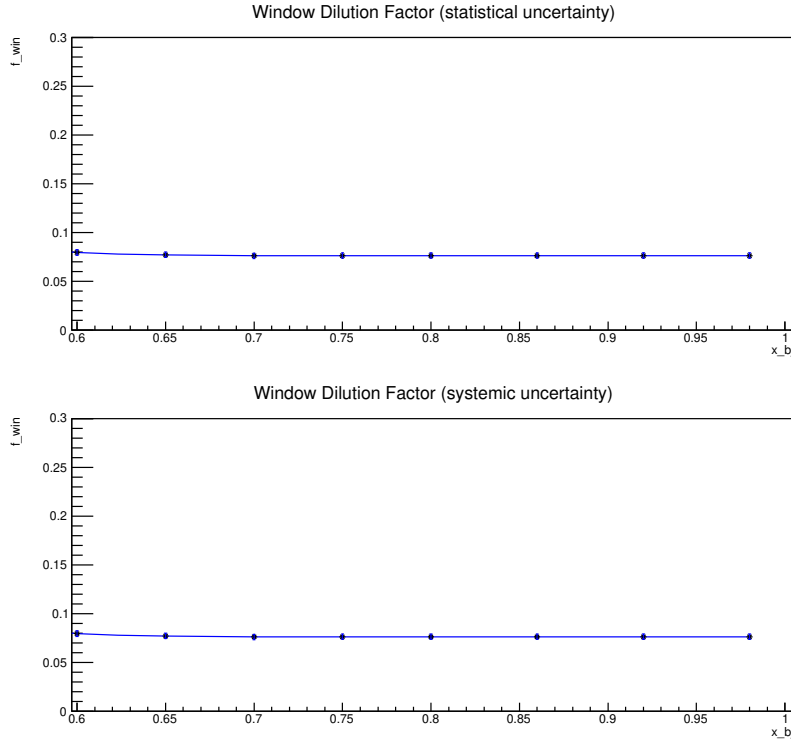
Figure A.12: Window dilution for cell Bigbrother at kine-C ($E_p = -2.6$GeV, 30°), with statistical uncertainty δf_{win_stat} shown in the top plot and the systematic uncertainty δf_{win_sys} shown in the bottom plot. For Δf_{win_sys}, uncertainty for production cell Bigbrother upstream (downstream) window thickness is $\pm 2 * 10^{-5}$ cm and for empty reference cell Will upstream (downstream) window thickness is $\pm 5.1 * 10^{-4}$ cm. While the uncertainty for production cell Bigbrother and empty reference cell Will upstream (downstream) window position is ± 0.2 cm. (SHMS 10345 was used for pol ^3He DIS run with holding field Longitudinal 180° and SHMS 10262 was used with target center z_{tg}^{recon} shifted by -0.6cm for empty DIS run with holding field Longitudinal 180°)

Appendix B

Spectrometer acceptance cuts

B.1   Theta, Phi Cuts Study
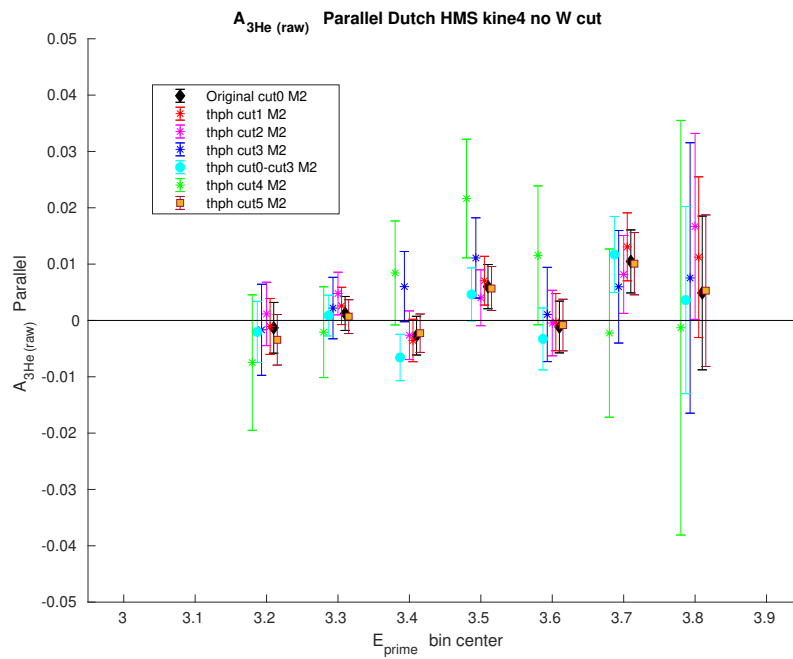
Figure B.1: Acceptance cut study for various HMS θ, ϕ cuts. Plot of $A_\parallel$ with different θ, ϕ cuts (listed in Table B1) and with no w cuts.
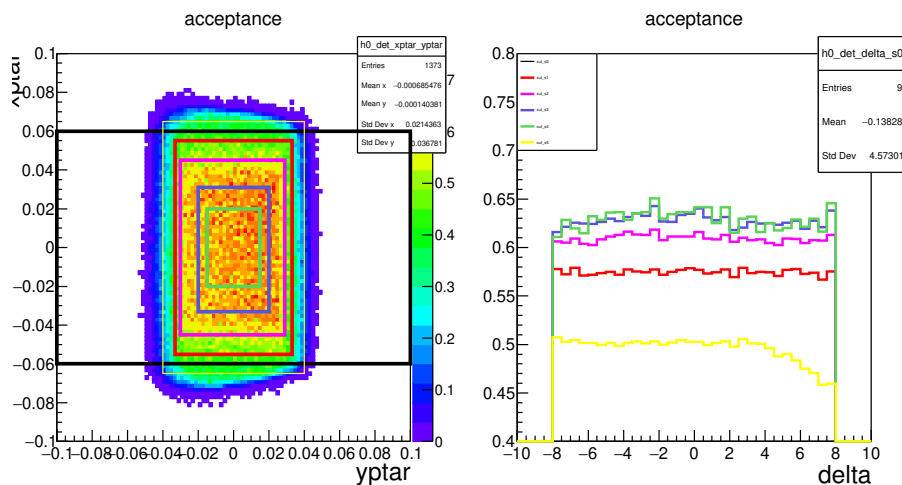
Figure B.2: Left: 2D plot of HMS acceptance over ϕ (XPtar) and θ (YPtar) for different θ, ϕ cuts (listed in Table B1) Right: HMS acceptance vs. delta plot for different θ, ϕ cuts (listed in Table B1).
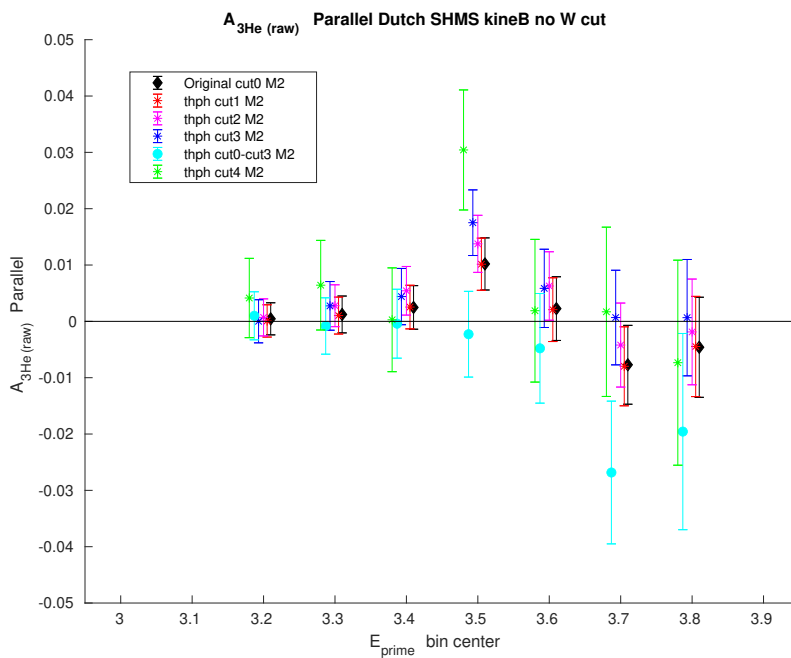
Figure B.3: Acceptance cut study for various SHMS θ, ϕ cuts. Plot of $A_\parallel$ with different θ, ϕ cuts (listed in Table B2) and with no w cuts.
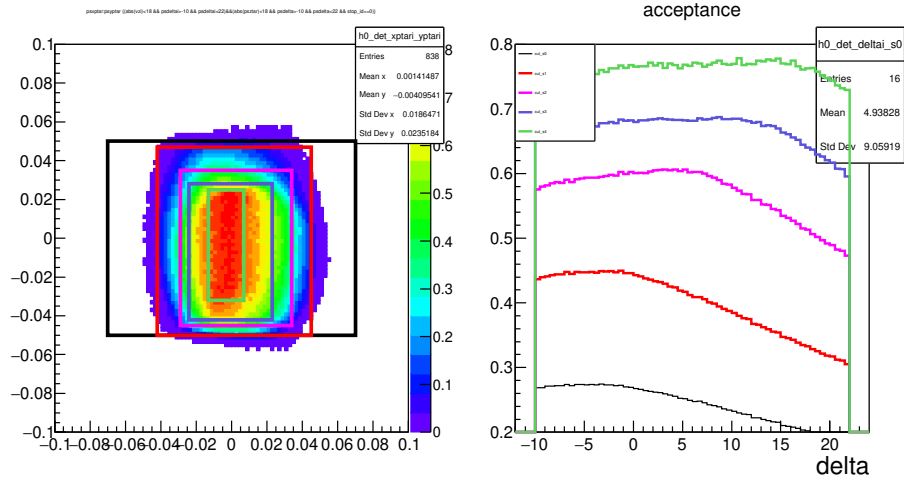
Figure B.4: Left: 2D plot of SHMS acceptance over ϕ (XPtar) and θ (YPtar) for different θ, ϕ cuts (listed in Table B2) Right: HMS acceptance vs. delta plot for different θ, ϕ cuts (listed in Table B2).

θ and ϕ Cuts (in mrad)	Cut on HCANA Leaf
Cut 0	$-60 < \theta < 60 \& -100 < \phi < 100$
Cut 1	$-55 < \theta < 55 \& -33 < \phi < 33$
Cut 2	$-45 < \theta < 45 \& -30 < \phi < 29$
Cut 3	$-31 < \theta < 33 \& -20 < \phi < 20$
Cut 4	$-20 < \theta < 20 \& -15 < \phi < 15$
Cut 5	$-65 < \theta < 65 \& -40 < \phi < 40$

Table B.1: List of various θ, ϕ cuts for HMS acceptance study.

θ and ϕ Cuts (in mrad)	Cut on HCANA Leaf
Cut 0	$-50 < \theta < 50 \& -70 < \phi < 70$
Cut 1	$-50 < \theta < 50 \& -42 < \phi < 45$
Cut 2	$-45 < \theta < 35 \& -29 < \phi < 34$
Cut 3	$-42 < \theta < 28 \& -24 < \phi < 23$
Cut 4	$-24 < \theta < 21 \& -13 < \phi < 7$

Table B.2: List of various θ, ϕ cuts for SHMS acceptance study.
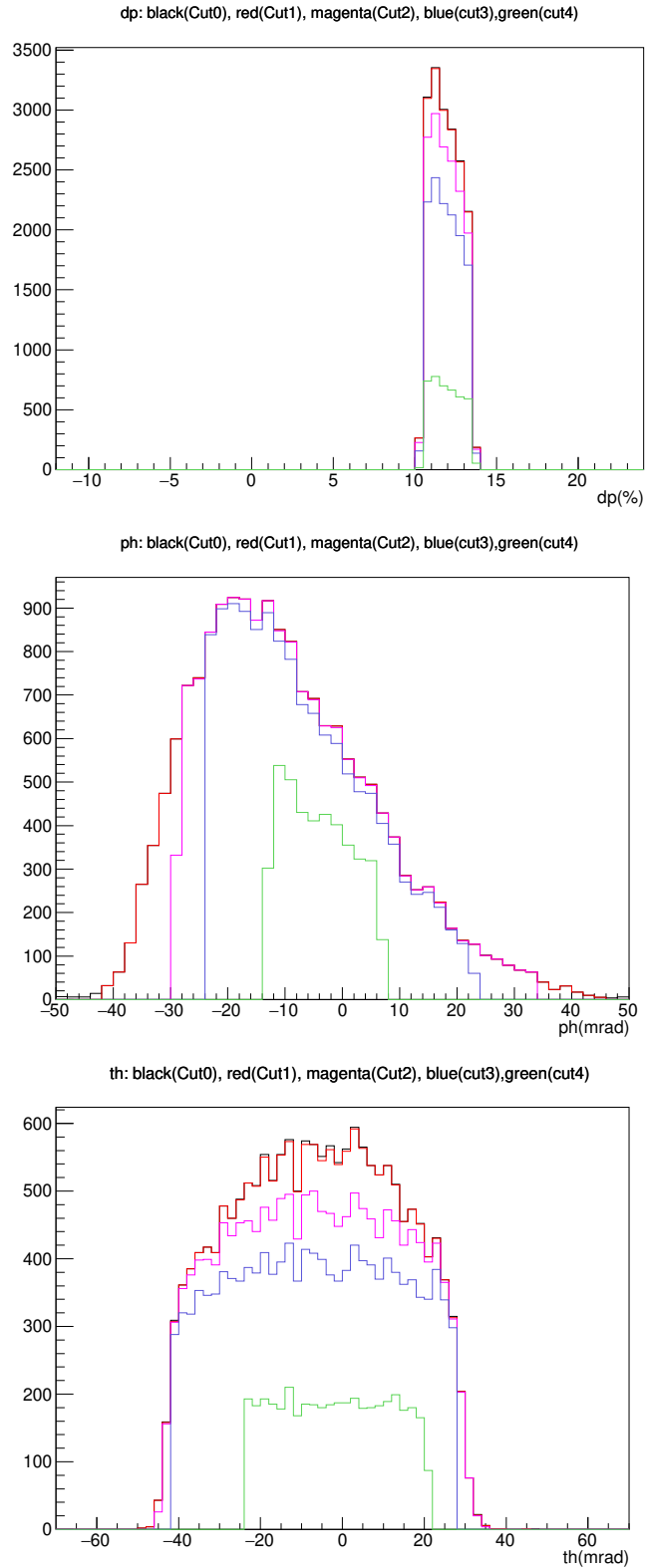
Figure B.5: SHMS event counts at $E' = 3.8$ GeV bin (100 MeV bin width) for different θ, ϕ cuts (listed in Table B2) Top: plot of SHMS event counts vs. delta. Middle: plot of SHMS event counts vs. ϕ. Bottom: plot of SHMS event counts vs. θ.
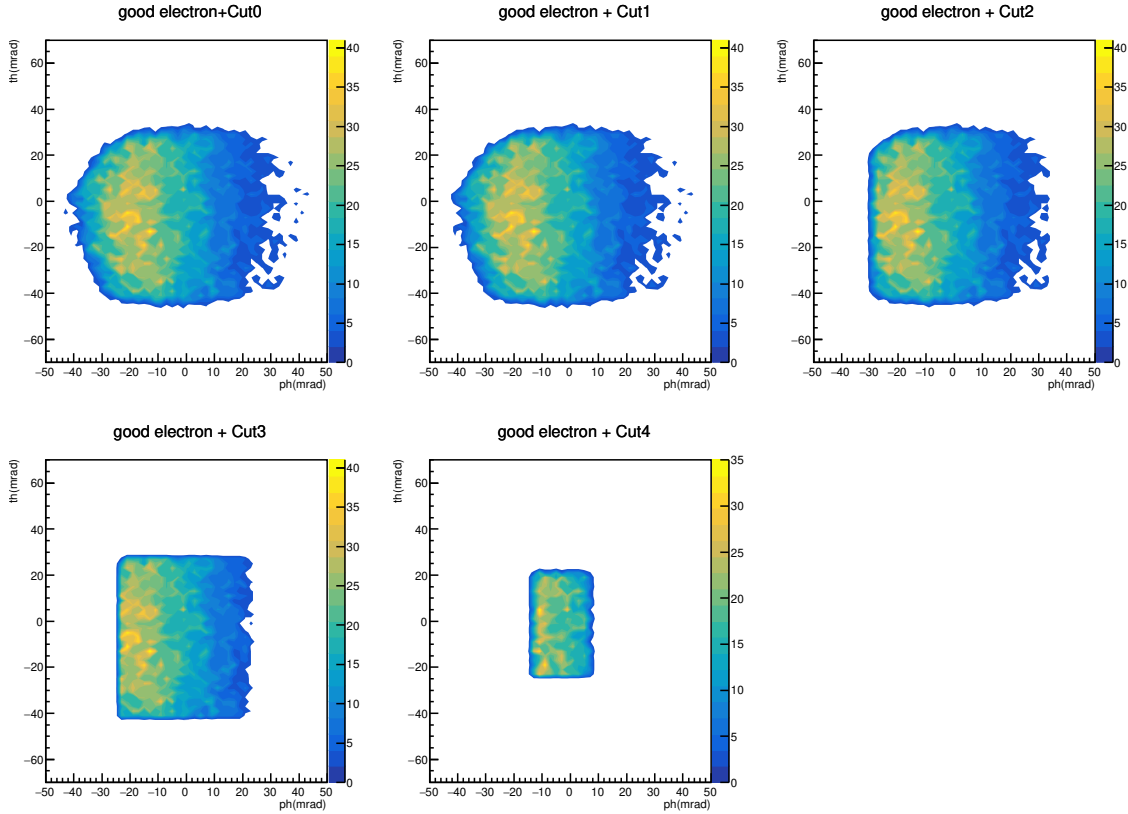
Figure B.6: 2D plot of SHMS event counts over ϕ (XPtar) and θ (YPtar) at $E' = 3.8$ GeV bin (100 MeV bin width) for different θ, ϕ cuts (listed in Table B2). The good electron cuts refers to the other spectrometer cuts used to select the electron events (listed in Table B4).

Variable	Cut on HCANA Leaf
Delta [%]	-8 < H.gtr.dp < 8
Z [cm]	-15 < H.react.z < 15
NPE	H.cer.npeSum>1.0
Cal E/P	0.8 < H.cal.etracknorm< 2.0

Table B.3: HMS: the good electron cuts needed for acceptance study. All in addition to a "ibcm1>3 μA" electron beam current cut.

Variable	Cut on HCANA Leaf
Delta [%]	-10 < P.gtr.dp < 22
Z [cm]	-15 < P.react.z < 15
NPE	P.ngcer.npeSum>2.0 (5-pass)
Cal E/P	0.8 < P.cal.etracknorm< 2.0

Table B.4: SHMS: the good electron cuts needed for acceptance study. All in addition to a "ibcm1>3 μA" electron beam current cut.

Appendix C

Tables for Physics Asymmetry

C.1 Systematic errors from PID Study

SHMS P_c	x	$\delta A_\parallel$	$\delta A_\perp$	HMS P_c	$\delta A_\parallel$	$\delta A_\perp$
2.6 GeV	0.4	0.0008	0.00073	2.9 GeV	NA	NA
	0.45	0.00098	0.00028		0.00197	0.00331
	0.5	0.00109	0.00087		0.00076	0.00357
	0.55	0.00116	0.00078		0.00059	0.00292
	0.6	0.0006	0.00297		0.00103	0.0057
	0.65	0.00224	0.01186		0.00054	0.00611
3.4 GeV	0.55	0.00166	0.00238	3.5 GeV	NA	NA
	0.6	0.00047	0.00121		0.00078	0.00375
	0.65	0.00067	0.00091		0.00068	0.00087
	0.7	0.00017	0.00085		0.00021	0.00127
	0.75	0.00028	0.00266		0.0002	0.00179

Table C.1: The systematic uncertainties from variations in the PID cuts for each x bin in both the SHMS and HMS. $\delta A_\parallel$ and $\delta A_\perp$ represent the magnitudes of the largest discrepancies observed when compared to the asymmetries generated using the standard PID analysis cuts (Cardona 2023).

C.2 Physics Asymmetry with DIS Wcuts

C.3 Physics Asymmetry with no Wcuts

E' (GeV)	x	Q^2 (GeV^2)	$A_\parallel$	$\delta A_{\parallel_{stat}}$	$\delta A_{\parallel_{sys}}$	$A_\perp$	$\delta A_{\perp_{stat}}$	$\delta A_{\perp_{sys}}$
3.22	0.64	8.60	0.00624	0.00544	0.00075	0.00273	0.01090	0.00108
3.24	0.64	8.64	0.00211	0.00486	0.00063	-0.00397	0.00976	0.00097
3.26	0.65	8.68	0.00019	0.00506	0.00065	0.00750	0.01000	0.00104
3.28	0.65	8.72	-0.00432	0.00521	0.00069	0.00862	0.01049	0.00110
3.30	0.66	8.76	-0.00209	0.00540	0.00070	0.00974	0.01077	0.00114
3.32	0.66	8.79	0.00955	0.00555	0.00083	-0.00927	0.01110	0.00116
3.34	0.67	8.82	-0.00834	0.00574	0.00082	-0.01908	0.01140	0.00141
3.36	0.67	8.85	0.00320	0.00595	0.00077	0.00136	0.01197	0.00117
3.38	0.68	8.88	-0.00824	0.00613	0.00044	0.00651	0.01228	0.00176
3.40	0.68	8.90	-0.01064	0.00633	0.00054	0.01003	0.01265	0.00184
3.42	0.68	8.93	0.00275	0.00658	0.00028	-0.00024	0.01318	0.00186
3.44	0.69	8.97	0.00490	0.00684	0.00035	-0.02380	0.01387	0.00223
3.46	0.69	8.98	-0.00092	0.00710	0.00028	0.01437	0.01421	0.00210
3.48	0.70	9.01	0.00040	0.00741	0.00029	-0.00244	0.01499	0.00212
3.50	0.70	9.02	0.00272	0.00777	0.00033	-0.00100	0.01572	0.00222
3.52	0.70	9.05	0.02326	0.00816	0.00109	-0.01720	0.01619	0.00241
3.54	0.71	9.06	-0.00512	0.00854	0.00040	0.03128	0.01707	0.00279
3.56	0.71	9.08	-0.00487	0.00897	0.00041	0.01435	0.01811	0.00263
3.58	0.71	9.09	-0.00375	0.00952	0.00041	-0.03095	0.01918	0.00304
3.60	0.72	9.11	-0.00979	0.01018	0.00059	-0.03235	0.02016	0.00319
3.62	0.72	9.13	0.00260	0.01094	0.00044	-0.00833	0.02179	0.00309
3.64	0.72	9.14	0.00579	0.01199	0.00054	-0.00952	0.02414	0.00343
3.66	0.73	9.16	0.01036	0.01335	0.00059	0.00932	0.02707	0.00387
3.68	0.73	9.17	-0.01048	0.01497	0.00062	-0.03992	0.02980	0.00459
3.70	0.73	9.20	0.03159	0.01717	0.00149	0.01883	0.03361	0.00485
3.72	0.74	9.21	0.00473	0.02090	0.00060	-0.01179	0.04201	0.00599
3.74	0.74	9.23	-0.01078	0.02680	0.00087	0.03740	0.05056	0.00737
3.76	0.74	9.21	0.00778	0.03847	0.00110	0.00264	0.07662	0.01088
3.78	0.75	9.25	0.16253	0.13672	0.00817	-0.16888	0.29904	0.04313

Table C.2: HMS physics asymmetries at high momentum $P_c = 3.5$ GeV with DIS $W > 2$ GeV cut.

E' (GeV)	x	Q^2 (GeV^2)	$A_\parallel$	$\delta A_{\parallel_{stat}}$	$\delta A_{\parallel_{sys}}$	$A_\perp$	$\delta A_{\perp_{stat}}$	$\delta A_{\perp_{sys}}$
2.66	0.499493	7.23568	0.00332	0.01021	0.00107	-0.02625	0.02741	0.00553
2.68	0.501243	7.24645	-0.00068	0.00601	0.00063	-0.01463	0.01675	0.00336
2.7	0.506768	7.30729	-0.01322	0.00661	0.00091	0.00500	0.01738	0.00343
2.72	0.511616	7.358	-0.00106	0.00648	0.00068	0.01783	0.01772	0.00358
2.74	0.516665	7.41118	-0.00356	0.00668	0.00071	0.01056	0.01789	0.00356
2.76	0.521586	7.46225	0.00309	0.00711	0.00075	0.01786	0.01847	0.00373
2.78	0.526541	7.51342	-0.00056	0.00724	0.00062	-0.00193	0.01851	0.00320
2.8	0.531343	7.56188	-0.00154	0.00730	0.00063	0.05564	0.01905	0.00413
2.82	0.536541	7.61576	-0.00518	0.00710	0.00065	-0.00117	0.01922	0.00333
2.84	0.541751	7.66935	-0.00044	0.00746	0.00064	-0.05857	0.01990	0.00433
2.86	0.546424	7.71515	0.00852	0.00763	0.00076	-0.01114	0.02000	0.00350
2.88	0.551655	7.76825	0.00415	0.00777	0.00069	0.00999	0.02071	0.00361
2.9	0.556905	7.82121	-0.00373	0.00703	0.00063	-0.00377	0.02056	0.00356
2.92	0.56206	7.87245	-0.00114	0.00767	0.00066	-0.01975	0.02118	0.00377
2.94	0.566476	7.91311	0.01606	0.00835	0.00102	-0.02347	0.02163	0.00389
2.96	0.571403	7.96045	0.00986	0.00854	0.00086	-0.03774	0.02196	0.00416
2.98	0.577639	8.02576	-0.01038	0.00813	0.00107	0.00418	0.02249	0.00596
3	0.583029	8.07882	0.00367	0.00845	0.00101	0.01022	0.02284	0.00607
3.02	0.589535	8.14683	-0.00559	0.00976	0.00118	0.00682	0.02346	0.00623
3.04	0.595194	8.20261	-0.03868	0.00930	0.00205	-0.01904	0.02390	0.00639
3.06	0.600074	8.24741	0.00091	0.00886	0.00105	-0.01181	0.02437	0.00648
3.08	0.607418	8.3255	0.01027	0.00895	0.00115	-0.01261	0.02610	0.00694
3.1	0.613612	8.38747	0.00055	0.00992	0.00117	0.02436	0.02676	0.00717
3.12	0.618593	8.43453	0.01900	0.01112	0.00156	-0.02997	0.03090	0.00830

Table C.3: HMS physics asymmetries at low momentum $P_c = 2.9$ GeV with DIS $W > 2$ GeV cut.

E' (GeV)	x	Q^2 (GeV^2)	$A_\parallel$	$\delta A_{\parallel_{stat}}$	$\delta A_{\parallel_{sys}}$	$A_\perp$	$\delta A_{\perp_{stat}}$	$\delta A_{\perp_{sys}}$
3.06	0.605201	8.31682	0.01607	0.00494	0.00085	0.01568	0.01255	0.00195
3.08	0.610043	8.3615	-0.00474	0.00458	0.00048	0.01459	0.01152	0.00179
3.1	0.615721	8.41621	-0.00915	0.00471	0.00060	0.00416	0.01177	0.00172
3.12	0.621818	8.47621	-0.00251	0.00485	0.00046	-0.00881	0.01213	0.00180
3.14	0.627788	8.53408	0.00864	0.00498	0.00080	0.01327	0.01250	0.00157
3.16	0.633791	8.5918	0.00609	0.00513	0.00077	-0.00767	0.01284	0.00153
3.18	0.639258	8.64195	-0.00191	0.00528	0.00075	0.00011	0.01309	0.00152
3.2	0.645786	8.70602	-0.00139	0.00541	0.00077	0.00253	0.01380	0.00160
3.22	0.651434	8.75769	0.00915	0.00558	0.00089	0.02022	0.01385	0.00185
3.24	0.65727	8.81143	-0.00109	0.00573	0.00081	-0.00373	0.01434	0.00167
3.26	0.662725	8.85966	0.00306	0.00583	0.00083	0.00694	0.01474	0.00174
3.28	0.667755	8.90203	0.00024	0.00599	0.00084	0.01805	0.01502	0.00192
3.3	0.673158	8.9486	-0.00867	0.00619	0.00096	-0.00472	0.01541	0.00180
3.32	0.677527	8.98141	0.01227	0.00638	0.00058	0.01740	0.01603	0.00165
3.34	0.682216	9.01788	0.00337	0.00661	0.00025	-0.00417	0.01635	0.00150
3.36	0.686525	9.04909	-0.00358	0.00690	0.00026	-0.00636	0.01709	0.00158
3.38	0.691186	9.08462	0.01066	0.00719	0.00052	-0.00615	0.01770	0.00163
3.4	0.695694	9.11778	0.00693	0.00754	0.00038	0.00004	0.01895	0.00172
3.42	0.698986	9.13474	0.00110	0.00781	0.00024	0.00175	0.01961	0.00179
3.44	0.703168	9.16298	-0.00419	0.00819	0.00031	-0.04109	0.02043	0.00262
3.46	0.706417	9.17874	0.02080	0.00863	0.00097	-0.01161	0.02165	0.00204
3.48	0.70959	9.19345	0.01289	0.00917	0.00064	-0.04147	0.02262	0.00277
3.5	0.713875	9.2221	0.00818	0.00966	0.00047	0.02920	0.02436	0.00257
3.52	0.717105	9.23693	-0.01603	0.01025	0.00078	0.01033	0.02582	0.00240
3.54	0.720755	9.25697	0.00165	0.01094	0.00034	-0.01738	0.02755	0.00263
3.56	0.723862	9.26993	0.01612	0.01193	0.00081	-0.01567	0.03003	0.00282
3.58	0.727732	9.29185	0.00108	0.01287	0.00041	-0.03256	0.03217	0.00606
3.6	0.730528	9.3003	0.00123	0.01389	0.00045	0.00648	0.03425	0.00627
3.62	0.733511	9.31089	-0.00470	0.01558	0.00054	-0.05535	0.03845	0.00746
3.64	0.736205	9.31771	0.00487	0.01753	0.00060	0.02448	0.04317	0.00798
3.66	0.738447	9.31848	0.00801	0.02003	0.00073	0.03170	0.04920	0.00912
3.68	0.741306	9.32691	0.02311	0.02376	0.00129	0.00683	0.05677	0.01039
3.7	0.743698	9.33012	0.02468	0.02772	0.00142	-0.09047	0.07140	0.01368
3.72	0.745773	9.32901	0.01053	0.03531	0.00122	0.19034	0.14075	0.02713
3.74	0.747817	9.33048	-0.04468	0.04447	0.00246	0.09549	0.11408	0.02131

Table C.4: SHMS physics asymmetries at high momentum $P_c = 3.4$ GeV with DIS $W > 2$ GeV cut.

E' (GeV)	x	Q^2 (GeV^2)	$A_\parallel$	$\delta A_{\parallel stat}$	$\delta A_{\parallel sys}$	$A_\perp$	$\delta A_{\perp stat}$	$\delta A_{\perp sys}$
2.34	0.42	6.41	-0.00615	0.00711	0.00078	-0.02459	0.01754	0.00128
2.36	0.43	6.45	-0.00292	0.00648	0.00119	0.02205	0.01563	0.00104
2.38	0.43	6.51	-0.00283	0.00659	0.00121	-0.00485	0.01608	0.00040
2.40	0.44	6.58	-0.01186	0.00671	0.00133	-0.00279	0.01626	0.00036
2.42	0.44	6.64	0.00185	0.00682	0.00124	0.02182	0.01656	0.00104
2.44	0.45	6.70	0.00480	0.00698	0.00129	0.00464	0.01705	0.00041
2.46	0.45	6.76	0.00375	0.00707	0.00130	0.00586	0.01701	0.00044
2.48	0.46	6.81	-0.00206	0.00719	0.00131	-0.03109	0.01722	0.00144
2.50	0.46	6.87	-0.01849	0.00727	0.00156	0.03012	0.01765	0.00140
2.52	0.47	6.92	-0.00245	0.00745	0.00136	0.00595	0.01783	0.00046
2.54	0.47	6.98	-0.00425	0.00753	0.00138	-0.00532	0.01833	0.00045
2.56	0.48	7.05	0.00897	0.00769	0.00145	0.00199	0.01867	0.00109
2.58	0.49	7.12	0.00067	0.00784	0.00142	-0.02650	0.01883	0.00161
2.60	0.49	7.18	-0.01054	0.00796	0.00152	0.01324	0.01927	0.00127
2.62	0.50	7.23	0.01290	0.00811	0.00158	-0.05101	0.01985	0.00256
2.64	0.50	7.29	0.01097	0.00825	0.00157	-0.00742	0.02015	0.00122
2.66	0.51	7.35	-0.00230	0.00852	0.00155	-0.00211	0.02050	0.00119
2.68	0.51	7.40	-0.00120	0.00864	0.00156	-0.04223	0.02131	0.00226
2.70	0.52	7.45	0.00470	0.00886	0.00162	0.03854	0.02088	0.00211
2.72	0.52	7.51	0.00644	0.00910	0.00167	-0.02259	0.02190	0.00162
2.74	0.53	7.56	-0.01083	0.00925	0.00149	0.00564	0.02233	0.00095
2.76	0.53	7.61	-0.01085	0.00945	0.00152	0.01367	0.02319	0.00113
2.78	0.54	7.67	-0.00083	0.00974	0.00148	-0.00200	0.02341	0.00096
2.80	0.54	7.73	-0.00322	0.01001	0.00153	0.04673	0.02376	0.00231
2.82	0.55	7.79	-0.01213	0.01023	0.00165	-0.00175	0.02456	0.00101
2.84	0.55	7.84	0.01056	0.01056	0.00167	0.02048	0.02495	0.00137
2.86	0.56	7.90	0.00520	0.01081	0.00166	0.05072	0.02645	0.00252
2.88	0.56	7.95	0.00434	0.01122	0.00172	0.00014	0.02697	0.00111
2.90	0.57	8.01	0.02758	0.01144	0.00213	-0.04516	0.02840	0.00234
2.92	0.58	8.06	-0.00035	0.01175	0.00069	-0.06276	0.02877	0.00439
2.94	0.58	8.12	-0.00136	0.01210	0.00072	0.00976	0.02946	0.00347
2.96	0.59	8.17	-0.00279	0.01258	0.00075	-0.01590	0.02967	0.00354
2.98	0.59	8.23	0.01255	0.01299	0.00095	-0.00894	0.03095	0.00364
3.00	0.60	8.29	0.01069	0.01323	0.00092	0.01177	0.03306	0.00390
3.02	0.60	8.36	0.00033	0.01376	0.00081	0.05214	0.03354	0.00457
3.04	0.61	8.40	0.01632	0.01399	0.00110	-0.01181	0.03437	0.00406
3.06	0.62	8.47	-0.01497	0.01455	0.00109	0.00095	0.03477	0.00407
3.08	0.62	8.52	0.01005	0.01509	0.00100	-0.05088	0.03692	0.00489
3.10	0.63	8.58	0.00975	0.01558	0.00218	0.00910	0.03776	0.01096
3.12	0.63	8.64	-0.00362	0.01601	0.00220	-0.03595	0.03892	0.01140
3.14	0.64	8.69	-0.01865	0.01672	0.00244	-0.01333	0.04012	0.01165
3.16	0.64	8.70	-0.00615	0.02040	0.00281	-0.03717	0.04799	0.01402

Table C.5: SHMS physics asymmetries at low momentum $P_c = 2.6$ GeV with DIS

E' (GeV)	x	Q^2 (GeV^2)	$A_\parallel$	$\delta A_{\parallel stat}$	$\delta A_{\parallel sys}$	$A_\perp$	$\delta A_{\perp stat}$	$\delta A_{\perp sys}$
3.22	0.640437	8.60838	0.00624	0.00543	0.00075	0.00268	0.01088	0.00107
3.24	0.645528	8.65403	0.00173	0.00484	0.00062	-0.00134	0.00973	0.00096
3.26	0.650898	8.70157	0.00109	0.00503	0.00065	0.00657	0.00994	0.00102
3.28	0.656345	8.74981	-0.00465	0.00516	0.00069	0.00901	0.01039	0.00110
3.3	0.661889	8.79883	-0.00067	0.00533	0.00068	0.01153	0.01063	0.00116
3.32	0.667443	8.84758	0.00908	0.00545	0.00081	-0.00991	0.01090	0.00116
3.34	0.672799	8.89337	-0.00803	0.00559	0.00080	-0.02058	0.01112	0.00143
3.36	0.678339	8.94114	0.00436	0.00575	0.00030	0.00095	0.01157	0.00163
3.38	0.684563	8.99751	-0.00319	0.00588	0.00027	-0.00274	0.01180	0.00167
3.4	0.689071	9.03082	-0.00773	0.00603	0.00042	0.00884	0.01205	0.00175
3.42	0.695502	9.08903	0.00165	0.00620	0.00025	0.00344	0.01237	0.00175
3.44	0.70228	9.15126	0.00404	0.00637	0.00031	-0.02154	0.01287	0.00206
3.46	0.70768	9.19509	0.00021	0.00651	0.00025	0.00974	0.01309	0.00190
3.48	0.713673	9.24622	-0.00260	0.00670	0.00029	0.00061	0.01362	0.00192
3.5	0.718338	9.27965	0.00701	0.00694	0.00041	0.00593	0.01397	0.00199
3.52	0.725061	9.33922	0.01964	0.00712	0.00090	-0.01656	0.01422	0.00215
3.54	0.729535	9.36962	-0.00576	0.00735	0.00033	0.03786	0.01459	0.00268
3.56	0.735856	9.42317	0.00207	0.00756	0.00022	0.00400	0.01512	0.00215
3.58	0.740704	9.45746	0.00378	0.00780	0.00027	-0.01695	0.01563	0.00235
3.6	0.746806	9.50725	-0.00448	0.00807	0.00030	-0.02427	0.01593	0.00251
3.62	0.754071	9.57142	0.00650	0.00835	0.00037	-0.01358	0.01668	0.00245
3.64	0.760789	9.62828	0.00326	0.00871	0.00028	-0.00930	0.01735	0.00250
3.66	0.768604	9.69834	0.00454	0.00906	0.00032	-0.01794	0.01814	0.00270
3.68	0.77475	9.74673	-0.00084	0.00946	0.00026	-0.03321	0.01880	0.00306
3.7	0.781299	9.79989	0.02490	0.00984	0.00115	-0.01939	0.01988	0.00295
3.72	0.789604	9.87437	0.00650	0.01039	0.00040	0.01515	0.02074	0.00302
3.74	0.796237	9.92746	0.01409	0.01084	0.00070	0.02169	0.02174	0.00324
3.76	0.803303	9.98626	-0.00288	0.01162	0.00034	-0.02231	0.02338	0.00347
3.78	0.803903	9.97201	0.02126	0.02662	0.00119	0.00833	0.05390	0.00766

Table C.6: HMS physics asymmetries at high momentum $P_c = 3.5$ GeV with no DIS cuts.

E' (GeV)	x	Q^2 (GeV^2)	$A_\parallel$	$\delta A_{\parallel_{stat}}$	$\delta A_{\parallel_{sys}}$	$A_\perp$	$\delta A_{\perp_{stat}}$	$\delta A_{\perp_{sys}}$
2.66	0.499493	7.23568	0.00332	0.01021	0.00107	-0.02625	0.02741	0.00553
2.68	0.501243	7.24645	-0.00068	0.00601	0.00063	-0.01463	0.01675	0.00336
2.7	0.506768	7.30729	-0.01322	0.00661	0.00091	0.00500	0.01738	0.00343
2.72	0.511616	7.358	-0.00106	0.00648	0.00068	0.01783	0.01772	0.00358
2.74	0.516665	7.41118	-0.00356	0.00668	0.00071	0.01056	0.01789	0.00356
2.76	0.521586	7.46225	0.00309	0.00711	0.00075	0.01786	0.01847	0.00373
2.78	0.526541	7.51342	-0.00056	0.00724	0.00062	-0.00193	0.01851	0.00320
2.8	0.531343	7.56188	-0.00154	0.00730	0.00063	0.05564	0.01905	0.00413
2.82	0.536541	7.61576	-0.00518	0.00710	0.00065	-0.00117	0.01922	0.00333
2.84	0.541751	7.66935	-0.00044	0.00746	0.00064	-0.05857	0.01990	0.00433
2.86	0.546424	7.71515	0.00852	0.00763	0.00076	-0.01114	0.02000	0.00350
2.88	0.551655	7.76825	0.00415	0.00777	0.00069	0.00999	0.02071	0.00361
2.9	0.556905	7.82121	-0.00373	0.00703	0.00063	-0.00377	0.02056	0.00356
2.92	0.56206	7.87245	-0.00114	0.00767	0.00066	-0.01975	0.02118	0.00377
2.94	0.566476	7.91311	0.01606	0.00835	0.00102	-0.02347	0.02163	0.00389
2.96	0.571403	7.96045	0.00986	0.00854	0.00086	-0.03774	0.02196	0.00416
2.98	0.577639	8.02576	-0.01038	0.00813	0.00107	0.00418	0.02249	0.00596
3	0.583029	8.07882	0.00367	0.00845	0.00101	0.01022	0.02284	0.00607
3.02	0.589535	8.14683	-0.00559	0.00976	0.00118	0.00682	0.02346	0.00623
3.04	0.595194	8.20261	-0.03868	0.00930	0.00205	-0.01904	0.02390	0.00639
3.06	0.600088	8.2476	0.00101	0.00886	0.00105	-0.01181	0.02437	0.00648
3.08	0.607431	8.32569	0.01015	0.00895	0.00115	-0.01261	0.02610	0.00694
3.1	0.613612	8.38747	0.00055	0.00992	0.00117	0.02436	0.02676	0.00717
3.12	0.618593	8.43453	0.01900	0.01112	0.00156	-0.02997	0.03090	0.00830

Table C.7: HMS physics asymmetries at low momentum $P_c = 2.9$ GeV with no DIS cuts.

E' (GeV)	x	Q^2 (GeV^2)	$A_\parallel$	$\delta A_{\parallel stat}$	$\delta A_{\parallel sys}$	$A_\perp$	$\delta A_{\perp stat}$	$\delta A_{\perp sys}$
3.04	0.61	8.43	0.02377	0.01875	0.00204	-0.03361	0.04988	0.00739
3.06	0.61	8.32	0.01607	0.00494	0.00085	0.01568	0.01255	0.00195
3.08	0.61	8.36	-0.00474	0.00458	0.00048	0.01459	0.01152	0.00179
3.10	0.62	8.42	-0.00915	0.00471	0.00060	0.00416	0.01177	0.00172
3.12	0.62	8.48	-0.00251	0.00485	0.00046	-0.00881	0.01213	0.00180
3.14	0.63	8.53	0.00864	0.00498	0.00080	0.01327	0.01250	0.00157
3.16	0.63	8.59	0.00609	0.00513	0.00077	-0.00767	0.01284	0.00153
3.18	0.64	8.64	-0.00191	0.00528	0.00075	0.00011	0.01309	0.00152
3.20	0.65	8.71	-0.00139	0.00541	0.00077	0.00253	0.01380	0.00160
3.22	0.65	8.76	0.00915	0.00558	0.00089	0.02022	0.01385	0.00185
3.24	0.66	8.81	-0.00109	0.00573	0.00081	-0.00373	0.01434	0.00167
3.26	0.66	8.86	0.00306	0.00583	0.00083	0.00694	0.01474	0.00174
3.28	0.67	8.91	0.00027	0.00599	0.00084	0.01805	0.01502	0.00192
3.30	0.67	8.97	-0.00854	0.00618	0.00095	-0.00398	0.01538	0.00179
3.32	0.68	9.02	0.01202	0.00633	0.00057	0.01514	0.01593	0.00160
3.34	0.69	9.07	0.00361	0.00652	0.00025	-0.00297	0.01613	0.00147
3.36	0.69	9.13	-0.00279	0.00674	0.00024	-0.00722	0.01670	0.00155
3.38	0.70	9.19	0.01047	0.00695	0.00051	-0.00825	0.01713	0.00160
3.40	0.71	9.26	0.00262	0.00720	0.00025	0.00613	0.01816	0.00168
3.42	0.71	9.30	0.00231	0.00737	0.00024	0.00221	0.01851	0.00169
3.44	0.72	9.35	-0.00393	0.00759	0.00029	-0.02574	0.01899	0.00208
3.46	0.72	9.40	0.02012	0.00787	0.00093	-0.01697	0.01977	0.00195
3.48	0.73	9.46	0.00898	0.00816	0.00048	-0.02947	0.02029	0.00394
3.50	0.74	9.50	0.01590	0.00842	0.00076	0.01339	0.02129	0.00394
3.52	0.74	9.55	-0.00838	0.00868	0.00047	-0.00188	0.02191	0.00401
3.54	0.75	9.61	0.00565	0.00900	0.00038	-0.00097	0.02266	0.00415
3.56	0.75	9.67	0.00763	0.00942	0.00046	-0.00116	0.02358	0.00432
3.58	0.76	9.72	0.00571	0.00974	0.00040	-0.05407	0.02431	0.00507
3.60	0.77	9.75	0.01080	0.01006	0.00058	0.02000	0.02507	0.00467
3.62	0.77	9.81	0.00179	0.01058	0.00035	-0.01598	0.02642	0.00489
3.64	0.78	9.87	0.01413	0.01092	0.00072	0.04221	0.02776	0.00542
3.66	0.79	9.91	-0.00370	0.01143	0.00040	0.04133	0.02815	0.00548
3.68	0.79	9.97	0.00149	0.01210	0.00039	-0.00218	0.02934	0.00537
3.70	0.80	10.01	0.01121	0.01231	0.00064	0.01498	0.05440	0.00998

Table C.8: SHMS physics asymmetries at high momentum $P_c = 3.4$ GeV with no DIS cuts.(first part of the table)

E' (GeV)	x	Q^2 (GeV^2)	$A_\parallel$	$\delta A_{\parallel stat}$	$\delta A_{\parallel sys}$	$A_\perp$	$\delta A_{\perp stat}$	$\delta A_{\perp sys}$
3.72	0.81	10.08	0.01812	0.01309	0.00091	-0.00597	0.03290	0.00603
3.74	0.81	10.13	0.00218	0.01370	0.00045	0.01186	0.03500	0.00643
3.76	0.82	10.19	0.01041	0.01427	0.00065	0.00540	0.03571	0.00654
3.78	0.83	10.24	-0.02739	0.01506	0.00132	-0.07586	0.03859	0.00784
3.80	0.83	10.29	0.01572	0.01552	0.00086	-0.01727	0.03887	0.00716
3.82	0.84	10.34	-0.00030	0.01647	0.00053	0.02941	0.04170	0.00774
3.84	0.85	10.38	0.00862	0.01735	0.00068	-0.07959	0.04284	0.00861
3.86	0.85	10.44	0.01011	0.01841	0.00074	-0.05684	0.04633	0.00885
3.88	0.86	10.51	-0.02822	0.01924	0.00141	0.04967	0.04706	0.00889
3.90	0.87	10.53	0.01673	0.02033	0.00099	-0.09592	0.04943	0.01002
3.92	0.87	10.55	0.02880	0.02147	0.00146	0.05906	0.05208	0.00989
3.94	0.88	10.63	0.01592	0.02277	0.00102	0.01282	0.05491	0.01006
3.96	0.89	10.69	-0.01096	0.02358	0.00090	-0.06426	0.06023	0.01139
3.98	0.90	10.77	0.01540	0.02491	0.00105	0.03402	0.06456	0.01191
4.00	0.90	10.77	0.02519	0.02696	0.00142	-0.06299	0.06428	0.01210
4.02	0.91	10.89	-0.01650	0.02769	0.00115	0.12857	0.07216	0.01441
4.04	0.92	10.90	0.06452	0.03004	0.00305	0.02501	0.07605	0.01396
4.06	0.92	10.94	-0.04348	0.03230	0.00221	0.01537	0.08490	0.01555
4.08	0.93	11.03	-0.01290	0.03367	0.00122	-0.00992	0.08471	0.01551
4.10	0.94	11.07	0.01520	0.03626	0.00135	-0.10556	0.08446	0.01617

Table C.9: SHMS physics asymmetries at high momentum $P_c = 3.4$ GeV with no DIS cuts. (continued table)

E' (GeV)	x	Q^2 (GeV^2)	$A_\parallel$	$\delta A_{\parallel_{stat}}$	$\delta A_{\parallel_{sys}}$	$A_\perp$	$\delta A_{\perp_{stat}}$	$\delta A_{\perp_{sys}}$
2.34	0.42	6.41	-0.00615	0.00711	0.00078	-0.02459	0.01754	0.00128
2.36	0.43	6.45	-0.00292	0.00648	0.00119	0.02205	0.01563	0.00104
2.38	0.43	6.51	-0.00283	0.00659	0.00121	-0.00485	0.01608	0.00040
2.40	0.44	6.58	-0.01186	0.00671	0.00133	-0.00279	0.01626	0.00036
2.42	0.44	6.64	0.00185	0.00682	0.00124	0.02182	0.01656	0.00104
2.44	0.45	6.70	0.00480	0.00698	0.00129	0.00464	0.01705	0.00041
2.46	0.45	6.76	0.00375	0.00707	0.00130	0.00586	0.01701	0.00044
2.48	0.46	6.81	-0.00206	0.00719	0.00131	-0.03109	0.01722	0.00144
2.50	0.46	6.87	-0.01849	0.00727	0.00156	0.03012	0.01765	0.00140
2.52	0.47	6.92	-0.00245	0.00745	0.00136	0.00595	0.01783	0.00046
2.54	0.47	6.98	-0.00425	0.00753	0.00138	-0.00532	0.01833	0.00045
2.56	0.48	7.05	0.00897	0.00769	0.00145	0.00199	0.01867	0.00109
2.58	0.49	7.12	0.00067	0.00784	0.00142	-0.02650	0.01883	0.00161
2.60	0.49	7.18	-0.01054	0.00796	0.00152	0.01324	0.01927	0.00127
2.62	0.50	7.23	0.01290	0.00811	0.00158	-0.05101	0.01985	0.00256
2.64	0.50	7.29	0.01097	0.00825	0.00157	-0.00742	0.02015	0.00122
2.66	0.51	7.35	-0.00230	0.00852	0.00155	-0.00211	0.02050	0.00119
2.68	0.51	7.40	-0.00120	0.00864	0.00156	-0.04223	0.02131	0.00226
2.70	0.52	7.45	0.00470	0.00886	0.00162	0.03854	0.02088	0.00211
2.72	0.52	7.51	0.00644	0.00910	0.00167	-0.02259	0.02190	0.00162
2.74	0.53	7.56	-0.01083	0.00925	0.00149	0.00564	0.02233	0.00095
2.76	0.53	7.61	-0.01085	0.00945	0.00152	0.01367	0.02319	0.00113
2.78	0.54	7.67	-0.00083	0.00974	0.00148	-0.00200	0.02341	0.00096
2.80	0.54	7.73	-0.00322	0.01001	0.00153	0.04673	0.02376	0.00231
2.82	0.55	7.79	-0.01213	0.01023	0.00165	-0.00175	0.02456	0.00101
2.84	0.55	7.84	0.01056	0.01056	0.00167	0.02048	0.02495	0.00137
2.86	0.56	7.90	0.00520	0.01081	0.00166	0.05072	0.02645	0.00252
2.88	0.56	7.95	0.00434	0.01122	0.00172	0.00014	0.02697	0.00111
2.90	0.57	8.01	0.02758	0.01144	0.00213	-0.04516	0.02840	0.00234
2.92	0.58	8.06	-0.00035	0.01175	0.00069	-0.06276	0.02877	0.00439
2.94	0.58	8.12	-0.00136	0.01210	0.00072	0.00976	0.02946	0.00347
2.96	0.59	8.17	-0.00279	0.01258	0.00075	-0.01590	0.02967	0.00354
2.98	0.59	8.23	0.01255	0.01299	0.00095	-0.00894	0.03095	0.00364
3.00	0.60	8.29	0.01069	0.01323	0.00092	0.01177	0.03306	0.00390
3.02	0.60	8.36	0.00033	0.01376	0.00081	0.05214	0.03354	0.00457
3.04	0.61	8.40	0.01632	0.01399	0.00110	-0.01181	0.03437	0.00406
3.06	0.62	8.47	-0.01497	0.01455	0.00109	0.00095	0.03477	0.00407
3.08	0.62	8.52	0.01005	0.01509	0.00100	-0.05088	0.03692	0.00489
3.10	0.63	8.58	0.00975	0.01558	0.00218	0.00910	0.03776	0.01096
3.12	0.63	8.64	-0.00362	0.01601	0.00220	-0.03595	0.03892	0.01140
3.14	0.64	8.69	-0.01865	0.01672	0.00244	-0.01333	0.04012	0.01165
3.16	0.64	8.70	-0.00615	0.02040	0.00281	-0.03717	0.04799	0.01402

Table C.10: SHMS physics asymmetries at low momentum $P_c = 2.6$ GeV with no